ANALYSIS OF SUB-MICRON MINERAL MATTER IN COAL VIA SCANNING TRANSMISSION ELECTRON MICROSCOPY*

Robert M. Allen and John B. VanderSande**

Materials Science Division
Sandia National Laboratories
Livermore, California 94550
**Department of Materials Science and Engineering
Massachusetts Institute of Technology
Cambridge, Massachusetts 02139

The mineral matter present in coal plays a deleterious role during the combustion of pulverized coal fuel in power generating boilers. Recent papers (1-3) on such problems as heat exchanger fouling and the emission of particulate pollutants from boilers have indicated that a fundamental understanding of these problems (and hence clues as to how they may be mitigated) may not depend solely on analyzing the fraction of mineral matter in the coal and its gross chemical composition. It may also prove necessary to obtain data on the actual size distribution of the original mineral particles and inclusions, and the distribution of these minerals among the particles of the pulverized fuel.

Such detailed information cannot be obtained by the traditional means of coal minerals analysis. However, recent advances in electron optical instrumentation and techniques, such as the use of a scanning transmission electron microscope (STEM) for high spatial resolution chemical microanalysis, show great promise for this type of characterization and have already been applied to coal research (4-7). The present work involves the use of a STEM both to obtain quantitative information about the ultra-fine (<100nm diameter) mineral inclusions present in several coals, and to examine the inorganic elements (hereafter referred to as inherent mineral matter) atomically bound into the organic matrices of these coals. It is anticipated that this type of information will be useful in modeling the combustion of pulverized fuel particles.

Sample Preparation

Samples of three different coals were examined in the present study: A lignite from the Hagel Seam in North Dakota, a semianthracite from the #2 Seam in Pennsylvania, and a sample of pulverized bituminous coal obtained courtesy of the Tennessee Valley Authority. The gross inorganic chemical analyses of the high temperature ash (HTA) of these three coals is shown in Table I.

Preparation of specimens for STEM examination was straightforward. Samples of each coal were ground to a fine powder using a mortar and pestle (except for the fuel coal which was already in pulverized form). A standard 3mm diameter 200 mesh copper transmission electron microscope grid coated with a thin carbon support film was then dipped into the powdered coal. Upon removal the grid was tapped several times to shake off excess and oversize particles. The final result was a sample consisting of a thin dispersion of fine coal particles clinging to the carbon support film.

Specimens prepared in this manner are well suited for STEM viewing and have several advantages compared to specimens thinned from the bulk by microtoming or ion milling. Their most notable advantage is of course the ease of preparation. Along with this, since nearly all the particles clinging to the grid have at least some area transparent to the electron beam, a much greater amount of thin area more randomly dispersed in origin from within the coal is potentially available for STEM examination than would be found in specimens thinned from bulk samples. Results obtained from powdered coal specimens should therefore be more representative of the overall mineral content of the initial coal sample.

*This work supported by U.S. Department of Energy, DOE, under contract number DE-AC04-76DP00798.

Table I: Compositions of High Temperature Ash (HTA)

Coal Name	Hagel Seam*	Cumberland Fuel**	Pennsylvania #2 Seam*
Coal Rank	Lignite	High Volatile Bituminous	Semianthracite
%HTA	9.66	18.8	30.74
SiO_2(%a)***	28.20	51.3	80.00
Al_2O_3(%a)	9.35	19.8	12.10
TiO_2(%a)	0.58	0.2	3.09
Fe_2O_3(%a)	8.20	17.0	1.47
MgO(%a)	5.91	1.2	0.05
CaO(%a)	24.50	4.9	0.30
Na_2O(%a)	2.81	0.9	0.05
K_2O(%a)	0.33	2.8	0.35
P_2O_5(%a)	0.10	0.2	0.05
SO_3(%a)	17.40	1.6	0.30
Trace Elements >1000ppm of HTA (in ppm of HTA)	Ba-6700 Sr-3150	Not Available	None Reported

*Information courtesy of the Penn State Coal Data Base
**Information taken from reference (8).
***%a - oxide % of HTA of dry coal

Experimental Procedure

The STEM used in the present study was a JOEL 200CX equipped with a Tracor-Northern TN2000 energy dispersive spectrometry (EDS) system for x-ray analysis. The features of STEM operation pertinent to this work are illustrated in Figure 1. The sample was illuminated by a narrow probe of 200kV electrons which was scanned across its surface. Transmitted electrons were used to form an image of the sample volume being scanned. The probe could also be stopped and fixed on some feature of interest in the sample, at which point the characteristic x-rays emitted by the atoms under the probe could be analyzed to obtain chemical information from a sample region with a diameter approaching that of the probe diameter. Chemical characterization could be accomplished in this manner for all elements with atomic number $Z \geq 11$.

For studies of mineral matter embedded in particles of powdered coal, advantage was taken of the difference in image contrast between the crystalline mineral particles and the surrounding amorphous organic matrix. The crystalline particles are capable of diffracting electrons, and so appeared in strong contrast when held at specific angles to the incident electron beam. The sample thus needed only to be tilted through some moderate range of angles (generally $\pm 45°$ from the horizontal) to quickly establish the locations of the minerals within a given coal particle. During the tilting such particles abruptly "winked" in and out of strong diffraction contrast, while the amorphous matrix changed contrast only gradually as a function of the change in sample thickness intercepted by the electron beam. An example of an image of a mineral particle visible by strong diffraction contrast amidst an amorphous coal matrix is shown in Figure 2. It is estimated that the imaging procedure could detect mineral particles with diameters ~ 2nm. Particles smaller than this would most likely remain indistinguishable from the amorphous matrix.

With the location of an embedded mineral particle thus determined, the probe was fixed on the mineral and an x-ray spectrum was acquired. Except in the instance where the mineral extended through the full thickness of the coal particle intercepted by the probe, this spectrum consisted of a superposition of a particle spectrum and a matrix spectrum. To determine the signal associated with the inclusion, the probe was subsequently moved 1-2 particle diameters away to a region of the matrix known to be free of other minerals (within the resolution limitation

discussed in the preceeding paragraph), where a second spectrum was collected. Comparison of the two x-ray spectra generally quickly revealed the primary elemental constituents of the mineral (again, for elements of atomic number $Z \geq 11$). Two examples of this type of analysis are shown for a Ti-rich particle in the Cumberland fuel coal in Figure 3, and a particle rich in Ba and S in the Hagel Seam coal in Figure 4.

Results and Discussion

The results of the STEM examination of the three coals are summarized in Table II. The first half of the table deals with the data obtained in a random sampling of mineral inclusions with mean diameters <100nm which were found embedded in the coal particles. Quantitative results are presented for the two most frequently observed mineral types in this size range for each of the three starting coals.

The second half of the table describes the results of the matrix measurements which were undertaken concurrently with the particle analyses. Aside from being necessary to correctly identify the constituents associated with the discrete mineral particles, the matrix spectra themselves provided additional information on the inherent mineral elements atomically bound into the organic coal matrix, without the danger of confusion from elements in discrete mineral particles (at least for particles larger than ~2nm in size). Recent work has suggested that such inherent mineral matter may comprise >15% of the total mineral matter in pulverized fuels (8).

Table II: Results of STEM Analysis

Coal Name		Hagel Seam	Cumberland Fuel	Penn.#2 Seam
Total # of Particles Analyzed (dia. ≤100nm):		29	30	27
Predominant Particle Types*				
#1	Major Elements	Fe	Ti	Ca
	Number Observed	15	14	11
	Average Diameter (nm)	43±17	45±22	45±27
	Possible species**	-	TiO_2(Rutile)	$CaCO_3$(Calcite)
#2	Major Elements	Ba,S	Ca	Ti
	Number Observed	7	5	10
	Average Diameter(nm)	60±28	50±17	36±13
	Possible species**	$BaSO_4$(Barite)	$CaCO_3$(Calcite)	TiO_2(Rutile)
# of Different Matrix Areas Analyzed:		25	21	24
Most Common Signal From Organic Matrix:		Ca	Si, Al	S
Frequency of Observation of Most Common Signal (% of Total # of Areas Analyzed):		96%	90%	42%
Frequency of Observation of S Signal from Matrix (% of Total # of Areas Analyzed):		28%	43%	42%

*The two most frequently observed particle types for particles with mean diameters ≤100nm. Categorization into types is based on major elements ($Z \geq 11$) observed in x-ray spectra attributable to particles.

**Tentative identification based on major elements ($Z \geq 11$) found in spectra. Species listed are the most common minerals found in coal which could produce the observed spectra. No clear choice exists for the Fe-rich particles in the lignite.

For all three coals, the predominant mineral species observed in the ≤100nm size range would not be predicted from the results of the chemical analyses of the high temperature ash of the coals. None of the major elements (Z>11) observed (with the exception of sulfur in the Ba,S-rich particles) constitutes more than 10% of the HTA for the respective coals; indeed, Ba in the lignite, Ti in the bituminous coal, and Ca in the semianthracite all make up less than 1% of the respective ashes. Encountering these elements as the major constituents in the predominant mineral species observed in a random sampling of particles <100nm in diameter indicates that the distribution of inorganic elements must not be uniform over all size ranges of mineral inclusions. In particular, for all three coals, the predominant mineral species observed in the <100nm size range must therefore differ from those species predominating at larger size ranges.

In analyzing the background spectra obtained in this work, it was found that for two of the coals a particular element or combination of elements was observed in greater than 90% of all matrix measurements: Ca for the Hagel Seam lignite and a combination of Si and Al for the Cumberland bituminous. Examples of these two characteristic elemental signatures may be found in the two matrix spectra in Figures 3 and 4.

The semianthracite had no elements of Z>11 which were nearly as consistently observed in association with the matrix. In this coal, the most frequently observed matrix signal was from S, which only appeared in 42% of the observations. Indeed, in all three coals a S signal was detected in association with organic matrix, but only on an irregular basis (i.e., in less than 50% of the areas examined). Other elements, such as Fe, were also occasionally observed in the coal matrices. Such a point-to-point variation in inherent (atomically bound) mineral content may be expected to further complicate attempts to model the evolution of pulverized fuel particles into fly ash during combustion processes.

Conclusions

1. The STEM is an instrument well suited for the characterization of the sub-micron sized mineral matter in coal and can also be used to identify inorganic elements atomically bound in the organic coal matrix.

2. For the three coals studied, a random survey was taken of mineral inclusions <100nm in mean diameter observed within coal particles in powdered coal samples. The results indicate that the predominant mineral species making up these inclusions differ from those species predominating in mineral particles at larger size ranges.

3. Two of the coals examined showed characteristic matrix "signatures" of inorganic elements which were observed in >90% of the matrix areas examined. The third coal did not. All three coals exhibited various elements with Z>11, most notably S, which were only irregularly associated with the matrix signal (i.e., found <50% of the time).

References

1. R.W. Bryers, J. Eng. Power (Trans. ASME) 101, 506 (1979).
2. T.F. Wall, et. al, Prog. Energy Combust. Sci. 5, 1 (1979).
3. R.D. Smith, Prog. Energy Combust. Sci. 6, 53 (1980).
4. L.A. Harris, et. al, in Microstructural Science Vol.5, ed. by J.D. Brown, et. al, Elsevier North-Holland, Inc. (New York 1977) p. 351.
5. J.A. Little, et. al., in Proc. 38th Annual EMSA Meeting, ed. by G.W. Bailey, Claitors Publishing Division, (Baton Rouge, 1980) p. 220.
6. H. Heinemann, in Proc. Int. Conf. Coal Science, Dusseldorf, 7-9 Sept. 1981, Verlag Gluckauf (Essen, 1981) p. 567.
7. C.A. Wert and K.C. Hsieh, in Proc. Int. Conf. Coal Science, Dusseldorf, 7-9 Sept. 1981 Verlag Gluckauf(Essen, 1981) p. 780
8. J.H. Pohl, Energy and Environmental Research Corp., 8001 E. Irvine Blvd. Santa Ana, CA 92705, private communication

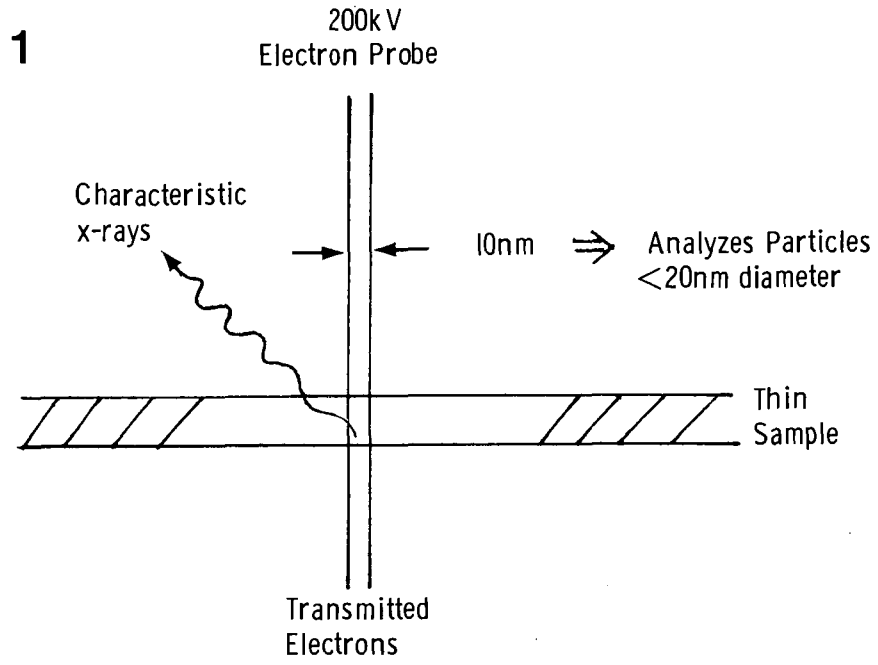

Figure 1: Schematic diagram of STEM operation during chemical microanalysis.

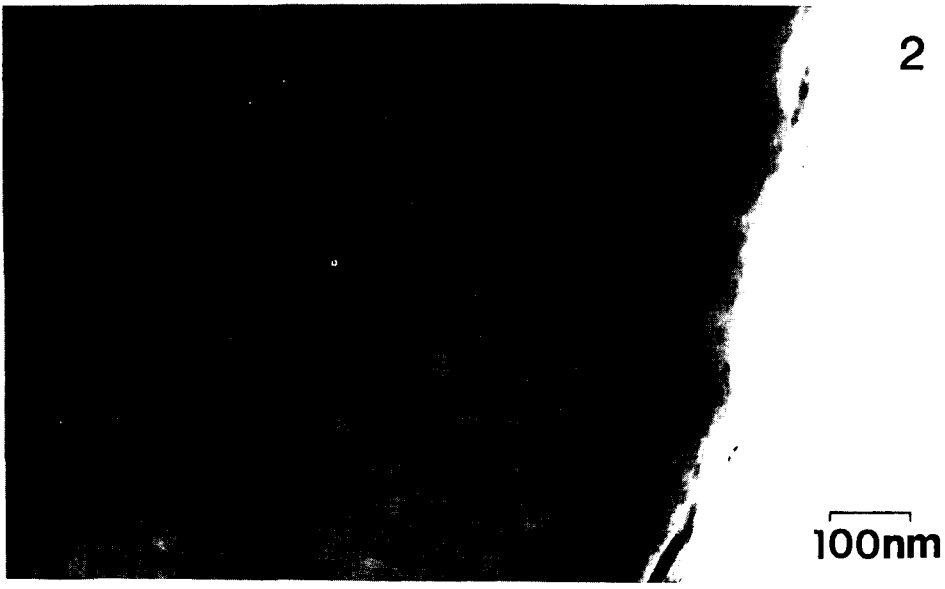

Figure 2: A transmitted electron image of a portion of a coal particle from the bituminous sample. A mineral inclusion is visible in strong diffraction contrast at A.

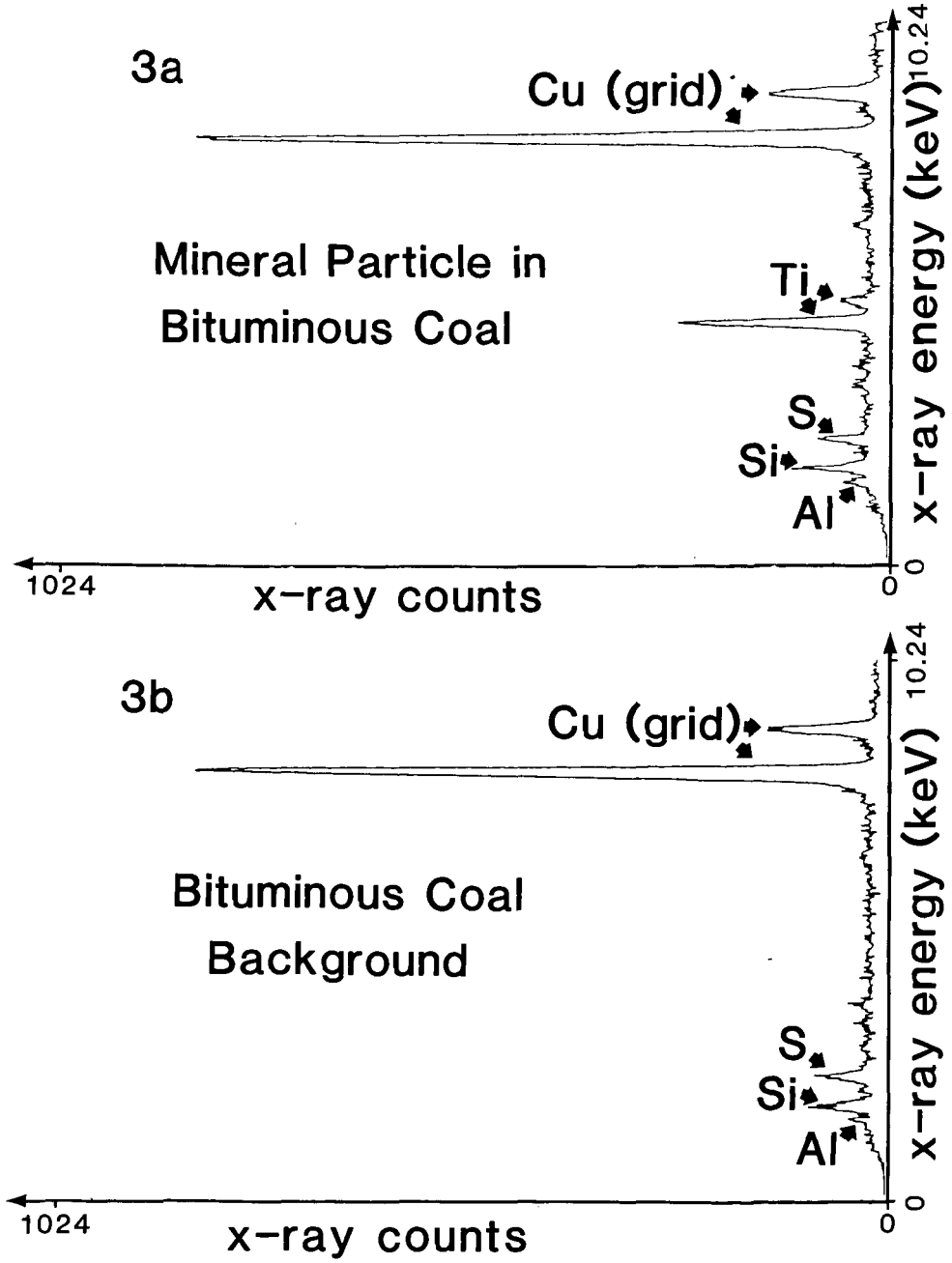

Figure 3: Examples of x-ray spectra from the bituminous sample.
a. Spectrum from particle shown in Figure 2.
b. Accompanying background spectrum.

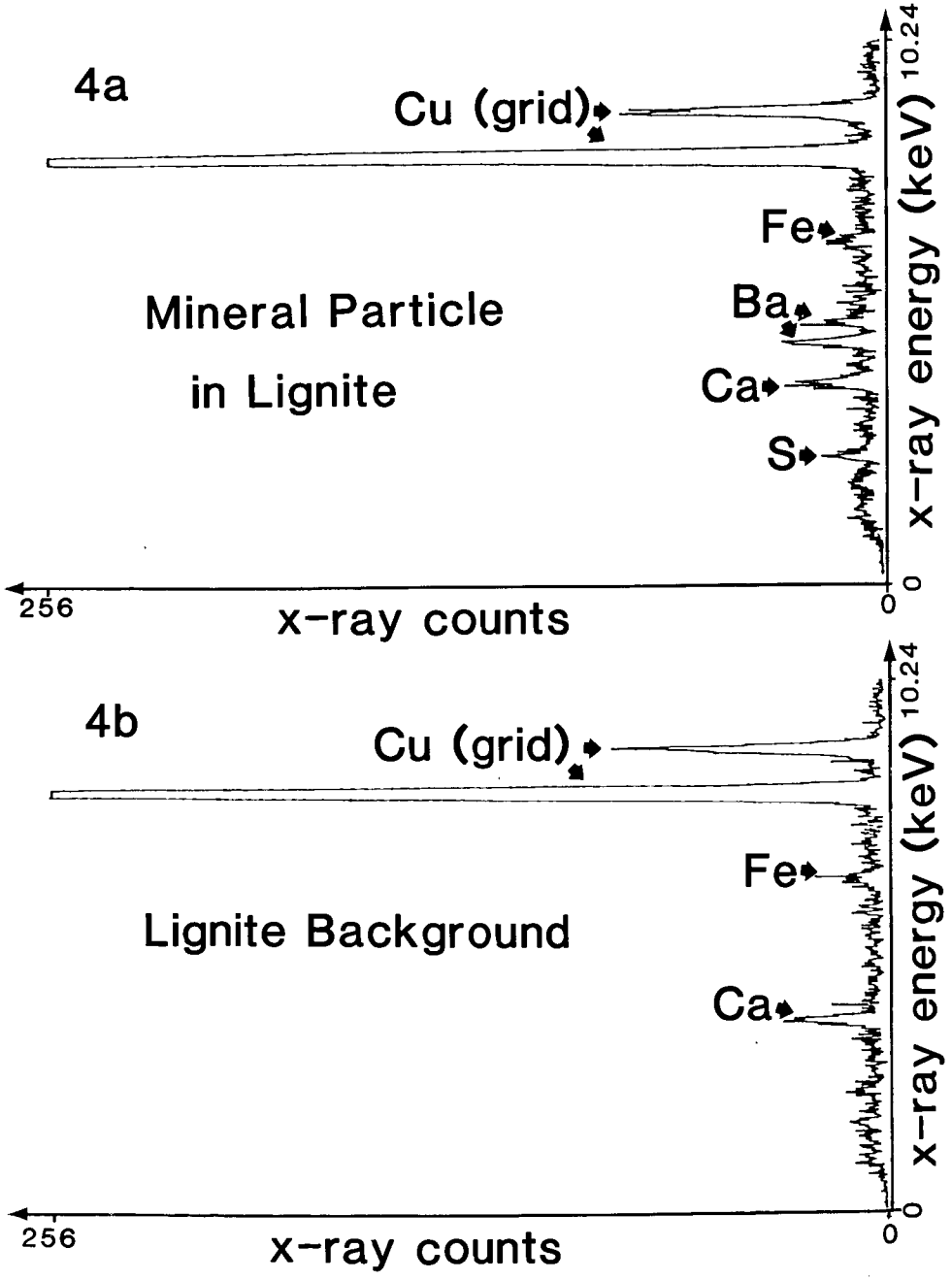

Figure 4: Examples of x-ray spectra from the lignite sample.
a. Spectrum from 40nm diameter particle.
b. Accompanying background spectrum.

The Determination of Mineral Distributions in Bituminous Coals by Electron Microscopy*

L. A. Harris

Oak Ridge National Laboratory
P. O. Box X
Oak Ridge, Tennessee 37830

INTRODUCTION

The chemistry and concentration of mineral matter in coals are factors that play important roles in coal combustion. For example, fouling, slagging, corrosion, and erosion are all mineral dependent processes that occur in coal-fired steam plants. Of these processes, fouling and slagging are probably the most detrimental to steam plant efficiency. Attempts to predict the fouling and/or slagging potential of a given coal have led to the development of equations based upon the ratios of base to acid minerals multiplied by either the sulfur or sodium content. (1,2) Essentially, these ratios take into account the lowering of the ash fusion temperature as a function of increased alkali bearing minerals.

In addition to the impact of mineral matter on steam plant operations, mineral matter also contributes to atmospheric particulates via steam plant stack emissions. Methods for reducing and/or altering the effects of minerals in coal are limited by the size and distribution of the minerals which is in turn related to the origin of the minerals, namely, whether syngenetic or epigenetic. As reported by Mackowsky (3) epigenetic minerals can be more readily removed from the coal because they are not as intimately mixed with the organic constituents (macerals) as syngenetic minerals. Furthermore, the epigenetic minerals may be considerably different from the syngenetic minerals due to differences in environments at the time of deposition and/or growth.

Currently, a common procedure for identifying minerals in coals consists of firstly low temperature ashing (L.T.A.) the coal and secondly analyzing the inorganic residue by means of x-ray diffractometry. Added information about the minral residue may be attained by utilizing a scanning electron microscope (SEM) with energy dispersive x-ray analysis (EDX) this procedure helps identify the minor minerals as well as locate trace elements. An advancement over the aforementioned SEM technique is one utilized by Finkelman (4) in which polished blocks were used so that not only the identity of minerals were obtained but also their relationship to the organic constituents could be determined.

In recent transmission electron microscopical studies of coals, (5,6) ultrafine minerals were observed (<1 μm). The observation and identity of these submicron minerals would have been difficult to achieve by use of the scanning electron microscope (SEM). However, the scanning transmission electron microscope (STEM) with energy dispersive x-ray analysis is an ideal analytical tool since it is capable of supplying elemental and diffraction data for particles as small as 30 nm in diameter. In this paper, we present observations and analyses of mineral matter in coals obtained through use of electron microscopes. These data significantly increase our knowledge of the mineral matter in coals as related to their affects on coal combustion.

---

*Research sponsored by the Division of Basic Energy Sciences, U.S. Department of Energy under contract W-7405-eng-26 with the Union Carbide Corporation.

EXPERIMENTAL

Sample Selection and Preparation

The samples used in this study were obtained from several high volatile bituminous coals of Eastern United States - Illinois No. 6, Kentucky No. 9, Elkhorn No. 3, and Hazard No. 4. Specimens were prepared for the transmission electron microscope studies from the above coals using a technique previously reported.(7) Optical thin sections approximately 10–15 μm thick were prepared. The thin sections were removed from the glass slides using acetone and subsequently mounted in an ion milling machine. Specimens were thinned (ion milled) using Argon gas and a liquid nitrogen cooled stage to insure against thermal damage to the specimen. Additional specimens consisting of polished blocks of coal were prepared for observation with the scanning electron microscope.

A high-voltage TEM (1MeV), a STEM (120Kv), and a SEM (JEM-U3) were used in this study. The STEM and SEM were fitted with energy dispersive x-ray analysis systems utilizing Si(Li) solid state detectors. Microchemical analyses of minerals for elements of atomic number 11 or greater could be attained for particles as small as 20 nm by using STEM with EDX.

RESULTS AND DISCUSSION

Submicron size minerals have been observed in all the high volatile bituminous coals that have been studied at this laboratory. A representative TEM micrograph of these coals (Fig. 1) reveals that these ultra-fine minerals are typically enclosed in a matrix consisting of vitrinite. These minerals are considered as syngenetic in orgin; (i.e., contemporaneously deposited in the peat basin with the organic constituents). Limited selected area diffraction (SAD) and energy dispersive x-ray analyses (EDX) of several of these minerals, using the STEM, showed that kaolinite (clay) is the dominant mineral species. However it must be noted that this analysis is strictly qualitative.

Moza et al. (8), in a study of minerals in coal as related to coal combustion systems, suggested that mineral fragments less than 8 microns would not be expected to gain enough momentum to collide with heat transfer tubes and these minerals would escape in the gas stream. However, from our present study of submicron micerals one can conceive of these particles fusing together to become substantially larger fragments. For example, a cubic μm of vitrinite may contain as much as 300 minerals, many of which actually touch.

Additional ultrafine syngenetic minerals have been observed to be intimately mixed with exinite (usually sporinite) and fragments of inertinite and vitrinite. These durain-like bands were probably derived from sediments consisting of degraded organic materials and mineral detritus deposited together in the peat swamp. The mineral species comprising these deposits are much more varied than those found in the vitrinite. In fact, these minerals usually contain many of the minor and trace elements associated with the mineral matter in coal (5) such as tin, nickel, zirconium titanium, and chromium. Typically, these minerals have a wider range of sizes varying from submicron particles to grains several microns long.

The TEM microstructure presented in Fig. 2 shows sporinite (S_P) segments bounded by regions consisting of granular maceral fragments and minerals (designated M-M). An aggregate of euhedral pyrite (P_Y) crystals located at one of the sporinite (S_P) boundaries is not an uncommon feature in many of the coals examined at this laboratory. The size of these pyrite crystals (~1 μm) appears to be identical to the

pyrite crystals in framboids located in vitrinite bands. It is worth noting that these minerals should prove more easily removed from the coal than those within macerals.

In Fig. 3, another view of mineral matter in durain-like bands is shown. A section of sporinite (S_P) interfaces with the inertinite maceral semifusinite (S_F). The region between these two macerals contains fine granular material including minerals. Additional minerals and organic debris are located within the collapsed sporinite walls (C_E). A large quartz grain (~6 μm) is located in a crushed cell in the semifusinite (S_F). Usually mineral inclusions within the vacant cell cavities of inertinite are considered as epigenetic. This point can be more clearly demonstrated by viewing an optical micrograph (Fig. 4) that shows epigenetic pyrite (P_Y) filling the crushed cell cavities in semifusinite (S_F).

Common structures found in bituminous coals are microfractures and/or joints that formed perpindicular to the bedding plane of the coal. These fractures (joints) are called cleat and originated in the coal after consolidation due to tectonic forces acting upon the earth's crust. In Fig. 5, a SEM micrograph of a polished block of coal, one can observe the appearance of cleat (CL). The epigenetic mineral filling the cleat (CL) was identified as calcite based upon EDX and x-ray diffraction analyses, the latter determination being performed on segments detached from the coal. The calcite forms a uniform mineral deposit approximately 10 μm thick and entends over several millimeters. A segment of the calcite sheet removed for analyses exposes one of the cleat walls (CLW). Typically, minerals in cleat can be readily separated from the organic constituents in coal, this is in contrast to the pyrite (P_Y) framboids (Fig. 5) enclosed in the vitrinite (V) band which would be extremely difficult to remove from the coal.

In addition to the presence of calcite in cleat, pyrite and kaolinite are also commonly found in cleat (9). The massiveness of the epigenetic mineral deposits in contrast to the syngenetic mineral distribution makes it apparent that the former mineral type constitute the major fraction of minerals in coal. The relative absence of calcite as a syngenetic mineral and its presence as a dominant cleat mineral in these coals suggests that calcite could readily be removed from the coal by current beneficiation methods. Indeed such cleaning of coals would also result in considerable reduction of pyrite and kaolinite. In general, the removal of calcite and pyrite should tend to increase the ash fusion temperature and consequently lead to a reduction in fouling and slagging.

CONCLUSIONS

1. Syngenetic and epigenetic minerals can be observed and identified by electron microscopy in conjunction with energy dispersive x-ray analysis.

2. Submicron micerals that are not readily identified or observed by scanning electron microscopy are easily viewed by use of transmission electron microscopy.

3. Calcite appears to be relatively scarce as a syngenetic mineral whereas calcite is an important epigenetic mineral usually occurring as cleat deposits.

4. Important minor syngenetic mineral assemblages appear to be associated with detritus. These minerals probably contain the major portion of minor and trace elements in coal.

5. Most of the epigenetic minerals should be readily removed from the coal resulting in a probable reduction in fouling and slagging.

REFERENCES

1. L. J. Garner, *J. of Institute of Fuel*, 40, 107 (1967).

2. R. C. Attig and A. F. Duzy, Proceeding of Am. Power Conf., 31, 290 (1969).

3. M-Th. Mackowsky, in Coal and Coal-Beating Strata, (Eds. D. G. Murchison and T. S. Westall), Elsevier, 309 (1965).

4. R. B. Finkelman and R. W. Stanton, *Fuel*, 57, 763 (1978).

5. L. A. Harris and C. S. Yust, Anvances In Chemistry Series 192, (Eds. M. L. Gorbaty and K. Ouchi), *Am. Chem. Soc.*, 321 (1981).

6. L. A. Harris, D. N. Braski, and C. S. Yust, *Microstructural Science*, 5, 351 (1977).

7. L. A. Harris and C. S. Yust, *Fuel*, 55, 233 (1976).

8. A. K. Moza, D. W. Strickler, and L. G. Austin, *Scanning Electron Microscopy/1980/IV*, 91, (1980).

9. L. A. Harris, O. B. Cavin, R. S. Crouse, and C. S. Yust, *Microscopica Acta*, 82, 343 (1980).

By acceptance of this article, the publisher or recipient acknowledges the U.S. Government's right to retain a nonexclusive, royalty-free license in and to any copyright covering the article.

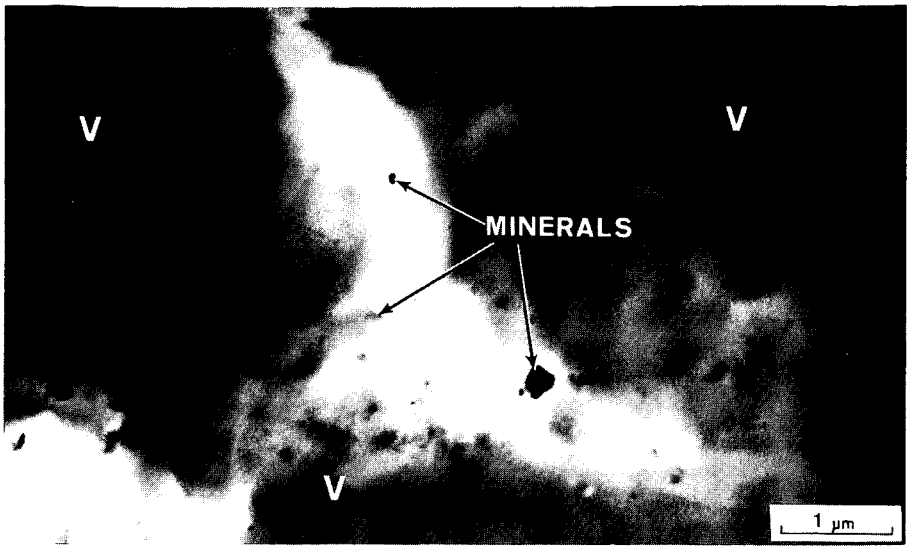

FIG. 1. TEM MICROGRAPH OF A HIGH VOLATILE BITUMINOUS COAL SHOWIN THE DISTRIBUTION OF SUBMICRON MINERALS (See Arrows) IN VITRINITE (V).

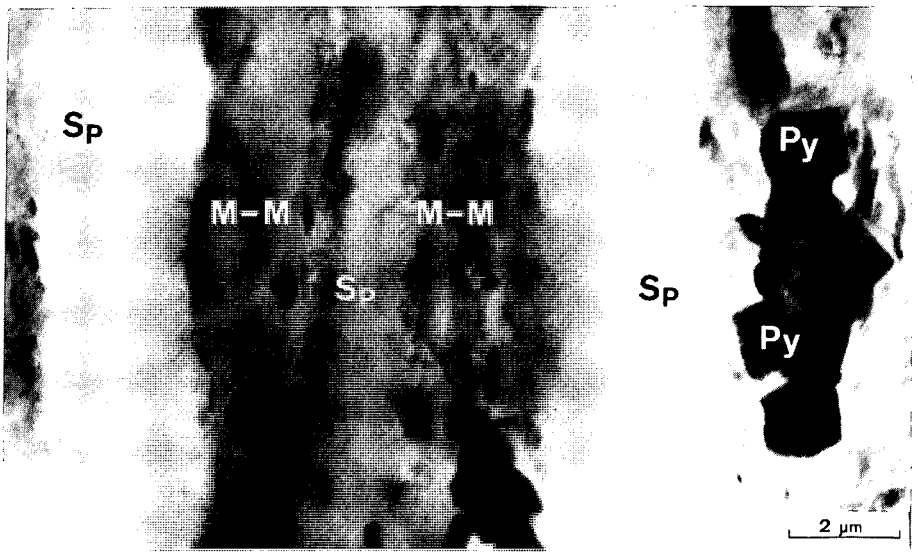

FIG. 2. TEM MICROGRAPH SHOWING THE RELATIONSHIP OF SPORINITE (S_p) WITH MINERAL BEARING BANDS (M-M). NOTE EUHEDRAL PYRITE (P_y) CRYSTALS AT SPORINITE (S_p) BOUNDARY.

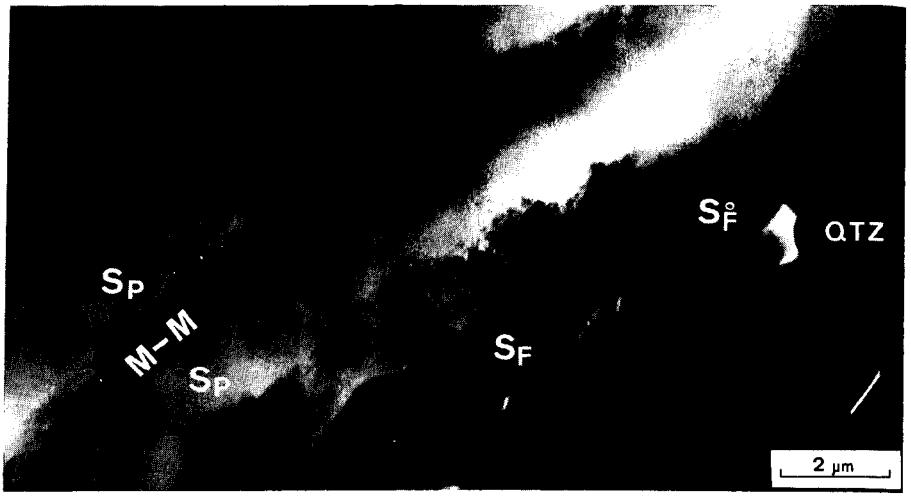

FIG. 3. TEM MICROGRAPH OF MICROSTRUCTURE CONTAINING SPORINITE (S_p) AND SEMIFUSINITE (S_F). A QUARTZ GRAIN (See Arrow) IS LODGED IN A CELL CAVITY IN THE SEMIFUSINITE (S_F).

FIG. 4. OPTICAL MICROGRAPH SHOWING EPIGENETIC PYRITE (P_Y) FILLING THE CRUSHED CELL CAVITIES IN THE SEMIFUSINITE (S_F).

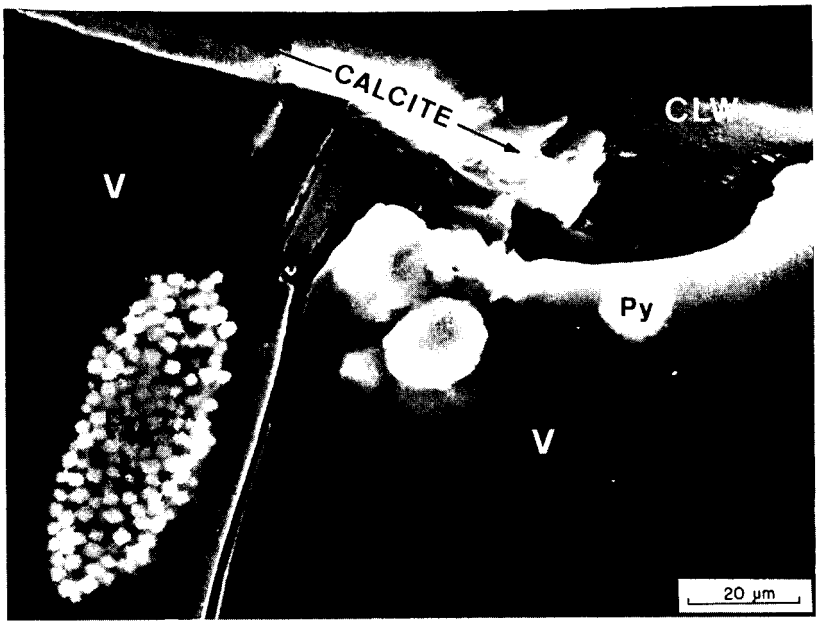

FIG. 5. SEM MICROGRAPH SHOWING CALCITE DEPOSIT (See Arrows) IN CLEAT. PYRITE (P_Y) FRAMBOIDS ENCLOSED IN VITRINITE (V) ALSO CAN BE SEEN.

THE FATE OF ALKALIS IN COAL COMBUSTION

G.W. Stewart and C.D. Stinespring
Aerodyne Research, Inc., Bedford, MA 01730

and

P. Davidovits
Aerodyne Research, Inc. and Department of Chemistry, Boston College
Chestnut Hill, MA 02167

INTRODUCTION

In the process of coal combustion, the ash particles deposited on various combustor components can cause serious materials damage. It has been shown that the alkali compounds contained in these particles are among the main causes of corrosion. Such corrosion may be especially damaging in proposed combined cycle power plants where the gas turbine blades are exposed to the combustor and therefore, are in direct contact with particles that escape filtering. To control the corrosive effects of the alkalis, it would be certainly useful to understand the mechanism governing the alkali contents of the particulates.

Over the past few years, a number of measurements have been made to obtain the concentration of trace elements in ash particles. Several of these studies measured the concentrations as a function of particle size.[1-6] In some of the experiments, the surface composition of the larger particulates has also been determined.[7-12] From these data, enrichment factors have been calculated for a large number of elements.[13] A selection from the available data is displayed in Figures 1 and 2 and Table I.

The composition of the smaller particles (a few microns or less) is of special interest since particles in this size range are more likely to escape filtering. It is commonly accepted that enrichment in the submicron particles, as well as on the surfaces of the larger particulates, is due to condensation of volatile species from the vapor phase. This would lead one to expect significant enrichment by elements that are themselves volatile or are found in coal as relatively volatile compounds. By and large, the measurements are consistent with these expectations. Thus, for example, elements such as Pb, Zn, Tℓ, Se, and As which are expected to be volatile, do indeed show significant enrichment in the smaller particles and, where data exist, also on the surfaces of the larger particles. However, an examination of the data shows that the alkalis exhibit a surprising departure from this trend. One would certainly expect the alkalis to be among the more volatile

species. In fact, combustion experiments done under laboratory conditions show significant vaporization of the alkalis.[14] Yet, the data gathered from actual coal combustion plants show that the smaller particles are not enriched by the alkalis. On the other hand, the surfaces of the larger particles do show significant enrichment by them.

The observation that the small ash particles are not enriched by the alkalis suggests that, contrary to expectations, the alkalis are not volatilized under actual case combustion conditions. If this is the case, the observed surface enrichment of the larger particles is not due to condensation, but must be produced by some other process, possibly diffusion from the interior to the surface.

Experiment Results

Evidence for these suggestions is found in the recent work of Stinespring and Stewart[15] and Stewart et al.[16] These experiments studied the behavior of the alkalis in model components under various coal combustion conditions. Since the alkalis are found in the organic as well as the inorganic components of coal, it is important to understand their behavior in both types of sites. Illite, which is a potassium containing aluminosilicate mineral, was chosen as a typical inorganic coal component. Sodium and potassium benzoate were chosen to represent the alkali containing organic fraction. These experiments examined the behavior of several elements; however, we will focus here only on the results relevant to the alkalis. Auger Electron Spectroscopy (AES) was used to determine the surface composition of aluminum silicate minerals which are heated in a well controlled environment. Differential thermal analysis (DTA) and thermogravimetric analysis (TGA) were performed on the model organic compounds to determine the extent of alkali release from the organic constituent.

The depth profiles for potassium indicate that the surface concentration of potassium begins to increase at temperatures as low as 200°C and it reaches an enrichment of about 13 at 1100°C. The depth of enrichment is about 100A. Order-of-magnitude calculations indicate that diffusion may occur on a time scale compatible with the residence time of ash particles in the combustor. From these results we conclude that alkali enrichment on the larger ash particles may indeed result from segregation rather than adsorption or condensation.

The DTA/TGA studies of sodium and potassium benzoate decomposition show that these model molecules initially decompose to form condensed ring organic molecules, alkali carbonate, and carbon dioxide. This initial decomposition process occurs over the temperature range of 400 to 600°C and is independent of the gas stream composition. Over this temperature range, there is no loss of alkali into the gas phase. Rather, all of the alkali is converted into the corresponding alkali carbonate. At higher temperature, the alkali carbonate decomposes and the course of this decomposition is determined primarily by the composition of the ambient gas. In an inert gas stream, the alkali carbonate decomposes over the temperature range of 700 to 900°C with release of carbon monoxide and atomic alkali. This decomposition has been confirmed by transporation mass spectrometer studies.[17] However, in a stream containing 20% CO_2 between 700 and 900°C, only carbon monoxide is released and the alkali is converted to alkali carbonate. This rection sequence occurs as long as residual carbon and carbon dioxide are present. Once the excess carbon has been converted to carbon monoxide, the alkali carbonate will decompose at temperatures in excess of 1200°C. Experiments were also performed with a combination of SO_2, CO_2, and O_2 in the gas stream. Here, it was found that the alkali carbonate is converted to the alkali sulfate with no indication of alkali loss over the temperature range studied (< 1300°K).

CONCLUSIONS

Thus, the results of the measurements and experiments discussed above do provide a plausible way to begin an explanation for the distribution of alkali in the ash particulates. To summarize:

1. Under typical coal combustion conditions in an atmosphere rich in CO_2 and/or SO_2, the alkalis in the organic fraction do not vaporize but remain bound in the ash as stable carbonates or sulfates.

2. The alkalis in the inorganic fraction diffuse to the surface producing enrichment by a factor of about 13 to a depth of about 100A.

The results, however, do not provide conclusive evidence about the fate of the alkalis. The effect of water vapor in the combustion stream has not yet been studied. Clearly, water could have an important effect on the vaporization process. Furthermore, the reasoning we have followed to explain the absence of alkali enrichment in the submicron particles requires that the volatilization of the alkalis in both the organic and inorganic fraction not be significant (say less than 20%).

It is possible to make a reasonably clear statement about the alkalis in the organic fraction under various combustion conditions. Here, the volatilization of the alkalis is primarily determined by the heterogeneous chemical reaction of the alkalis with the gas stream. Such detailed information, however, is not available for the alkalis in the inorganic fraction. Here, experimental data were not obtained under appropriate conditions. Thus, the combustion experiments of Mims et al., which do show significant alkali vaporization, were performed in an O_2 atmosphere without CO_2 or SO_2 enrichment. The experiments of Stinespring and Stewart, with the inorganically bound alkalis, measured only enrichment and did not study vaporization. The results of recent vaporization studies of Hastie et al.[18] were also not performed under conditions directly applicable to coal combustion. Clearly, a wider range of experimental data will have to be obtained. Specifically, the effects of surface chemistry on the alkali in the inorganic fraction will have to be studied before a more conclusive statement can be made about the fate of the alkali in coal combustion.

ACKNOWLEDGMENTS

This work was supported by the U.S. Department of Energy/Morgantown Energy Technology Center under Contract No. DE-AC21-81MC16244.

REFERENCES

1. D.F.S. Natusch and J.R. Wallace, Science 186, 695 (1974).

2. R.L. Davison, D.F.S. Natusch, J.R. Wallace, and C.A. Evans, Jr., Environ. Sci. & Technol. 8, 1107 (1974).

3. J.M. Ondov, R.C. Ragaini, and A.H. Biermann, Environ. Sci. & Technol. 13, 947 (1979).

4. D.G. Coles, R.C. Ragaini, J.M. Ondov, G.L. Fisher, D. Silberman, and B.A. Prentice, Environ. Sci. & Technol. 13, 455 (1979).

5. L.E. Wangen, Environ. Sci. & Technol. 15, 1081 (1981).

6. R.D. Smith, Prog. In Energy & Comb. Sci. 6, 53 (1980).

7. R.W. Linton, A. Loh, and D.S.F. Natusch, Science 191, 852 (1976).

8. J.A. Campbell, R.D. Smith, and L.E. Davis, Appl. Spectrosc. 32, 316 (1978).

9. S.J. Rothenberg, P. Denee, and P. Holloway, Appl. Spectrosc. 34, 549 (1980).

10. R.W. Linton, P. Williams, C.A. Evans, Jr., and D.S.F. Natusch, Anal. Chem. 49, 965 (1977).

11. L.D. Hulett and A.J. Weinberger, Environ. Sci. & Technol. 14, 965 (1980).

12. L.D. Hansen, D. Silberman, and G.L. Fisher, Environ. Sci. & Technol. 15, 1057 (1981).

13. Enrichment factors are obtained by normalizing to the bulk composition of the large particles (say > 30 μm).

14. C.A. Mims, N. Neville, R.J. Quann, and A.F. Sarofim, "Laboratory Studies of Trace Element Transformation During Coal Combustion," Presented at the 87th AIChE Meeting, August 1979, Boston, Mass.

15. C.D. Stinespring and G.W. Stewart, Atmos. Environ. 15, 307 (1981).

16. G.W. Stewart and A. Chakrabarti, High Temperature-High Pressure (In press) (1982).

17. A. Chakrabarti, D.W. Bonnell, G.W. Stewart, and J.W. Hastie, To be published (1981).

18. J.W. Hastie, E.R. Plante, and D.W. Bonnell, Interim Report No. NBSIR 81-2279, U.S. Department of Commerce, National Bureau of Standards, Washington, DC 20234 (1981).

SURFACE AND BULK ENRICHMENT OF COAL COMBUSTION ASH FOR SELECTED ELEMENTS

ELEMENT	ENRICHMENT		
	BULK*	BULK**	SURFACE***
As	9.4	13.4	---
Cd	11.5	---	---
Cr	2.4	6.2	3.3
Pb	3.8	8.4	11.0
Sb	7.9	---	---
Se	10.4	5.4	---
Tl	---	4.9	10.0
W	7.1	---	---
Zn	7.8	6.2	7.2
Al	1.0	1.6	1.1
Ca	1.1	1.0	1.6
Cl	1.1	1.0	---
Cs	1.2	---	---
Fe	1.3	1.3	0.8
K	1.1	1.3	7.6
Mg	1.3	---	0.9
Mn	1.5	1.7	6.4
Na	1.5	---	15.2
Rb	1.1	1.7	---
Ti	1.2	1.2	0.9
Be	1.6	---	6.0
Cu	2.3	2.2	
V	3.8	2.7	2.0

*Bulk enrichment defined as the ratio of the concentration in a 1μ particles to that in an 18.5μ particle, from D.G. Coles, R.C. Ragaini, J.M. Ondov, G.L. Fisher, D. Silberman, B.A. Prentice, Environ. Sci. & Tech., 13, 455 (1979).

**Bulk enrichment defined as the ratio of the concentration in a 0.15μ particle to that in a 20μ particle, from R.D. Smith, Prog. in Energy & Comb. Sci., 6, 53 (1980).

***Surface enrichment defined as the ratio of the surface composition divided by the composition at 500 Å, from R.W. Linton, P. Williams, C.A. Evans, Jr., and D.S.F. Natusch, Anal. Chem., 49, 1514 (1977).

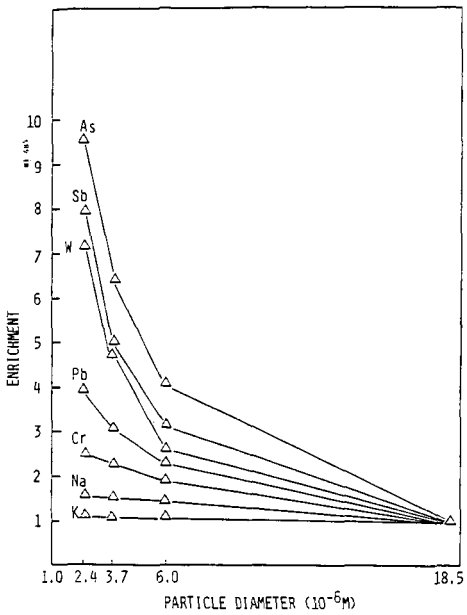

Figure 1, Enrichment vs. Particle Size, Based on Data from Coles et al., Environ. Sci. and Tech., 13, 455 (1979).

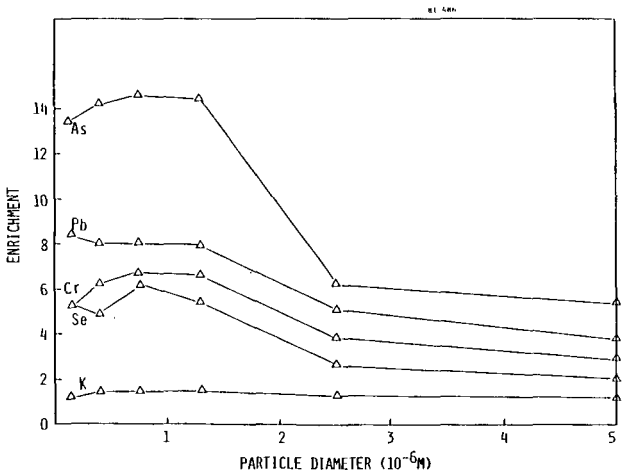

Figure 2. Enrichment vs. Particle Size, Based on Data by Smith, Prog. Energy and Comb. Sci., 6, 53 (1980).

Coal Ash Sintering Model and the Rate Measurements

E. Raask

Central Electricity Research Laboratories
Kelvin Avenue
Leatherhead, Surrey, UK

INTRODUCTION

In spite of innumerable laboratory investigations and the wealth of practical experience, there remains some enigmatic facets in the formation of sintered ash and slag deposit on heat exchange surfaces in coal-fired boilers. That is, occurrences of massive build-up of ash deposits can take boiler design and operation engineers by surprise. This would suggest that the engineers are receiving incomplete or incorrect information on the deposit-forming propensity of ash in different coals.

Traditional methods of assessing the behavior of deposit-forming impurities in high temperature boiler plants are based on ash fusion tests as described in different national standards for coal analysis and testing, e.g., ASTM (1968), British Standard (1970), DIN (1976) and Norme Francaise (1945). These ash fusion tests have been developed from refractory material technology, and are based on observations of the change in shape and size of an ash sample on heating. It has been realized that the results of ash fusion tests are frequently imprecise, and can lead to a mistaken assessment of the likely severity of boiler fouling and slagging.

There has been a number of suggestions made for ash fouling and slagging indices to predict more accurately the rate of deposit build-up with different coals as reviewed by Winegartner (1974). The empirical formulae, e.g., silica ratio, basic to acidic oxide ratio, and sodium and sulphur contents of coal, are based on the chemical analysis and have a limitation that they apply to particular coals. That is, there is no universal formula of predicting the severity of boiler fouling based on ash fusion tests and chemical analysis with all types of coal.

It is therefore evident that further research is necessary on the mechanism of ash particle-to-particle bonding at high temperatures. This work sets out to redefine an ash sintering model in terms of measurable parameters, surface tension, viscosity, electrical conductance, temperature, particle size and time. In the experimental work, novel methods of measuring the rates of ash sintering were applied, in order to test the validity of the sintering model.

SINTERING MODEL

Frenkel (1945) has derived an equation relating the growth of the interface between two spherical particles:

$$x^2 = \frac{3r\gamma t}{2\eta} \qquad (1)$$

where x is the radius of the interface, r is the original radius of the spheres, γ is the surface tension and t is the time. Rearranging the equation in terms of x/r and t, it becomes:

$$\frac{x}{r} = 1.225 \left(\frac{\gamma}{\eta r}\right)^{1/2} t^{1/2} \qquad (2)$$

and it is applicable when $\frac{x}{r} < 0.3$.

Sintering by viscous flow is the principal mechanism for the formation of deposits in coal fired boilers and the rate of sintering of different size particles for a given viscosity (10^8 N s m^{-2}) can be seen in Fig. 1 where the ratio of x/r is plotted against time on a logarithmic scale. The surface tension of fused ash was taken to be 0.32 N m^{-1} as measured previously by Raask (1966). Fig. 2 shows plots where the ratio of x/r represents the degree of sintering of 5 μm radius particles having different viscosities. Table 1 lists four arbitrary stages of sintering of ash deposit on boiler tubes from the initial contact between the ash particles to the formation of fused slag where the shapes of initial constituent particles are no longer distinguishable.

Table 1. Degree of Sintering Based on the Ratio of Neck Bond Radius to Particle Radius ($\frac{x}{r}$)

Ratio of x/r	Degress of Sintering	Comment
0.001	Onset of sintering	Deposit of this degree of sintering on boiler tubes would not have significant cohesive strength and would probably fall off under the action of gravity and boiler vibration.
0.01	Slightly sintered matrix	The deposit on boiler tubes would probably be removed by soot blowing.
0.1	Strongly sintered deposit	The deposit on boiler tubes would be difficult to remove by soot blowing.
>0.3	Slagging	The ash particles lose their original identity and the deposit on boiler tubes cannot be removed by soot blowing.

Rapid formation of sintered boiler deposits and slags is usually explained by the presence of a liquid phase or molten surface layer on ash particles. In high temperature glass and slag technology (blast furnace slag), a liquid phase is considered to have a viscosity value below 10 N s m^{-2}. The plots in Fig. 1 and 2 show that with small particles it is not necessary to evoke the presence of a liquid phase for a rapid sintering. For example, particles 0.1 m in diameter would require about 10 milliseconds to form a substantial sinter bond, when the viscosity has a high value of 10^8 N s m^{-2}. With the same viscosity 10 μm particles would require about 10 seconds to achieve the same degree of bonding.

The two parameters which govern the rate of sintering, namely the surface tension and the viscosity, both decrease with temperature as shown in Fig. 3. The temperature coefficient of surface tension is small (Curve A) and it is approximately proportional to the inverse of square root of temperature as discussed by Boni and Derge (1956) whereas the viscosity changes exponentially with temperature as shown by Curve B. It is therefore evident that the rate of sintering will show an inverse relationship with the viscosity and will increase exponentially with temperature.

PARTICLE-TO-PARTICLE NECK GROWTH MEASUREMENTS

The model for coal ash sintering discussed in the previous section is based on the viscous deformation and flow at the contact points between spherical particles. It would, therefore, be logical to consider determining the rate of sintering by a technique where the measurements are based directly on Frenkel's equation. Kuczynski (1949) has

carried out such sintering measurements by placing spherical particles on the surface of a glass slab of the same composition. Raask (1973) has reported some results of sintering rate measurements with coal ash slag particles based on a similar technique. The method requires spherical particles of ash and these can be prepared by passing ground coal minerals or slag through a vertical furnace as described by Raask (1969). Subsequently the particles were placed in a narrow groove on a platinum foil as shown in Fig. 4a. The particles were then introduced into a preheated furnace and kept at a constant temperature in air, or in a gas mixture for a period of five minutes to several hours. The radius of the sinter neck between the particles (Fig. 4b) was measured microscopically at the ambient temperature.

Fig. 5 shows the rate of neck growth between spherical particles of slag, 60 μm in radius, when heated in air. The spherical particles were prepared from boiler slag of a typical British bituminous coal ash which has caused some boiler fouling. The time for a firm degree of sintering, ($x/r = 0.1$, Table 1) was 135 seconds and 70 seconds at 1375 K and 1425 K, respectively. From these measurements the time required for a given degree of sintering can be calculated for the ash particles of different sizes. For example, the ash deposited on boiler tubes in pulverized coal fired boilers contains a larger number of particles of 0.5 to 1.0 μm in diameter, and these particles require only a few seconds to form a strongly sintered deposit in the same temperature range.

MEASUREMENTS OF ASH SINTERING RATES BY SIMULTANEOUS DILATOMETRIC AND ELECTRICAL CONDUCTANCE TECHNIQUES

Particle-to-particle sinter bonding usually results in a shrinkage of the external dimensions of a powder compact, and the dilatometric shrinkage measurements have been extensively used to determine the rate of sintering of glass and refractory materials. Smith (1956) has used a dilatometric shrinkage technique to study the sintering characteristics of pulverized fuel ash and an intercept of the shrinkage curve on the temperature axis was taken to define the sinter point. The measurements can give useful information and the results can be related to different degrees of sintering as outlined in Table 1. With some coal ashes, however, anomalous results can be obtained where the shrinkage measurements show no change although a significant degree of sintering has taken place. This deviation in the sintering behaviour from the Frenkel model makes it necessary to monitor another parameter which relates to the process of particulate ash coalescence.

Viscosity measurement by the rod penetration method has been applied by Boow (1972), Raask (1973) and Gibb (1981) to assess the sintering characteristics of different coal ashes. However, the rate of initial sintering cannot be measured by this technique, and Raask (1979) therefore considered the use of a method of electrical conductance measurements for monitoring the rate of sintering of coal ashes. Previously Ramanan and Chaklader (1975) had used the same technique to study sintering of glass sphere and nickel powder compacts.

The essential premise of this method is that the particulates are of an electrically conductive material, e.g., nickel, or that the glassy and ceramic materials contain some cations, e.g., alkali-metals which constitute an ionic conductance path when an electrical potential is applied. The method is, therefore, not applicable to measure the rate of sintering of nonconductive powders, e.g., alumina. This is not a limitation with coal ashes as all ashes contain sufficient amounts of cationic species; 0.1 per cent by weight quantity of sodium, potassium or calcium is likely to be adequate for the purpose of providing a conductance path.

A powder compact before sintering has a low conductance because of lack of particle-to-particle contacts. As the cross-sectional area of sinter bonds grows on heating the conductance is increased according to the equation:

$$\Lambda = A \left[\left(\frac{D}{D_o}\right)^{2/3} - 1 \right] \exp\left(\frac{-E}{RT}\right) \qquad (3)$$

where Λ is the conductance, D_o and D are the densities of sample before and after sintering, E is the energy of activation of sintering, R is the thermodynamic (gas) constant, T is the temperature and A is a constant. When the degree of sintering does not change, e.g., on cooling after the process of particle coalescence has reached the stage of density D, the equation (3) reduces to:

$$\Lambda = A_1 \exp\left(\frac{-E}{RT}\right) \qquad (4)$$

Rask (1975) has described a furnace assembly sketched in Fig. 6 for simultaneous measurements of the electrical conductance and the dilatometric shrinkage measurements. Fig. 7a shows the furnace in its down position for exposure of the sample well; sample crucible and three pellets of sintered ash from previous runs are shown at the well. Fig. 7b shows the furnace in the operation position. The heating rate of 0.1 K s^{-1} (6 K min^{-1}) was the same as that used in the ASTM (1968) ash fusion tests and the sinter tests can be carried in air or in simulated flue gas. Care is needed to stop heating when the ash sample has decreased 30 per cent in height to avoid slagging; once slag is formed it is difficult to remove the frozen material from the crucible.

Initial experiments were made with a soda glass, ground below 100 μm in particle size, of known viscosity/temperature characteristics published by Napolitano and Hawkins (1974). This was done to establish the validity of the simultaneous dilatometric and conductance measurements for determining the rate of sintering of powder compacts. The results are shown in Fig. 8 where Line A_1 depicts thermal expansion of the alumina support tubes and the sample, and Curve A shows the linear shrinkage of 10 mm high sample of powdered glass. The intercept of Curve A on the temperature axis, 875 K can be defined as the sinterpoint temperature.

The conductance plot (Curve B gives the same sinterpoint temperature and the results increase exponentially with temperature. On cooling Curve C shows a large hysteresis effect, that is, these are significantly higher than the corresponding results on heating. On reheating, however, the conductance measurements fit closely to Curve C. This behavior is in accord with the sintering model and the measurements on first heating when sinter bonds are formed, fit equation (3). Since on subsequent cooling and reheating, the process of particle coalescence is "frozen," the conductance change is governed by the exponential temperature as defined by equation (4).

Fig. 9 shows that there was in inverse relationship between the viscosity and the electrical conductance with respect to temperature. The conductance is dependent on the mobility, i.e., on the rate of diffusion of sodium and calcium ions in the glass matrix, and thus an inverse relationship between viscosity and self-diffusion is established as stipulated by Frenkel's sintering model. The results of conductance measurements plotted in Fig. 9 cover the viscosity range of 10^6 to 10^{10} N s m^{-2}, and it has been suggested previously by Raask (1973) that this is a relevant viscosity range for the formation of sintered deposits in coal fired boilers. That is, strong sinter bonds can form in this viscosity range within a few minutes or several days depending on the particle size (Figs. 1 and 2).

A number of British and US bituminous coal ashes have also been investigated for their sintering characteristics by the simultaneous shrinkage and conductance measurements. Fig. 10 shows typical shrinkage curve and the conductance plots on heating and on cooling which were obtained with an Illinois coal ash. It was evident that with

this ash and other bituminous coal ashes tested, sintering proceeded according to equation (3). The conductance data can be examined in more detail on the log n against 1/T plot as depicted on Fig. 11. The conductance plot on heating is nonlinear as expected from equation (3), whereas on cooling the plot was linear in accord with equation (4).

The conductance plot on heating can be divided into three sections where the logarithmic conductance values in S (micro-Siemen) are as follows: 1 to 10, 10 to 100 and 100 to 1000 units. Fig. 12 shows schematically the conductance path and shrinkage in three different degrees of sintering. The strength of the sintered pellet to crushing was determined at room temperature at the end of the sinter run. The presentation shows that an increase of 155 K from the initial sinter point temperature of 1125 K to 1180 K resulted in a high degree of sintering where the conductance readings were above 100 μS.

There are some coal ashes which exhibit in their sintering behavior a remarkable degree of divergence from the particle coalescence model as defined by equation (3). Fig. 13 shows that the nonbituminous coal ash, Leigh Creek, Australia, commenced to sinter at 1100 K according to the conductance measurements (Curve B). There was, however, no shrinkage of the ash pellet before temperature reached 1350 K (Curve A). That is, there was a gap of 250 K between the ash sinterpoint temperature indicated by the conductance measurements and that deduced from the shrinkage measurements. The reason for this nonconformist behavior must be that there was a significant degree of particle-to-particle bonding of the infusible material, e.g., quartz by a low viscosity phase at temperatures of 1100 to 1350 K. This may be an explanation for severe boiler fouling with high sodium coal ashes as discussed by Boow (1972) which is inconsistent with the results of conventional ash fusion tests. Leigh Creek ash had another unusual sintering feature; after an initial rise in conductance with temperature there was a decrease with an inflection point at 1325 K (Fig. 12). This was probably because the high amount of sodium in ash, 6.3 per cent of Na_2O by weight, resulted in crystallization of sodium alumino-silicate or aluminate in the temperature range of 1275 and 1325 K thus reducing the concentration of sodium ion in the glassy matrix.

Laboratory prepared ashes can be categorized according to the results of simultaneous measurements of shrinkage and the electrical conductance on sintering of an ash compact. The majority of ash compact coalesce and shrink according to the model as defined by equation (3) and particle-to-particle bonding is accompanied by the external shrinkage and a change in shape of an ash sample in early stages of sintering. With these ashes the conventional ash fusion tests, e.g., ASTM-Method (1968) usually give meaningful results. There are, however, some coal ashes rich in sodium which can give anomalous results when sinter tested as exemplified by the conductance and shrinkage curves in Fig. 12. That is, there can be a high degree of the internal particle-to-particle adhesion resulting in the formation of ash compact or deposit of high strength without the corresponding external shrinkage and these ashes should be tested by the electrical conductance technique to give meaningful results in the early stages of sintering.

NEED FOR AUGMENTING CONVENTIONAL ASH FUSION TESTS BY SINTERING RATE MEASUREMENTS

Ash fusion tests are based on the external change in shape, deformation, shrinkage, and flow of a pyramidic or cylindrical pellet of ash when heated in a laboratory furnace. A pyramidic shape is often used because it is easier to observe rounding of the pointed tip of the specimen than that of the edge of a cylindrical pellet. The methods are empirical, and strict observance of the test conditions is necessary to obtain reproducible results and these are laid down in the US ASTM (1968), British Standard (1970), German (DIN 1976) and French (Norme Francaise, 1945) procedures.

It has been recognized by many researchers that although ash fusion tests can given useful information regarding the fouling and slagging propensities of coal ashes, there are serious shortcomings. First, the tests are based on subjective observations and not precise scientific measurements, and they have a large margin of error. For example, the ASTM-method which is widely used in many countries allows for a 55 K margin of reproducibility in the initial deformation, softening hemisphere temperatures in an oxidizing atmosphere, and a 70 K margin of uncertainty in determining the initial deformation temperature in a reducing atmosphere. Within that 70 K margin the viscosity can change by an order of magnitude and consequently the rate of ash sintering will change by the same factor.

Another, more serious, shortcoming with the ash fusion method is that when testing some coal ashes there occurs an extensive degree of particle-to-particle bonding without any visible sign of deformation in the shape of an ash pellet. It is, therefore, evident that an additional method is needed to assess the sintering characteristics of coal ashes. A choice of sinter measuring techniques is given in Table 2.

TABLE 2. REVIEW OF ASH SINTERING TECHNIQUES

Measuring Technique	Equipment	Comments
Neck-growth measurements between spherical particles (Kuczynski, 1949), Raask, 1973)	A furnace and a microscope	This is suitable for homogeneous material when available in the form of spherical particles. It is not suitable for routine sinter testing of coal ashes.
Simultaneous shrinkage and electrical conductance measurements (Raask, 1979)	Needs a purpose-built furnace assembly for more accurate measurements. A simpler version uses platinum wire electrodes as described by Raask (1979) and by Cumming (1980)	Each ash could be provided with sintering rate curves. The method needs to be tested and assessed by different researchers.
Crushing strength measurements of sintered ash pellets (Atting and Barnhard, 1963; Gibb, 1981)	A furnace and a crushing strength measuring device	The method has been used by several researchers but there is no agreed procedure
Ash agglomeration by sieving test (Stallman and Neavel (1980)	A furnace and a sieving machine	This is one of the simplest methods of testing for initial sintering, and it warrants more systematic tests
Ash plug flow method	A tubular furnace tube with perforated plate to support an ash plug	So far no experimental results have been found in literature

The brief review in Table 2 shows that there are several laboratory methods of sinter testing coal ashes, which can give some useful information regarding their deposit

forming propensity. However, none of these techniques could be written as recommended methods, and a coordinated test program involving specialist researchers in different laboratories would be required to assess their general applicability.

CONCLUSIONS

1. Frenkel's sintering model is a useful introduction to understanding of the mechanism of formation of boiler deposits in the crucial early stages of particle-to-particle bonding. The model sets out unequivocally the rate controlling parameters in sintering, namely surface tension (the driving force for particle coalescence) viscosity (the temperature sensitive parameter) and particle size.

2. Measurements of the rate of neck-growth between the spherical particles demonstrate the validity of the sintering model, but the technique is not suitable for routine assessment tests of the sintering characteristics of different coal ashes.

3. A method of simultaneous measurements of dilatometric shrinkage and electrical conductance has been developed for assessing the deposit forming propensity of coal ashes. The measurements are based on a sintering model which stipulates that the formation of particle-to-particle bonding leads to enhanced conductance and increased density of ash test samples and boiler deposits.

4. There are some coal ashes, rich in sodium which do not behave as predicted from sintering models. With these ashes the sinterpoint temperature defined by the electrical conductance measurements can be over 250 K lower than that indicated by the results of conventional ash fusion tests.

ACKNOWLEDGEMENT

The work was carried out at the Central Electricity Research Laboratories and the paper is published by permission of the Central Electricity Generating Board.

REFERENCES

1. ASTM, Fusibility of Coal and Coke Ash, D1857-68 (1968).

2. R. C. Attig and D. H. Barnhardt, "A Laboratory Method of Evaluating Factors Affecting Tube Bank Fouling in Coal-Fired Boilers," Proceed. Int. Conf., Mechanism of Corrosion by Fuel Impurities, Marchwood, England, 1968, Butterworths Publ. p. 183.

3. R. E. Boni and G. Derge, "Surface Structure of Non-Oxidizing Slags Containing Sulphur," Trans. AIME, Journ. Metals, p. 59 (1956).

4. J. Boow, "Sodium and Ash Reactions in the Formation of Fireside Deposits in Pulverized Fuel Fired Boilers," Fuel, 51, 170 (1972).

5. British Standard, "The Analysis and Testing of Coal and Coke, BS Method 1016, Part 15 - Fusibility of Coal and Coke Ash," 8rit. Stand. Inst., London (1970).

6. J. W. Cumming, "Communication: The Electrical Resistance of Coal Ash at Elevated Temperatures," Journ. Inst. Energy, 53, 153 (1980).

7. DIN, "Determination of Ash Fusion Behavior," German Standard, DIN 51730 (1976).

8. J. J. Frenkel, "Viscous Flow of Crystalline Bodies Under the Action of Surface Tension," Journ. Phys. (Moscow) 9, 385 (1945).

9. W. H. Gibb, "The Slagging and Fouling Characteristics of Coals - 1. Ash Viscosity Measurements for the Determination of Slagging Propensity," Power Ind. Research, 1, 29 (1981).

10. G. C. Kuczynski, "Study of the Sintering of Glass," Journ. Appl. Phys. 20, 1160 (1949).

11. A. Napolitano and G. E. Hawkins, "Viscosity of a Standard Soda-Lime-Silica Glass," Journ. Res. US Nat. Bur. Stan. Sec. A., 68, 439 (1964).

12. F. Norme, "Determination of Ash Fusibility Curves," NF MO3-012 (1945).

13. E. Raask, " Slag/Coal Interface Phenomena, "Trans. ASME for Power, Jan. p. 40, (1965a).

14. E. Raask, "Fusion of Silicate Particles in Coal Flames," Fuel, 48, 366 (1969).

15. E. Raask, "Boiler Fouling - The Mechanism of Slagging and Preventive Measures," VGB Kraftwerkstechnik, 53, 248 (1973).

16. E. Raask, "Sintering Characteristics of Coal Ashes by Simultaneous Dilatometry - Electrical Conductance Measurements," Journ. Therm. Anal., 16, 91 (1979).

17. T. Ramanan and A.C.D. Chaklader, "Electrical Resistivity of Hot-Pressed Compacts," Journ. Am. Ceram. Soc., 58, 476 (1975).

18. E. J. D. Smith, "The Sintering of Fly Ash," Journ. Inst. Fuel, 29, 1 (1956).

19. J. J. Stallman and R. C. Neavel, "Technique to Measure the Temperature of Agglomeration of Coal Ash," Fuel, 59, 584 (1980).

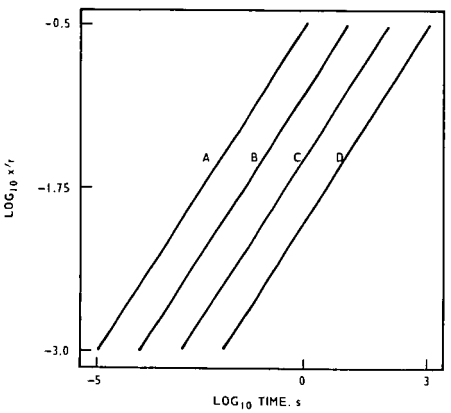

FIG. 1 LOG-LOG PLOT OF DEGREE OF SINTERING (x/r) AGAINST TIME VISCOSITY – 10^8 N s m^{-2}

PARTICLE RADIUS: A – 0.05 μm B – 0.5 μm
C – 5.0 μm D – 50 μm

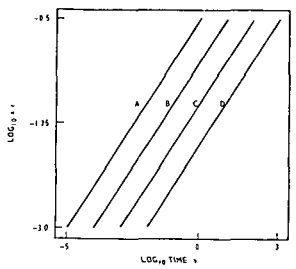

FIG 1 LOG-LOG PLOT OF DEGREE OF SINTERING (x/r) AGAINST TIME VISCOSITY - 10^8 N s m^{-2}

PARTICLE RADIUS A - 0.05 μm B - 0.5 μm
C - 5.0 μm D - 50 μm

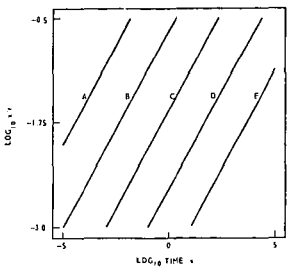

FIG 2 LOG-LOG PLOT OF DEGREE OF SINTERING (x/r) AGAINST TIME PARTICLE RADIUS - 5 μm

VISCOSITY (N s m^{-2})

A - 10^4 B - 10^6
C - 10^8 D - 10^{10}
E - 10^{12}

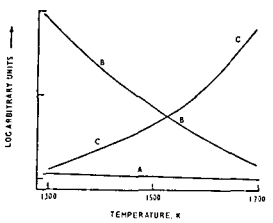

FIG 3 THE EFFECT OF TEMPERATURE ON ASH SINTERING PARAMETERS

A - SURFACE TENSION B - VISCOSITY
C - RATE OF SINTERING

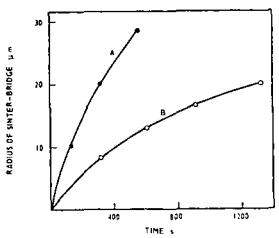

FIG 5 GROWTH OF SINTER BRIDGE BETWEEN PARTICLES, RADIUS - 60 μm

A - AT 1475 K B - AT 1375 K

(b) SINTER BRIDGED PARTICLES

(a) SLAG PARTICLES ON PLATINUM PLATE BEFORE SINTERING

FIG. 4 SINTERING OF SPHERICAL PARTICLES OF COAL ASH SLAG

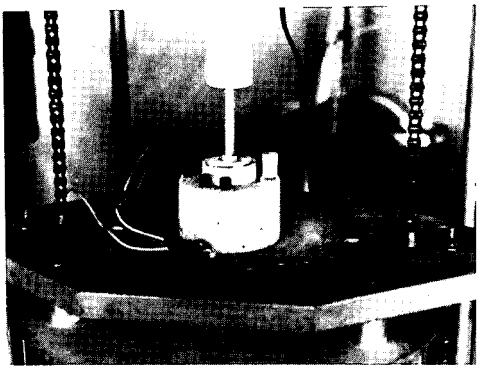

(a) DOWN POSITION FOR SAMPLE CHANGE

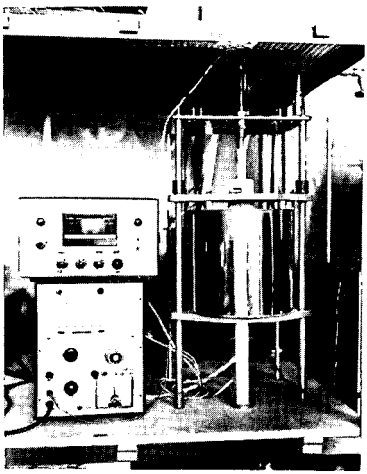

(b) OPERATION POSITION

FIG. 7 FURNACE ASSEMBLY FOR THE ASH SINTERING MEASUREMENTS

PLEASE RETURN THIS ORIGINAL TO DRAWING OFFICE

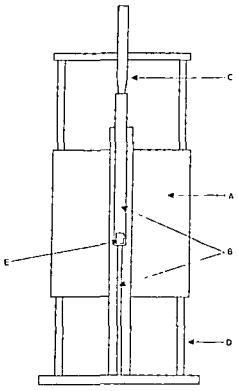

A FURNACE
B CONDUCTANCE LEADS AND THERMOCOUPLE
C DISPLACEMENT PROBE
D FURNACE HAS BALANCED LOWERING AND RAISING ACTION
E SAMPLE

FIG 8 SCHEMATIC OF FURNACE FOR SIMULTANEOUS SHRINKAGE AND CONDUCTANCE MEASUREMENTS

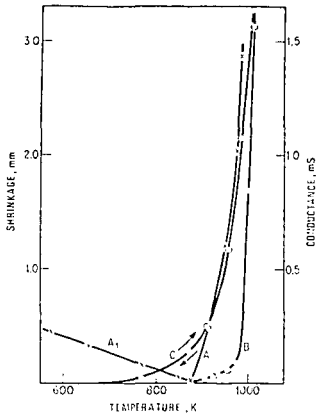

FIG 8 SIMULTANEOUS SHRINKAGE & ELECTRICAL CONDUCTANCE MEASUREMENTS OF SODA GLASS

A_1 - THERMAL EXPANSION
A - SHRINKAGE
B - CONDUCTANCE ON HEATING
C - CONDUCTANCE ON COOLING & REHEATING

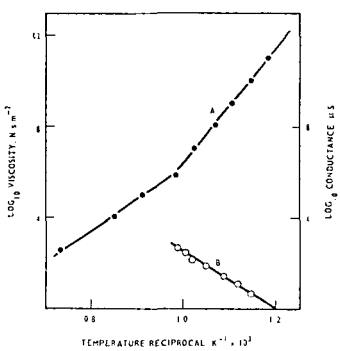

FIG 9 ARRHENIUS PLOTS OF VISCOSITY (A) AND CONDUCTANCE (B) OF SODA-GLASS

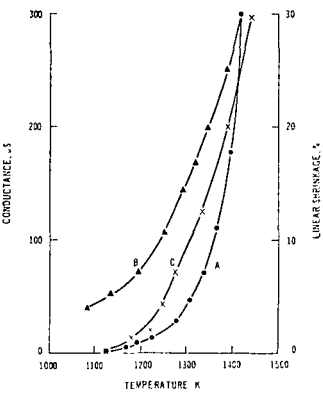

FIG 10 CONDUCTANCE AND SHRINKAGE PLOTS ON SINTERING OF ILLINOIS COAL ASH

A - CONDUCTANCE ON HEATING 5 K min^{-1}
B - CONDUCTANCE ON COOLING 5 K min^{-1}
C - SHRINKAGE ON HEATING 5 K min^{-1}

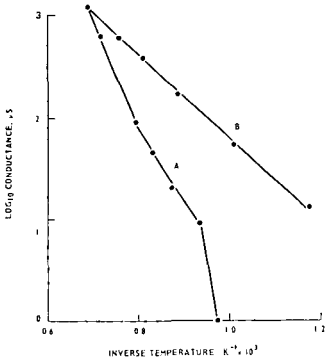

FIG 11 CONDUCTANCE LOGARITHM/INVERSE TEMPERATURE PLOT ON SINTERING OF COALITE BREEZE ASH

A – HEATING 5 K min⁻¹
B – COOLING 5 K min⁻¹

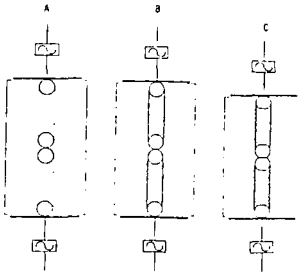

FIG 12 THREE STAGES IN THE SINTERING OF ILLINOIS COAL ASH – 12 mm HIGH, 8 mm DIA PELLET BETWEEN PLATINUM PLATES

	TEMP , K	COND , μS	SHRINK , %	STRENGTH kg cm⁻²
A FIRST CONTACT	1125	1 0	0 07	0
B INITIAL SINTER	1195	10	2 0	0 1
C RAPID SINTER	1280	100	10	1 0

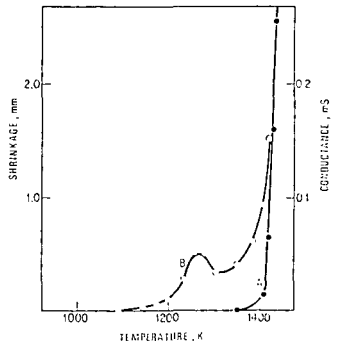

FIG 13 SIMULTANEOUS SHRINKAGE/ELECTRICAL CONDUCTANCE MEASUREMENTS ON LEIGH CREEK, AUSTRALIA, COAL ASH

THE CAPTURE AND RETENTION OF SULFUR SPECIES BY CALCIUM COMPOUNDS DURING THE COMBUSTION OF PULVERIZED COAL

P. L. Case, M. P. Heap, C. N. McKinnon, D. W. Pershing and R. Payne

Energy and Environmental Research Corporation
8001 Irvine Blvd., Santa Ana, Calif. 92705

1. INTRODUCTION

Coal is the United States most abundant source of fossil fuel energy however its utilization poses several problems for society, among which are those associated with the formation of atmospheric pollutants during its combustion. Coal is not a pure hydrocarbon fuel, it contains inorganic matter (ash), nitrogen and sulfur which, in turn, form particulates (fly ash), nitrogen oxides and sulfur oxides. The emission of such pollutants to the atmosphere is undesirable and can be avoided by removing the pollutants from the combustion products, preventing their formation, or removing the constituents which form pollutants from the coal. This paper describes bench scale experiments which will establish whether and under which conditions calcium containing sorbents can be used to capture sulfur during pulverized coal combustion. Having established that sulfur capture is possible, the studies will then concentrate upon whether it is practical since sorbent injection into boilers could have a serious impact upon boiler operation. Sorbent injection will increase particulate mass loading, change slagging and fouling characteristics and will change fly ash properties.

The use of sorbents to control emissions of sulfur oxides from coal fired power plants is a conceptually simple process. A pulverized, calcium containing sorbent is injected into the combustion chamber of a boiler where it flash-calcines to lime (CaO) and, at the same time, reacts with sulfur dioxide and oxygen to form calcium sulfite and/or calcium sulfate. Considerable effort was expended in the late 1960's and early 1970's on development and demonstration projects (1), and although pilot plant studies showed promise, the results could not be duplicated in full scale systems. The lack of success was attributed to a combination of loss of reactivity of the lime due to deadburning and maldistribution of the sorbent. Recent pilot scale studies (2, 3) with low NO_x coal burners suggest that sorbent injection could be more effective under conditions which minimize NO_x formation in pulverized coal flames.

Nitrogen oxides are formed from two sources during pulverized coal combustion; molecular nitrogen which is part of the combustion air and nitrogen which is chemically bound in the organic coal matrix. Low NO_x pulverized coal burners are effective because they produce a fuel rich zone which minimizes fuel NO formation and lowers peak flame temperatures, which, in turn, reduces the rate of thermal NO production. If a sorbent is injected into a combustor fired with low NO_x burners it will experience lower peak temperatures and more reducing conditions than if the combustor was fired with "normal" burners. The opportunity to control both nitrogen and sulfur oxide emissions by preventing their formation may be given by the use of sorbent injection into low NO_x burners.

Sulfur capture by sorbent injection involves three processes, namely:

- Sorbent activation - the sorbent particles are heated and calcined. Ultimate particle reactivity will depend mainly upon initial properties and peak particle temperature. If the particle temperatures are too high, the sorbent loses its reactivity (deadburns).
- Capture - sulfur species (H_2S, COS or SO_2) react with the sorbent producing either sulfate or sulfide. The rate of absorption will depend upon

temperature, sulfur species concentration and sorbent characteristics.

- Regeneration - under certain conditions, the spent sorbent may decompose regenerating gas phase sulfur species.

The general reaction describing sulfur capture under oxidizing conditions is:

$$CaO + SO_2 + 1/2\ O_2 \rightarrow CaSO_4 \qquad 1)$$

The rate of this reaction, the rate of calcination, and the maximum calcium utilization imposed by pore blockage has been studied extensively in thin bed and dispersed flow reactors by several workers (4, 5). None of these studies duplicated the time temperature conditions that prevail in pulverized coal flames.

Borgwardt (6) has suggested that reactions such as:

$$CaCO_3 + H_2S \rightarrow CaS + H_2O + CO_2 \qquad 2)$$

$$CaO + H_2S \rightarrow CaS + H_2O, \qquad 3)$$

involving reduced sulfur species could become significant under fuel rich conditions. Extrapolation of rate data for such reactions (obtained by Ruth and Squires (7)) to pulverized coal flame conditions indicates that the reaction of H_2S with $CaCO_3$ is sufficiently fast to allow significant sulfur capture.

Consequently, it appears that there are two possible modes of sulfur capture by calcium based sorbents in a pulverized coal fired combustor operating under low NO_x conditions. Under oxidizing conditions, reduced peak temperatures will reduce deadburning and allow reaction 1 to proceed. If the sorbent is injected into the fuel rich region, reaction 2 may become significant, but calcium sulfide could be lost when the partially oxidized fuel is burned out. Thus retention of the sulfur becomes an important factor in the overall process. Figure 1 shows the effect of temperature and stoichiometric ratio on equilibrium calcium distribution. It indicates that under rich conditions (50% theoretical air) calcium sulfide is very stable compared to calcium sulfate under lean conditions (100% theoretical air or SR = 1.0). These calculations imply that if the sulfide is formed in the rich zone, then the transition to oxidizing conditions should be carried out quickly to prevent prolonged times under new stoichiometric conditions, and that the temperature during this transiton should be reduced. An experimental study has been carried out to determine whether either of the two routes referred to above are likely to allow simulataneous control of sulfur and nitrogen oxide emissions from pulverized coal fired boilers.

2. EXPERIMENTAL

A bench scale facility has been constructed which is capable of duplicating the history of the solid particles (coal and sorbent) and the products of combustion in a pulverized coal fired power plant. As shown in Figure 2, the system consists of three major components:

- The radiant furnace, a horizontal refractory lined cyclinder, which simulates the region close to the burners. Heat extraction is varied by adding or removing cooling tubes.

- The post flame cavity which simulates the volume above the burner zone of a boiler before the superheater.

- The convective section, cooled by banks of air cooled stainless steel tubes, which simulates the superheater, reheater and air heater sections of the boiler.

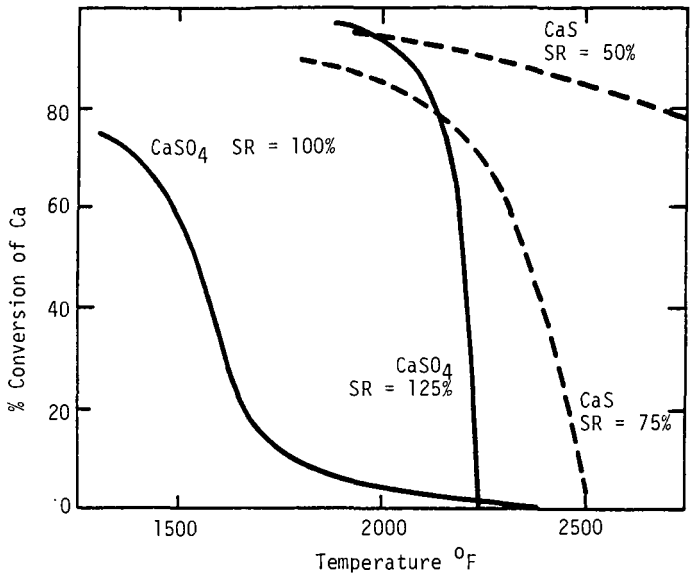

Figure 1. Effect of Temperature and Stoichiometric Ratio on Equilibrium Calcium Distribution - % Ca as $CaSO_4$ or CaS (Ca/S = 1)

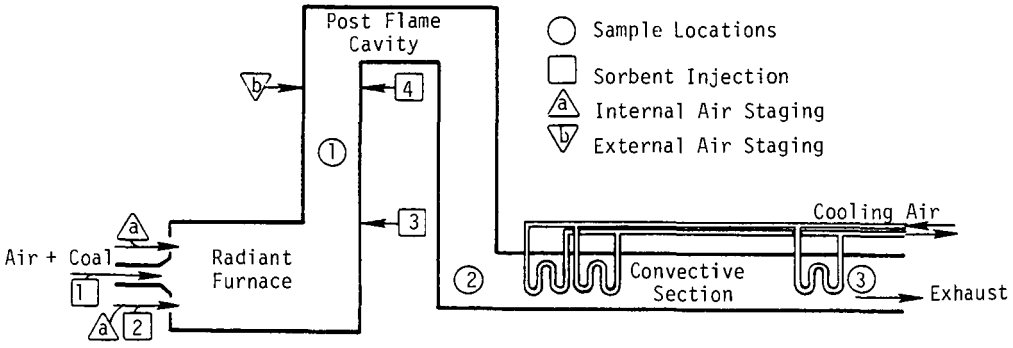

Figure 2. Schematic of Test Furnace Showing Location of Sample Ports, Staged Air Addition and Sorbent Injection.

The facility is fired with coal using a small scale low NO_x burner which could be operated in two modes - internally and externally staged. When the burner was operated with the second stage air supplied at the firing face through the staged air injectors, only the burner zone was fuel rich. This is referred to as internally staged. Alternatively, when the staging air was added downstream in the post flame cavity, the whole of the radiant furnace operated fuel rich. This is referred to in the text as external staging. The sorbent was added in any of four locations: 1) with the coal, 2) with the staged air at the burner face, 3) at the entry of the post flame cavity, and 4) with the downstream staged air when operating in the externally staged mode.

The measurement of sulfur species in combustion products containing active sorbents introduces several problems related to sample acquisition. A "phase discrimination" probe has been designed, constructed and tested which minimizes gas-solid contacting after sample extraction. SO_2 was measured with a non-dispersive ultra-violet absorption instrument. H_2S and COS were measured by gas chromatography using a flame photometric detector. Sulfur capture was based on SO_2 measurements with and without sorbent in every test case.

3. RESULTS

A series of experiments has been carried out with the coal and sorbent listed in Tables 1 and 2 in both the external and internal staging modes.

Indiana Coal

Ultimate Analysis, % Dry Basis

C	69.91
N	5.18
H	1.54
S	2.53
O	11.00
Ash	9.84

Calorific Value (dry bais)	12,515 Btu/lb
Moisture, average, as burned	7.0%

Table 1. Coal Properties

Vicron 45-3, Pfizer

Composition, typical, %

$CaCO_3$	97.0
$MgCO_3$	1.6
SiO_2	1.0
Al_2O_3	0.5
Fe_2O_3	0.05
Moisture	0.2

Specific Gravity	2.71
Particle Shape	rhombic
Oil absorption	14
Surface area (m^2/gm)	1.4

Table 2. Sorbent Properties

Internal Staging

Figure 3 shows the percentage capture as a function of the calcium to sulfur molar ratio when the sorbent was added with the staged air (location 2), and an additional 15% (over the normal heat loss) of the input heat was extracted from the radiant zone. Data are presented showing the relative capture in the radiant zone (sample port 1), the post flame section (between 1 and 2) and the overall capture (sample port 3). The capture in the post flame section is based upon the gas phase sulfur dioxide concentration entering the section and free calcium oxide (that which was not used in the radiant section). The data presented in Figure 3 indicate that when heat is extracted from the radiant zone capture occurs in both the radiant zone and the post flame section. These data were obtained with the burner zone operating at a stoichiometric ratio of 0.6 and a total air input equal to 120% of stoichiometric.

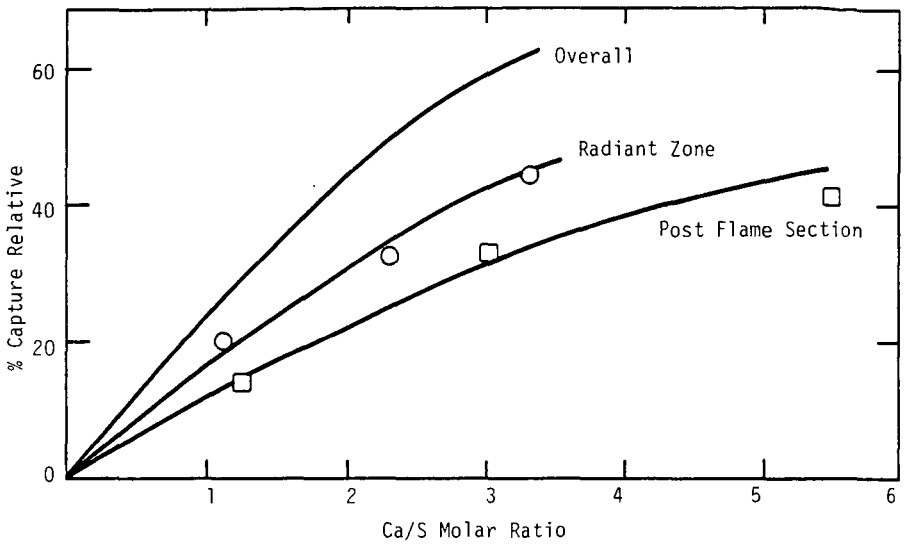

Figure 3. Relative SO_2 Capture, Sorbent Injected With the Staged Air Internal Mode With Heat Extraction in the Radiant Zone.

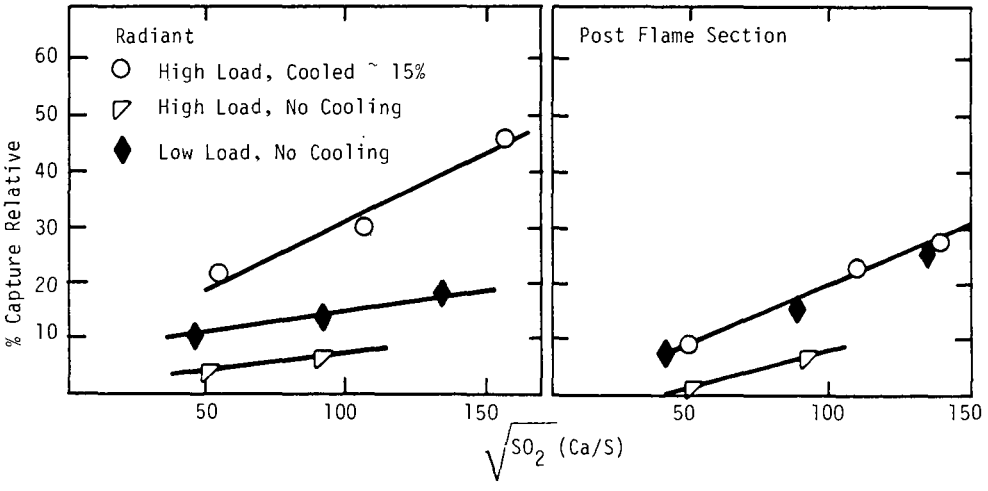

Figure 4. The Impact of Load and Radiant Zone Cooling on Sulfur Capture.

Tests have been carried out to determine the influence of burner zone stoichiometry on sulfur capture in the internally staged mode. Provided the burner zone stoichiometry does not rise above 80% the sulfur capture appears almost to be independent of burner zone stoichiometry. However as the staging air is reduced to a minimum and the burner zone becomes fuel lean the sulfur capture is reduced. In these experiments this reduction is probably caused by a reduction in sorbent velocity and because of the increase in peak flame temperatures as the burner zone stoichiometry increases.

In the internal staging mode thermal environment has a very significant impact upon sulfur capture. This is illustrated by the data presented in Figure 4 which shows the sulfur capture in both the first two zones as a function of the product of the calcium to sulfur ratio and the square root of the sulfur dioxide concentration in that zone. Three conditions are shown: high load with and without radiant zone cooling and low load without cooling. Reducing the load will lower temperatures and increase residence times. At high load cooling the radiant zone dramatically increases the sorbent reactivity. At low load reactivity in the radiant zone is less than that with cooling at high load but the reactivity in the post flame section is similar to the high load, cooled case.

External Staging

The purpose of the external staging tests was to determine whether sulfur dioxide emissions could be reduced by adding limestone under reducing conditions and then burning the fuel completely by the addition of second stage air downstream. This requires that the majority of the sulfur captured under reducing conditions be retained by the sorbent as the fuel burns out. Equilibrium calculations indicate that under fuel rich conditions hydrogen sulfide is the dominant sulfur species while measurements in the fuel rich region indicate that sulfur dioxide, hydrogen sulfide and carbonyl sulfide all are present. Sulfur dioxide concentrations decrease and hydrogen sulfide concentrations increase as the primary zone stoichiometry decreases. Thus, the sorbent may react with any of three sulfur species. Initial reaction rates for the reaction of H_2S and COS with CaO have been measured (7, 8) and are similar.

The data from two different external staging experiments are shown in Figures 5 and 6. In one experiment sorbent was added with the coal (location 1) and measurements of sulfur species at the exit of the rich zone (port 2) were made with and without sorbent. Figure 5 shows the percent capture of SO_2, COS and H_2S as a function of first stage stoichiometric ratio. It can be seen that all three species were captured. The data in Figure 6 are from an experiment comparing calcium utilization firing with two fuels, coal and propane doped with H_2S to give the same sulfur content as the coal. The sorbent was added at the base of the post flame section (location 2) and the staging air was added in the post flame cavity (location b). SO_2 was measured with and without sorbent for both fuels at sample port 3 (exit of furnace). Total calcium utilization as a function of first stage stoichiometry is shown in Figure 6. Measurements indicate that as much as 50 percent of the input coal remains as solid at the lower first zone stoichiometries. The data for coal presented in Figure 6 has been plotted as a function of the actual gas phase stoichiometry. It can be seen that the ultimate sulfur capture decreased with decreasing gas phase stoichiometric ratio for coal but increased for propane doped with H_2S. It should be noted that the data shown in Figure 6 represent the sum of sulfur species capture under reducing conditions in the first zone, retention of sulfur during burnout and the sulfur capture under oxidizing conditions in the second stage.

4. CONCLUSIONS

An investigation has been carried out in a bench scale facility to determine

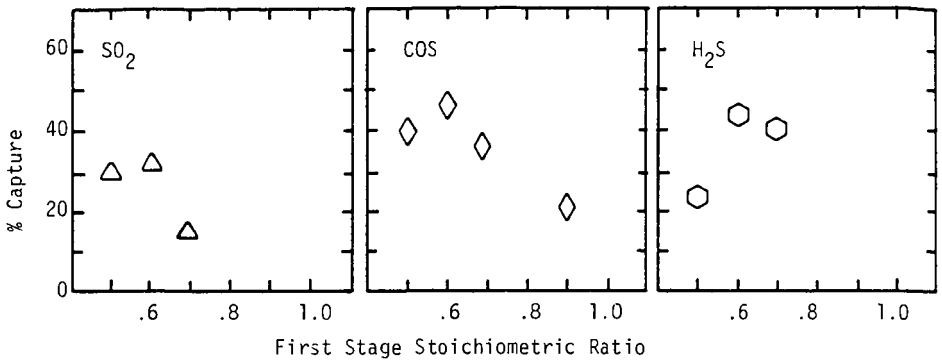

Figure 5. % Capture of Sulfur Specie in Rich First Stage (External Mode) Sorbent Injected With the Coal.

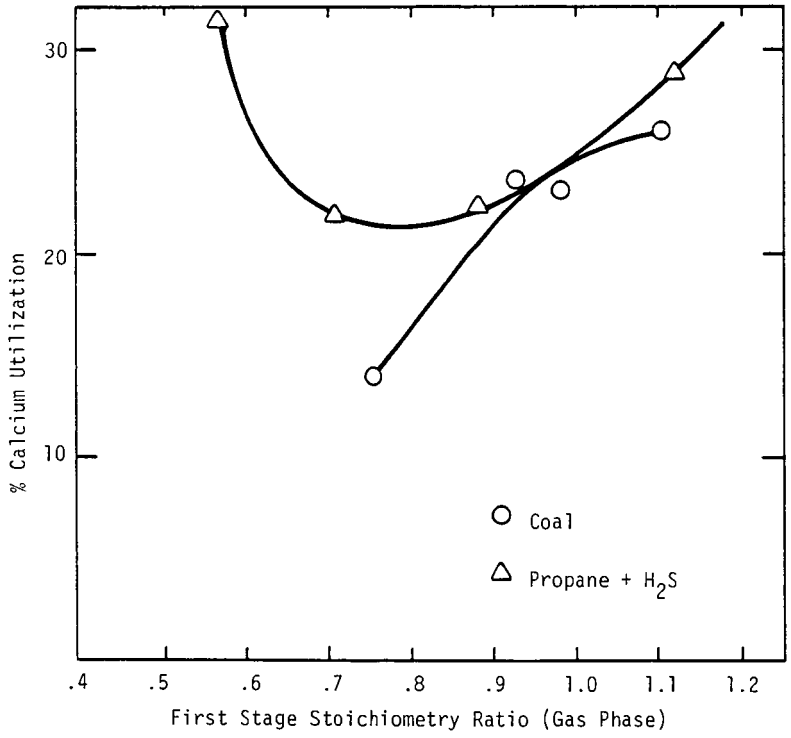

Figure 6. Capture and Retention of Sulfur Under External Staged Conditions for Coal and Propane Doped with H_2S.

under which conditions sulfur species generated during the combustion of pulverized coal can be captured and retained by calcium containing sorbents. Two series of experiments were carried out: one in which any capture would take place primarily under oxidizing conditions and the other in which significant residence times in the rich zone would allow capture under reducing conditions. Under oxidizing conditions the thermal environment experienced by the sorbent particle appears to be the dominant parameter controlling sulfur capture. This is probably because of deadburning. If a sorbent particle's temperature exceeds a certain limit (which depends on the particular sorbent) the sorbent deadburns and loses its reactivity (4).

The processes controlling capture and retention when the sorbent is maintained under reducing conditions for a prolonged time are more complex. The principle gas phase sulfur specie are H_2S, SO_2 and COS and, even though the sulfur species are absorbed the possibility that the sulfide will decompose during burnout exists. The data presented in Figure 6 shows a significant difference between the behavior of coal and propane doped with H_2S. This difference can be attributed to:

- With coal part of the fuel remains in the solid phase and for a given input stoichiometry the gas phase stoichiometry in the reducing zone is higher than with gas. Reference to Figure 1 indicates that the stability of calcium sulfide is strongly dependent upon stoichiometry ratio;

- With coal up to 50 percent of the sulfur remains in the solid phase under rich conditions thus the gas phase concentration is lower than the corresponding concentration with propane as the fuel;

- The conditions during burnout in the second stage will be different for the solid and gaseous fuels and this could affect retention of the sulfur during burnout.

These tests indicate that there is the potential to remove greater than 50 percent of the input sulfur with Ca/S molar ratios of two when coal is burned under low NO_x conditions. Further work is necessary to insure that the controlling conditions can be achieved in practical combustors and that the sorbent injection does not adversely impact combustor performance.

References

1. Gartrell, F.F., "Full Scale Desulfurization of Stack Gas by Dry Limestone Injection", EPA-650/2-73-019 a, b, c, 1973.

2. Zallen, D.M., Gershman, R., Heap, M.P., Nurick, W.H., "The Generalization of Low Emission Coal Burner Technology", Proceedings, Third Stationary Source Combustion Symposium, EPA-600/7-70-050 b, 1979.

3. Flament, G., "The Simultaneous Reduction of NO_x and SO_2 in Coal Flames by Direct Injection of Sorbents in a Staged Mixing Burner", IFRF doc. no. G 19/a/10, 1981.

4. Coutant, R.W., et al., "Investigation of the Reactivity of Limestone and Dolomite for Capturing SO_2 from Flue Gas", Batelle Memorial Institute, Final Report, EPA Contract PH-86-67-115, 1970.

5. Borgwardt, R.H., "Kinetic of the Reaction of SO_2 with Calcined Limestone", NAPCA, Vol. 4, p. 59, 1970.

6. Borgwardt, R.H., Presentation at the EPA SPO Contractors Meeting, Raleigh, North Carolina, October 1981.

7. Ruth, L.A., Squires, A.M, Gratt, R.A., "Desulfurization of Fuels with Half-Calcined Dolomite: First Kinetic Data", Environmental Science & Technology, Vol. 6, p. 1007, 1972.

8. Yang, R.T., Chen, J.M., "Kinetics of Desulfurization of Hot Fuel Gas with Calcium Oxide. Reaction Between Carbonyl Sulfide and Calcium Oxide", Environmental Science & Technology, Vol. 13, p. 549, 1979.

Acknowledgments

This work has been supported under EPA Contract 68-02-2667. The authors are pleased to acknowledge the encouragement and ideas provided by Dr. D. C. Drehmel and G. B. Martin of EPA and the contributions of their colleagues at EER in the execution of the experiments.

TITANIUM AS A TRACER FOR DETERMINING COAL BURNOUT

Ray S. Pace, Paul O. Hedman, and L. Douglas Smoot

Combustion Laboratory
Department of Chemical Engineering
Brigham Young University
Provo, Utah 84602

INTRODUCTION

Background. Extensive research on coal combustion at this laboratory (1-6) has focused on developing an understanding of the physical and chemical mechanisms and reaction rates of coal burnout and nitrogen and sulfur pollutant formation. Local samples of combustion products have been extracted from the pulverized coal combustor using water-quenched sample probes. To complete mass balances and determine important local parameters, chemically inert tracers have been used in the reactor. Argon added to the primary air has been used as the gas phase tracer to determine the mixing rates of the primary and secondary air streams and the volume of combustion gases from the coal. Carbon conversion is also determined from gas composition, coal feed rate, and a forced argon balance.

Coal burnout has been calculated from the percent ash in the residual char and in the raw coal in previous phases of this study (4-6). However, the use of ash as a particle tracer has not been satisfactory. Ash is not a suitable tracer because it contains many inorganic compounds which decompose and/or vaporize. Kobayashi, et al. (7) and Sarofim, et al. (8) have shown that as much as 20-60 percent of the original coal ash can be volatilized depending on the temperature history of the ash.

Collecting samples of combustion products with a water-quench probe produces a char-water mixture which is filtered and dryed to obtain the solid char sample. Many constituents of ash are soluble in the water and more losses are incurred in the total measured ash content. Harding, et al. (6) have shown that up to 10 percent of the ash can be dissolved in the probe quench water.

High losses of ash negate its usefulness as a solid tracer by introducing large errors into the mass balance and burnout calculations. Consequently, there has been an interest in finding another particle tracer which could more accurately determine coal burnout, and also to help understand the fate of the ash and slag.

Mims, et al. (9) have characterized the volatilization of ash with temperature. At higher temperatures, compounds formed from elements such as arsenic, manganese, magnesium, sodium and antimony showed strong vaporization trends. Aluminum, silicon and other known refractory compounds also showed significant losses at high temperatures. Compounds formed from such elements as titanium, scandium, barium and lanthanum were found to be more stable. Because of their low concentrations in the coals, scandium and lanthanum were not considered as feasible tracers. Titanium was selected as a possible tracer because it forms relatively stable high boiling point compounds (i.e., TiO, TiC, TiO_2, Ti_4O_7), and is found in most coals in easily detectable amounts.

Objectives. The purpose of this study was to develop an analytical procedure which could be used to measure the concentration of a solid particle tracer and apply the techniques to representative samples from the pulverized coal combustor. Techniques commonly used to analyze elements in the ash are atomic absorption (AA), instrumental neutron activation analysis (INAA), x-ray diffraction (XRD), and x-ray fluorescence (XRF). XRF was chosen because of the ease of analysis (sample preparation time 10-15 minutes and analysis time of 40-120 seconds), and availability of a suitable instrument. Comparison of AA, INAA and XRF results for

fly ash and coal analysis have been found to give good agreement for most elements (10).

This study was divided into three tasks: (1) set-up and calibration of the XRF instrument in order to measure titanium trace element concentration in char from the combustor, (2) analysis of char samples from combustor tests to determine the usefulness of titanium in the ash as a tracer, and (3) use of the titanium tracer data to compute mass balances and consequently coal burnout.

TEST FACILITIES

A diagram of the pulverized coal combustor with major dimensions is shown in Figure 1. The reactor, with a coal feedrate of about 13.6 kg/hour, was constructed of five interchangable sections of 33 cm (14 in.) schedule 40 pipe. Each section was 30.4 cm in length and lined with 6.4 cm of castable aluminum oxide refractory. One of the five sections contained a water-quench, traversing probe which was used to sample the flame at different axial locations in the reactor. This section could be interchanged with any of the other sections in order to obtain gas and char samples at various radial and axial locations, effectively mapping the reactor. A more detailed description of the combustor and its supporting facilities has been reported (4-6).

In order to obtain an adequate sample of combustion char for ASTM ash and XRF Ti analysis, a special larger exit sample probe was used. The probe detail of Figure 1 shows the design of the probe tip that permitted centerline char sample collection near the reactor exit without interfering with other combustor experiments. Both probes were similar in design, differing only in size. Complete details on the design and operation of the probes have been documented (6, 11, 12).

INSTRUMENTATION

A Phillips 1410 vacuum path x-ray fluorescence (XRF) spectrometer was used to analyze titanium in the coal samples. XRF is known for the relatively quick sample analysis time and sample preparation time (10). Quantitative measurements of Ti on the XRF required values for five correction factors: detector dead time, background count, peak overlap, absorption corrections, and instrument electronic and power drift. Each factor is briefly discussed below.

Dead Time. Dead time is the time required for the electronics and detector to register one count of radiation. If a second burst of radiation arrives at the detector before the first burst is registered, the second burst will not be registered. The bursts of radiation are assumed to be statistically random and a simple correlation is used to quantify the dead-time correction (13).

Background Counts. Natural scattering of the x-rays causes a small count to be present at every angle on the XRF. The background counts vary non-linearly and compensation is made by estimating the background at the peak using an average of the background at angles below and above the peak.

Peak Overlap. Peaks within one or two degrees of the measured peak may add to the number of counts at the desired peak position. Corrections for these overlaps are made by measuring pure disks of the interfering element and determining the height of the peak at the desired angle.

Absorption and Instrument Drift. Fluorescence from an element within the sample matrix could be absorbed by another element, altering the intensity of the peak of the desired element. Carbon and other lighter elements are strong absorbers at the wavelength of radiation from titanium. This causes major problems when organic concentrations in the char vary from 0 to 94 percent. This problem is circumvented by using the internal standard method of calibration. Instrument drift

on the XRF is caused by variations in the voltage, sample placement, and goniometer accuracy on the machine. These are also compensated by the internal standard method (14).

XRF Calibration. The internal standard method of calibration (14) was chosen as the calibration technique. Scandium as Sc_2O_3, which has an absorption edge near those of the element being measured, was added to the char sample in a known concentration. Since absorption effects are similar for the two elements, the ratio of the concentrations of the unknown to the standard element was related to the ratio of the intensities by a constant factor A:

$$W_{Ti}/W_{Sc} = A\, C_{Ti}/C_{Sc} \qquad (1)$$

where A is a constant factor, C_{Ti} and C_{Sc} are the measured counts of radiation at the peaks for titanium and scandium in the sample, respectively. This ratio technique eliminates the need for absorption corrections because the peaks are in the same sample, and the absorption correction factors are nearly equal. Calibration after every third sample prevented major errors due to machine drift. Calibration consisted of analyzing a cellulose blank to determine background factors and then analyzing a NBS fly ash standard (NBS Standard Reference Material 1633a) for titanium to determine the value of A in Eqn. 1.

XRF Error Analysis. The counting statistics and equations for the XRF error analysis are explained in detail by Jenkins and DeVries (13). The arrival of bursts of radiation from the sample can be modeled as a Chi Square distribution which approaches a Gaussian distribution. A total XRF counting error of ±0.4 percent (relative[1]) was realized for the tests conducted. This gave a limit of detection of 45 ppm (mass). The raw coal contained about 400-600 ppm titanium (dry basis), well above the minimum.

The XRF counting errors were very small. The major errors were introduced by the sample preparation techniques. Samples were prepared by weighing 400 mg of char, 40 mg of high purity cellulose and 10 mg of Sc_2O_3 into a small vial with a 6mm glass ball. A commerical dental mixer was used to mix and grind the sample for 3 minutes. The sample was then pressed onto a support with a cellulose backing at 4.58×10^6 kg/m^2. The major errors introduced in weighing the Sc_2O_3 accurately were ±1 to 2 percent. Increasing the percent Sc_2O_3 did not significantly increase the accuracy because of increased error due to increased scandium counts.

TEST PROGRAM

Fifteen combustor tests were performed at four different values of secondary air swirl number[2] (S_s^e = 0.0, 1.4, 3.2, and 4.5), and over a range of stoichiometric ratios[3] (SR) of 0.59 to 1.65. The coal used was a Wyoming subbituminous coal with about 5.0 weight percent ash (as received) and 0.8 weight percent titanium in the dry ash. The proximate analysis of the coal gave values of 27.8 percent, 32.9 percent, 34.3 percent, and 0.4 percent for moisture, volatiles, fixed carbon, and

---

[1]Relative error is error divided by percent titanium present times one hundred.

[2]Swirl number (S_s^e) is defined as the flux of angular momentum divided by the product of duct radius and axial flux of momentum.

[3]Soichiometric ratio (SR) is defined as the air/fuel ratio divided by the stoichiometric air/fuel ratio. SR values less than one are fuel rich while SR values greater than one are oxidizer rich.

sulfur respectively. The ultimate analysis on a dry basis gave 6.9 percent ash, 4.4 percent hydrogen, 76.3 percent carbon, 1.1 percent nitrogen, 0.5 percent sulfur and 10.8 percent oxygen. The char sample probe was located on the center line of the reactor near the reactor exit (ca 150 cm from the burner inlet). Coal burnout was determined at each test condition from ASTM analysis of the ash sample, and by XRF analysis for titanium in the char sample.

TEST RESULTS

Coal burnout results determined from a titanium mass balance in the char samples obtained are shown in Figure 2. Coal burnout was shown to be primarily a function of stoichiometric ratio, increasing from about 80-87 percent at SR = 0.6 (fuel rich) to greater than 95 percent at SR > 1.1 (Figure 2(a)). The tests were not all conducted at a consistent set of stoichiometric ratios. Nevertheless, interpolation of the curves (Figure 2(a)) at SR = 0.6, 0.9, and 1.2 has permitted the effect of swirl in the secondary air stream to be determined (Figure 2 (b)). The effect of stoichiometric ratio is still quite pronounced. The effect of secondary swirl on coal burnout is small. The combustion of pulverized coal is very complex and the influences of secondary swirl, mixing rate, stoichiometric ratio, etc. are just beginning to be understood (1-6).

An ASTM analysis of the char samples for ash and titanium as a tie component are given in Figure 3. Titanium burnout is higher in every case than the ash burnout, indicating that titanium is a better tracer than ash.

The extent of ash loss, equivalent to an ash burnout, has also been determined from the titanium data. A set of parametric ash loss lines have also been constructed on Figure 3 for comparison (10 percent, 20 percent, 30 percent, 40 percent, and 50 percent). Ash losses of 15 to 60 percent can be observed by the superposition of the data on the various ash loss lines. The extent of ash loss is large compared to earlier work at this laboratory with a bituminous coal (6). However, the difference in coal type, ash composition, and moisture level could account for these differences.

Ash loss has little effect on coal burnout at very high burnout levels. Figure 4 shows the error in burnout due to ash loss at several different burnout levels. At burnout values of 95 percent, ash losses of 40-50 percent create differences of only 2-3 percent in burnout estimates. Hence at moderate ash loss (20-40 percent) and high burnout values (greater than 95 percent burnout) the ash tracer burnout values are almost as accurate as the titanium-based burnout values. However, if burnout is below 95 percent then burnout based on titanium gave significantly improved results.

Asay (12) has recently completed as set of pulverized coal combustion tests at the same secondary swirl numbers and at nearly the same stoichiometric ratios for this Wyoming coal. Carbon burnout data obtained from these tests with a complete gas coumposition and an argon tracer mass balance are compared in Figure 5 to the titanium analysis coal burnout data reported above. In general, coal burnout is expected to be from 1-2 percent higher than carbon burnout because of the more complete release of the hydrogen from the coal. In general, the agreement between burnout values from the gas analysis and from the titanium analysis is good at SR > 0.9. At SR = 0.6 however, the burnout values determined from the gas analysis are much lower. Asay (12) is still reviewing this discrepancy but it is thought that the data from the titanium analysis are superior. One possible explanation is that the gas data represent an integration of radial gas composition profiles near the reactor exit while the titanium data are based on centerline samples.

CONCLUSIONS

Titanium can accurately be determined in char samples by using the internal standard method of XRF calibration. Errors of ± 2-3 percent are incurred mostly from sample preparation inaccuracy. X-ray fluorescence instrument error is less than ± 0.4 percent.

Titanium compounds in ash are more stable than the total ash constituents and hence provide a solid phase tracer to complete overall mass balances with increased accuracy. Burnout calculations are improved by as much as 20 percent at burnout values less than 95 percent and with high ash loss. When coal burnout level is above 95 percent, titanium provides only 1-2 percent increased accuracy in the burnout calculation.

Use of the titanium tracer also provides a method of calculating ash loss. Up to 60 percent of the ash was lost in these combustion tests. This loss is the sum of the losses due to vaporization in the flame and dissolution into the quench water.

ACKNOWLEDGEMENTS

Blaine Asay, Steven Zaugg, and Rodney LaFollette assisted in the combustion tests while technician, drafting, and secretarial services were provided by Michael R. King, Kathleen Hartman, and Ruth Ann Christensen, respectively.

This research project was supported by the EPRI under contract RP-364-2 with Mr. John Dimmer as project officer, and by the Brigham Young University Research Division.

REFERENCES

1. L.D. Smoot, P.O. Hedman. "Mixing and Kinetic Processes in Pulverized Coal Combustors." Final report prepared for EPRI, Contract No. RP-364-1, August 1978.

2. L.D. Smoot, P.O. Hedman, and P.J. Smith. "Mixing and Kinetic Processe in Pulverized Coal Combustors." Final report prepared for EPRI, Contract No. RP-364-1-3, October 1979.

3. L.D. Smoot, P.O. Hedman, and P.J. Smith. "Combustion Processes in a Pulverized Coal Combustor." Final report prepared for EPRI, Contract No. RP-364-2, August 1981.

4. J.R. Thurgood, L.D. Smoot, and P.O. Hedman. "Rate Measurements in a Laboratory-Scale Pulverized Coal Combustor." Combustion Science and Technology, 21, 1980, pp. 213-225.

5. D.P. Rees, L.D. Smoot, and P.O. Hedman. "Nitrogen Oxide Formation Inside a Laboratory Pulverized Coal Combustor." 18th Symposium (International) on Combustion, The Combustion Institute, Pittsburgh, Pennsylvania, 1981, pp. 1305-1311.

6. N.S. Harding, L.D. Smoot, and P.O. Hedman. "Nitrogen Pollutant Formation in a pulverized Coal Combusor: The Effect of Secondary Stream Swirl." accepted for publication in AIChE Journal, 1982.

7. H. Kobayashi, J.B. Howard and A.F. Sarofim. "Coal Devolatilization at High Temperatures." 16th Symposium (International) on Combustion, Combustion Institute, Pittsburgh Pennsylvaniz, 1977, p. 411.

8. A.F. Sarofim, J.B. Howard, A.S. Padia. "The Physical Transformation of the Mineral Matter in Pulverized Coal Under Simulated Combustion Conditions," Combustion Science and Technology, 16, 1977, pp. 187-204.

9. C.A. Mims, M. Neville, R.J. Quann and A.F. Sarofim. "Laboratory Studies of Trace Element Transformations During Coal Combustion." 87th AIChE National Meeting, August 19, 1979.

10. R.D. Smith. "The Trace Element Chemistry of Coal During Combustion and the Emissions from Coal-Fired Plants." Progress in Energy and Combustion Science, Vol. 6, Number 1, 1980, pp. 53-119.

11. R.S. Pace, "Titanium as a Tracer for Determining Burnout in a Laboratory Pulverized Coal Combustor," M.S. Thesis, Brigham Young University, in preparation, December, 1981.

12. B. Asay, "Measurement of Nitrogen Pollutants and other Combustion Products in a Swelling Pulverized Coal Flame," Ph.D Dissertation, Brigham Young University, in preparation, 1982.

13. R. Jenkins and J.L. DeVries. Practical X-Ray Spectrometry. 2nd ed., New York: Springer-Verlag Inc., Great Britain, 1969.

14. K. Norrish and B.W. Chappell. "X-Ray Fluorescence Spectrography." ed. by J. Zassman, Physical Methods in Determination Minerology, New York: Academic Press, 1967, pp. 201-272.

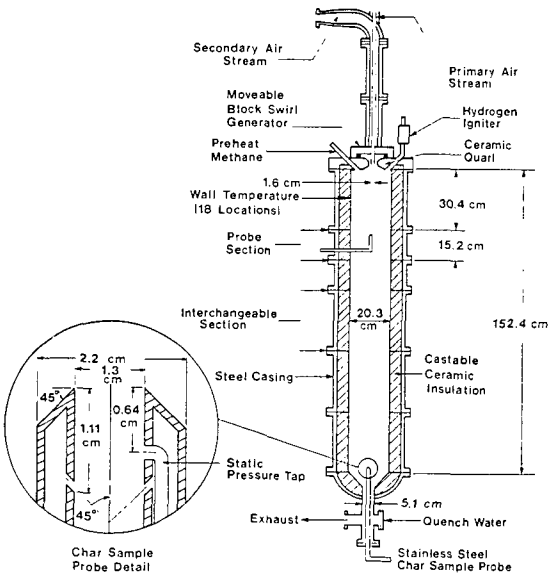

Figure 1. Schematic of atmospheric combustor (Adapted from Harding (6)).

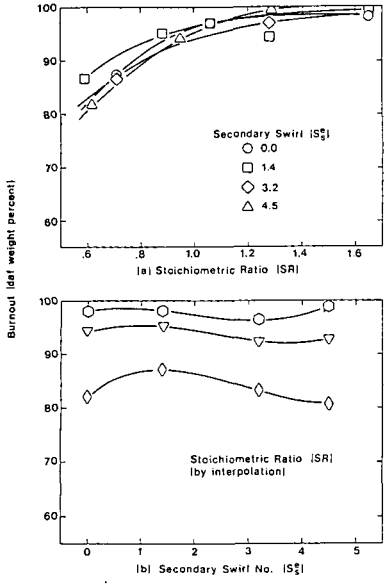

Figure 2. Effect of stoichiometric ratio and secondary swirl number on coal burnout by titanium analysis.

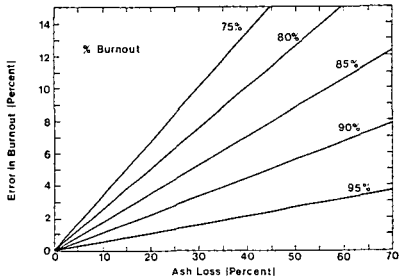

Figure 4. Percent change in burnout due to ash volatilization.

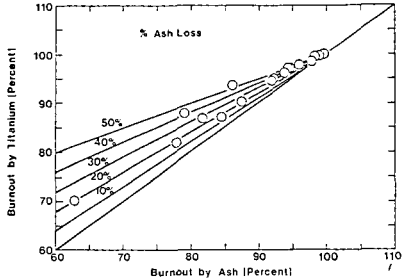

Figure 3. Burnout using titanium compared with burnout using ash as tracer.

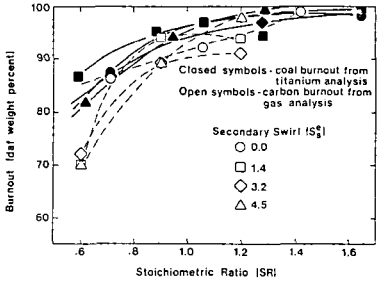

Figure 5. Comparison of carbon burnout by gas and analysis and coal burnout by ash tracer.

BED AGGLOMERATES FORMED BY ATMOSPHERIC FLUIDIZED BED COMBUSTION OF A NORTH DAKOTA LIGNITE

Steven A. Benson, Frank R. Karner, and Gerald M. Goblirsch
Grand Forks Energy Technology Center
U.S. Department of Energy
Grand Forks, North Dakota 58202

David W. Brekke
Department of Geology
University of North Dakota
Grand Forks, North Dakota 58202

INTRODUCTION

The goal of atmospheric fluidized bed combustion (AFBC) research at the Grand Forks Energy Technology Center is to provide a data base for design, operation, process control, and emission control requirements for low-rank coals. The application of the AFBC process has the potential to solve some of the problems associated with conventional combustion. These problems are ash fouling on heat exchange surfaces, the expense and reliability of SO_2 control devices such as scrubbers, and the system sensitivity to fuel variables (moisture, Na_2O concentration, etc.).

These problems can be reduced by the AFBC process for low-rank coals because the alkaline characteristics of the ash or sorbent added directly to the combustion zone provides the sulfur retention, which would eliminate or reduce the need for post combustion SO_2 controls. The temperatures in the combustion zone are at the right levels to provide maximum reaction of SO_2 and alkali to form solid alkali sulfate waste. One problem which the fluidized bed combustion of low-rank coals seems to exhibit is a tendency toward the formation of agglomerates of the material which are used to make up the bed. Agglomerates in this case are defined as a cluster of individual bed material particles held together by a substance not yet well understood, and manifest in many differing forms. The understanding of the mechanism of formation of these agglomerates is vital to their control, and therefore the full utilization of low-rank coal in AFBC.

Once formed these agglomerates will tend to decrease heat transfer, and fluidization quality resulting in poor combustion efficiency and loss of control of bed operational parameters (i.e., excess air, temperature, etc.). In severe cases the formation of agglomerates can lead to a forced premature shutdown of the system.

While the addition of limestone, or calcium bearing materials into the fluid bed, or the forming of the bed itself by limestone particles has shown a tendency to inhibit the formation of agglomerates, agglomerates of a severe nature have been observed in a bed of limestone alone, or limestone and sand particle mixtures while burning a high sodium coal for an extended period of time.

In general with a high sodium coal the agglomeration of limestone bed material is dependent only on the length of run time, if the run is long enough agglomeration in a limestone bed will occur, and can be as devastating as those which occur with a silica bed.

GFETC constructed a 0.2 square meter experimental AFBC. A detailed description of the unit is given by Goblirsch and others (1). The combustor can be operated over a wide range of conditions as listed below:

Average bed temperature	--	700 to 982°C
Superficial gas velocity	--	0.9-2.7 m/sec
Excess air	--	10 to 50%
Ash reinjection (% of primary cyclone catch)	--	0 to 100%.

The nominal coal feed rate is 80 kg/hr at 1.8 m/sec superficial gas velocity and 20% excess air.

This paper discusses the performance of quartz or limestone as a bed material during the combusting of high sodium North Dakota lignite. The lignite is from the Beulah mine of Mercer County, North Dakota. The composite coal and coal ash analysis is summarized in Table 1. The lignite was partially dried before this series of tests; its as-mined moisture content was 36%, and its heating valve 15,000 J/g.

TABLE 1. TYPICAL COAL AND COAL ASH ANALYSIS OF HIGH Na BEULAH LIGNITE

Ultimate Analysis, As Fired			Coal Ash Analysis, % of Ash	
Carbon	52.65	%	SiO_2	15.8
Hydrogen	4.59		Al_2O_3	12.1
Nitrogen	0.75		Fe_2O_3	9.9
Sulfur	1.33		TiO_2	0.8
Ash	9.7		P_2O_5	1.0
Moisture	20.0		CaO	17.5
Heating Valve (8372 Btu/lb)	19,459 J/g		MgO	6.2
			Na_2O	8.8
			K_2O	0.0
			SO_3	27.2

Other important considerations are the operation of the combustor and how operational parameters affect the performance of the bed material, sulfur retention on coal ash and bed material, and heat transfer. The most important operational parameters of the AFBC for the tests to be discussed here are listed in Table 2.

TABLE 2. AFBC OPERATIONAL PARAMETERS

Run Number	2181	2281	2481
Coal Type	Beulah	Beulah	Beulah
Bed Material	Quartz	Limestone	Limestone
Average Bed Temperature (°F)	1467	1460	1450
Superficial Gas Velocity (M/sec)	1.8	2.0	1.8
Excess Air (%)	25.49	22.65	24.98
Additive	None	*	*
Ash Reinjection (%)	None	100	100
Coal Feed Rate (kg/hr)	53	57	48

*Addition of supplemental bed material to maintain bed depth.

The tendency for the bed to agglomerate has been shown through extensive testing to depend on the following parameters:

1. Bed temperature (higher temperature increases tendency)
2. Coal sodium content (increased coal sodium content shows increased severity of agglomeration)

3. Bed material composition (high calcium content tends to delay, and decrease the severity of agglomerates formed)
4. Ash recycle (increased recycle of ash tends to increase agglomeration tendency)
5. There appears to be a bed design parameter such as position of coal feed points, and distributor plate performance which affect bed material agglomeration.

The bed material used in baseline run 2181 was 10 mesh quartz sand. Upon startup the bed was sampled every eight hours for the duration of the 69 hour run. At the end of the run the system was cooled and opened to expose the inside of the combustor. The bed material was removed and several agglomerates were found, which varied in size and shape, with the largest having a diameter of 6 cm. These agglomerates were found both free floating in the bed and attached to the inside wall of the combustor.

The limestone bed material was tested in run 2281 using 100% ash reinjection for a duration of 73 hours. The bed was sampled in the same manner as 2181. The formation of agglomerates in the run was very minimal with no major agglomerates found. On the other hand, run 2481 which used a limestone bed ran for 160 hours with 100% ash reinjection and had severe problems with agglomeration. After the run numerous agglomerates were found loose in the bed. In addition, a large agglomerate was found on top of the distributor plate at the bottom of the combustor. The agglomerate had dimensions of 30.5 cm X 30.5 cm X 12.5 cm; it weighed 10 kg and covered 30% of the distributor plate.

The bed material and agglomerates were characterized by polished thin section study, polarized light microscopy, and scanning electron microscopy/microprobe (SEM) - both secondary electron (SEI) and backscatter electron (BEI) images were used. Bulk samples were analyzed by x-ray diffraction and x-ray fluorescence. The goals in characterizing the bed material and agglomerates are to identify the stages which lead to agglomeration and possibly postulate a mechanism of their formation to thereby determine methods and procedures to control their growth.

RESULTS AND DISCUSSION

Quartz Bed Agglomerates

Agglomeration of quartz bed material is typified by run 2181 utilizing high-Na Beulah lignite and ash injection. Samples of bed material taken at various intervals during the run are illustrated in Figures 1 to 11 with chemical analyses data given in Table 3. The following four stages can be used to summarize the agglomeration process:

Stage 1. Initial ash coating.

Initial samples of bed material have a fine coating, about 50 microns thick, consisting of sulfated aluminosilicate particles (Figure 1). The coatings contain some coarser ash materials in the outer parts and the inner parts have penetrated the quartz grains slightly along gently curved or cuspate embayments. The quartz grains are extensively fractured, apparently as a result of thermal stresses.

Stage 2. Thickened nodular coatings.

Longer bed usage results in the development of thicker ash coatings about 100 - 300 microns thick with nodular outer surfaces resulting from incorporation of larger ash particles (Figure 2). Sulfating, shown by lighter colored areas in the SEM photographs, is common within both the finer and coarser ash particles of the coating.

Stage 3. Sulfated ash-cemented agglomerates.

In this stage the quartz grains are loosely held together by a cement of sulfated aluminosilicate ash (Figure 3). Penetration of quartz grains by fine grained ash is more extensive.

Stage 4. Glass-cemented agglomerates.

In the final stage quartz grains are bonded by sulfated ash which has partly melted and crystallized through reaction of the hot ash and the quartz grains. Resultant cooled agglomerates consist of quartz grains of the bed material bonded by a mixture of sulfated ash and Ca-rich, S-poor glass (Figure 4), with an intermediate reaction zone made up of an S-depleted, Si-enriched ash portion with a fringe of melilite or augite crystals projecting into the glass (Figures 5 and 6). Some quartz grains are partly melted and/or recrystallized to cristobalite or other phases.

Limestone Bed Agglomerates

Agglomeration of limestone bed material appears to be dependent on ash deposition and sulfation combined with extensive reaction and deterioration of the bed material.

Ash buildup on the grains and sulfating is comparable to reactions that occur with the quartz bed material. However, the limestone grains appear to undergo the following reactions:

1. Loss of CO_2 and conversion to CaO with addition of S, Fe, Na and other elements. These reactions produce concentric alteration zones, high Ca and S contents and the reddish color that characterizes typical grains (Figure 7).

2. Continued reaction produces thicker sulfated ash coatings and more thoroughly altered bed grains.

3. Bed grains disintegrate extensively and become mixed with ash coatings producing a weakly bonded agglomerate consisting of masses of sulfated ash and altered limestone bed grains and fragments (Figure 8). The altered limestone appears to recrystallize to coarse crystals of anhydrite in a fine-grained matrix containing abundant Ca, S and Si (Figure 9). Other phases, not yet identified, occur in the limestone agglomerates including crystalline Fe-Ca oxides as shown in Figure 10, and other iron-rich zones and coatings.

Where quartz and limestone bed materials are combined mutual interactions produce reaction zones on the quartz containing secondary needles of an unknown calcium silicate mineral (Figure 11).

Bulk x-ray diffraction analyses were performed on the bed material agglomerates to identify the phases present. The crystaline phases found in the quartz bed agglomerates from run 2181 include quartz, a member of the series $Ca_2Al_2Si0_7$-$Ca_2Mg_2Si0_7$ which includes melilite, and $CaS0_4$. The major phases identified in the limestone bed agglomerate are $CaS0_4$, $CaSi0_4$ and CaO. This data supports the SEM microprobe data.

X-ray fluorescence analysis was performed on bed material sampled continually throughout the run to determine the changes in composition of major ash constituents. The most appreciable changes which occurred in the quartz bed run were: $Si0_2$ decreased from 95 to 47% of the bed because of dilution; $S0_3$ increased to 24% because of adsorption by alkali constituents of the coal ash in the bed; CaO increased to 11% and Na_20 increased to 7% of the bed. The CaO and Na_20 reacted with the $S0_3$ and adhered to the quartz grains of the bed. Al_20_3, Fe_20_3 and MgO remained relatively constant throughout the run after the initial eight hours. The

components of the limestone bed of run 2481 changed as follows: CaO decreased by dilution to 37% by the coal ash; SO_3 increased to 28% by adsorption; and Na_2O increased to 7.7% of the bed. SiO_2, Al_2O_3, Fe_2O_3 and MgO remained constant throughout the run after the initial eight hours.

The concentrations of alumina and silica remain constant during the run indicating that the aluminosilicate clay particles leave the bed during combustion. On the other hand, the calcium oxide and sodium oxide which largely originate from the organic structure of the lignite are free to react with the SO_2 and bed material increasing their concentration.

TABLE 3. CHEMICAL ANALYSIS DATA FOR FIGURE 1 TO 11.
WT. %

OXIDE	A	B	C	D	E	F	G
SiO_2	10.76	12.45	8.22	12.16	31.20	47.80	48.32
Al_2O_3	11.70	11.20	18.94	8.94	19.13	10.03	10.61
FeO	4.82	0.55	6.94	3.02	13.14	9.95	9.48
MgO	5.71	1.14	11.86	5.73	10.27	4.44	6.26
CaO	18.11	32.86	12.63	12.83	19.82	20.28	20.29
Na_2O	12.70	3.99	10.14	17.97	2.04	6.11	3.73
SO_3	34.45	37.25	30.80	38.27	3.39	0.43	0.52

OXIDE	H	I	J	K	L	M
SiO_2	15.50	19.66	12.39	1.81	0.89	31.50
Al_2O_3	10.28	0.15	5.13	5.91	1.87	8.20
FeO	0.75	0.37	1.15	0.32	81.69	0.56
MgO	3.84	0.09	0.93	0.17	0.91	0.00
CaO	40.45	53.36	44.23	39.58	13.55	44.19
Na_2O	1.91	1.74	0.78	0.40	0.00	2.76
SO_3	21.49	24.39	35.37	51.66	6.33	11.89

CONCLUSIONS

Agglomeration of the bed material can be manifested in many different ways depending on the chemical composition of the bed. The elements which have a major effect are sodium, calcium and sulfur which react with the bed material possibly forming possibly a molten phase. This phase causes other ash constituents to adhere to the bed particles. As this phenomenon reoccurs many times, agglomeration becomes more severe.

REFERENCE

1. Goblirsch, G.M., Vander Molen, R.H., and Hajicek, D.R., AFBC Testing of North Dakota Lignite, Sixth International Fluidized Bed Conference, Atlanta, Georgia, April, 1980.

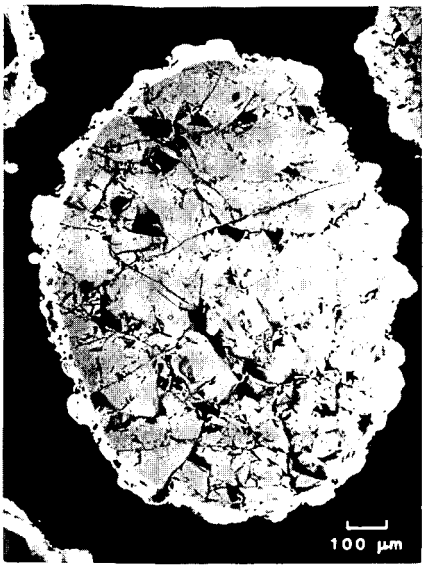

FIG. 1. Initial ash coating on quartz bed material. SEM/BEI image. Analysis A (Table 3). Run 2181, 40 hrs.

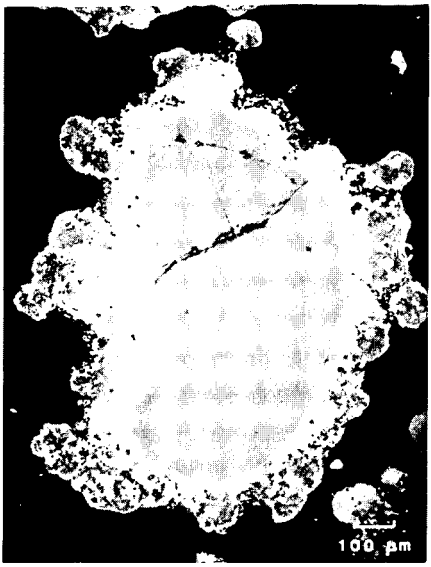

FIG. 2. Thickened nodular ash coating on quartz bed material. SEM/BEI image. Analysis B of fine light sulfated ash and C of darker interior of coarser ash particle (Table 3). Run 2181, 54 hrs.

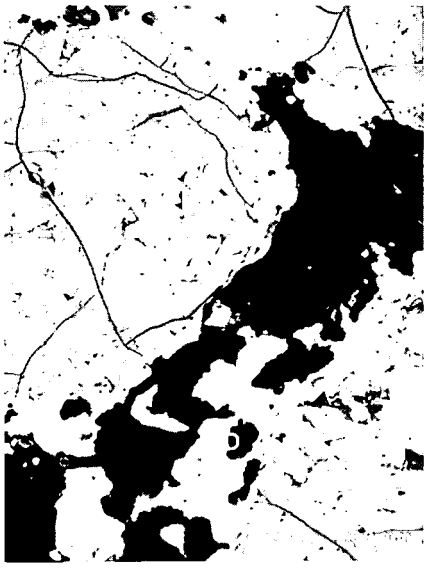

FIG. 3. Quartz bed grains loosely cemented by sulfated aluminosilicate ash. SEM/BEI image. Analysis D given in Table 3. Run 2181, 69 hrs.

FIG. 4. Quartz bed agglomerate bonded by altered sulfated ash, bottom of the dotted boundary (analysis E); Ca-rich, S-poor glass, top of the dashed line (analysis F); and intermediate fringe of melilite or augite crystals. SEM/BEI image. Run 2181, 69 hrs.

FIG. 5. Transmitted light image (partially crossed polars) of lower center of Figure 4 showing light quartz grain, gray glass, and crystals of melilite or augite crystals projecting into glass. Run 2181, 69 hrs.

FIG. 6. Detail of lower center of Figure 5, showing dendritic crystal form of melilite or augite. Analysis G given in Table 3. SEM/SEI image. Run 2181, 69 hrs.

FIG. 7. Concentric alteration zones and reacted limestone bed material. Analysis H given in Table 3. SEM/BEI image. Run 2481, 169 hrs.

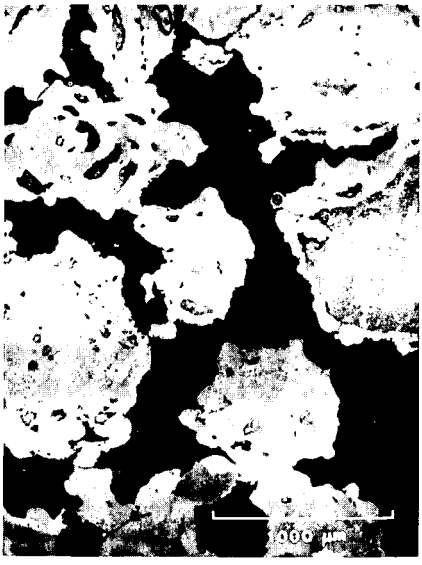

FIG. 8. Weakly bonded agglomerate of sulfated ash and altered limestone bed grains and fragments. Analysis I and J are given in Table 3. SEM/BEI image. Run 2481, 169 hrs.

FIG 9. Limestone bed material altered to coarse crystals of $CaSO_4$ in a fine-grained matrix of Ca, S, and Si. Light area to left is ash coating. Analysis K given in Table 3. SEM/BEI image. Run 2481, 169 hrs.

FIG. 10. Bladed crystals of Fe-Ca oxides in limestone agglomerate. Ash coating to right. Analysis L given in Table 3. SEM/BEI image. Run 2481, 169 hrs.

FIG. 11. Reaction zone consisting of secondary needles of an unknown Ca-silicate mineral on a quartz grain contained in the limestone bed. Analysis M given in Table 3. SEM/BEI image. Run 2481, 169 hrs.

Experimental Research on Lignite Fluidized Bed Combustion

Yang Min-Shin, Yang Li-Dan, Bao Yi-Lin, Chin Yu-Kun

Harbin Institute of Technology
The People's Republic of China

Burning Characteristics of Lignite Fuel

Lignite fuel is highly volatile and has a low ignition temperature, and is consequently easy to burn. In practice, however, when burning low grade lignite fuel in stokers or pulverized coal furnaces, some difficulties may occur due to high moisture content and low ash fusing point. In general, the moisture content of lignite fuel is above 30% and the sum of the moisture content and ash content is higher than 50%. Its heating value is about 2,000-2,500 kcal/kg and the ash-deformation temperature is higher than 1,100 C.

Burning lignite fuel in fluidized beds has many obvious advantages:

(1) High heat accumulation of the fuel bed. This provides a sufficient heat source to dry and preheat the lignite and helps high moisture lignite to ignite in time, resulting in a stable combustion condition.

As an example, a factory installed a fluidized-bed boiler with steam capacity of 10 t/hr. During the first winter of boiler operation, the air required for combustion was delivered into the furnace by drawing in outside air, which was approximately -30°C. In order to prevent the frozen coal from partially melting into a large lump in the coal bunker, the bunkers were installed outdoors. During the winter, frozen coal, together with ice particles, was delivered directly into the furnace via belts. The walls became covered with ice frost like the outside of a refrigerator. Despite such difficult conditions, the combustion process in the furnace was normal and the combustion was stable as long as the temperature of the fuel bed was above 600°C.

Another factory trial successfully fired three lignites with high moisture content. The measured characteristics of the fuels are given in Table 1.

Table 1. Typical Analysis of Lignites Fired in Trials

Type	I	II	III
Moisture content as fired (%)	27.21	46.01	56.82
Ash content as fired (%)	26.2	23.37	16.13
Volatile matter as fired (%)	24.1	19.83	14.91
Fixed carbon (%)	22.4	10.43	12.14
Lower heating value (kcal/kg)	2551	1470	1230

(2) The normal temperature range for fluidized beds is 850-950°C. This is much lower than the lignite ash-deformation point, and the temperature field is even, with no possibility of slagging.

(3) Ash erosion is not usually high. This is because the fly-ash particles flying out of the fluidized bed are not subjected to temperatures above their fusion point. Thus the erosion potential of the fly-ash is probably lower than that leaving conventional furnaces.

(4) Since the operating temperature for a lignite fluidized bed boiler may be relatively low, the load range can be much wider. As the temperature of the fluidized bed varies from 600°C to 900°C, the load range for a single fluidized bed can be easily varied from 50% to 100%. Using a separated fluidized bed operation, the minimum load can be further reduced, resulting in a much lower value than the low load stable operating range of a pulverized-coal furnace.

(5) The erosion of the submerged tubes in lignite fluidized-bed boilers is not serious due to the relatively loose character of lignite ash. In most fluidized bed boilers operated for many years, the erosion of the submerged tubes has not been a problem, although there may be some exceptions.

(6) The specific gravity of lignite ash is relatively low. For this reason the air pressure of the plenum may have a lower value than when using high low-grade coals. The plenum air is usually supplied at a pressure of 500 mm water.

(7) It's easier to ignite a lignite fluidized-bed boiler. We have ignited run of the mine (ROM) lignite fuel successfully many times when the temperature of the fuel bed was about 400°C.

(8) When lignite fuel is thrown into the high-temperature fuel beds, the fuel is suddenly heated and crumbles easily by itself, allowing coal particles as-fired to be very coarse. Operating experiments in Heilang Jiang and Yunnan provinces also proved that the maximum diameter of particles may be raised to 20-25 mm, slightly reducing power consumption for crushing and making it easier to sieve.

Fluidized Bed Boilers with a Rear-Installed Cyclone Furnace

At present, one of the main problems for existing fluidized-bed boilers is low combustion efficiency. The main reason for lower combustion efficiency and higher unburned combustible solids losses is the high carbon content in the fly-ash. The small particles may be blown off the high-temperature fluidized bed, resulting in an unburned carbon loss in the fly-ash.

Another important characteristic of lignite fuel is its high volatile content. The heat released from the volatile matter is about one-half of the coal heating value. In addition, lignite particles may break up during the burning process, forming many small coal particles. Therefore, one of the important characteristics for firing lignite in fluidized-bed boilers is possibly that more volatile matter and small coal particles are burning in the suspension chamber (freeboard).

The optimization of the combustion process in the suspension chamber to obtain better performance is an important factor in determining the combustion efficiency of lignite fluidized-bed boilers. One effective measure for reducing the fly-ash carbon content is using a fly-ash recycle for refiring in the fluidized beds or applying fly-ash refiring beds. However, this will complicate the system and its construction for small-capacity, fluidized-bed boilers. Practically, providing high temperature within the suspension chamber (freeboard) may exert an afterburning action for various fuels. For this reason, we suggest limiting the heat exchange surface as much as possible or not placing them in the freeboard. This will raise the gas temperature in the upper part of the furnace as high as possible. The ignition temperature for lignite fuel is relatively low. Thus, the increased temperature will exert sufficient afterburning action on the suspension chamber (freeboard). Providing a sufficiently high temperature in the suspension chamber is an important condition in achieving better combustion.

Another important condition is how to organize the aerodynamic field of the suspension chamber. In 1972, we designed a fluidized-bed boiler with a rear-installed cyclone furnace, shown in Fig. 1. Good results were obtained. Afterwards, we designed several dozen fluidized-bed boilers for lignite, the majority using rear-installed cyclone furnaces. The design of this cyclone furnace is based on the characteristics of a horizontal cyclone furnace. The aerodynamic field for a cyclone furnace is very complex. Its complexity assists in sufficient mixing of combustibles and oxygen in the gas flow. This is due to the increase in the relative velocity between the gas flow and the fly-ash and thus an increase in the diffusion velocity of oxygen to the fly-ash. These effects result in an increased burning velocity for coal particles. Furthermore, the residence time for fly-ash in the cyclone furnace is obviously prolonged. This is especially true for ash particles having a medium diameter. The carbon content for this part of the fly-ash, in general, gives the highest value. In addition, a cyclone furnace collects dust within the furnace. It may reduce erosion on the convection heating surfaces and reduce the load on the dust-collecting plants.

Note that although the dimension of the convex collar for cyclone furnace outlets is not large, its effect on the aerodynamic field is quite important. The scheme for an aerodynamic field in a cyclone furnace with and without a collar is shown in Fig. 2. It was also shown by cold modeling that the separation efficiency for cyclone furnaces with collars is much higher than for those without collars.

Aerodynamic Fields for Horizontal Cyclone Furnaces

In order to recognize the mechanism for the separating and afterburning action in the cyclone furnace and to investigate for a more reasonable construction, we have performed cold modeling for the horizontal cyclone furnace and tested the aerodynamic field in this type of furnace.

The maximum particle size leaving the cyclone furnace is expressed by the following relationship:

$$d_{max}^{1.6} = 13.88 \frac{W_r^{1.4} R''^2 r_g v^{0.6}}{W_t'^2 R_o r}$$

where

w_t' = velocity in inlet of cyclone furnace (m/sec)

w_r = radial velocity (m/sec)

R'' = radius of the exit (m)

r_g = specific gravity of gas (kg/m^3)

v = coefficient of kinematic viscosity of gas, (m^2/sec)

R_o = radius of the lower boundary of inlet (m)

r = specific gravity of particle (Kg/m^3)

From the above, we can approximate the diameter of a particle in cyclonic motion at the exit boundary of a cyclone furnace. Some large particles of diameter above d_{max} near the wall will be moved towards the wall and then pass down the wall. The other large particles will continue their circumferential movements in various values of the radius until the wall is reached or their diameter is reduced to less than d_{max}. The particles of diameter less than d_{max} may be moving with the air flow out of the cyclone furnace, but the small particles near the wall may also be separated from the gas flow. Therefore, d_{max} may be considered as the limit of the

maximum particle diameter leaving the cyclone furnace. Because particles are not spherical d_{max} obtained from the above equation should be divided by a coefficient ϕ, called the particle shape coefficient, as a correction. Only after this may the value be considered as the actual size.

For the cold modeling experiment, the above expression for d_{max} gives a value of about 94 μm. Experimental measurements show a maximum particle diameter of 142 μm. If this value is corrected for particle sphericity (ϕ = .66) a value of 93.72 μm is found which is very close to d_{max} from the above expression.

For conditions typical of an operating cyclone furnace, the maximum particle diameter leaving the furnace from the above equation is about 320 μm. For some factory furnaces the experimental value is about 500 μm. This is equivalent to a spherical diameter of 330 μm (ϕ = 0.66) which is close to 320 μm.

Summarizing, the principal causes of afterburning action in cyclone furnaces are:

(1) Large particles of fly-ash are thrown by the high centrifugal force toward the wall. These particles then pass rapidly down the inner walls of the cyclone furnace. Although these particles are separated rapidly, due to the high relative velocity they can be burned up within a short time. Since large particles have partially burned within the fluidized bed, the carbon content of these particles would not be as high.

(2) Based on the above principle, medium particles will move around the circumference with different radii until they have burned to a size less than d_{max} and then leave the cyclone furnace. So the residence time of the medium particles within the cyclone furnace is greatly increased resulting in greater char combustion.

In addition, the action of the collar mounted at the throat forces the air flow at and around the throat to change its direction repeatedly (rotating 180°). This forms an intense turbulence and recirculating movement of the particles (see Fig. 1). The latter recirculates in the cyclone axially and at the same time rotates around the cyclone axis, also increasing the residence time of the particles within the cyclone furnace. Cold modeling has confirmed that some medium-size particles are rotating continually within the cyclone furnace until the fan is shut down.

Based upon theoretical analysis and some experimental data from the domestic research unit, it has been found that particles of medium size have the highest carbon content, and that this type of particles is in the majority. For example, experimental data obtained in the fluidized bed boiler burning local coal at Che-Jiang University has shown that the heat loss for particles ranging from 0.13 to 0.375 mm is over 70% of the total heat loss of fly-ash. The majority of these particles may be just the rotating particles within the cyclone furnace. Therefore, the cyclonic action of the cyclone furnace may be very effective in reducing the carbon-content of fly-ash.

Experimental Research on the Cyclone Furnace Under Thermal State

The carbon content of the ash samples taken from various parts of the boiler flue gas were determined and are summarized in the following table.

Table 2. Ash Size Distribution and Carbon Content in Various Parts of Flue Gas

Granularity mm	Ash separated in cyclone furnace		Ash in precipitating chamber		Ash in dust collector	
	proportion by weight %	carbon content %	proportion by weight %	carbon content %	proportion by weight %	carbon content %
	1.87	1.18				
1-2	5.83	1.76				
0.5-1	36.4	1.08	4.64			
0.28-0.5	25.8	1.3	15.4	18.48	1.25	35.86
0.09-0.28	24.8	0.93	59.3	9.91	33	18.89
0.09	5.2	1.05	20.66	4.12	65.18	8.53

In a typical boiler, a two-stage dust collector is used. About 60% of the total fly-ash is collected in the precipitating chamber. The remaining ash is then removed by the dust collector. Based on the above data, we can draw the following conclusions:

(1) The ash particle size in precipitating chambers and dust collectors is scarcely larger than 0.5 mm. It is reasonable to assume that particles greater than 0.5mm will not leave the cyclone furnace. This is in accordance with the results from the cold modeling experiment.

(2) Ash particles with diameters of 0.25 - 0.5mm in the fly-ash have the highest carbon content. However, most of this fly-ash size fraction has been separated from the gas flow in the cyclone furnace and its proportion by weight in the fly-ash is not high. When a boiler operates at normal capacity, the average carbon content for fly-ash is 11.85%. This value may be considered relatively low.

(3) The ash particles separating from the gas flow in the cyclone furnace have a significantly lower carbon content than that observed in the ash overflow. In general, the medium particles of fly-ash have higher carbon content, while the carbon content of ash particles ranging from 0.28 to 0.5 mm separated in the cyclone furnace is only 1.3%. This shows that the degree of burn-up for ash separated within cyclone furnaces is rather high.

(4) Since the separation efficiency for cyclone furnaces is rather high (about 50%), the ash particles burn more completely with the result that the boiler combustion efficiency increases. During operation periods at rated capacity, the unburned combustible solid losses are 3.8% and the unburned gas losses are 0.67% while the combustion efficiency can be as high as 95.47%.

When the temperature of fluidized bed section is 900^{o}C at rated capacity, the gas temperature measured at the cyclone furnace exit is 920^{o}C, that is the temperature difference between the latter and the former is 20^{o}C. This shows that there are some combustibles still burning in the suspension chamber and in the cyclone furnace. According to calculations, the total fraction burned in the suspension chamber and cyclone furnace is 0.3.

In experimental tests with another lignite fluidized bed boiler of the same type, the fraction burned in the cyclone furnace itself was found to be 0.172.

The results of the data for the above two experiments are basically the same. It can be seen from the above summary that the total fraction of combustion in

suspension chambers and cyclone furnaces in fluidized bed boilers is relatively high. Thus the organization of the combustion process is highly significant in obtaining better boiler combustion efficiency.

The separation efficiency for cyclone furnaces, η_f, is the ratio of ash separated in the cyclone furnace, ΔG, to ash leaving the cyclone furnace, G", plus the ash separated, ΔG, that is

$$\eta_f = \frac{\Delta G}{G'' + \Delta G} \times 100\%$$

The unburned carbon content of the ash is included in the above expression. The results of the tests are summarized in Table 3.

Table 3. Separation Efficiency for a Cyclone Furnace as a Function of Ash Particle Size

Granularity mm		>1	0.5-1	0.28-0.5	0.09-0.28	<0.09
Separating efficiency	η_f %	100	93.7	75.3	39.3	13.7

The average separating efficiency is about 50%.

Conclusions

(1) Lignite of high moisture content is not an easy to burn fuel. At present, for typical industrial boilers in our country, there has not been a furnace-type which has the ability to burn high moisture content lignite fuels economically with the exception of fluidized bed furnaces. Burning lignite fuel in utility boilers presents many significant difficulties also. Existing experiments show that fluidized bed boilers can successfully burn low-grade lignite fuel having moisture content up to 56.82% or ash content up to 46.8%.

(2) Rear-installed cyclone furnaces have an obvious effect of increasing oombustion efficiency for lignite fluidized bed boilers. The combustion efficiency for boilers of such types may be as high as 95%. Its main function consists of prolonging the residence time of the medium particles which contain higher carbon content within the furnace. This creates better conditions for carbon combustion. The total fraction of combustion in the suspension chamber and cyclone furnace is about 0.3.

(3) The separation efficiency for cyclone furnaces is about 50%. The majority of particles having diameters larger than 0.5mm may be separated from the gas flow in the furnace. The approximate maximum particle diameter leaving the cyclone furnaces may be obtained from the following formula.

$$d_{max}^{1.6} = 13.88 \frac{W_r^{1.4} R''^2 \ 0.6}{W_t'^2 R_o r}$$

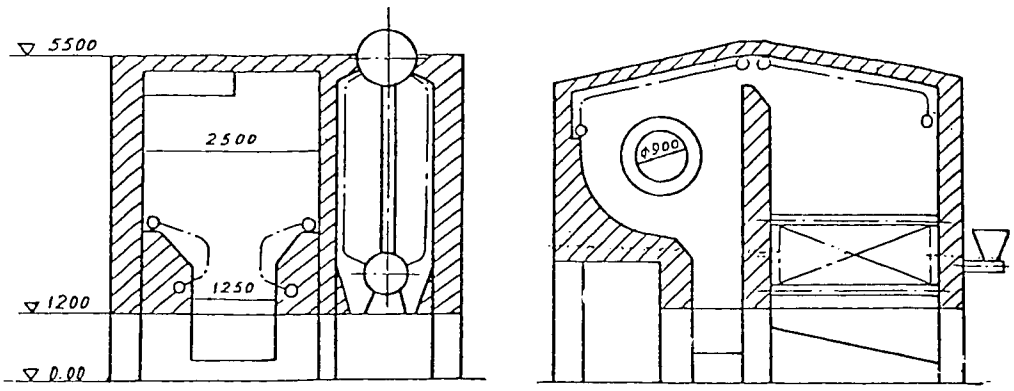

Figure 1. Fluidized-Bed Boiler with Rear-Installed Cyclone Furnace

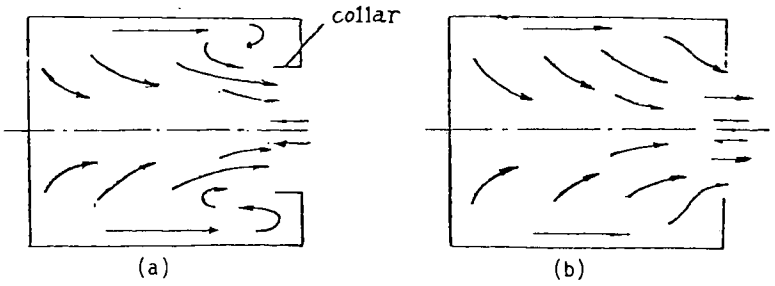

Figure 2. Effect of Collars on the Aerodynamic Field in a Cyclone Furnace: (a) With Collar. (b) Without Collar.

Pilot Plant of a Coal Fired Fluidized Bed Boiler in Japan

S. Tamanuki

The Coal Mining Research Center
Kanda Jinbocho 2-10 Chiyoda-ku
Tokyo, Japan

H. Karayama, S. Kawada

Kawasaki Heavy Industries, Ltd.
Babcock-Hitachi K.K.

A pilot plant of an atmospheric fluidized bed combustion boiler which is capable of evaporating 20 t/h at the steam conditions of 60 atg and 540°C was constructed and started operation at the beginning of April, 1981.
A description of the project and its results are presented in this paper.

1. Introduction

Brief History of FBC Development in Japan

The project named 'Research on Fluidized Bed Combustion Technology' was started in 1978 to support Japan's national effort for coal utilization technology development. This project has been financially supported by the government and steered by a joint committee of several related agencies and companies. The Coal Mining Research Center has been filling the leading role in this committee since it was organized in 1978.

During 1978 and 79 component tests and fundamental studies using bench scale units were performed. In parallel with these a feasibility study for a 500 MW power generation unit was carried out. The previously expected advantages of fluidized bed boilers over the conventional pulverised coal combustors were examined. It has been found that most of the advantages of fluidized bed combustion such as the possibility of eliminating flue gas desulfurization and denitrification and the capability of handling wide range of coal types are still effective for Japanese social and economical situations.

The whole program of the fluidized bed boiler development is shown in Table 1. A pilot plant with a 20 t/h evaporation capacity was constructed in Wakamatsu Thermal Power Plant of the Electric Power Development Co. and the test runs are performed for testing the instrumentations and components and determining the optimum operating conditions of the fluidized bed boiler. A survey program on the design conditions for various components and devices for a 240 t/h class

demonstration plant is also running.

Organization

To carry out this project effectively, the pilot plant program Steering Committee was organized by The Coal Mining Research Center, Electric Power Development Co., Kawasaki Heavy Industries, Ltd. and Babcock-Hitachi K.K. As a sub-committee of the Steering Committee, the Pilot Plant Executive Office was organized. This Office has taken charge of the construction, test and operation of the pilot plant.

Wakamatsu Pilot Plant Test Items

The planned pilot plant test items are as follows:

(1) NOx and SOx emission control
(2) Reduction of the required quantity of desulfurizing sorbent
(3) Controllability of the fluidized bed boiler
(4) Reliability of the fluidized bed boiler
(5) Suitable types of coal
(6) Performance of the dust collector

2. 20 t/h Pilot Plant

Basic Concepts

The fluidized bed boiler consists of a main bed cell (MBC) and a carbon burn-up cell (CBC). The design was made so that various imported coals and low grade coals can be burned.

Crushed coal has been used as a feed coal. Before feeding, the coal is pretreated-drying, crushing screening, etc. Coal feeding is done by both pneumatic feeders and overbed spreaders.

Fine grain coal is fed to the bottom of the bed through a pneumatic conveyer and coarse grain coal sprinkled over the fluidized bed by a spreader. The capacity of the feeders are designed so that total required quantity of coal can be fed by one of these two method. Natural limestone whose sizing has been completed at the mine is used as a desulfurizing sorbent. The sorbent is fed through a pneumatic conveyor.

A multi-cyclone is installed at the outlet of the MBC. The design was made so that the collected coal ash can be reburned either in MBC or CBC.

A balanced draft systems is used.

MBC was designed so that it can be diveded into two parts. The installation position of heat exchange tubes in the free board of MBC can be changed. The duct connected to the rear flue can be removed so that the height of free board can be changed.

Hot stoves and over bed burners are used for starting up the boiler. Steam generated by the boiler is changed back to water by an air condenser. The water can be reused. Discharged ash is wetted and transferred to the ash yard to be discarded.

After the fiscal year 1982, the following expansion or modification will be made.

A. A sorbent regeneration unit: applicable for both limestone and synthetic sorbent.

B. A new dust — collector for testing is planned for the dust discharge quantity 10 mg/Nm^3, and for the gas flow rate of approximately 1,000 Nm^3/h.

Design Conditions

(1) Main boiler specification

Boiler type:	Natural and forced circulation type drum boiler; indoor type.
Evaporation:	20 t/h
Steam pressure:	60 kg/cm^2 G at the outlet of the superheater
Steam temperature:	540°C at the outlet of the superheater
Feedwater temperature:	133°C at the inlet of the fuel economizer
Boiler efficiency:	87.37% (high calorific value base)
Fuel consumption:	2,450 kg/h (wet coal base)
Fuel calorific value:	7,100 kcal/kg (high heating value for dry coal.) 6,603 kcal/kg (high heating value for wet coal)
Combustion flue gas:	20,293 Nm^3/h (wet)

(2) Target value of emission control
SOx: 95% desulfurization for coal containing 3% S
NOx: 60 ppm for coal containing 1% N and O_2 6% equivalent.

(3) Properties of planned coal: Refer to Table 2.

(4) Desulfurizing sorbent: natural limestone and synthetic sorbent

Plant Outline

(1) Boiler

Fig. 1 shows a section of the boiler elevation.

The MBC consists of the combustion furnace which is composed of a natural circulation membrane structure water wall and the refactory wall rear flue. In the fluidized bed with a 2.17 m x 4.34 m area, the forced circulation type evaporator by a boiler circulating water pump and the primary and secondary superheaters are installed. The fluidized bed is divided into two parts so that one side operation can be done.

Outside the bed, the evaporator and flue economizer are installed. This evaporator, as shown in Fig. 2, can be removed to the free board of the combustion furnace or rear flue. This, together with a change in the installation level of the duct connecting to the rear flue, enables the test for a change in free board conditions. In the free board of the combustion furnace, double stage combustion air feeding ports (8 rows x 5 stages) are installed to enable various comparison tests to be conducted.

CBC is composed of a natural circulation water wall (0.91 m x 0.91 m). In the free board of the CBC, a fuel economizer is

installed.

The height of the overflow is variable. Overflow ash is cooled by air. To monitor the temperature distribution in the fluidized bed and the temperature behavior in the major parts of the boiler tubes, tens of thermocouples are installed and connected to a data processor evaluate and analyse the test operating conditions and performance of the boiler.

(2) Coal and Limestone Feeder

The coal charged into the feed coal hopper is temporalily stored in the feed coal bunker and sent to the dryer to remove moisture, then crushed screened for classification into fine and coarse fractions of coal.

The coal dryer of an indirect steam heating type.

Coal is crushed in two stages before drying. Limestone whose grain size has been adjusted at the mine is used and supplied into MBC together with fine grain coal through pneumatic conveying.

(3) Instrumentation

The instrumentation of this plant consists of the boiler control system, a centralized operation monitoring system and a precessing system. The data further can be displayed on the color CRT screen.

(4) Ash handling Equipment

Ash discharged from the overflow pipe of MBC and CBC is cooled and sent to the overflow tank, then sent to the ash storage silo by the pneumatic conveyer system.

3. Present State of the Test

Outline of the results of the operation up to June, 1981 together with several examples of the operation data are as follows:

(1) Operation Results

Since coal feeding started in early May, 1981, operation time has accumulated to 628 hours by September, 1981. Taiheiyo coal, typical low sulfur non swelling bituminous coal of Japan, is currently used. Properties of this coal and limestone are shown in Table 3 and Table 4 respectively.

The size of coal is -6 mm and the average particle diameter is about 2.5 mm. The limestone size is -3 mm.

Up to now so far, 10 cold starts and 17 hot starts have been carried out.

(2) Operation Data

Table 5 shows an example of operation data. In the Table, the NOx values are from the single stage and two stage combustion. These values are sufficiently low compared to the values of the government regulation. The SOx value is for the present low S coal. The desulfurization performance will be checked by using medium S coal in later test.

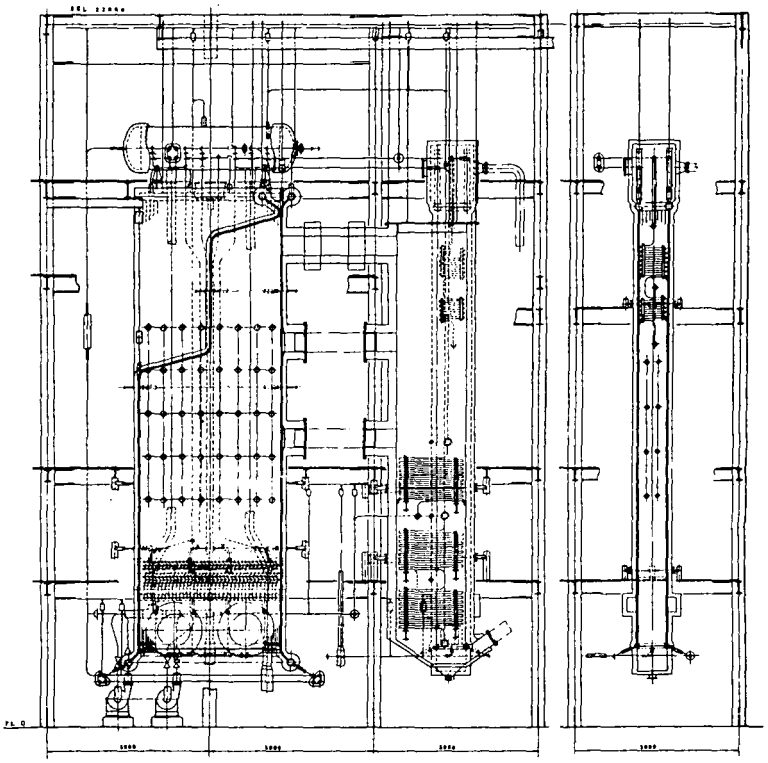

MBC CBC

Fig. 1 Boiler Structure

Fig. 2. Possible configulation of free board and tube arrangement in 20 t/h Fluidized Bed Boiler Test Module

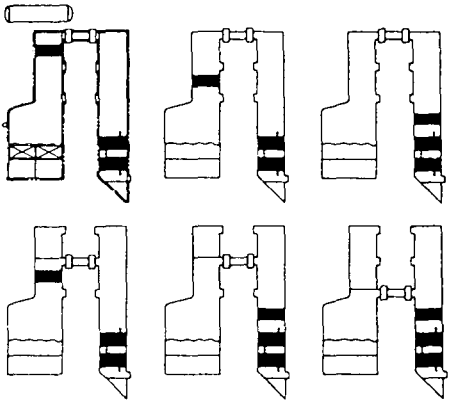

Table 1. Fluidized Bed Boiler Development Program

Item \ Fiscal year	1978	'79	'80	'81	'82	'83	'84	'85	'86
Preliminary study									
Feasibility study 500 MW plant									
20 t/h pilot plant		Design	Manufacture and installation	Operating test					
240 t/h demonstration plant (75 MW class)				Design		Manufacture and installation		Operating test	

Table 2. Coal Properties

Type of coal			Planned coal
Drycoal high heating value (kcal/kg)			7100
Surface moisture			7.0
Proximate analysis	Moisture	(%)	2.8
	Ash	(%)	9.5
	Volatile matter	(%)	28.5
	Fixed carbon	(%)	59.2
Ultimate analysis	C	(%)	73.8
	H	(%)	4.0
	N	(%)	0.8
	O	(%)	11.0
	Total sulfure	(%)	0.8

Table 4. Properties of Limestone

	Item		Analysis
Component	CaO	(%)	55.38
	MgO	(%)	0.30
	SiO_2	(%)	0.28
	Fe_2O_3	(%)	0.03
	Al_2O_3	(%)	0.10
	Others	(%)	0.90

Table 3. Properties of Coal

Type of coal			Taiheiyo coal
High Heating Value (Kcal/kg)			6330
Surface moisture (%)			1.6
Proximate analysis	Moisture	(%)	3.0
	Ash	(%)	15.3
	Volatile matter	(%)	44.2
	Fixed carbon	(%)	37.5
Ultimate analysis	C	(%)	64.1
	H	(%)	5.8
	N	(%)	0.8
	O	(%)	13.4
	Combustible S	(%)	0.1
	Incombustible S	(%)	0.1

RESEARCH AND DEVELOPMENT OF COAL-FIRED FLUIDIZED-BED BOILER

Bao Dong-wen and Ruan Yi-shao

Research and Development Division
Dong-fang Boiler Works
Zigong, Shichuan, China

INTRODUCTION

The power industry in many countries is now facing a problem: how to achieve the inevitable shift from oil and natural gas to coal and low-grade coals while remaining in compliance with the regulatory limits on emissions. Fluidized-bed combustion (FBC) has demonstrated its potential to solve this problem, because it has the advantages of adaptability to low-grade coals and feasibility for sulfur emissions control. Due to FBC's relatively low combustion temperatures, NO_x emissions from a fluidized bed are lower than those from conventional furnaces.

As a new technology it is natural that there are many technical problems to be investigated and difficulties to be overcome in the development of fluidized-bed boilers (FBB).

Since 1971, Dong-fang Boiler Works (DBW) has carried out developmental work in FBB in the following areas:

- Combustion efficiency.
- Arrangement of fluidized-bed heating surfaces.
- Immersed superheater.
- Erosion of immersed tubes.
- Start-up of fluidized bed.

A 463 x 324 mm FBC test unit was built to investigate methods of improving the combustion efficiency of the FBB. Later, a 24 t/h stoker-fired boiler was converted into an FBB by DBW. It has now been successfully operated for

more than 3 years, since 1977. The performance of the unit has been satisfactory to the user. Figure 1 shows the general arrangement of this modified boiler. Its major parameters are as follows:

Steam capacity	24 t/h
Steam pressure	32 kg/cm^2
Superheated steam temperature	450°C
Feed water temperature	150°C
Gas temperature at boiler exit	200°C
Designed fuel	Bituminous coal

Natural circulation was adopted for the immersed evaporating surface. To date no problem in water circulation has occurred. An experimental immersed superheater was placed in the bed and its behavior observed. For distribution of combustion air, a refractory covered bubble cap plate was installed. In order to facilitate bed start-up and load changes, the windbox was divided into four separate compartments. Because bituminous coal was to be used, no carbon recycling was considered; thus the uncertainty of a recycle system was avoided. The once-through combustion efficiency (i.e., without reburning of elutriated fines) was measured as 94.8 to 95.5 percent.

TEST RESULTS AND DISCUSSION

A. Combustion Efficiency

When compared with pulverized coal firing, carbon losses from a fluidized bed are high as a result of the relatively coarse coal particulates and low combustion temperature. Combustion efficiency depends on the bed velocity and temperature, excess air, and on the coal characteristics (which have significant influence on carbon losses). Coal with high ash content and less volatile matter would have lower combustion efficiency. The following experimental data from the test rig demonstrate that c.e. values in burning different coals may differ greatly, even when the superficial velocity, bed temperature, and excess air rate are approximately the same.

	Volatile matters on combustible basis	Ash on analytical basis	Total carbon losses
Bituminous coal	35.48	31.40	3.77
Lean coal	17.50	39.04	10.67
Colliery wastage	48.09	76.50	7.95

If anthracite is burned, carbon losses will be higher than the above values. It is evident that application of FBC in utility boilers will require significantly increased combustion efficiencies.

Two approaches for improving combustion efficiencies are: using a carbon burnup bed (CBB) and fly ash reinjection into the main fluidized bed.

The effect of the CBB was examined using the 463 x 324 mm rig. The tests showed that with the use of a CBB (an efficiency of 80 percent was assumed for the cyclone dust collector), combustion efficiencies may reach values of 97.5-98.0 percent when bituminous or lean coals are burned.

The recycling or reinjecting of elutriated fines has not been tested, but judging from the literature of other countries and experiences in application of carbon recycling in some FBB in China, we can say that particulate recycling (especially for coals with high volatile matter content) is also an effective measure. For example, the combustion efficiency of a bituminous coal-fired combustor may attain ~ 98 percent.

When a CBB is used, in order to avoid high dust loading, the gas stream from the CBB must be directed to an individual gas flue. Therefore, the CBB is in essence a separate fluidized-bed boiler, which operates at different conditions from the main bed and needs its own particulate removal system. In addition to being a more complex system, the reliable combined operation of a CBB with the main fluidized bed is rather difficult because of the inevitable fluctuation of coal characteristics and the main bed exploitation; the recycle system is much simpler. The main disadvantage of recycling the dust recovered from the dust collector is the resulting high dust loading of the gas stream. The erosive characteristics of the dust must be determined by operating a demonstration unit over an extended period of time.

In our view, with regard to industrial FBB, the carbon recycling system may be more desirable in most cases. Where less reactive coal such as anthracite is burned and the high combustion efficiencies which are required for a utility boiler are pursued, the CBB system may have to be used.

The even distribution of coal over the bed has proved to be of significance for attaining good combustion efficiency. It has been reported that satisfactory coal distribution can be achieved if one feed point is provided for every 0.84 m of bed area. This would result in nearly 70 points for a 130 t/h unit. In order to meet the above requirement, a pneumatic method of transporting crushed coal may be necessary. However, for large FBB (e.g., 200 MW units) the feed lines and control system would become very complicated; therefore, a method to improve the area per feed point must be found if the pneumatic feed system is to be simplified.

For purposes of this test a pneumatic feed system was not considered, but four screw-type coal feeders were installed on the front wall. The area of distributing plate for the 24th FBB unit was 8 m^2; this provided one feed point for every 2 m bed area. To promote even coal distribution, a coal spreading method was developed. During the tests of this method on the 24 t/h FBB unit only two feeders were put into operation,

which temporarily raised the area per feed point to 4 m^2. It was demonstrated that when the spreading device was used, combustion efficiencies were increased by 3.5-5.0 percent.

B. Arrangement of Bed Heating Surface

Vertical immersed tubes are generally used for small FBB. They are convenient for maintenance, and are more resistant to abrasion than horizontal tubes.

For larger units, to allow the necessary surface area required to be placed in the bed, horizontal or inclined buried tubes (staggered or in-line) are generally adopted. It is common knowledge that so far as convection surfaces are concerned, staggered tubes have higher heat transfer rates than tubes arrayed in-line. Given this information, is it still correct to use immersed tubes in FBB? To answer this question, special comparison tests were carried out. The results showed that, owing to the specific nature of the in-bed heat transfer, heat transfer coefficients for the in-line array of tubes fully compared with those for staggered tubes.

Initially, the immersed tubes of the 24 t/h unit were staggered. When the unit was put into operation, it was immediately discovered that excessive pulsations occurred and the erosion rates of the staggered inclined tubes and the fire brick walls were high.

On the basis of the above tests, it was decided to change the staggered tubes into in-line array. After the modification the steam output was maintained, the fluidizing quality became normal, and the abrasion rates were reduced.

C. Immersed Superheater

An industrial FBB can be designed with only an evaporating surface in the bed; this appears adequate to absorb the required amount of heat from the bed. In contrast, a certain portion of the superheating or reheating surface of a utility boiler must be placed in the bed in addition to the generating immersed surface. It seems useful to examine some problems of the buried superheater.

Because of the high heat transfer to immersed tubes (generally 220-250 kcal/m $\cdot h \cdot {}^{o}C$), it is of great importance to find out whether the wall temperatures of buried superheater tubes will exceed the limits. To this end, the character of the heat flux distribution along the periphery of an immersed tube must be determined. Special tests showed that this distribution was uneven, and surprisingly, the highest heat flux point was found at the upper part of a horizontal buried tube (Figure 2). The maximum heat flux exceeded the average value by 15-30 percent (in some cases even more), which means there exists an intense circulating flow of particulates within the "cap area" above the immersed tube. Figure 3 illustrates the approximate manner of particulate circulation.

ϕ42 x 5.5, 12 Cr/MoV steel tubes were used for the experimental submerged superheater. The steam velocity was ~ 35 m/s and the mean exit steam temperature ~ 420 C. Thermocouples were placed on the outer surface of the lower part of two buried superheater tubes. No thermocouple was placed on the upper part of the tubes, because it was thought that the maximum heat flux area must be at the lower half periphery; thus, the maximum tube wall temperature was not measured. The temperatures taken from the lower half periphery were 530°-550° C. It was clear that the wall temperature at the top of the tubes must have been higher. After about 3 months of operation, a metallographic examination was made of the tube. It was found that grade 3 spheriodization had taken place at the top of the tube, which meant that although the steam temperature was as low as 420° C, using the 12Cr/MoV steel tube was not safe. It appears that the tube wall temperature must be considered carefully and high-quality heat resistant alloy steel will have to be used when superheating or reheating surfaces need to be placed in the bed.

The protection of the immersed superheater during start-up and bed slumping was also of considerable concern. As operating experience had proved, the buried superheating tube temperature would not exceed the allowed value during start-up and slumping, provided the surface was arranged properly and partial bed start-up sequence (a portion of the bed where the immersed superheater is located, lit up only after an adequate steam flow is established) was adopted. When the boiler was to be shut down and the bed slumped, the immersed superheater would be safe. The immersed superheater was arranged above the slumped bed and its wall temperatures, measured during slumping, were all lower than 530° C. The temperatures measured in the space between the superheater and slumped bed did not exceed 600° C.

The temperature distribution over the bed was relatively even, and the deviation in heat absorption among the individual tubes was not great. Generally speaking, the deviation coefficient is about 1.1, provided the surface is appropriately designed. The temperature gradient along the feeder axis may be somewhat greater; therefore, the tubes of an immersed superheater would preferably be oriented in parallel with the feeder axis (as shown in Figure 1). If bed temperature unevenness along the feeder axis is significant and the superheater tubes are at right angles to the feeder axis, higher deviation coefficients of 1.20-1.26 may be reached, depending on the bed temperature gradient.

D. Erosion of Immersed Tubes

At present, rather coarse coal particulates are generally used in China. Consequently, high fluidizing velocity has been adopted. Many years of operational practice has shown that in most cases the abrasion of inclined buried tubes is very severe. For example, tubes (20 carbon steel) with a thickness of 3 mm may wear out after only ~ 4000 hours of operation. The most serious abrasion usually occurs in the first (lower) row of inclined buried tube surfaces. Along the inclined tubes certain more severely abraded sections can be observed. The abrasion rate is very uneven along the tube periphery. Figure 4 illustrates the severe abrasion of a 20-carbon steel tube with a thickness of 6.25 mm (no antiabrasive treatment used) after 8682 hours of operation. The

abrasion rate at the bottom of the tube is three times as high as that at the top. Several types of antiabrasive treatments for immersed tubes were tried, and some of them have showed effect. However, when relatively hard coals are burned these measures can only extend tube life to a certain degree, therefore the abrasion problem cannot be regarded as solved. Lignite-fired, fluidized-bed boilers may be the only exception. The erosion rate of their immersed tubes is not high, owing to the softness and light weight of the lignite.

It seems to us that low fluidizing velocity should be accepted as the primary measure for extending the life of immersed tubes, with additional antiabrasive treatment when necessary. This may be the final solution to the erosion problem. Besides the diminished tube abrasion, low fluidizing velocity may offer other benefits such as higher combustion efficiency, better SO_2 absorption (when limestone or dolomite is added to beds where high-sulfur coal is burned), and the possibility of using shallow beds to reduce the amount of blower power required. In order to lessen the abrasion rate, the immersed tubes should be reasonably arranged to avoid excessive pulsations and gas flow imbalances in the bed.

E. Start-up of Fluidized Bed

The process of start-up is, in essence, to heat the bed material to a temperature high enough for stable combustion of coal. It seems very simple, but when boiler service is initiated operators often run into trouble.

"Fixed state" start-up is a method adopted in the initial period of FBB development in China. In this process, the bed remains fixed at the beginning of start-up. When the bed material has been heated to the appropriate degree, the bed is tranformed from a fixed to a fluidized state and continues to be heated to the required temperature. During the start-up process, clinkering or flame failure may easily take place if the heat balance is not properly controlled. Exploitation depends to a great extent on the operator's experience, so it is not completely reliable. Furthermore, the time required for starting up is rather long.

Through the search for a better method, the so called "fluidized state" start-up technology has been developed. The major feature of this process is that the bed is brought to fluidization at the very beginning of start-up. The fluidized bed is heated up by an oil burner; the heating is uniform and steady. In 10-20 minutes, a bed with an area of 4 m^2 can be heated from ambient temperature to 900 -1000 C. It is much quicker than the "fixed state" method, and oil consumption can thus be reduced. Figure 5 shows a typical bed start-up curve in which the "fluidized state" method was used.

CONCLUSION

The main reason for developing fluidized-bed boilers in China is to burn high-ash coal of low calorific value, and thus broaden the scope of energy resources. This appears to be especially important in the southern pro-

vinces. Practice over a number of years has indicated that FBB are promising, at least for industrial boilers and small electricity generating units in China. The application of FBB to utility power plants, however, depends on future development, economic factors, and the success of intermediate demonstration units.

There is no doubt that many areas still need further investigation and that equipment could be improved, but we are convinced that a good start has already been made. Dong-fang Boiler Works now produces commercial FBB with steam capacity of up to 35 t/h. Units of greater capacity are under consideration.

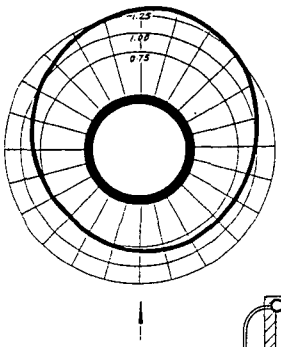

Fig.2 - Heat Flux Distribution

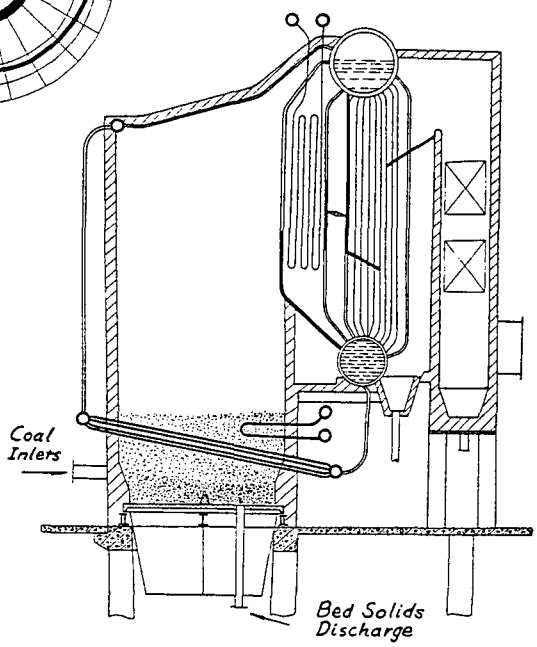

Fig.1 - 24 t/h Fluidized Bed Boiler (modified)

5:vm:513:4

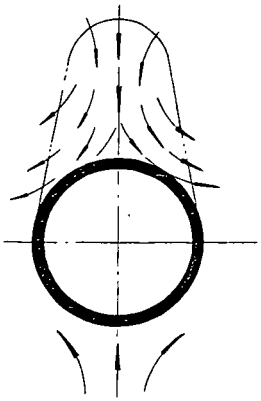

Fig. 3 - Particulate Circulation in "Cap Area"

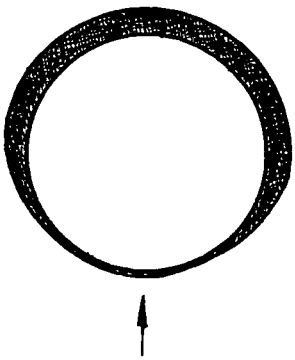

Fig. 4 - Wornout Tube

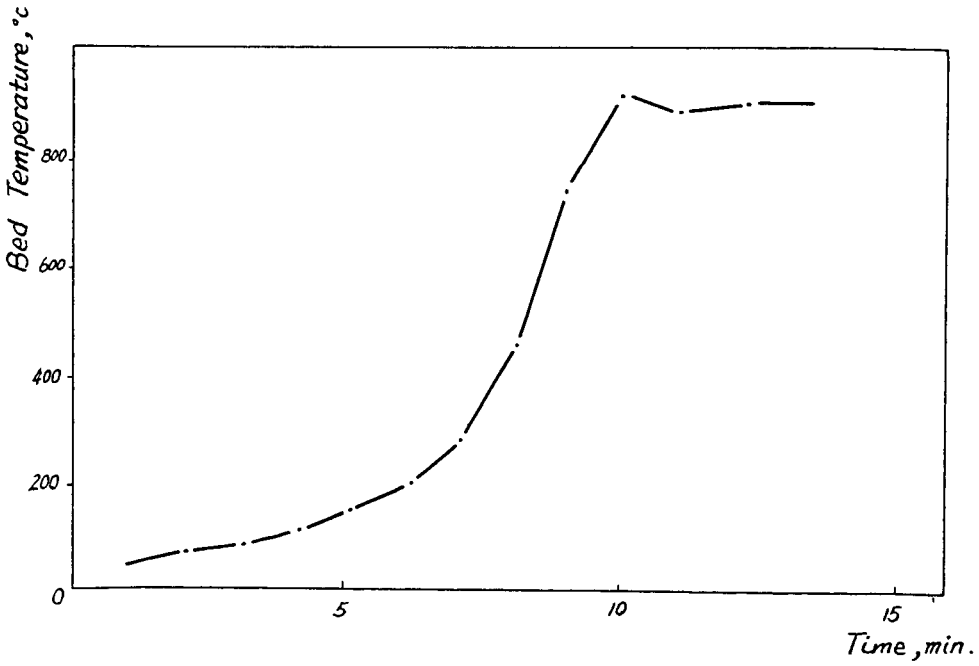

Fig. 5 - Bed Start-up Curve

A DATA ACQUISITION AND CONTROL SYSTEM FOR A FLUIDIZED BED COMBUSTION UNIT

D. W. Church and D. G. Pincock
Applied Microelectronics Institute, P. O. Box 1000,
Halifax, Nova Scotia B3J 2X4

INTRODUCTION

The Centre for Energy Studies at the Technical University of Nova Scotia is currently developing a small scale fluidized bed combustion unit for domestic heating purposes. The Electrical Engineering Department at the University was called upon to provide the electronics necessary to control and gather operating data on an improved prototype. The purpose of the present system is to develop an efficient control algorithm. If the fluidized bed proves feasible, the hardware can be simplified to an inexpensive microprocessor controller.

OVERALL SYSTEM DESIGN

The main requirement of the electronic system is to maintain the temperature of the fluidized bed between the limits of 750° - 950°C. The method of control is to monitor not only the bed temperature but also the stack temperature and concentration of pollutants and then adjust the ratio of fuel and air input to achieve complete combustion. Since the fluidized bed is integrated with a back-up domestic oil-fired hydronic heating system, control of boiler temperature is also a system requirement. In addition alarms are energized and appropriate actions taken when the fluid bed temperature is outside the desired range.

To aid in development of the control algorithm,the fluidized bed and back-up heating unit are fitted with a variety of sensors. Examples include thermocouples for temperatures, gas analyzers for oxygen and carbon monoxide, and pressure transducers for air flow rates. Since the total number and type of sensors is variable, expansion and modification of both hardware and software by the user is highly desirable. With these points in mind, the system of Figure 1. was developed.

The general philosophy is to employ the desktop computer in the role of a "host", controlling data flow and perfoming arithmetic calculations. The host also acts as an interface between the console (user) and the data acquisition unit when system configuration changes are desired. The printer provides a record of the system status and operating conditions.

The next section briefly describes the components selected to realize the system of Figure 1.

System Hardware

Since the project is of a developmental nature it was thought highly desirable to select major components which are general purpose in nature and, hence, useful in future applications. To this end, the STD BUS was selected as the basis of the microprocessor controlled data acquisition unit. The STD BUS was developed by Pro-Log and MOSTEK and is now quite popular. A wide variety of plug-in cards and complete systems are available from manufacturers such as Pro-Log, MOSTEK, Intersil and Analog Devices.

The STD BUS standardizes the physical and electrical aspects of modular 8-bit microprocessor card systems. The standard permits any card to work in any slot of the bussed motherboard which provides internal communication. All other connections to the outside world are by connectors at the opposite ends of the cards. Available cards include all the popular 8-bit processors, memory expansion, digital

I/O, analog I/O, industrial I/O (relays and triacs) and peripheral interfaces.

The data acquisition unit contains 4 plug-in cards, two of which are custom built. Figure 2 shows how the various functions are distributed. The processor card uses an 8085A and has sufficient random access and program memory on-board. With the exception of signal conditioning for low-level signals, the entire analog I/O subsystem is contained on the RTI-1225 card manufactured by Analog Devices Corp. It is designed specifically for interfacing real time analog signals to microcomputer systems. On the input side there are 16 channels multiplexed to a sample and hold amplifier and a 10 bit A to D converter. The output side has 2 channels with 8 bit resolution. Communication is memory mapped and appears as five contiguous address locations which are used to control the functions of the card and pass data to and from the microprocessor.

The custom built cards combine two functions on each. One handles thermocouple signal conditioning and digital I/O while the other contains a real time clock and a UART for interfacing to the desktop computer. Four thermocouples of any type can be handled by the present card, with gain and cold junction compensation software selectable. Additional cards may be added as required. All temperature channels are multiplexed into channel one of the A to D converter, leaving 15 single-ended 0-10 volt analog input channels.

Operating data other than temperatures are supplied by the monitoring instruments (e.g. oxygen analyzer). The outputs from such instruments are in general fully compensated and conditioned 4-20 mA currents or selectable low level voltages. Instruments with 0-10 volt outputs can thus connect directly to the A to D converter. In our system, carbon monoxide and carbon dioxide monitors produce only a 0 - 5 volt output, which still provides adequate resolution and accuracy with a direct connection. Instruments with current loop outputs also connect directly by terminating the loop at the A to D input with a 500 ohm resistor to produce a 2-10 volt signal range. If other low level sensors such as strain guages are required, they can be amplified externally with modules which produce either current loop or 0-10 volt outputs. Examples include the Analog Devices 2B50 series.

The host computer is a desktop unit which does the calculation of the control algorithm and prepares system status information for display at the console and printer. This computer is a Superbrain (Intertech Data Systems, Columbia, South Carolina) based on the Z-80A microprocessor and using the CP/M operating system. It is a self-contained unit having a CRT, keyboard, two floppy disk drives, 64K of memory and 2 I/O ports.

In keeping with the overall philosophy of hardware selection, the printer is a Decwriter LA-120 which provides the user with a very flexible and attractive hard-copy terminal for future use.

System Software

The system software was develpped in two stages. First the data acquisition unit program was written in PL/M. Compilation was done on a large time-shared system and the result downloaded to a PROM programmer. Included in the I/O portion is a segment which enabled testing and calibration of the analog hardware as the program was expanded. Following this the host computer program was written and tested a portion at a time with the working data acquisition unit. Rapid development of relatively unsophisticated processing, combined with ease of program maintenance by the users led to the selection of BASIC as the host language.

The main tasks assigned to the data acquisition unit are temporary storage of raw binary data from all sensors, conversion to ASCII of this same data, response

to requests by the host computer and monitoring alarm conditions in the fluidized bed. Single letter codes sent by the host initiate any desired actions. Examples include passing of the latest data, adjustment of fuel or air motors, or changes in system configuration such as number of active channels.

PL/M is a programming language designed for Intel's 8 bit microcomputers. The language is structurally similar to PL/I so that programs are somewhat self-documenting and easily altered and maintained. A memory map for the data acquisition unit is shown in Figure 3. The program is stored in read-only memory and the analog I/O subsystem is placed at the top of the 64k address space. This application uses about 1k bytes of the available on board ROM.

The supervisory BASIC program gets the latest data from all sensors, converts to appropriate units and formats and displays this information on the console and printer. Time of day and update interval are provided by the real time clock, which is software settable from the host. For non-linear sensor readings, disk files containing appropriate tables are used for interpolation. Such is the case for all thermocouple readings. The converted data is then utilized by the control algorithm to determine if fuel and air feed corrections are required. If so, this information is passed to the data acquisition unit and out the D to A channels to motor controllers. Finally, a second check on the fluidized bed temperature is done by the host to alert the operator in the event of a failure of the hardware alarms.

Conclusion

A data acquisition and control system for a fluidized bed combustion unit has been described. It should be re-emphasized that the developed algorithm can be easily moved to read-only memory in a low cost controller. It is believed that the choice of major components has resulted in a system which is sufficiently general in nature to not only serve the current project but also to prove useful in future applications. The type of system described should find application wherever monitoring, recording and control of analog or digital signals and processes is required.

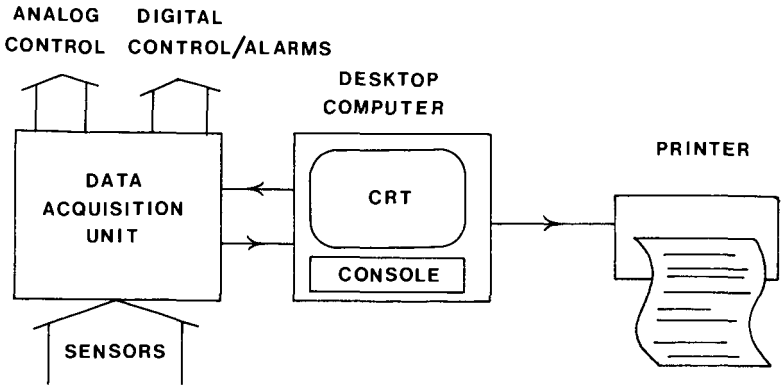

FIGURE I. OVERALL SYSTEM.

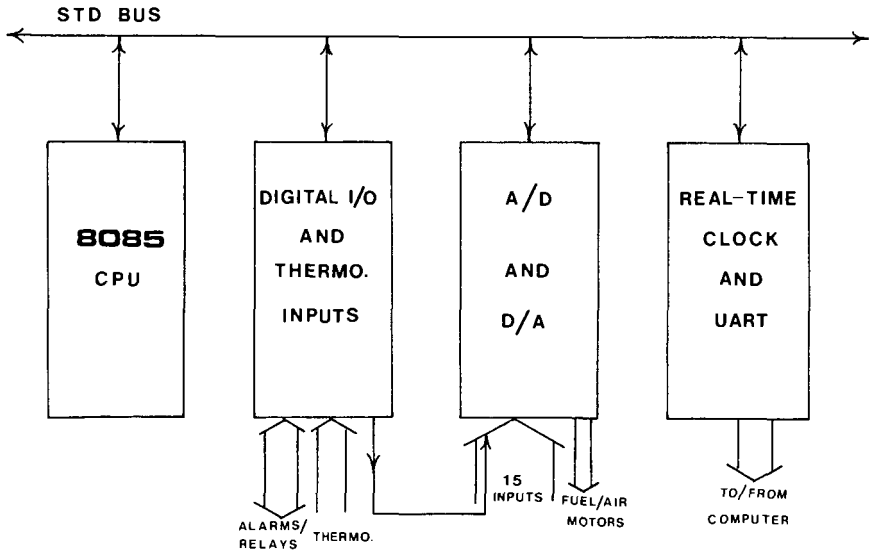

FIGURE 2. DATA ACQUISITION UNIT.

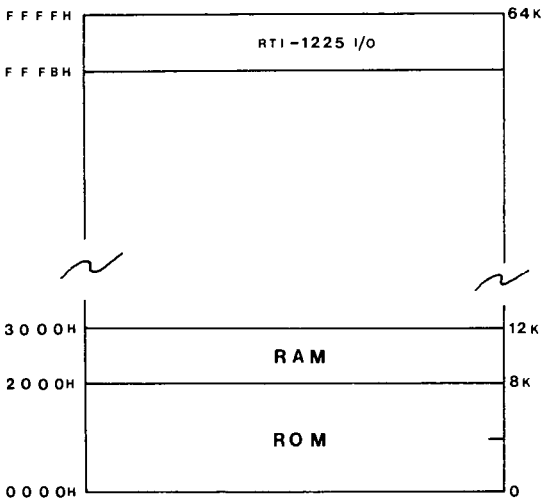

FIGURE 3. D.A.U. MEMORY MAP.

SAMPLING SYSTEM FOR FLUIDIZED BED APPLICATIONS - RESULTS OF FOUR YEARS OF TESTING ON B&W/EPRI's 6' x 6' FLUIDIZED BED TEST FACILITY

K. L. Loudin and P. W. Maurer

The Babcock & Wilcox Company
Research and Development Division
Alliance Research Center
Alliance, Ohio 44601

W. Howe

Electric Power Research Institute
Palo Alto, California 94304

INTRODUCTION

In cooperation with The Electric Power Research Institute (EPRI), The Babcock & Wilcox Company (B&W) has built and is operating a 6-foot x 6-foot (6' x 6') Atmospheric Fluidized Bed Combustion (AFBC) Development Facility at its Alliance Research Center in Alliance, Ohio. A complete description of the facility design details is contained in EPRI Final Report CS-1688. An artist's rendition (Figure 1) identifies the major components of the facility.

The 6' x 6' size was selected as being large enough to bridge the gap between bench-scale units then in operation and larger, future units in the proposal and/or construction stages. The facility design is flexible (versatile to modifications) in many areas -- number of feed points, immersed tube bundle configurations, ash recycle configurations, interchangeable gas sample systems, etc. -- and is highly instrumented (controls, interlocks, data acquisition, and sampling) to closely simulate utility boiler designs. The size, design, and equipment selections have produced a hot test facility with the capability of generating significant performance data over extended periods of steady operation for a multiple number of planned test conditions.

The facility construction was completed in October 1977. Following a 5-month startup and debugging phase, the first test series was conducted in April 1978. Since that time, approximately 2000 hours of testing (five to eight test series) per year have been logged.

GAS SAMPLING SYSTEMS

Evaluation of the performance of the 6' x 6' AFBC test facility mandated accurate sampling and gas concentration measurements. For example, measurements of CO_2, CO, and Hydrocarbons are used in calculating combustion efficiency while the measurement of SO_2 is needed to calculate sulfur capture. Oxygen measurements, also used in performance calculations, are used by the operators in setting the desired facility operating test conditions. Figure 2 shows the location of the main gas and solids sample points on the 6' x 6' unit.

Obtaining gas concentration data required the use of a sampling system that included the use of many special instruments and/or equipment. The original system layout and details are shown on Figure 3 and Table 1, respectively. The two independent systems that make up the complete system are identified as the mobile and furnace outlet systems. Sampling flexibility is gained by being able to

interchange systems and/or components. The original system has been expanded to include NO_x and Hydrocarbon measurements at the furnace outlet and CO_2 measurement at in-bed and freeboard locations.

Table 1

Tabulation of Gas Sampling System Details

Tank Farm Calibration Gases	SO_2, CO, O_2, NO, CO_2, Air, and N_2	
Instrument Air System	60 - 100 psig (2 - 3 SCFM)	
GAS SAMPLE SYSTEMS	Furnace Outlet Probe	Mobile Probe
SO_2, CO, O_2, NO_x, and CO_2 Analyzers	Yes	Yes
Hydrocarbon Analyzer	Yes	No
Common Tank Farm	Yes	Yes
Common Instrument Air Supply	Yes	Yes
Separate Sample Probes	Yes	Yes
Separate Filter-Cyclone Assemblies	Yes	Yes
Separate Heated Sample Lines	Yes	Yes
Separate Filter-Pump Systems	Yes	Yes
Instrument Air to Pump Control Switch	10 psig @ 1200 cc/minute	10 psig @ 1200 cc/minute
Cooling Water to Probes	20 gph maximum	20 gph maximum
GAS SAMPLING SOURCE	Stack (Furnace Out)	"In-Bed" and Freeboard
Approximate Source Gas Temperature	900°F	1650°F
Sample Gas Temperature @ Probe Discharge	310°F	310°F
Sample Gas Temperature in Sample Line	300°F	300°F
Sample Gas Temperature @ Pump Inlet	180°F	180°F
Sample Gas Temperature After Analyzers	Ambient (80°F)	Ambient (80°F)
Sample Gas Flow From Source	5 liters/minute	5 liters/minute
Sample Gas to O_2 Analyzers	250 cc/minute	250 cc/minute
Instrument Air to O_2 Analyzers	10 psig	10 psig
Sample Gas to SO_2, CO, and CO_2 Analyzers	1000 cc/minute	1000 cc/minute
Sample Gas to NO_x Analyzers	1200 cc/minute	1200 cc/minute
Instrument Air to NO_x Analyzers	35 psig	35 psig
Recorder "A" Gas Printout	SO_2, CO, O_2, and CO_2	
Recorder "B" Gas Printout		SO_2, CO, O_2, and NO_x

GAS SAMPLING WITH ORIGINAL PROBE-FILTER ASSEMBLIES

Furnace Outlet Gas Sample Location

The gas analysis from the furnace outlet is used in performance calculations and additionally to set and control the facility test conditions. This system must operate on a continuous basis. Figures 4 and 5, respectively, show the probe installation in the furnace outlet duct and the original probe-filter assembly. The water-cooled probe has an open-ended, concentric quartz tube for sample flow. In turn, the tube is connected to an in-line particulate filter assembly (glass cyclone collector/drop out bottle and frit-fiberglass filter unit) through which the gas sample flows enroute to the heated sample line. The particulate filter assembly, located in an electrically-heated cyclone oven (size - 9-1/2 inches square x 21-1/2 inches long), is maintained at 300°F. At normal operating conditions (no dust recycle), the particulate filter assembly had to be changed twice during each 24-hour operating period.

Freeboard Sample Locations

The mobile gas sampling system and probe installation shown in Figure 6 are used to traverse the freeboard at the locations previously shown in Figure 2. A typical traverse at one location would include taking gas samples at 12 or 13 points across the width of the facility. A complete traverse, conducted with the drive mechanism on either "hand mode" or "automatic mode", requires from 60 to 90 minutes to complete. Except for the difference in length, the furnace outlet and mobile probe-filter assemblies are identical.

In-Bed Sampling Locations

The in-bed gas sampling probe installation, shown in Figure 7, is used for traversing in the fluidized bed. The original in-bed probe-filter assembly is shown in Figure 8. The filters are 3/4 inches in diameter x 1-3/4 inches long with a pore size of approximately 1 micron. The ceramic collar is cemented to the filter at a position that is 1/4 inch away from the open end. The collar is clamped in the probe head at a location that presents an active filter flow area of approximately 2 square inches.

Typically, the ceramic filter had to be cleaned (nitrogen back-purged) at 15- to 20-minute intervals.

GAS SAMPLING PROBLEMS

The original gas sampling probes operated satisfactory and allowed accurate gas concentration measurements during no dust recycle test conditions. However, operation of the 6' x 6' AFBC unit has shifted to the use of dust recycle to improve performance. Dust loadings as high as 10,000 lb/hr have been run at temperatures up to 1750°F and at gas velocities of about 100 ft/sec. The high dust recycle increased the particulates that were entrained in the gas samples. This condition necessitated frequent filter changes, caused problems with glassware breakage due to increased handling, and required more frequent nitrogen back-purging of the in-bed filter.

Problems associated with gas sampling at the furnace outlet, freeboard, and in-bed locations are discussed in the following paragraphs.

Furnace Outlet Gas Sample Location

With high dust recycle rates, the filters required continual attention. Each filter change involved disconnecting and reconnecting five joints in the flow system. In a few instances, slight amounts of air infiltration (induced by negative pressure in the sample line) into the gas sample produced incorrect gas concentrations. Increased handling of the glassware and quartz tube produced some breakage problems. In certain instances, the breakage would occur as a crack that was difficult to detect. Undetected cracks, on a couple of occasions, permitted air infiltration into the sample in such a small quantity that the incorrect concentration readings went unnoticed for a few hours. These problems instigated a modified probe-filter assembly design that would provide more effective filtering. The modified design would eliminate the fragile components, such as glass and quartz, and would minimize the number of connection joints.

Freeboard Sample Locations

Problems with the probe-filter assembly were similar to those encountered at the furnace outlet location. Due to continual filter pluggage, the probe could not be used in the fringe area of the bed i.e., the lower sets of freeboard ports. Additionally, the long probe length (approximately 9 feet) and relocating the probe to all sample ports produced occasional breakage to the fragile components. Such actions also caused occasional air infiltration into the numerous connection joints.

In-Bed Sampling Locations

The solids density of the bed has always required the use of a nitrogen back-purge to clean the ceramic filter. A combination of the small active filter area (only 2 square inches) and the increased solids concentration increased the "blow-back-cleaning frequency". The resulting time required to conduct a traverse more than tripled that required for the no ash recycle test condition.

SOLUTIONS FOR SOLVING SAMPLING PROBLEMS

A review of sampling at all locations indicated that the components included in the probe-filter assemblies were responsible for the problems. Further review of the problems encountered at each location suggested that a modified probe-filter design could be adapted for sampling at all locations. The modified design actions included the following:

- Install a primary solids filter at the sample inlet to the probe. A ceramic filter, supplied by the Coors Porcelain Company, with an active filtering area of approximately 12 square inches was selected for this application. This filter (size - 1-1/4 inches OD x 3/4 inch ID x 4 inches long) with a pore size of 100 microns was included on the modified probe-filter assembly shown in Figure 9.

- Install a secondary filter between the sample probe and the heated sample line. A cartridge-type filter with two inches of kaowool insulation (also shown in Figure 9) was proposed to protect other components of the sample train in the case of a failure of the primary filter. This secondary filter would eliminate the glassware and plastic components which in turn would decrease the number of connection joints where possible air infiltration could occur. The insulation around the filter would eliminate the cyclone oven, controls, etc. thereby reducing the bulkiness of the installation.

- Remove the quartz tube (gas sample flow tube) from the center of the probe. This would eliminate another fragile component by allowing the sample to flow down the center (stainless steel tube) of the probe.

PERFORMANCE DATA SUPPORTS MODIFIED SYSTEMS

Primary Filter Performance

- The ceramic filter was initially tested at the furnace outlet gas sample location. At first, problems developed in sealing the ceramic filter and the metal tube. After obtaining a good seal, the ceramic filter performed to maximum expectations as shown by the following table:

Gas Temperature (°F)	Solid Flow Rate (lb/hr)	Gas Velocity (ft/sec)	Ceramic Filter Performance
800	3000	100	Sample system operated continuously for a period of 12 days (288 hours). Minimal wear to upstream side of filter.
800	10,000	100	Sample system required a filter change every 2 or 3 days. Minimal wear to upstream side of filter.

The above tests were conducted without back-purging (with nitrogen) the filter. When the pressure drop across the filter reached its pre-determined maximum limit, the filter was changed.

- The filter tests in the freeboard area indicated that no pluggage occurred while sampling at any of the ports. No back-purge system was used and the filters showed no wear after extended periods of operation.

- The in-bed filter tests indicated that no pluggage occurred during a complete traverse across the bed. The original probe-filter assembly had to be back-purged with nitrogen every 15 or 20 minutes during each traverse. The nitrogen back-purge cleaning feature was available, but was not used during these latter tests. It appeared that the filters could be used indefinitely with no indications of wear.

Secondary Filter Performance

The secondary filter tests at the furnace gas outlet and freeboard sampling locations indicated the cartridge-type filter wrapped with two inches of kaowool insulation met all performance expectations. This filter served its initial purpose of protecting other components in the sample train in the case of a failure of the primary filter. It also replaced the fragile components and served to decrease the number of connection joints (possible air infiltration sources) in the sample train. The insulation contributed to the elimination of the cyclone oven which made the assembly less bulky and easier to handle. A combination of the insulated filter and controlled setting of the cooling water to the probe retained the gas temperature well above the dew point as the gas passed through the secondary filter enroute to the heated sample line. These tests were conducted in the most severe environment possible in both sampling locations. The secondary filter on the original in-bed

probe-filter assembly was not changed, thus no secondary filter tests were conducted at this sampling location.

Quartz Tube Versus Stainless Steel Tube Performance Data

The original probe-filter assemblies used at the furnace gas outlet and freeboard sample locations contained a quartz tube through which the gas sample was drawn. Due to the fragile nature of the quartz, it was desirable to eliminate the quartz tube and instead use a stainless steel tube. Some concern existed that a gas-stainless steel reaction -- more likely at high gas temperatures -- could possibly produce incorrect gas concentrations (particularly with NO_x). By adjusting the water cooling rate on the probe, the temperature of the gas along its path of contact with the stainless steel was reduced to a low, non-reactive temperature level (200° to 400°F).

The results of the quartz tube versus stainless steel tube tests, conducted at the furnace gas outlet and freeboard sample locations, are shown in the following performance tabulation:

Sample Location	Sample Tube Diameter/Material (Inch)	Source Gas Temperature (°F)	Sample Gas Temperature In Probe (°F)	Gas Concentration Comparisons
Furnace Outlet	5/8 SS	800	300 Max	Gas concentrations for O_2, CO_2, CO, SO_2, and NO_x were essentially identical for both the quartz and stainless steel tube sample probes.
Furnace Outlet	5/8 Quartz	800	300 Max	
Freeboard	5/8 SS	1700	280 - 305	Gas concentrations for O_2, CO_2, CO, SO_2, and NO_x were essentially identical for the quartz tube and the two (5/8" and 3/8" diameter) stainless steel tube sample probes.
Freeboard	3/8 SS	1700	325 - 400	
Freeboard	5/8 Quartz	1700	155 - 220	

SUMMARY

Gas sampling and analysis form a major portion of the performance evaluation of the 6' x 6' AFBC facility. The analysis requires measuring the concentration of six different gases at three sample locations -- in-bed, freeboard, and furnace gas outlet. Sample flow rates of 6 to 10 liters per minute are needed for analyzing these gases.

Accurate sampling and analysis from the high-temperature - high velocity, dust-laden environment of the fluidized bed unit requires the use of a system that includes certain special equipment. An "efficient particulate filter" is needed to clean the large-volume gas samples removed from the adverse environment of the 6' x 6' unit. A ceramic filter -- constructed of inert material, self-cleaning, having minimum pressure drop, and able to withstand high temperatures and abrasive wear -- served as the primary particulate filter in our final design.

A cartridge-type secondary filter eliminated the glassware and decreased connection joints, while serving its main function of protecting the remaining sample system components in the case of a failure of the primary (ceramic) filter. Eliminating the quartz tube has produced a design that includes no fragile (glassware or quartz) components.

The modifications have been combined to produce a refined gas sampling system that can be used at sample locations of interest in fluidized beds. It has been used for collecting and for accurately analyzing gas data over extended test periods for a multiple number of planned test conditions. These results have played a major role in the evaluation of the AFBC performance. The refined gas sampling system -- developed for the 6' x 6' fluidized bed application -- is recommended as a reliable system for fluidized bed units.

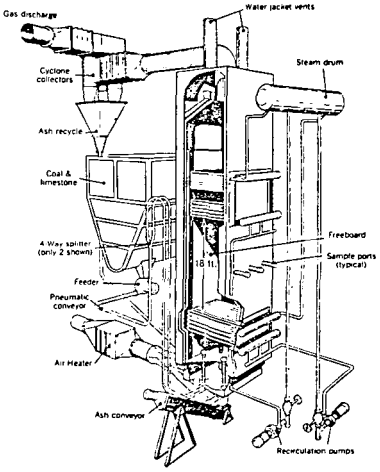

Figure 1 6' x 6' Fluidized Bed Combustion Facility

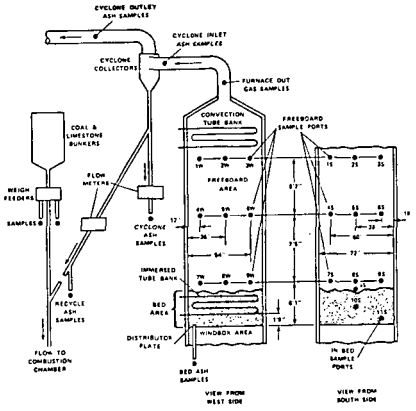

Figure 2 Relative Sample Locations for the 6' x 6' AFBC Facility

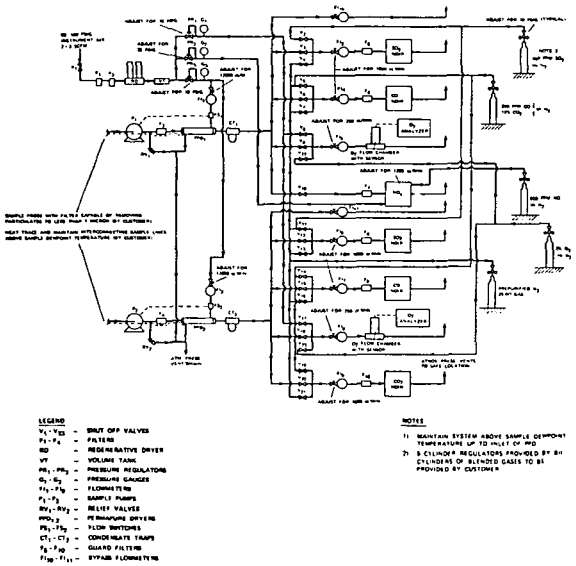

Figure 3 Complete 6' x 6' AFBC Facility Sampling System

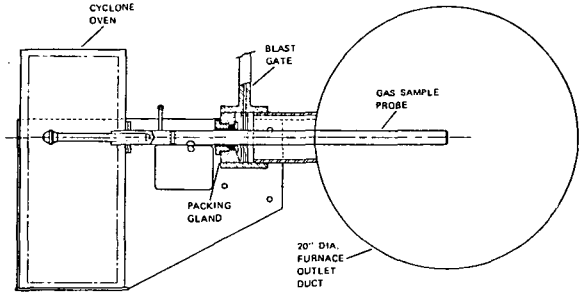

Figure 4 Furnace Outlet Gas Sampling Probe Installation

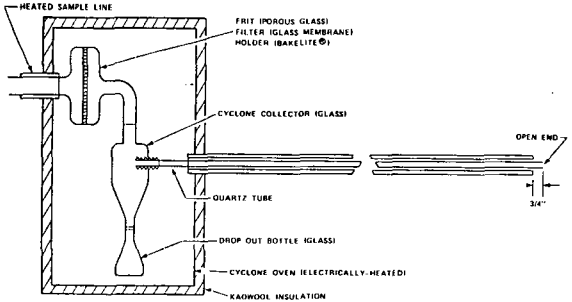

Figure 5 Original Furnace Outlet Gas Probe-Filter Assembly

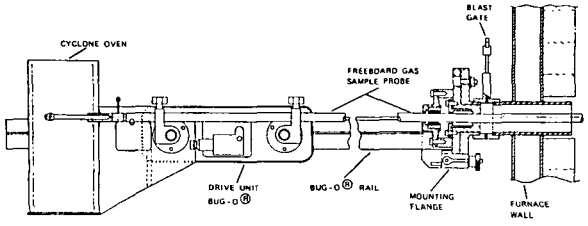

Figure 6 Freeboard Gas Sampling Probe Installation

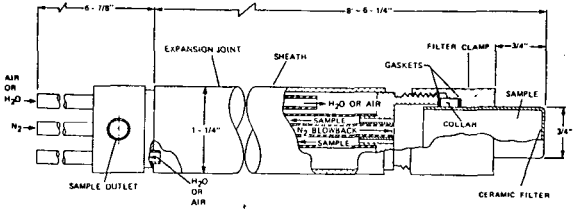

Figure 8 Original In-Bed Sampling Probe

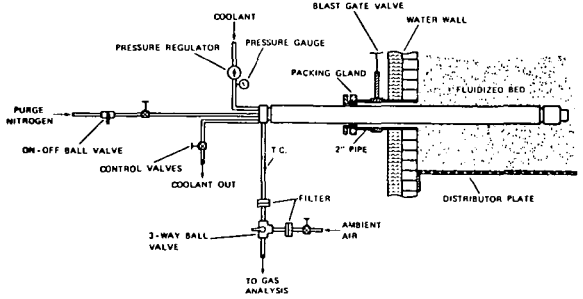

Figure 7 In-Bed Gas Sampling Probe Installation

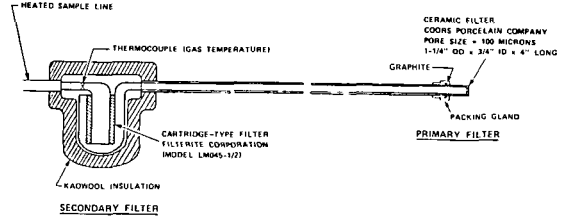

Figure 9 Modified Furnace Gas Outlet Probe-Filter Assembly

The Influence of Varying Operational Parameters on Both the Combustion Efficiency in and the Emission of Pollutants from Fluidized Bed Plants [1]

by: Dr. H. Münzner, Dr. H.-D. Schilling VDI, Essen

Bergbau-Forschung GmbH, P.O. Box 13 01 40, 4300 Essen 13, Fed.Rep. of Germany

1. Methods and Apparatus

Our method of determining the influence of different operational conditions on fluidized bed plants consists in a stepwise alteration of one single operational parameter while maintaining the others as constant as possible (1). It is well known that this is easiest on a laboratory scale, whereas with increasing plant size the procedure becomes more and more onerous. If beyond operational parameters also the design concept and the size of a plant are varied, one obtains useful hints how to generalize and scale-up the results achieved.

Present findings were obtained using several types of laboratory equipment with thermal performances between 2 and 20 kW as well as from a semi-technical plant of 300 kW. Figure 1 is a schematic drawing of the shapes and dimensions of fluidized bed reactors used. Apparatus no. I is a tube reactor of 6 cm diameter and 60 cm height on top of which has been arranged a freeboard of approx. 35 cm hight and 10 cm diameter. Apparatus no. II is a tube reactor of 6 cm diameter and about 120 cm high. Here the ash is retained by an integrated inertial separator. Apparatus no. III represents a two-stage secondary air reactor with the following dimensions:

lower section: 6 cm diameter, 60 cm high,
upper section: 10 cm diameter, 80 cm high,

integrating an inertial separator. Unit no. IV is a pressurized reactor allowing combustion pressures up to 10 bar. Its reaction tube has a diameter of 6 cm and a height of 1 m, and incorporates an inertial separator. An early version of the pressurized reactor, operated at 4.5 bar, was of a similar shape and size as apparatus no. I. The reactor space provided by the semi-technical plant, finally, has a cross-section of 40 by 80 cm, a height of approx. 1 m, with a freeboard of 80 by 80 cm cross-section and approx. 2 m height.

The coal is fed pneumatically, along with all of the combustion air, to the electrically pre-heated laboratory units, whereas in the semi-technical plant coal is fed with a small fraction of the total air from one side into the fluidized bed. The atmospheric laboratory units, due to their high surface-to-volume ratio, are equipped with a heat insulation allowing to maintain a combustion temperature as high as approx. 950 °C. The pressurized unit, however, requires a variable heat exchanger for thermal discharge since in this case the heat release rate is higher by a factor of 10. As to the atmospheric semi-technical unit, it also needs heat exchangers which are immersed in the fluidized bed.

---

[1] The present project has been sponsored by the Federal Ministry of Research and Technology (project no. ET 1024 B)

With regard to the similarity particularly of the laboratory equipment to bigger plants, one had to compromise on this. On the one hand a contact time between gas and solids comparable to that of a bigger fluidized bed plant had to be attained which requires an adequate height of the fluidized bed. On the other hand the thermal performance was to be kept low, i.e. within the limits of a laboratory unit. As a compromise between these requirements resulted an elongated reactor shape which, seen under the aspect of flow mechanics, due to its high length/diameter ratio can at first view not be compared with a bigger plant since it tends to aggregative fluidization and pulsations. In order to be able to use these easy to be handled reactors and to obtain reliable results nonetheless, elongated wire spirals were introduced in the reactor spaces. This helped to avoid the formation of big bubbles and strong pulsations and to bring about a more particulative fluidization (2).

An essential design difference of the laboratory units consists in the substitution of the enlarged cross-section of the free board by an inertial separator. The objective of this constructional modification is to determine the functionality and need of such a high-volume free-board.

2. Results

The results were obtained from an evaluation of analysis on the feed materials, flue gases, ash, and from the material balance of throughputs.

Figure 2 is a schematic summary of the variations of the main operational parameters, including their range and direction of variation as well as relevant standard values plus qualitative effects on: specific heat release rate, C-loss, CO-, SO_2-, and NO_x-concentrations in the flue gas.

Depending on the slope and inflexion of the arrow indicating the direction of parameter variations of a given component, such variation has a stronger or weaker influence on throughput and emission; a horizontal arrow stands for invariance in respect of the independent parameter. The specific heat release rate, expressed as MW/m^2, goes up along with both increasing fluidizing velocity and pressure, i.e. along with those parameters determing the throughput of air and also of coal. The performance drops along with rising excess air, i.e. in a situation where an increasing proportion of the air throughput is no longer utilized. The other parameters, however, hardly exert any influence. The dependence of the specific heat release rate on the apparatus design, therefore, is negligible and will be -- with an excess of air $\lambda \approx 1.3$ (5 % O_2 in the flue gas) -- approx. 1.2 to 1.5 MW/m^2. This correspondends to the values which in the meantime have been observed also at demonstration plants (3). Most of the arrow constellations revealing a sizeable influence are backed by measuring data plotted on diagrams, a selection of which is given hereunder.

2.1. C-Loss and CO Emissions

The C-loss is a critical factor for the economics of fluidized bed plants, whereas keeping the CO content in the flue gas within admissible limits generally does not pose any problems. As can be taken from figure 2, the two data sets are of a striking parallelity. The reason for this is that the more CO will be generated at reduced temperatures within the local and thermal transition zone between reactor zone and flue gas duct, the more carbon passes through this transitional zone as char carry over. Tars and volatile hydrocarbons were not observed. On being introduced into the hot ash of the fluidized bed, the coal will be dispersed immediately and exposed to the excess air whose oxygen reacts first with the volatile matter.

Diminishing C-loss along with pressure rise is related to an increased O_2 concentration, whereas diminishing C-loss along with rising temperature is attributed to higher reaction velocity. Increasing fluidizing velocities reduce the residence time of the coal in the reactor and, thus, cause higher C-losses. If one found a means of extending this residence time -- be it by appropriate plant design or/and by coal preparation -- the specific heat release rate could be improved proportionately to the fluidizing velocity.

A longer residence time of the coal by means of increased bed height will diminish C-losses, too.

C-loss may be influenced also by coal preparation measures. As shown on figure 3, the C-loss will, when fueling closely sized coal fractions, pass through a maximum as soon as the particle diameter approches the elutriation cut point. Coarse coal grains will remain in the bed up to the moment where they are burnt down to a size allowing their elutriation or preventing them from being recycled by the inertial separators. With sufficiently small fractions (coal dust) the reaction time is apparently shorter than the residence time in the reactor space so that the coal particles are almost completely burnt up. As far as industrial plants are concerned, the logical conclusion from this is to separate coal dust from the coarser fractions and blow the dust pneumatically into the fluidized bed from below, in order to allow a maximum residence time of the dust and avoid erosion in the feed ducts, whereas the coarse fractions, being introduced from above, are allowed sufficient time to spread over the bed while being burnt up. In this case it can be taken from the diagrams, e.g. figure 3, where the preparation cut points for each specific plant are viz. which granular fraction should be separated and/or further comminuted.

Examination of the carbon carry-over by means of screening for its size distribution does not yield accurate results since char aggregations will disintegrate. The results of figure 3 are, however, reconfirmed by this approximative evaluation. Moreover it can be verified from fly ash separation in two subsequent cyclones that the fine dust from the second cyclone is very low in carbon, whereas the "coarse dust" of the first one will always contain the bulk of the unburnt carbon.

Apart from the determinable and adjustable operational parameters, C-loss is also a function of the specific plant parameters. Measuring data can best be reproduced in laboratory equipment. When doing so, one observes other and so far not measurable operational conditions which bear on the results. Among these have to be considered the size distribution of the fluidized bed ash particles which changes during operation, or changing fluidity and cohesive properties of the bed ash when adding various gradations of limestone.

A comparison of the C-loss measured in reactor no. 1 with that of the semi-technical plant V (figure 5) -- the cross-section of the free-board has been enlarged in both units -- shows good coincidence. It should be borne in mind, however, that here varying particle gradations and bed heights compensate each other in a way not clearly identified so far.

As was expected, there are differences also in the C-losses for the different laboratory reactor types since inertial separators are not optimized. This is not disturbing as long as feed materials, viz. types of limestone and coal, are compared by measurements in one reactor only. As soon as it comes to scaling up results, however, one has to know about the reasons and influences of specific operational conditions.

2.2. SO_2 Emission and NO_x Emission

Statements on the pressure-dependences of SO_2 and NO_x emissions (figure 2) are so far based on measurements of two pressure levels (1.1 and 4.5 bar). When moving to the higher pressure SO_2 and NO_x emissions will be diminished by more than 50 %. The qualitative evaluations of early orientation tests on the new pressure apparatus IV where measurements at several pressures between 1 and 10 bar are to be carried out, do reconfirm this improvement.

Figure 10 shows the strong dependence of SO_2 emissions on the size of the limestone (at one fixed Ca/S ratio). It is, however, striking and so far not explainable (figure 5) that varying sizes of one same type of limestone lead to different temperature dependencies. Dolomite shows a similar behaviour (figure 6). When adding coarse material, SO_2 emission will slump with rising temperatures, whereas the opposite happens when material of small grain sizes is added.

Excess air (figure 7) has a weak influence on SO_2 emission, while its effect on NO_x emission is strong since in this case the oxygen concentration is decisive for the conversion of that proportion of fuel-nitrogen which is transformed to NO. (Due to the low temperatures in a fluidized bed plant, 10 to 30 % only of the fuel-nitrogen and no nitrogen from the air is converted to NO.) A lack of O_2 favours rather the competing reaction which yields molecular N_2.

The dependencies of SO_2 and NO_x emissions are mostly active in opposite directions (figure 2). A good insight into the conditions leading to NO formation is possible with the secondary air reactor. When plotting the NO_x emission against different incremental primary air/secondary air ratios, a NO_x minimum is met at a distribution of primary versus secondary air of 50 : 50. This effect was most obvious in reactor no. 1 (4), whereas it was less pronounced in the bigger reactor no. III where, at the same time, the maximum emission values were reduced. The lowest values were observed in the semi-technical reactor (figure 8); they were in the same order of magnitude which prevails also in other larger plants. From this may be concluded that the NO emissions measured in the laboratory reactors are atypically high. The formation of coarse bubbles in big reactors bring about a certain distribution of O_2 as high as into the upper bed zones. Such by-pass effect can be compared with the feed of secondary air. Consequently, the way how oxygen acts on the coal and, possibly, the removal of reducing volatile coal components are main determinants for NO_x emission. Emissions from the semi-technical plant may be considered typical for NO_x emissions from full-scale plants (figure 8), with 1 g NO_2/kWh being approximately equivalent to 200 ppm NO. So, even though the numerical values obtained from laboratory measurements are exaggerated in respect of their absolute value and do not allow any generalization as to NO_x emissions, one may nonetheless derive certain tendencies (e.g. dependence on excess air) which can be scaled-up to bigger plants.

Typical figures for SO_2 emissions cannot be identified since the main influential factor on SO_2 emission will be the amount of limestone added. SO_2 emission, therefore, is only to a small extent typical for a given plant. Figure 9 shows a dependence on the limestone/sulphur mole ratio when feeding different coals high in ash and with varying sulphur contents, but adding one same limestone at pressures of 1.1 and 4.5 bar. It is the spontaneous desulphurization of coals rather than their sulphur content which brings about the difference in SO_2 emissions, -- emissions which on a laboratory scale can be reduced to zero. To find out the limestone with optimum sulphur capturing efficiency (i.e. accomplishing the desired desulphurization with admixture of the possible minimum sorbent amount), some three dozens of limestomes of different geological formations, deposits, and trade marks were tested (5). Geologically young and porous limestones appear to be best suited.

Similar differences as to sulphur capturing properties can be observed also among dolomites. In this case only the $CaCO_3$ proportion acts as a sulphur capturing medium. Optimum desulphurization is a function of the size of limestone particles (6). As can be seen on figure 10, limestone dust < 10 µm is an excellent sulphur capturing medium due to its big surface and thorough distribution in the fluidized bed and this notwithstanding its short residence time. Unlike this, the residence time of coarser fractions with a more reduced total surface is too short as to allow adequate reaction with SO_2. Those particles, however, which are not elutriated and, therefore, accumulate in the fluidized bed on having been fed continuously to it, provide again a very good sulphur capturing efficiency. As soon as particle sizes increase further, however, this beneficial effect is lost again. Such loss of efficiency along with increasing particle size is less pronounced with dolomite due to the fact that here the percentage of magnesium carbonate enlarges the pore volume during combustion and this volume does not get blocked by sulphate formation.

2.3. Halogen Emission

At the temperatures prevailing in a fluidized bed plant, fluorides and chlorides as mineral components of the coal are released as HF and HCl also in the presence of lime. Early results have shown that on condition of low temperatures in the flue gas duct, HF and HCl can be bound by lime-containing fluidized bed flue ash. Trials on an optimization of these bonding conditions have been initiated.

3. Summary

The experiments on a laboratory scale and in the semi-technical plant have releaved a considerable development potential for fluidized bed plants (7) as well as the fact that tests on a smaller scale may sizeable contribute to this end so that results from the different plants are appreciated as being complementary to each other.

References

(1) Münzner, Heinrich: Einfluß von Betriebsparametern auf die Schadstoff-Emissionen einer Wirbelschichtfeuerung im Labormaßstab. VDI-Bericht Nr.266 (1977), S. 79

(2) Schilling, Hans-Dieter, Münzner, Heinrich, Bonn, Bernhard, Wiegand, Detlef: Die Wirbelschichtfeuerung und ihre Bedeutung für den Wärmemarkt. Erdöl und Kohle 9 (1981).

(3) Langhoff, Josef, Kirschke, Hermann, Lemiesz, D., Marnitz, Chr.: Die Wirbelschichtanlage Flingern - Aufbau und erste Betriebserfahrungen. Vortrag VGB-Fachtagung "Kohlefeuerung 1980" Essen, 21.11.1980, und Mannheim, 5.12.1980.

(4) Bonn, Bernhard, Münzner, Heinrich: Schadstoffemissionen bei Wirbelschichtfeuerungen. VDI-Bericht Nr. 322 (1978), S. 103/109

(5) Münzner, Heinrich: Schwefelbindung an Kalk in Wirbelschichtfeuerungen. VDI-Bericht Nr. 345 (1979), S. 319/322

(6) Münzner, Heinrich, Bonn, Bernhard: Sulfur Capturing Effectivity of Limestones and Dolomites in Fluidized Bed Combustion. Vortrag 6th Int'l Conference on Fluidized Bed Combustion, April 1980, Atlanta, USA.

(7) Schilling, Hans-Dieter: Technischer Stand und wirtschaftliche Chancen der Wirbelschichtfeuerung zur Strom- und Wärmeerzeugung aus Kohle. Chem.-Ing.-Techn. 51 (1979), Nr. 3, S. 184/191.

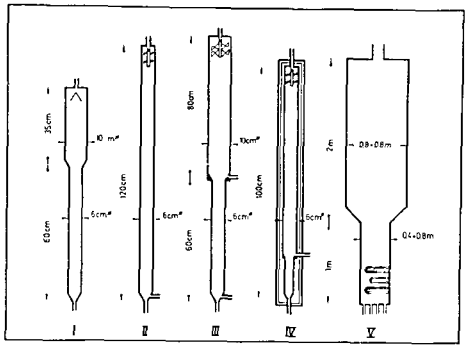

Figure 1: Shapes of the fluidized bed reactors used

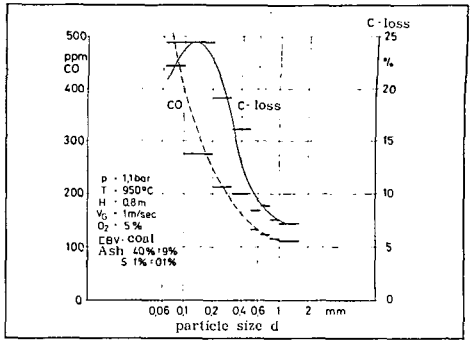

Figure 3: C-loss and CO emission as a function of grain size

Parameter Range (Standard)	MW m^2	%C-Loss	g CO kWh	g SO_2 kWh	g NO_2 kWh
Pressure 1 -- 4,5 bar (1,1 bar)	↗	↘	↘	↘	↘
Temperature 750 -- 950°C (850°C)	→	↘	↘	⌣	↗
Excess air in the 0,5 -- 12% O_2 flue gas (5%)	↘	↘	→	→	↗
Fluidizing velocity 0,3 -- 1,5 m/sec (1m/sec)	↗	↗	→	↗	↗
Bed height (fluidized) 0,2 -- 1,2 m (0,8m)	→	↘	↘	↘	→
Secondary air 0-66 % (0)	→	↘	↘	→	→
Ca/S 0-3 mol/mol (1)	→	→	→	↘	→
Particle size of coal 0-2 mm (0,1-1mm)	→	⌢	↘	→	→
Particle size of limestone 0-2 mm (0-0,1mm)	→	→	→	⌢	~

Figure 2: Variation of operational parameters in fluidized bed reactors on laboratory scale

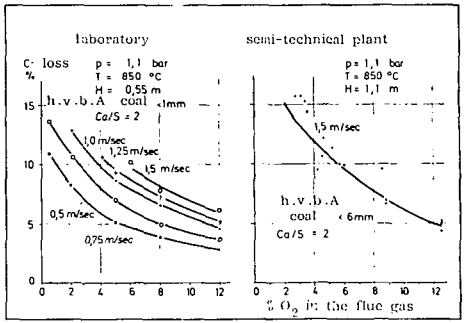

Figure 4: Carbon loss as a function of excess air

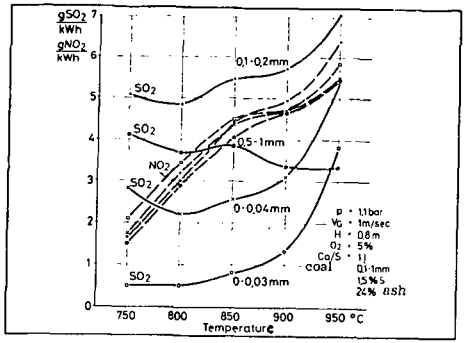

Figure 5: SO_2 and NO_x emissions for different sorbent sizes of cretaceous limestone as a function of temperature

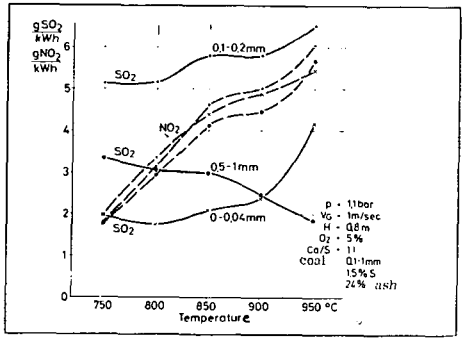

Figure 6: SO_2 and NO_x emissions for various sorbent sizes of dolomite as a function of temperature

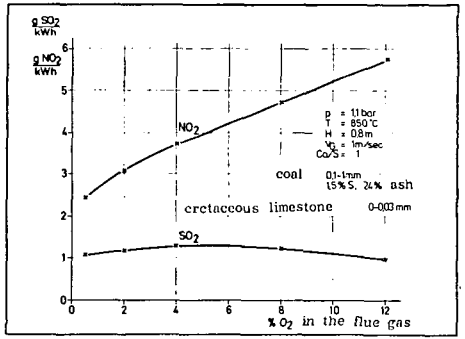

Figure 7: SO_2 and NO_x emissions as a function of excess air

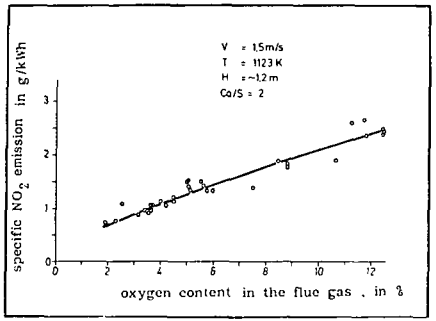

Figure 8: Specific NO_2 emission from the semi-technical fluidized bed plant

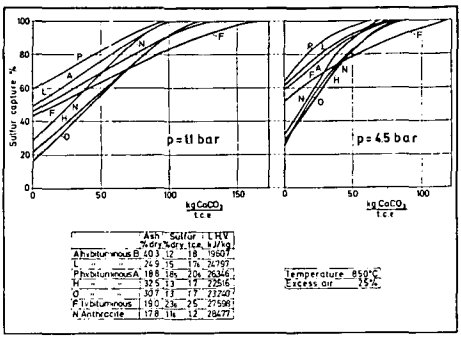

	Ash % dry	Sulfur % dry	t.c.e. kJ/kg
A Hvbituminous B	10.3	1.2	1.8 29807
L " "	24.9	1.5	1.4 24797
P Hvbituminous A	18.8	1.85	2.04 26346
H " "	32.5	1.3	1.7 22516
O " "	30.7	1.3	1.7 23727
F Tvbituminous	19.0	2.35	2.5 27596
N Anthracite	17.8	1.4	1.2 28477

Figure 9: Sulphur capture as a function of the amount of limestone added per t.c.e.

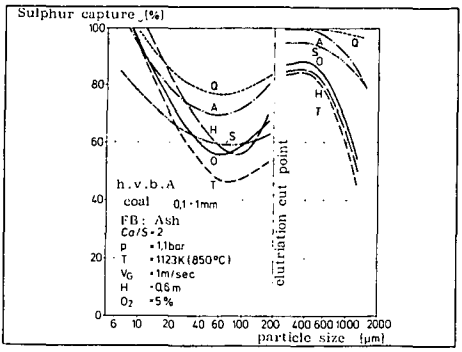

Figure 10: Sulphur capture as a function of limestone particle size

SULFUR CAPTURE AND NITROGEN OXIDE REDUCTION ON THE 6' X 6' ATMOSPHERIC FLUIDIZED BED COMBUSTION TEST FACILITY

T. M. Modrak and J. T. Tang

The Babcock & Wilcox Company
Research and Development Division
Alliance Research Center
Alliance, Ohio 44601

C. J. Aulisio

Electric Power Research Institute
Palo Alto, California 94304

INTRODUCTION

Atmospheric fluidized bed combustion (AFBC) is being developed as a cost-effective, low-polluting method of direct coal utilization for electric power generation. An earlier state-of-the-art assessment (EPRI Final Report FP-308) concluded that the existing AFBC data base was inadequate for the design of utility-scale units -- that is, the available data were limited in scope, and since they had been derived mainly from laboratory-scale equipment, it was doubtful whether they could be applied to the design of utility boilers. The need for a large, well- instrumented facility capable of long-term testing was clearly indicated.

As a result, a 6-foot x 6-foot (6' x 6') AFBC Development Facility was built at The Babcock & Wilcox Research Center in Alliance, Ohio. A complete description of the facility design details are contained in EPRI Final Report CS-1688.

PROJECT RESULTS

Construction of the 6' x 6' facility was completed in October 1977. Following a 5-month startup and debugging phase, the first test series was begun in April 1978. Since then, approximately 2000 hours of testing per year have been logged at the facility. The facility has demonstrated the capability for long-term, steady-state operation, with tests typically lasting from 300 to 500 hours. The AFBC unit is large enough to result in gas-solid residence times for the various zones of the combustor that are typical of those expected for utility-scale units. A wide range of conditions can be tested at the facility. Also, the computerized data acquisition system has been shown to provide accurate, comprehensive documentation of the test results.

SUMMARY OF TESTS

Testing completed as of July 1981, along with a short description of each test series is summarized below:

Test Series	Date	Hours Firing Coal	Comments
1	May 1978	277	Initial characterization
2	June 1978	248	Long duration test to characterize performance
3	August 1978	278	Recycle
4	September 1978	241	Coal size variation, temperature variation
5	November 1978	204	Limestone and coal size variation, temperature variation
6	February 1979	406	New distributor plate, Battelle emission testing - Pittsburgh #8 coal
7	March 1979	171	Single coal feed point - 36 ft^2, bed depth variation, coal and limestone variation
8	May 1979	427	Recycle; underbed single point, temperature variation
9	June 1979	298	Coal size variation, temperature variation
10	July 1979	194	Recycle; overbed and 4-point underbed with coal and limestone
11	August 1979	96	Pulverized coal
12	December 1979	265	New in-bed tube bundle, new baghouse, GCA emission testing - Pittsburgh #8 coal
13	January 1980	318	Recycle; underbed single point, limestone size variation, excess transport air
14	February 1980	277	Recycle; underbed single point and overbed, slumped bed heat transfer study test
15	April 1980	382	Fuller Kinyon pump characterization, baghouse recycle, lignite test
16	May 1980	147	Turndown (slumping) test
17	June 1980	344	Limestone size variation, center recycle
18	July 1980	326	New distributor plate, 4 ft/sec characterization test
19	October 1980	365	4 ft/sec testing, recycle
20	December 1980	344	Feed nozzle design testing, 8 ft/sec
21	January 1981	170	Feed nozzle design testing, 8 ft/sec
22	March 1981	380	NO_x reduction tests
23	June 1981	485	12 ft/sec testing

Significant data were generated in the areas of fly ash recycle, coal particle size, limestone particle size, 5 ft/sec, 8 ft/sec, and 12 ft/sec fluidizing velocity operation, combustion of lignite, and nitrogen oxide reduction. Testing continued to emphasize fly ash recycle as a means of improving combustion efficiency and sulfur capture. In addition to center underbed recycle, overbed recycle with gravity and pneumatic feed as well as baghouse ash recycle configurations were tested. Recycled fly ash testing continued to result in combustion efficiencies on the order of 98%. The highly successful lignite test resulted in combustion efficiencies approaching 99%. The lignite test proved the capability of a fluidized bed combustor (FBC) to combust fuels which can be troublesome. One test was devoted to testing feed nozzles designed to prevent feedline pluggage during slumping. A power outage simulation test was also carried out. The test was designed to determine minimum flow rates through the in-bed tube bundle required to prevent tube overheating during a power outage. Results indicated that tube overheating may be prevented with minimal design considerations.

Tests were also conducted to evaluate bed height reduction as a means of load control in an AFBC facility. These variable bed height tests provided the data needed to design an automatic load control system that will be installed on the 6' x 6' in 1982.

One series of tests was devoted to two-stage combustion, i.e., allowing a portion of the forced draft air to bypass the bed, recombining with the fluidizing gas in the freeboard region. These tests, aimed at NO_x reduction, are discussed later in this paper.

A significant amount of data covering AFBC have been generated on the 6' x 6'. Some of these data have been summarized and discussed in various technical papers

and, therefore, will not be repeated in this paper. Sulfur capture and nitrogen oxide reduction are the two items that will be discussed in the following sections.

SULFUR CAPTURE

No Fly Ash Recycle

Numerous non-recycle tests have been run on the 6' x 6' AFBC at a fluidizing velocity near 8 ft/sec. This large data bank provides information enabling a better understanding of sulfur capture with various operating parameters. A plot of percent sulfur removal versus calcium-to-sulfur ratio showed that sulfur removal is a strong function of the amount of fresh limestone feed (Figure 1). However, the data is quite scattered, indicating that other factors such as particle size, entrainment loss, bed temperature, coal combustion, and sulfur release level may also have a significant influence on sulfur capture efficiency. To more thoroughly investigate these factors, data from a narrow range of Ca/S ratio were subjected to analysis. Sulfur removal was shown to be related to the size of limestone being fed into the unit (Figure 2). The plot indicates that larger limestone feed sizes result in a decreased ability to remove sulfur, a trend which is most pronounced at higher Ca/S values. This suggests that the effect of the fresh limestone feed is predominant since the spent bed lime utilization in these tests range between 23% and 40%. Consequently, the rate of sulfur capture for the bed material is many times smaller than for freshly calcined limestone at all size ranges that exist within the FBC unit. For average limestone feed sizes below 1200 microns (weight-mass average), a significant drop in sulfur retention occurred as a result of high elutriation loss of limestone feed. Further analyses were performed by restricting both the Ca/S ratio and limestone feed size. The data scatter, evident in Figure 2, was found to be related to the effects of bed particle size, extent of bed lime utilization, and bed voidage (Figures 3 and 4). Sulfur removal decreases with:

1. An increase in bed particle size for a narrow range of bed lime utilization (0.30 - 0.33).

2. High bed lime utilization.

3. Higher bed voidage.

Also, spent bed lime utilization is related to both residence time and Ca/S feed ratio, reaching 35% with a residence time of 13 hours at a Ca/S of 2.5 (Figure 5).

Increasing the fluidizing velocity to 12 ft/sec resulted in lower sulfur capture, as shown in Table 1. We believe the causes of this reduction to be: 1) higher elutriation of limestone from the bed, and 2) increased freeboard combustion of coal and its volatile matter. The table shows that carbon and limestone carryover losses were 12% and 55%, respectively. These are about 50% and 34% more than the loss at 8 ft/sec, respectively.

Reducing fluidizing velocity to about 5 ft/sec generally resulted in an improvement in sulfur capture. This was due to smaller limestone feed size and lower elutriation loss (Table 2). In addition, spent bed lime utilization reached 40%.

Table 1

Comparison of Sulfur Capture Efficiency and NO_x Emissions for 8 ft/sec and 12 ft/sec Fluidizing Velocities Under Similar Conditions of: 1) Non-Recycle and 2) Ca/S : 2.4 - 2.8

Item	Fluidizing Velocity 8 ft/sec	12 ft/sec
$\%SO_2$ Capture	78.5	46.2
Combustion Efficiency - %	92	88
NO_x - ppm	285	158
CO - ppm	106	1696
Bed Voidage	0.62	0.72
Limestone Feed Size (weight mean average)	2908μ	984μ
Spent Bed Size (weight mean average)	2337μ	1279μ
Spent Bed Lime Utilization - %	31	29
Elutriation of Available Lime Per Limestone Feed	41	55
Elutriation of Carbon Per Carbon Feed From Coal	8	12

Table 2

Comparison of Sulfur Capture Efficiency and NO_x Emissions for 5 ft/sec and 8 ft/sec Fluidizing Velocities Under Similar Conditions of: 1) Non-Recycle and 2) Ca/S : 1.6 - 1.8

Item	Fluidizing Velocity 5 ft/sec	8 ft/sec
$\%SO_2$ Capture	58	54
Combustion Efficiency - %	94	92
Spent Bed Lime Utilization - %	40	33
% Carbon in Carryover Per Carbon Feed	7.7	9.6
NO_x - lb/MKb	0.22	0.39
Bed Voidage	0.55	0.66
Limestone Feed Size (weight mean average)	815μ	1200μ
Spent Bed Size (weight mean average)	923μ	824μ
CO in Stack Gas - ppm	173	126

Fly Ash Recycle

Operation of the 6' x 6' since May 1979 has emphasized fly ash recycle operation. Recycle has generally improved sulfur capture as shown on Figure 6. Generally speaking, for a given test condition and a narrow range of limestone to coal feed rate, one expects the total available mole of calcium to each mole of coal sulfur to increase as the recycle ratio (recycle rate/coal rate) increases (Figure 7a). The total available calcium oxide is defined as the combined calcium oxide from the limestone feed and the unreacted calcium oxide in the recycle stream; it is designated as $(CaO)_R + (CaO)_L$. The available calcium oxide can change by varying the limestone feed rate or the recycle ratio.

Figure 7b is a plot of the expected trend of the effect of recycle ratio on sulfur capture for two different Ca/S feed ratios. Ideally, for a given set of conditions, sulfur capture should increase with increasing recycle ratio due to an increase in the total available calcium-to-sulfur ratio. The rate of increase in sulfur capture (slope of the curve) will gradually diminish as the reactivity of the recycled lime decreases due to higher calcium utilization. As the curve begins to level off, a point is reached beyond which any further increase in the recycle rate has little benefit on sulfur capture. The recycle ratio for which this occurs should increase as:

1. The particle size of the recycle stream decreases since the smaller lime size results in better reactivity at higher calcium utilization levels.

2. The limestone feed rate increases (higher Ca/S ratio). High limestone feed rates generally result in greater elutriation of freshly calcined limestone. This helps to increase the reactivity of the recycle stream, thus promoting SO_2 capture.

3. The reactivity of recycled lime improves. The improvement can be achieved through either grinding or partial hydration.

The recycle analysis was conducted by first choosing all tests with and without recycle. The data were compared by restricting the Ca/S feed ratios to narrow ranges. Figure 8 shows that the available calcium-to-sulfur ratio, $[(CaO)_L + (CaO)_R]/S$, increases dramatically as the recycle-to-feed ratio is increased. Figure 9 shows the effect of recycle on sulfur capture at three Ca/S ratios. Figure 10 shows that 90% sulfur capture can be obtained at a recycle-to-coal ratio of about 1.3 with a Ca/S feed ratio of 2.5 - 2.9.

By extrapolation, a recycle ratio of about 4 - 5 will be required at a Ca/S feed ratio of 1.5 - 2.0.

Figure 11 shows sulfur capture as a function of fluidizing velocity for both the non-recycle and recycle operating conditions. Note the significant decrease (approximately 20 percentage points) in sulfur capture for the high fluidizing velocity (12 ft/sec) tests as compared to the 8 ft/sec tests. The major reason for this reduction is attributed to the increased freeboard combustion. This, of course, causes more sulfur release in the freeboard.

NITROGEN OXIDE REDUCTION

Single-Stage Combustion

The mechanism of NO_x formation in an AFBC unit is extremely complicated, involving the formation and destruction of NO_x through various chemical reactions that occur in the bed and in the freeboard. Thus, it depends upon the coal devolatization rate and its volatile content, excess air, bed temperature, CO and SO_2 concentrations in the emulsion phase, and the bed hydrodynamics.

At 8 ft/sec fluidizing velocity, NO_x emissions were generally in the 300 ppm - 400 ppm range. However at 5 ft/sec, the NO_x was found to change with the Ca/S feed ratio as shown on Figure 12. It is believed that this effect is a result of the following mechanisms as noted by Exxon [1]:

$$CaO + SO_2 \longrightarrow CaSO_3$$

$$CaSO_3 + 2NO \longrightarrow CaSO_3 (NO)_2$$

$$CaSO_3 (NO)_2 \longrightarrow CaSO_4 + N_2 + 1/2\ O_2$$

As pointed out by Exxon's study, the above mechanisms could only occur in the presence of sulfated lime and with a deficit of oxygen. The rate of NO_x reduction was found to be directly proportional to concentrations of both NO and SO_2 in the gas phase as follows:

$$\frac{1}{W} \quad \frac{d(NO)}{dt} = K\ (NO)^n\ \ (SO_2)^m$$

Where W is the bed weight and n has a value between 0.53 - 0.67 for the temperature range of 1400° - 1600°F. The proposed mechanisms qualitatively appear to provide an explanation to our observation for the low velocity tests. It is generally believed that the relatively smaller spent bed size in these tests resulted in a fast bubbling bed with the relative excess gas velocity $(U - U_{mf})/U_{mf}$, ranging from 8 to 12. Consequently, a majority of oxygen along with air would bypass the emulsion phase via the bubble phase, resulting in a reducing atmosphere in the emulsion phase that enhanced the NO_x reduction through the mechanisms proposed by Exxon.

The NO_x emission data taken from non-recycle tests with Ohio #6 coal and 8 ft/sec fluidizing velocity appeared related to the operating excess air. However, the results were quite scattered, especially at levels below 25% excess air (Figure 13). These scattered NO_x data were found to be associated strongly to the extent of the reducing condition in AFBC where the NO_x level was usually below 200 ppm if the CO concentration in the stack gas exceeded 200 ppm (Figure 14). Further analysis of the data indicated that the high NO_x emissions were associated closely with the bed voidage, where the effect became more pronounced at higher oxidizing conditions (Figure 15).

The effect of carbon loading in the freeboard on NO_x reduction was quite evident at a high fluidizing velocity (12 ft/sec) and a recycle ratio of 1.0 - 1.4. A reduction of NO_x emissions from 0.43 to 0.23 lb/million Btu was observed (Figure 16) as carbon loading increased from 14% to 19%.

Two-Stage Combustion

Staged combustion has been proposed as a means of reducing NO_x from an AFBC unit. Several investigators [2, 3, and 4] have conducted tests to quantify the NO_x reduction with staging. However, these tests were run in small units and only overall effects were measured. To aid in evaluating the effect of staging on NO_x reduction and performance variables, the 6' x 6' AFBC facility was modified to allow air injection at an elevation of 96 inches above the distributor plate. This elevation was chosen based on data from previous tests [2]. Two injection ports -- on opposite walls of the unit -- were installed with valves to control flow and an orifice to measure flow.

Tests were conducted at the conditions listed in Table 3.

Table 3

Summary of Operating Conditions and Measured Performance Variables

Condition/Variable	Test					
	1a	1b	2a	2b	3a	3b
Bed Temp, °F	1564	1546	1544	1547	1512	1553
Bed Height - inches	51.8	52.5	50.0	49.8	47.7	47.8
Superficial Velocity - ft/sec	7.3	8.0	7.1	7.1	6.5	7.0
Coal Feed - lb/hr	1887	2042	2070	2064	2192	2228
Ca/S Ratio	2.7	2.7	2.1	2.5	2.7	2.5
Recycle - lb/hr	2560	2680	2800	2920	2280	2280
In-Bed Air Flow - lb/hr	19500	21500	19400	19400	18300	18900
Overbed Air Flow - lb/hr	0	0	2300	2300	4850	4670
Flue Gas						
O_2 - %	2.9	2.9	2.9	3.1	2.9	2.7
SO_2 - ppm	170	265	562	527	461	458
CO - ppm	208	185	247	203	248	248
NO_x - ppm	416	372	195	175	88	117
Sulfur Capture - %	91.6	86.1	77.1	75.1	74.9	76.1
Combustion Efficiency - %	98.1	97.4	96.8	96.7	96.0	96.1

At each test condition, gas traverses were made at six heights along the centerline of the unit. The gas concentration profiles obtained in-bed (16 inches above the distributor plate) are shown on Figure 17. Note the peak in O_2 and the drop in other gas concentrations near the 36-inch insertion depth. This is probably due to the recycle stream which is being injected with transport air at the 36-inch distance. Profiles above the bed (in the freeboard) were considerably more uniform.

An integrated average of the profile obtained at each elevation was calculated. This average was then plotted versus distance above the distributor plate for CO, SO_2, and NO_x as shown on Figures 18, 19, and 20. There are several points that are readily apparent from these figures.

- With zero overbed air, there is a significant reaction occurring in the freeboard, e.g., reduction of CO and NO_x.
- Two-stage combustion produces the expected trends in reducing NO_x while increasing SO_2 and CO in the bed.

- The addition of air at the 96-inch elevation allows further combustion to occur in the freeboard, thus increasing SO_2 and reducing CO and NO_x.
- Reducing the NO_x level in the bed reduces NO_x throughout the process.
- Gas concentrations measured at the 240-inch elevation, using the freeboard sampling system and analysers, agree remarkably well with the similar, but completely separate, furnace outlet system and analysers.

Figure 21 shows a plot of the furnace outlet NO_x and SO_2 gas concentrations at the three test conditions -- 0%, 10%, and 20% overbed air.

CONCLUDING REMARKS

Twenty-three test series have been completed on the 6' x 6' AFBC Development Facility covering over 7100 hours of operation. Data obtained thus far have clearly shown that fly ash recycle can improve combustion efficiency to the level needed for commercial operation. Recycle also improves sorbent utilization, thus reducing the limestone needed for sulfur capture. Measured NO_x emission levels from the 6' x 6' AFBC unit are well below current EPA limits. However, two-stage combustion tests have shown that NO_x can be reduced to about 0.15 lb/million Btu. Additional work needs to be completed to improve sulfur capture and combustion efficiency with two-stage combustion.

Information obtained thus far has allowed a significant improvement in our understanding of the AFBC process and should prove useful to researchers in this field. Further, design of prototype hardware and other equipment developed and tested on the 6' x 6' should prove useful for commercial design.

REFERENCES

[1] G. A. Hammons and A. Skoop, "NO_x Formation and Control in Fluidized Bed Coal Combustion Processes," presented at the ASME Winter Annual Meeting, Washington, DC; November 28 - December 2, 1971.

[2] J. Tatebayashi, Y. Okada, K. Yano, and S. Ikeda, "Simultaneous NO_x and SO_2 Emission Reduction With Fluidized Bed Combustion", 6th International Conference on Fluidized Bed Combustion, Atlanta, GA; April 1980.

[3] T. Hirama, M. Tomita, T. Adachi, and M. Horio, "An Experimental Study for Low NO_x Fluidized-Bed Combustor Development 2 - Performance of Two Stage Fluidized-Bed Combustion"; EST, Vol. 14, No. 88; pp. 960-965.

[4] T. E. Taylor, "NO_x Control Through Staged Combustion in Fluidized Bed Combustion Systems", 6th International Conference on Fluidized Bed Combustion, Atlanta, GA; April 1980.

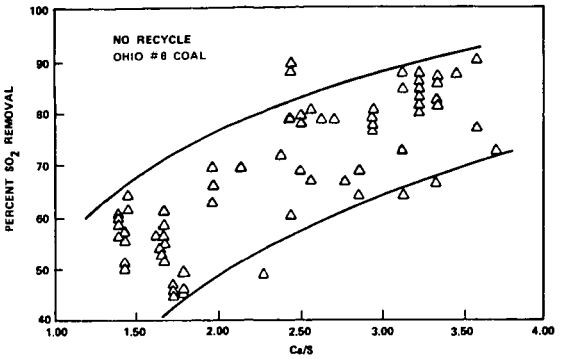

Figure 1 Sulfur Capture as a Function of Calcium/Sulfur (Ca/S) Feed Ratio

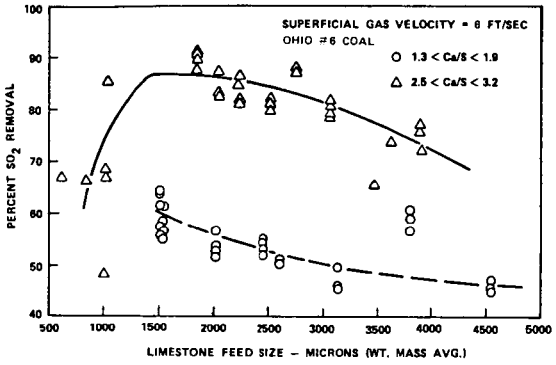

Figure 2 Sulfur Capture as a Function of Limestone Feed Size

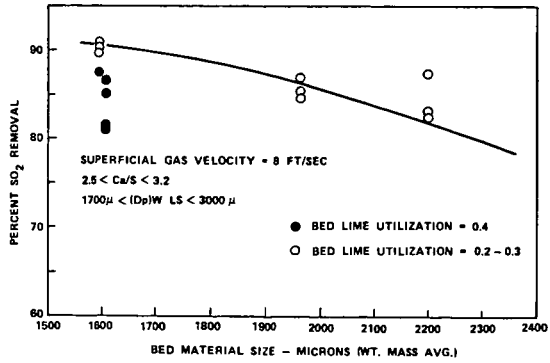

Figure 3 Sulfur Capture as a Function of Bed Particle Size

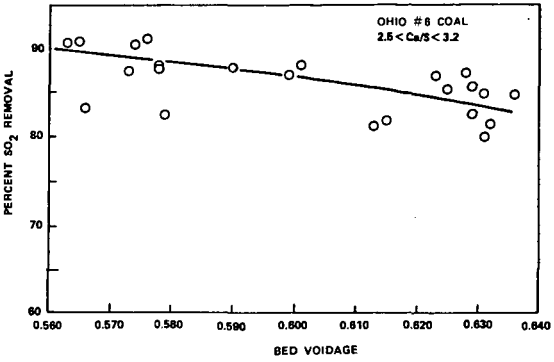

Figure 4 Sulfur Capture as a Function of Bed Voidage

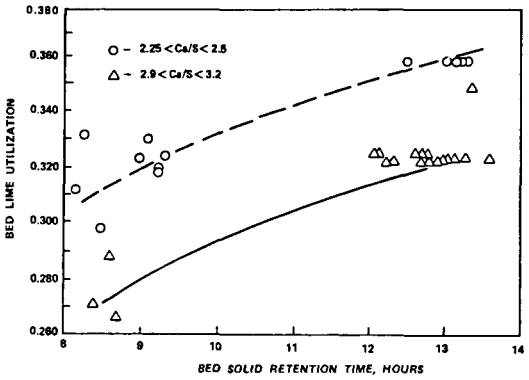

Figure 5 Bed Lime Utilization as a Function of Retention Time

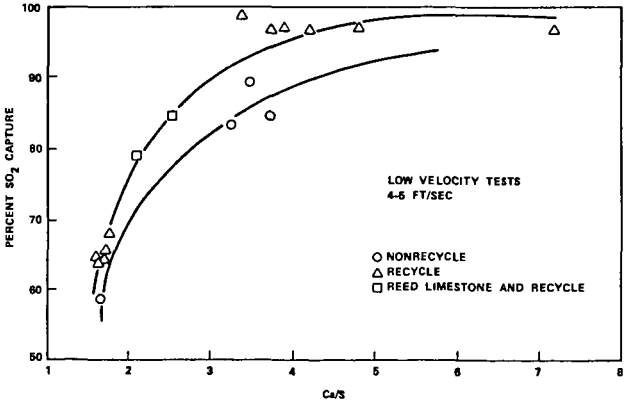

Figure 6 Sulfur Capture as a Function of Calcium to Sulfur Feed Ratio

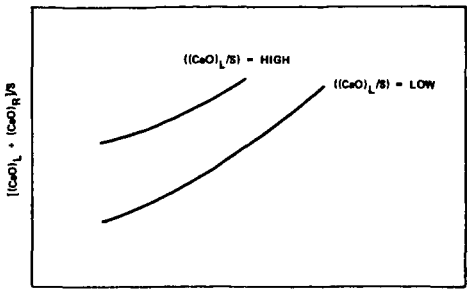

(a) TOTAL AVAILABLE CALCIUM PER SULFUR RATIO VERSUS RECYCLE RATIO

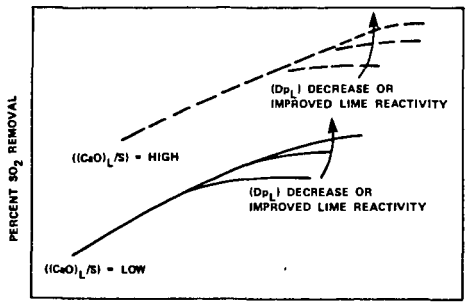

(b) EFFECTS OF THE TOTAL AVAILABLE CALCIUM PER SULFUR RATIO ON PERCENT SO_2 CAPTURED

Figure 7 Effect of Recycle on Sulfur Capture

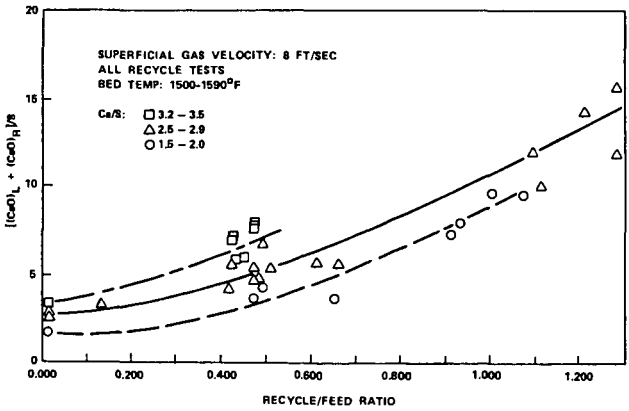

Figure 8 Effect of Recycle on the Available Calcium to Sulfur Ratio

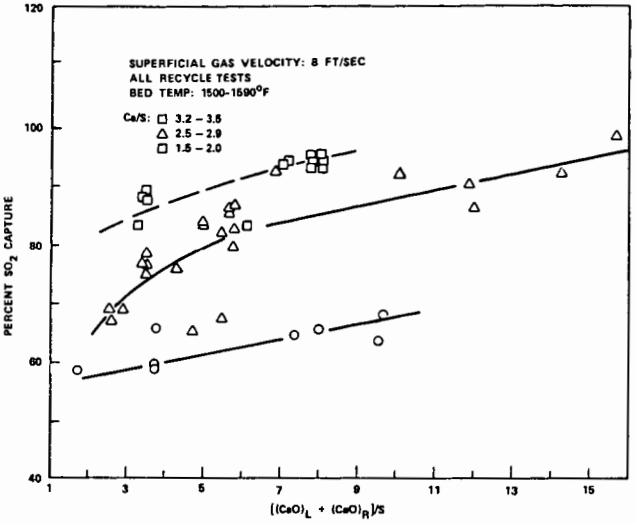

Figure 9 Effect of Available Calcium to Sulfur (Recycle) on Sulfur Capture

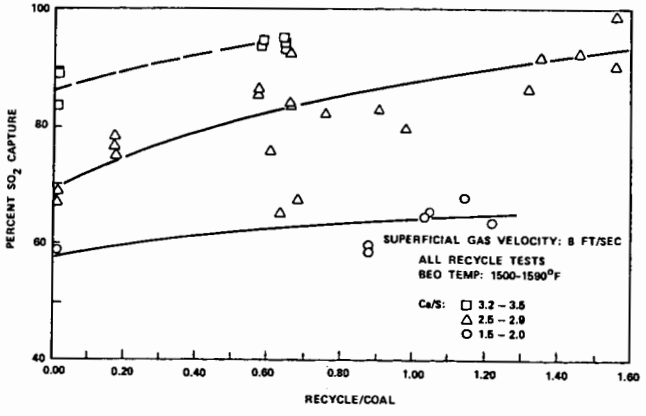

Figure 10 Sulfur Capture as a Function of Recycle Ratio

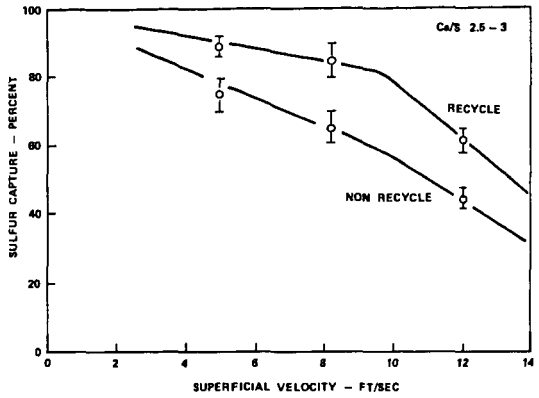

Figure 11 Sulfur Capture as a Function of Fluidizing Velocity

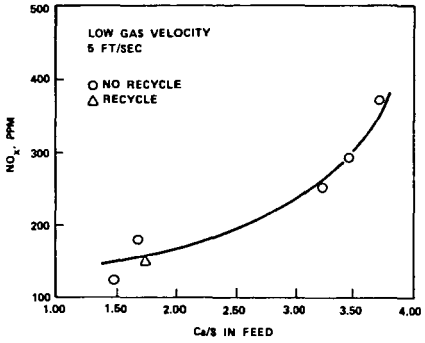

Figure 12 Nitrogen Oxide as a Function of Ca/S Feed Ratio

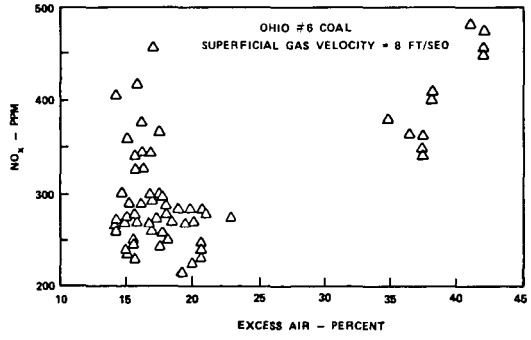

Figure 13 Nitrogen Oxide as a Function of Excess Air

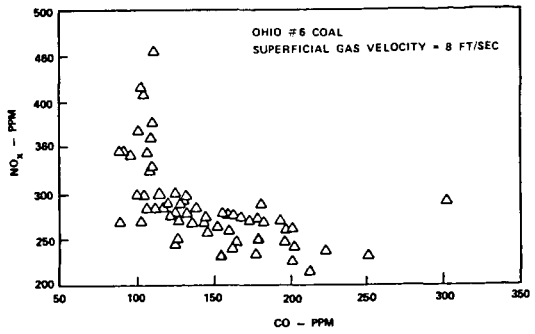

Figure 14 Nitrogen Oxide as a Function of Carbon Monoxide

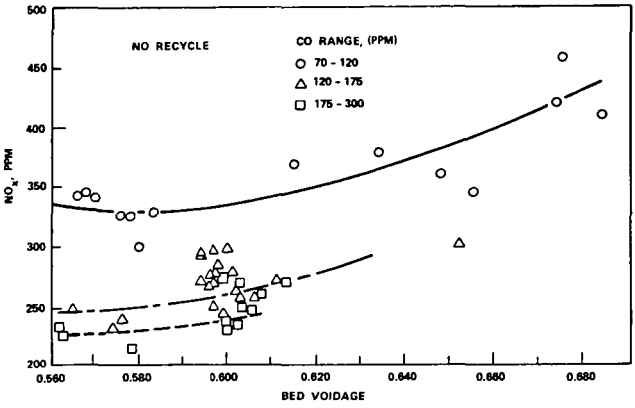

Figure 15 Nitrogen Oxide as a Function of Bed Voidage

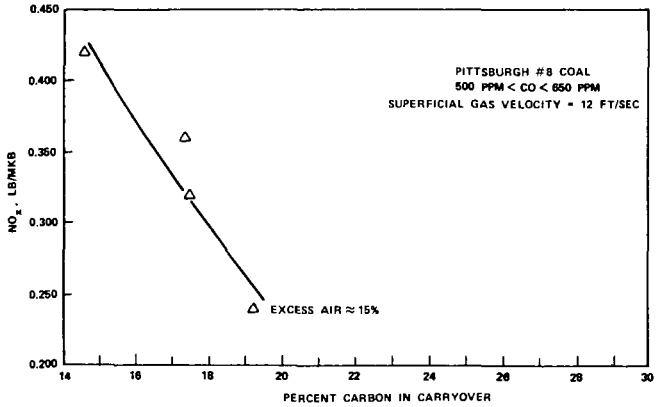

Figure 16 Nitrogen Oxide as a Function of Carbon Loading

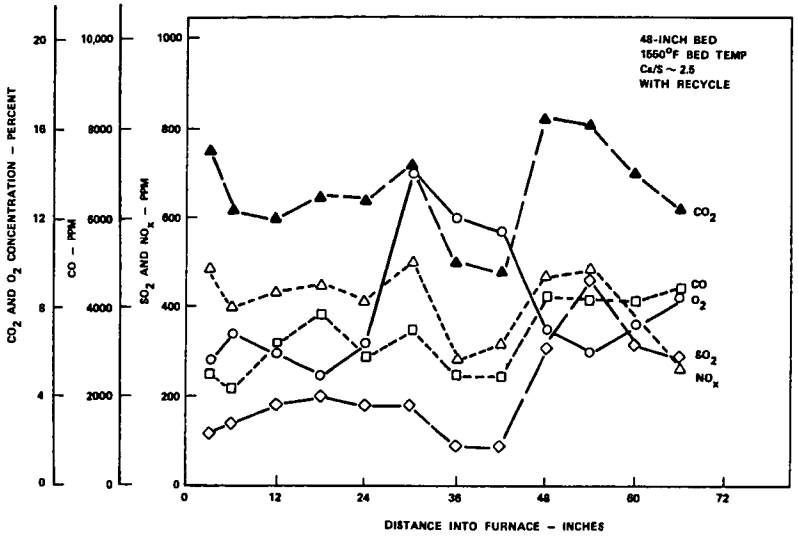

Figure 17 Gas Concentration Profiles – In-Bed
(16 Inches Above the Distributor Plate)

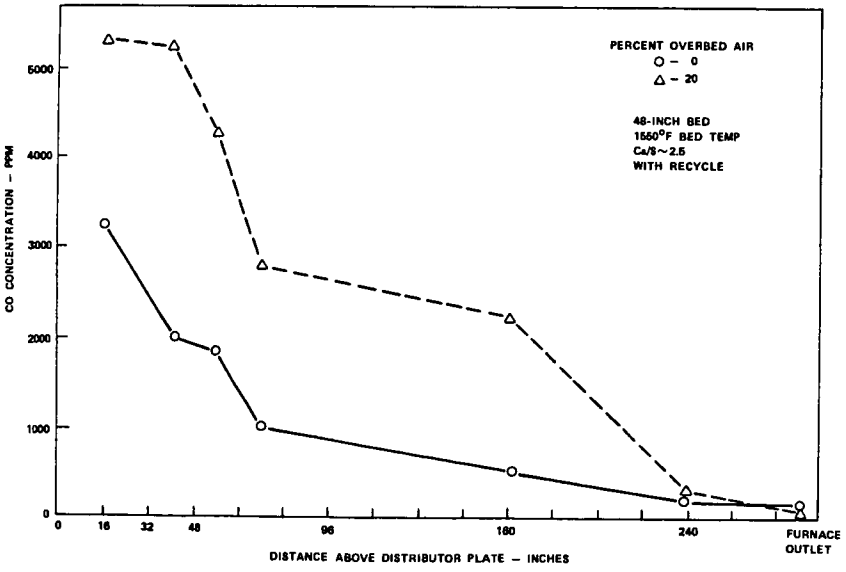

Figure 18 Average Carbon Monoxide Concentration as a Function of
Distance Above the Distributor Plate

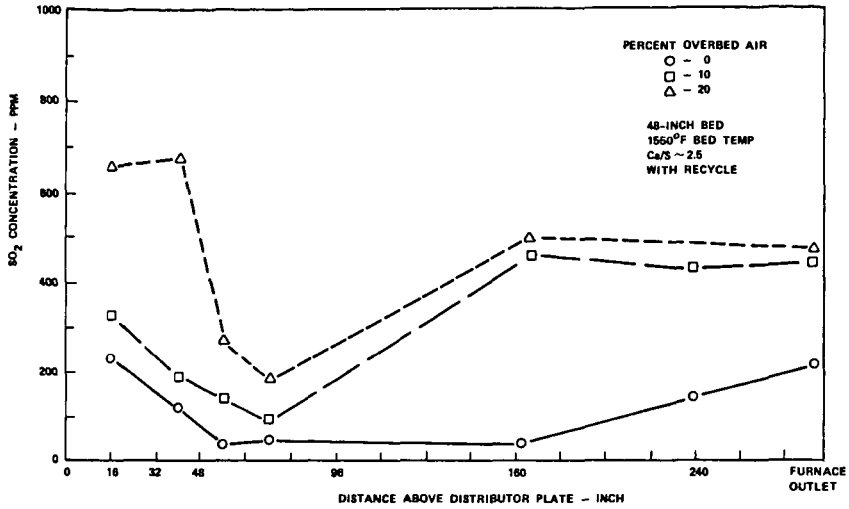

Figure 19 Average Sulfur Dioxide Concentration as a Function of Distance Above the Distributor Plate

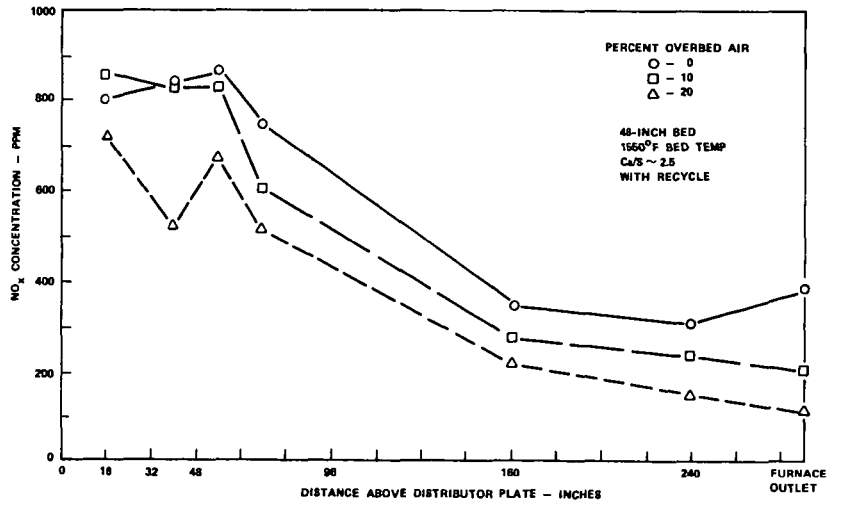

Figure 20 Average Nitrogen Oxide Concentration as a Function of Distance Above the Distributor Plate

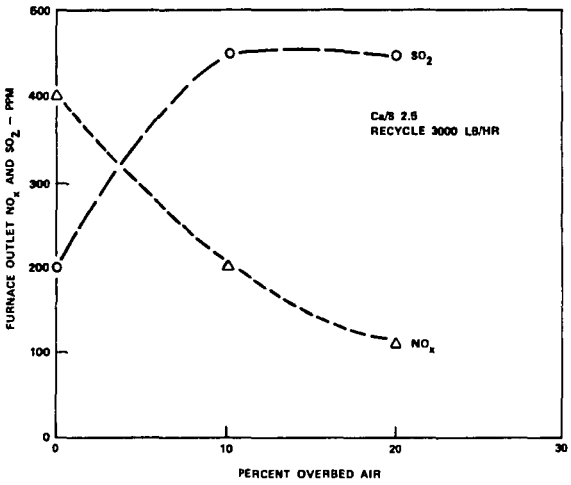

Figure 21 Measured Outlet Gas Concentrations at Various Percent Overbed Air Rates

PARTICLE ENTRAINMENT AND NITRIC OXIDE REDUCTION IN THE FREEBOARD OF A FLUIDIZED COAL COMBUSTOR

P. M. Walsh, T. Z. Chaung, A. Dutta, J. M. Beér, and A. F. Sarofim

The Energy Laboratory and Department of Chemical Engineering
Massachusetts Institute of Technology, Cambridge, MA 02139

1.0 Introduction

Economic design of fluidized bed combustors requires a combination of fluidizing velocities and particle sizes which result in the unavoidable carry over of bed solids, coal char particles and unburned gaseous combustion products into the freeboard. Depending upon the design parameters, the last 5 to 10% of the combustibles will burn, and also significant reduction of SO_2 and NO_x will take place in the freeboard of the fluidized combustor - between the top of the bed and the first row of the convective tube bank. Despite the importance of the freeboard to the efficient and clean operation of fluidized combustors, until recently little attention was paid to the understanding of the freeboard reactions. Pereira et al (1) and Gibbs et al (2) have determined chemical species concentration variation along the height of a 30 x 30 cm cross section fluidized bed and found that significant reduction of NO_x takes place above the bed surface. Okada et al (3) have shown that the fine sorbent particles entrained into the freeboard will enhance sulfur capture and that the entrained char particles will react with NO_x and reduce its emission.

In earlier designs of fluidized combustors the problem posed by unacceptably high carbon carry over at fluidizing velocities was resolved by the introduction of the fines precipitated from the flue gas into a "carbon burn-up cell," an uncooled fluidized bed operating at lower fluidizing velocity. In recent designs, instead of the carbon burn-up cell the method of fines reinjection into the fluidized bed is adopted. In order to achieve operational simplicity the fines in most practical applications are added to fresh feed and returned into the bed. Fines reinjection significantly increases the fine particle concentration in the bed and in the freeboard with the consequence of further enhancing the rate of the heterogeneous reactions of char oxidation, and SO_2 and NO_x reduction in the freeboard.

Modeling of the freeboard reactions has been hindered by incomplete understanding of the processes which govern the entrainment of bed solid particles into the freeboard and the mixing of these solids with the reactant gas. Entrainment models by George and Grace (4), Wen and Chen (5) and Horio et al (6) have fulfilled an important role in predicting solids concentration in the freeboard, but due to a dearth of experimental information on entrainment rate as a function of the fluidization parameters of the bed, these models could not be rigorously tested and developed to the stage where they can be incorporated into FBC combustion models with sufficient confidence.

The importance of the NO-carbon reaction for the reduction of NO in fluidized combustion of coal was recognized and experimentally demonstrated by Pereira and Beér (7), Gibbs et al (2) and Furusawa et al (8). Kinetic parameters for this reaction were reported by Beér et al (9), Kunii et al (10) and Chan (11). Chan also found that the NO-char reaction can be significantly enhanced in the presence of CO.

The problems of predicting NO_x reduction in the freeboard with sufficient accuracy are not only due to uncertainties about solids entrainment but also about the relative significance that CO, coal volatiles, volatile nitrogen compounds, or hydrocarbons may have on NO reduction (Sarofim and Beér (12), Yamazaki et al (13)). In recent experimental studies at MIT detailed hydrocarbon species concentration measurements by Walsh et al (14) have shown that CO and hydrocarbon concentrations are high in the "splash zone" immediately above the bed so that their effect on NO reduc-

tion in this region may not be neglected.

In the following, model calculations are presented of the reduction of NO along the height of the freeboard of the MIT 0.6 x 0.6m cross section, 4.5m high fluidized bed. In the model a new approach is made to the prediction of solids concentration in the freeboard (Chaung (15)) which is assisted by measurement data on the descending flux of particles. The NO reduction along the height above the bed is then predicted from experimental information on the carbon content of bed solids and the chemical kinetic rate equation on the NO-carbon reaction. The NO reductions so calculated are then compared with measurement data obtained burning bituminous and subbituminous coals in the 0.6 x 0.6m MIT experimental facility.

2.0 Particle Entrainment in the Freeboard

2.1 Theory of Particle Entrainment

A model has been developed for the entrainment of particles from the bed into the freeboard of a fluidized combustor. Its purpose is to provide an estimate of the total surface area of each solid species participating in chemical reactions in this zone. The model is based on the following assumptions:

1. Bursting bubbles eject particles into the freeboard.
2. Particle-particle interactions and wall effects are negligible.
3. The changes in mass and size of a particle due to chemical reaction while in the freeboard are negligible.
4. Interaction of the concentration, temperature, and velocity gradients surrounding each particle are negligible.
5. The initial velocities of particles ejected from the bed are given by a semi-empirical log-normal distribution having a geometric mean value proprotional to bubble velocity.
6. Bubble diameters are determined by the heat exchanger tube spacing and the bubble growth model of Mori and Wen (16).

The sequence of steps in the calculation of particle density (mass of particles/volume of gas-particle mixture) is as follows:

1. The initial velocities of the particles leaving the bed are given by the assumed semi-empirical velocity distribution.
2. The initial flux of particles is proportional to the flux of bubbles at the top of the bed. The proportionality factor is determined by equating the kinetic energies of a bursting bubble and the particles which it ejects.
3. The equation of motion is solved for each particle size and initial velocity to determine the particle trajectories.
4. The particle density is determined from the ratios of flux to velocity at each freeboard height. Total density is found by summing the contributions from all sizes and initial velocities.

Because solution of the equations of motion is time-consuming, for the required range of particle sizes and initial velocities, a simplified version of the model was also developed, based on two additional assumptions:

7. Small particles, having $u_t < u_g$, ascend with constant velocity, $v_s = u_g - u_t$.
8. The drag force is negligible on particles having $u_t \geq u_g$.

Chaung (15) showed that the deviation of the particle fluxes predicted by the two models was less than the uncertainty in the results of the more accurate version.

Detailed description of the essential features of the model.

Initial velocity distribution.

A log-normal fit was made to the distribution of ejected particle velocities given by George and Grace (4), which were normalized to the absolute bubble velocities, u_b. The geometric mean particle velocity and standard deviation were 2.44 u_b and 1.43, respectively.

Initial Entrainment

George and Grace (4), defined a parameter, ξ, equal to the ratio of the volumes of entrained particles and bursting bubble. Using this parameter, the entrainment from the bed surface, E_o, can be expressed by

$$E_o = \xi\, Q_b\, \rho_s\, (1 - \varepsilon_{mf})\, A_t \qquad 1)$$

Glicksman et al. (17) give an expression for the visible bubble flow rate, Q_b, valid over the entire range of bubble volume fraction, δ:

$$Q_b = u_g - (1 - \delta)\, [1 - \frac{\pi}{2}\, \ell n\, (1 - \frac{6\delta}{\pi})]\, u_{mf} \qquad 2)$$

The total energy of a bubble before bursting can be equated to the energy of the entrained particles and the energy of the bubble through-flow gas. The total energy of the bubble is given by the following equation from Davidson and Harrison (18):

$$(KE)_b = \frac{1}{2}\, m_{b,eff}\, u_b^2 \qquad 3)$$

where the effective mass of a bubble, $m_{b,eff}$, is

$$m_{b,eff} = \frac{1}{2}\ (\text{mass of fluid displaced by the bubble})$$

$$= \frac{2}{3}\, \pi\, R_b^3\, \rho_s\, (1 - \varepsilon_{mf}) \qquad 4)$$

Defining the root-mean-square velocity of the entrained particles as $\bar{v}_p$, the total kinetic energy of the particles ejected by the bubble is:

$$(KE)_p = \frac{1}{2}\, [\, \xi\, (\frac{4}{3}\, \pi R_b^3)\, \rho_s\, (1 - \varepsilon_{mf})]\, \bar{v}_p^2 \qquad 5)$$

where

$$\bar{v}_p = [\, \int v_p^2\, dm_p\,]^{1/2} \qquad 6)$$

The kinetic energy of bubble through-flow gas is approximately

$$(KE)_g \cong \frac{1}{2}\, [\rho_g\, \pi R_b^2\, (u_b + 3\, u_{mf})]\, (u_b + 3\, u_{mf})^2 \qquad 7)$$

which is usually negligible compared with $(KE)_b$ or $(KE)_p$. The energy balance, i.e., $(KE)_b \cong (KE)_p$, then yields:

$$\xi = \frac{u_b^2}{2\, \bar{v}_p^2} \qquad 8)$$

The absolute bubble velocity is given by

$$u_b = u_g - u_{mf} + 0.711\ (gd_b)^{1/2} \qquad 9)$$

The bubble diameter, d_b, at the top of the bed was found by assuming an initial diameter equal to the spacing of the heat exchanger tubes, and growth according the correlation of Mori and Wen (16). This result; with the assumed velocity distribution; Equations 2, 8, and 9; and the appropriate experimental data; provide the information required to calculate the initial entrainment by Equation 1. No assumption has been made regarding the source of the particles, i.e., whether they originate in the wake or the cap of a bubble.

Calculation of Particle Density

The equation of motion of the particles is

$$v_s \frac{dv_s}{dZ} = -\frac{3}{4} \frac{C_d \rho_g (v_s - u_g) |v_s - u_g|}{\rho_s d_p} - \frac{(\rho_s - \rho_g) g}{\rho_s} \qquad 10)$$

Subject to the initial conditions

$$v_s = v_{si} \text{ at } Z = 0 \qquad 11)$$

The total particle density profile along the freeboard is obtained by summing up all the contributions from ascending and descending particles.

$$\rho(Z) = \sum_{i} \sum_{j} \left[\frac{E_u (d_{pi}, v_{sj})}{v_u (d_{pi}, v_{sj})} + \frac{E_d (d_{pi}, v_{sj})}{v_d (d_{pi}, v_{sj})} \right] \qquad 12)$$

(all particle sizes)

(all initial velocities)

The calculation must be repeated 6000 times if the particle size range is divided into 60 intervals and the initial velocity distribution into 100 intervals.

The Simplified Model

In order to save computer time the model was simplified by neglecting the transient term for small particles and the drag force term for large particles. The equations to be solved are then:

for small particles ($u_t < u_g$), $v_s = u_g - u_t$

for large particles ($u_t \geq u_g$), 13)

$$v_s \frac{d v_s}{dZ} = -\frac{(\rho_s - \rho_g) g}{\rho_s} \qquad 14)$$

which gives for ascending particles

$$v_s = \sqrt{v_{si}^2 - 2gZ \frac{(\rho_s - \rho_g)}{\rho_s}} \qquad 15)$$

The maximum height that a large particle can reach is

$$H_{max} = \frac{\rho_s v_{si}^2}{2(\rho_s - \rho_g)g} \qquad 16)$$

for descending particles

$$v_s = -\sqrt{2g\left(\frac{\rho_s-\rho_g}{\rho_s}\right)(H_{max}-Z)} = -\sqrt{v_{si}^2 - 2gZ\left(\frac{\rho_s-\rho_g}{\rho_s}\right)} \qquad 17)$$

Since the local velocity of each particle is obtained in analytic form, the particle density (Equation 12) yields a closed-form expression:

$$\rho(Z) = \int_{\sqrt{2gZ\,(\rho_s-\rho_g)/\rho_s}}^{\sqrt{2gH_f\,(\rho_s-\rho_g)/\rho_s}} \frac{2(1-y_c)E_o\, f_i dv_{si}}{\sqrt{v_{si}^2-2gZ(\rho_s-\rho_g)/\rho_s}} \quad \text{(Large particles not elutriacted)}$$

$$+ \int_{\sqrt{2gH_f(\rho_s-\rho_g)/\rho_s}}^{v_{si_{max}}} \frac{(1-y_c)E_o f_i dv_{si}}{\sqrt{v_{si}^2-2gZ(\rho_s-\rho_g)/\rho_s}} \quad \text{(Large particles elutriated)}$$

$$+ \int^{d_{pc}} \frac{y(dp)\cdot E_o \cdot d(dp)}{u_g\, u_t\,(dp)} \quad \text{(Small particles elutriated)} \qquad 18)$$

where $y_c = \sum^{o}_{u_t(d_{p_i}) < u_g} y(d_{p_i})$ is the mass fraction of small particles, and $f_i\, d\, v_{si}$ represents the mass fraction of particles with an initial velocity between v_{si} and $v_{si} + dv_{si}$. The validity of the approximations made in simplifying the model was by comparing the particle densities predicted by the two methods (15). The maximum discrepancy was less than 30% of the particle density predicted by the complete model, and the significant features of both density profiles were identical. The results presented here were obtained using the simpler model.

Two Component Bed

When the bed has two components, for example a very small amount of char mixed with stone, the initial entrainment of the char, $E_{o,c}$, is a small fraction of the total initial entrainment. Assuming that the stratification factor is equal to the density ratio,

$$E_{o,c} = E_o \frac{\rho_s}{\rho_{s,c}}\, Y_c \qquad 19)$$

The initial velocity distribution for the char is the same as for the stone, and the total char density is found by the same procedure as before, with $\rho_{s,c}$ in place of ρ_s.

2.2 Measurement of Particle Flux

All of the experiments described in the present paper were performed using the M.I.T. Fluidized Combustion Research Facility, shown in Figure 1. The combustor has a square cross-section, 0.6m x 0.6m; and the total height, from distributor to exit, of 4.5m. The system has been described in detail elsewhere, (Beér et al. (19)).

The mass fluxes of particles extrained in the freeboard at various superficial gas velocities were measured in cold flow experiments by collecting descending particles at various heights above the surface of the fluidized bed. The particle collecting probe was formed by cutting a 22mm diameter tube in half lengthwise, so that it collects particles falling through a narrow strip on one axis of the combustor cross-section. The bed was a single batch of Ottawa Silica Sand (grade #20). Fine particles were removed from the bed by running for several hours prior to making the flux measurements. During the experiments attrition of bed particles and elutriation of fines were negligible. The bed particle size distribution had a geometric mean diameter of 720 $\pm$ 50μm, determined by sieve analysis. The bed was fluidized by ambient air supplied by forced-draft blowers. Bed temperature (average) and pressure (at the distributor) were 330 $\pm$ 20 K and 111 $\pm$ 2 kPa, respectively. Superficial velocity, calculated for the empty tude at the bed temperature and pressure, was varied from 0.42 to 0.86 m/s. The superficial velocity and void fraction at minimum fluidization were 0.37 $\pm$ 0.02 m/s and 0.50 $\pm$ 0.01, respectively.

For measurement of the particle fluxes, the probes were first oriented upside-down until steady bed conditions were achieved at the desired superficial velocity; the probe was then rotated to face upward and collect the descending particles. After sufficient time had elapsed to approximately half-fill the probe, the blowers were stopped, and the particles removed and weighed. Sampling times varied from 1 minute to 10 hours, depending on height and superficial velocity. The method relies upon the assumption that the paths of particles in the vicinity of the probe, moving either upward or downward, are not significantly affected by the motion of the gas around the probe.

2.3 Comparison of the Measured and Predicted Particle Flow Rates

The complete set of experimental particle flow data were reported by Mayo (20). An exponential decay of the particle flow rate with height was observed, having a characteristic length which increased with increasing gas velocity.

Some representative data points are shown in Figure 2, together with the corresponding flow rates calculated using the entrainment model. The predicted profiles show a small region of approximately constant particles flow rate just above the bed, followed by an approximately exponential decay higher in the freeboard. The model thus displays a property analogous to the "splash zone" observed at the top of bubbling fluidized beds. Agreement between the calculated and experimental profiles is best for the intermediate gas velocities, with the predicted flow rates generally larger than the observed values.

The fluxes of ascending and descending particles, and the particle density for the case with gas velocity equal to 0.53 m/s, are shown in Figure 3. The model predicts a maximum in the density near the bed surface, where most of the large particles change direction and return to the bed. Ascending particle flux and density become constant at a height of about 2 m, where only small particles, moving at constant velocity equal to $u_g - u_t$, continue upward. This point is the so-called "transport disengaging height".

3.0 Nitric Oxide Reduction in the Freeboard

3.1 The Mechanism of Nitric Oxide Reduction

The model for NO reduction in the freeboard has been under development for some time. An earlier version, having a less complete description of particle entrainment, was employed by Beer et al (21) for the prediction of NO profiles. Destruction of NO in the freeboard is assumed to occur by heterogeneous reactions with the coal char entrained from the bed:

$$NO + C = CO + 1/2\ N_2$$

$$2\ NO + C = CO_2 + N_2$$

Plug flow is assumed for the gas phase, and the char particle density is calculated using the model for particle entrainment described in Section 2, above. The rate of change of NO concentration with height is given by:

$$u_g \frac{dC_{NO}}{dZ} = - k A \rho_c(Z) C_{NO} \qquad 20)$$

where A is the specific surface area of char available for reaction, and ρ_c is the calculated char particle density. Rate coefficients in the temperature range of interest have been reported by Chan (11).

$$k = 5.95\ T \exp(- E_a/R_o T)\ m/s$$

$$E_a = 81.6 \times 10^6\ J/kmol$$

$$T \leq 1016\ K$$

and by Song (22):

$$k = 4.1 \times 10^3\ T \exp(- E_a/R_o T)\ m/s$$

$$E_a = 136.8 \times 10^6\ J/kmol$$

$$T > 1016\ K.$$

The surface area assumed for the subbituminous coal char was based on the CO_2-BET surface areas reported for lignite and brown coal chars by Guerin et al. (23), Smith and Tyler (24), and Ashu et al (25). These workers reported specific surface areas ranging from 5 to 7 x 10^5 m^2/kg for particle sizes from 89 to 2000 μm. A value of 6 x 10^5 m^2/kg was used in the present calculations. The surface area of the bituminous char was taken near the lower limit of the range reported by Smith (26): 1.5 x 10^5 m^2/kg. The char is treated as if all of its internal surface area were exposed to NO at the concentration and temperature found at the exterior of the particles (effectiveness factor of unity).

Nitric oxide profiles are found by integrating Equation 20, starting with the experimentally measured concentration at, or near, the surface of the bed.

3.2 Measurement of Gas Composition and Char Properties

Gas samples were withdrawn from the combustor through stainless steel probes. With the exception of the continuous sampling probe 4.1m above the distributor, all the probes were water cooled. Probes located in the bed were equipped with sintered quartz filters having pore sizes varying from 90 to 150 μm and sample openings 14.3 mm in diameter. Those located in the freeboard had quartz wool filters. The

accuracy of the reported axial positions of the probes is subject to an uncertainty of ± 40 mm; the probe tip locations relative to the centerline of the combustor varied from 50 to 170 mm. The gas sample continuously withdrawn at z = 4.1m passed through a KF 310 Heated Bypass Filter (Permapure Products, Oceanport, N.J.) to a heated line, and was dried by permeation distillation. This sample was analyzed using Beckman Model 865 non-dispersive IR analyzers for CO and CO_2, a thermoelectron Model 10 Chemiluminescent NO_x analyzer, and a Beckman Model 755 Paramagnetic oxygen analyzer. The total sample flow rate was about 10^{-4} m^3/s (NTP). The gas samples from the other probes were dried by permeation distillation, collected in 250 cm^3 bulbs for analysis on a HP 5830 A gas chromatograph. Hydrocarbons C_1 through C_3 were detected using flame ionization, and CO, CO_2, N_2, and O_2 by thermal conductivity. A thermoelectron Model 10 NO_x analyzer, was also used to measure the NO mole fraction in this sample. The flow rate was 2 to 20 x 10^{-6} m^3/s (NTP).

A gas sample withdrawn from the bed and mixed in a bulb is, in a simplified picture, a mixture of gases withdrawn from the emulsion and bubble phases. At typical operating conditions the composition is heavily biased toward the emulsion (Walsh et al (27)). In order to distinguish the NO contents of the emulsion and bubble phases, the length and diameter of the sample line to the NO analyzer were minimized so that a time-dependent NO mole fraction was observed. The measured NO mole fractions are shown in Figures 4-9, with bars indicating the maximum and minimum values recorded. An analysis by Pereira et al (28) concluded that, in the presence of excess air, NO is greater in the emulsion than in bubbles; and that under stoichiometric or sub-stoichiometric conditions the NO concentrations in the two phases are identical. To determine the mixed-mean NO mole fraction at the top of the bed, the average of the relative maxima observed in the time-dependent NO signal was assigned to the emulsion, and the average of the relative minima was assigned to the bubbles. The two averages were then weighted according to the relative flow rates of bubble and emulsion gas:

$$\bar{\bar{X}}_{NO} \simeq \bar{X}_{NO,max} \left[\frac{(1-\delta)u_{mf}}{u_g}\right] + \bar{X}_{NO,min} \left[1 - \frac{(1-\delta)u_{mf}}{u_g}\right] \qquad 21)$$

This weighted value is shown as a data point at the top of the bed in Figures 6-8; it is the initial value used when Equation 20 is integrated starting at Z=0.

Bed solid samples were withdrawn using a probe located 0.66m above the distributor. The probe was stainless steel, water cooled, and had a N_2 quench stream cocurrent with the sample. The outer and inner diameters of the probe were 44mm and 19mm, respectively. The extracted particles were separated from the gas stream in a water cooled cyclone and collected in a cooled vessel. The inert bed material was Ottawa silica sand. The coal char was separated from ash and sand particles collected in Runs C25-28 in order to determine the char particle size distribution. This was done by froth flotation. A representative sample of the bed solids was introduced into a flotation cell which contained a stirred kerosene-water emulsion together with 4-methyl-2-pentanol. The stirrer keeps the solids in suspension, breaks the kerosene into fine droplets, and disperses it uniformly. Nitrogen was introduced through a sintered stainless steel filter at the bottom of a cell, forming bubbles which adhere to the char particles and lift them up forming a froth, while the sand and ash particles were selectively depressed. The froth was collapsed in a filtering funnel and the char particles collected on the filter. The char was air dried for 24 hours and its size distribution determined using a Joyce Leobl "Magiscan" Image Analyzer. The size of each particle was defined as the diameter of the sphere with volume equal to the volume of the spheroid generated by rotation, about the major axis, of the ellipse defined by the length and breadth of the particle. An apparent char density, $\rho_{s,c}$, was determined from the calculated volume of the particles and the total mass of char; the results are given in Table 2. The char size distribution for Run C22 was found by sieving the bed sample and measuring the weight loss on ignition of each size fraction; in Run A14 the distribution was

assumed to be identical to that of the feed coal. The solid densities of the char in Runs A14 and C22 were estimated from published data.

Two coals were used in the present experiments: bituminous coal from the Arkwright mine in the Pittsburgh seam and subbituminous coal from the Colstrip mine in the Rosebud seam in Rosebud County, Montana. The composition of these coals is given in Table 1.

The size distribution of the fuel and bed particles were determined by sieve analysis. All of the size data for fuel, bed, and char particles were fit by log-normal distribution functions. The geometric means (mass basis) and standard deviation are listed in Table 2. The sizes were converted to a specific surface area basis for the computations. The fluidized combustor operating conditions and relevant experimental data are also listed in Table 2. The data from Runs A14 and C22 were first reported by Beer et al (19).

3.3 Comparison of the Measured and Predicted Nitric Oxide Profiles

The NO profiles predicted by the model are shown in Figures 4-9, together with the experimental data. When the calculation is started at the bed surface (solid line in Figures 4 and 5, dotted line in Figures 6-8) the agreement with experiment is good for Runs A14, C22, and C25; but very poor for Runs C26 and C28, in which there is a very rapid decrease in NO just above the bed, and a discrepancy of about 200 mole ppm between the predicted and observed NO mole fractions. There are not enough data to support a correlation of this behavior with operating conditions, however, it can be seen from the data in Table 2 that C26 and C28 have the lowest bed temperatures and lowest gas velocities. When calculation of the NO concentration for these two runs is started at the next higher data point, excellent agreement with experiment is obtained from that point upward (solid lines).

In Run C27 the combustor was operated using two-stage addition of the combustion air, with the secondary air injector located 1.7m from the distributor. The air/fuel ratio in the bed was sub-stoichiometric, giving very low NO near the top of the bed. The increase in NO mole fraction on addition of the secondary air indicates that some fuel nitrogen species, not detected in the NO mode of the NO_x analyzer, are present in the gas leaving the bed. When the calculation of the NO profile is begun after mixing of the secondary air, the mechanism of the char entrainment/NO-char reduction model is still consistent with the experimental data.

The predictions of the combined model for char entrainment and NO reduction are in good agreement with the observed NO profiles at distances above 0.5m from the bed, in the absence of staged air addition; the model is not able to account for the rapid reduction of NO observed in the splash zone under some conditions. There are several phenomena, not incorporated in the model, which might account for a steep gradient in NO concentration in the splash zone. First, the reduction of NO may only be an apparent one due to uncertainty in the determination and weighting of the bubble and emulsion gas compositions. The estimate of the mixed mean gas composition in the bed (Equation 21) depends on the model used to estimate partitioning of the gas between bubble and emulsion. Other factors may contribute to the uncertainty in bed gas composition, for example, variation in the sample flow rate with the concentration of solids at the probe tip; and mixing of the sample in the probe, sample line, and reaction chamber of the NO analyzer. A second set of phenomena which might account for rapid reduction of NO in the splash zone is the alternate reaction pathways for destruction of NO, including reduction by CO, hydrocarbons, and NH_3. Chan (11) has shown that the NO-char reaction is enhanced in the presence of CO, the effect increasing with decreasing temperature. Reaction of NO and CO, catalyzed by coal ash, is also possible. Mori and Ohtake (29) measured an NO decomposition rate of 273 mole ppm/s.m^2 on alumina, in the presence of 1000 mole ppm CO at 1041 K. The rate of reaction was approximately first order in CO and zeroth order in NO, for NO above 300 mole ppm.

Nitric oxide reduction by methane, with reduction of up to 700 mole ppm NO in 0.5 s, was observed in $NO-CH_4-O_2-CO_2$-Ar mixtures at 1323 K by Yamazaki et al (13). The temperature dependence of the rate is not reported so the possible contribution of this process at 1040-1100 K cannot be determined. Although the reduction of NO was only significant for O_2/CH_4 mole ratios of about 0.5 to 2.0, such conditions might exist locally during mixing of gases in the splash zone of the fluidized bed.

Reactions of NO with NH_3 such as:

$$NO + NH_3 = H_2O + N_2 + 1/2H_2$$

(Duxbury and Pratt (30)) are another possible contribution to the rapid NO disappearance at the top of the bed. Neither ammonia nor NO_x was measured in the present experiments, so the contribution of this reaction cannot be precisely estimated. However, the increase in NO observed in run C27 on addition of secondary air is evidence that N-containing species other than NO may be present in the freeboard at least under sub-stoichiometric conditions. De Soete (31) determined an overall rate expression for the homogeneous reaction between NO and NH_3 giving N_2 from measurements in ethene/oxygen flames over the temperature range 1800 to 2400 K. The reaction is first order with respect to both NO and NH_3. The applicable temperature range is far from fluidized combustor conditions, however, the rate expression predicts an initial NO destruction rate of 140 mole ppm/s at 1040 K in a mixture containing 600 mole ppm each of NO and NH_3. It is possible that this reaction contributes to NO reduction in the splash zone. If it does contribute, the optimum (from the point of view of NO emissions) primary stoichiometric ratio in a configuration with staged air addition, may be one at which some NO is left unreduced at the top of the bed, providing a reactant for direct conversion of NH_3 to N_2 in the splash zone.

4.0 Conclusions

A mechanistic model for particle entrainment into the freeboard has been developed and used in conjunction with a chemical kinetic description of the NO-char reaction for prediction of the reduction of NO along the height of the freeboard in fluidized coal combustion. Bed conditions, including the mass fraction of char in the bed, are input to the model. Predicted NO profiles showed good agreement with experimental data obtained while burning bituminous and subbituminous coals under a variety of operating conditions. The steep reduction in NO observed in the splash zone immediately above the bed in some cases could not be adequately explained by the present model. This result points to the importance of the reactions in the splash zone, where it is thought that NO reducing reactions other than the NO-char reaction will have to be taken into account for satisfactory prediction of the NO profile under all conditions. The model is now in a form in which it can be integrated into system models for predicting NO emissions as a function of operating conditions.

Acknowledgements

The development of the models for particle entrainment and nitric oxide reduction was supported by DOE under Contract No. EX-76-A-01-2295. The experimental work was supported by DOE under Grant No. DE-FG22-80PC30215, Dr. H. A. Webb, Project Manager.

Nomenclature

A	Specific BET surface area of char (m^2/kg)
A_t	Cross sectional area of the bed (m^2)
C_D	Drag coefficient
C_{NO}	NO concentration ($kmole/m^3$)
d_b	Bubble diameter (m)
$\bar{d}_B$, $\bar{d}_c$, $\bar{d}_f$	Geometric mean diameters of bed particles, char particles, and fresh coal particles, respectively (m)
E_a	Activation energy (J/kmol)
E_d, E_u	Mass flow rates of downward and upward moving particles, respectively (kg/s)
E_o, $E_{o,c}$	Initial entrainment rates of stone and char particles from the bed surface, respectively (kg/s)
H_f	Total freeboard height (m)
k	Rate coefficient (units variable)
L_f	Expanded bed height (m)
m_p	Mass of a single particle (kg)
Q_b	Visible bubble volume flow rate (m^3/s)
R_o	Gas constant = 8314 J/kmol · K
R_b	Bubble radius (m)
T	Temperature (K)
T_B	Bed temperature (K)
T_g	Gas temperature (K)
u_b	Absolute bubble velocity (m/s)
u_g	Superficial gas velocity (m/s)
u_{mf}	Minimum fluidization velocity (m/s)
u_t	Particle terminal velocity (m/s)
v_d, v_u	Downward and upward particle velocities, respectively (m/s)
v_s, v_{si}	Particle local velocity and particle initial velocity, respectively (m/s)
$\bar{v}_p$	Root-mean-square particle initial velocity (m/s)

X_k	Mole fraction of species k
Y_c	Mass fraction of char in the bed
z	Distance above the distributor (m)
Z	Distance above the bed surface (m)
ξ	Volume fraction of particles ejected per bursting bubble
ε_{mf}	Bed voidage at minimum fluidization
$\rho(Z)$, $\rho_c(Z)$	Local density of stone and char particles, respectively, at freeboard height Z, (kg/m^3)
ρ_g	Gas density (kg/m^3)
ρ_s, $\rho_{s,c}$	Solid densities of stone and char, respectively (kg/m^3)
δ	Bubble volume fraction
σ_f, σ_B, σ_c	Geometric standard deviations of fresh coal particles, bed particles and char particles, respectively

TABLE 1. ANALYSIS OF COALS

Analysis (wt %)	Bituminous, Arkwright, Pittsburgh Seam	Subbituminous, Colstrip Mine, Rosebud Seam, Rosebud County, MT
Proximate	(as received)	(as received)
moisture	1.6	19.19
ash	8.01	8.29
volatile matter	33.93	28.74
fixed carbon	56.46	43.78
Ultimate	(daf)	(dry)
C	76.36	67.80
H	5.23	4.45
N	1.47	1.00
S	2.61	.59
O	5.26	15.91
ash	-	10.25

TABLE 2. OPERATING CONDITIONS AND EXPERIMENTAL DATA
(pressure = 101 kPa)

Run Number	A14	C22	C25	C26	C27**	C28
Coal Type	Bitum-minous	Subbitu-minous	Subbitu-minous	Subbitu-minous	Subbitu-minous	Subbitu-minous
$\bar{d}_f$ (μm)	674	1000	1750	1750	2100	2100
σ_f	1.87	1.8	1.83	1.83	2.12	2.12
Stoichiometric air/fuel ratio	1.19	1.22	1.21	1.25	1.02	1.07
T_B (K)	1105	1134	1110	1050	1095	1040
T_g(z=4.1 m)	-	-	1002	932	1043	988
u_g(m/s)	0.98	1.46	1.00	0.80	0.94	0.86
X_{O_2} (z=0.9 m) (mole %)	6	8	4.1	-	1.7	2.3
X_{O_2} (z=4.1 m) (mole %)	-	-	3.2	4.0	3.5	1.5
X_{CO}(z=0.9 m) (mole %)	2	0.9	1.5	0.25	2.1	0.9
X_{CO}(z=4.1 m) (mole %)	-	-	<0.005	<0.005	0.11	0.14
X_{HC}(z=0.9 m) (mole %)	0.2	0.02	0.32	0.03	0.78	>0.33
$\bar{d}_B$ (μm)	815	1300	800	800	760	720
σ_B	1.42	1.32	1.44	1.44	1.35	1.37

Table 2 Cont'd

Run Number	A14	C22	C25	C26	C27**	C28
Coal Type	Bitum-minous	Subbitu-minous	Subbitu-minous	Subbitu-minous	Subbitu-minous	Subbitu-minous
$\bar{d}_c$ (μm)	674*	1123	2300	2300	2300	2400
σ_c	1.87*	1.41	1.55	1.54	1.52	1.55
Apparent char solid density $\rho_{s,c}$ (kg/m^3)	1400	1200	915	909	930	920
Estimated bubble fraction, δ	0.2	0.2	0.125	0.128	0.226	0.196
Carbon mass fraction in the bed, Y_c	0.01	0.0012	0.0015	0.0011	0.0056	0.0023
$\bar{\bar{X}}_{NO}$ at bed surface (mole ppm)	380	500	717	561	~ 2	595
BET specific surface of char (m^2/kg)	1.5×10^5	6×10^5	6×10^5	6×10^5	6×10^5	6×10^5

*The char size distribution in the bed for Run No. A14 is assumed to be the same as the feed size distribution.

**Run No. C27 used staged addition of the combustion air.

References

1. F. J. Pereira, J. M. Beér, B. Gibbs, and A. B. Hedley, Fifteenth Symposium (Int'l) on Combustion, The Combustion Institute, Pittsburgh, PA, 1975, p1149.

2. B. M. Gibbs, F. J. Pereira, and J. M. Beér, Inst. Fuel, Symposium Series No. 1, Fluidized Combustion Paper D.6, 1975, pp1-13.

3. Y. Okada, J. Tatebayashi, and R. Yamamura, "Experimental Emission Control on Fluidized Bed Combustion of Coal," presented at AIChE Annual Meeting, San Francisco, CA, 1979.

4. S. E. George and J. R. Grace, AIChE Symposium Series, No. 176, Vol. 74, 1978, p67.

5. C. Y. Wen and L. H. Chen, The Proceedings of the Sixth International Conference on Fluidized Bed Combustion, USDOE, CONF-800428-Vol. 3, p1115.

6. M. Horio, A. Taki, Y. S. Hsieh, and I. Muchi, in Fluidization, Grace and Matsen, eds., Plenum, N.Y., 1980, p509.

7. F. J. Pereira and J. M. Beér, Deuxième Symposium Européen sur la Combustion, Orléans, France, 1975, p339.

8. T. Furusawa, D. Kunii, A. Oguma, and N. Yamada, Proc. Soc. Chem. Eng., Japan, 4 (1978)562.

9. J. M. Beér, A. F. Sarofim, L. K. Chan, and A. M. Sprouse, The Proceedings of the Fifth International Conference on Fluidized Bed Combustion, The MITRE Corporation, Vol. II, McLean, VA, 1978, p577.

10. D. Kunii, T. Furusawa, and K. T. Wu, in Fluidization, Grace and Matsen, eds., Plenum, N.Y., 1980, p175.

11. L. K. Chan, Kinetics of the Nitric Oxide-Carbon Reaction Under Fluidized Bed Combustor Conditions, Dissertation, MIT, Cambridge, MA, 1980.

12. A. F. Sarofim and J. M. Beér, Seventeenth Symposium (Int'l) on Combustion, The Combustion Institute, Pittsburgh, PA, 1979, p189.

13. S. Yamazaki, M. Hiratsuka, and Y. Fujitani, Combustion Science and Technology, 20 (1979)25.

14. P. M. Walsh, M. Nicastro, C. Sundback, J. M. Beér, W. R. Brooks, A. Dutta, C. J. Giallombardo, L. R. Glicksman, and M. C. Zhang, "Experimental Studies for Testing of Models and for Scale-up of Fluidized Bed Combustion," Technical Report for the Period April 14 to August 14, 1981, prepared for the Tennessee Valley Authority under Contract No. TV-55783, August 25, 1981.

15. T. Z. Chaung, "Further Studies on the Mechanistic Freeboard Model; Simulation and Measurements of Solid Flux in the Freeboard," In J. F. Louis and S. E. Tung, "Modeling of Fluidized Bed Combustion of Coal, Quarterly Technical Progress Report No. 20, prepared for DOE/Morgantown under Contract No. EX-76-A-01-2295, 1981.

16. S. Mori and C. Y. Wen, AIChE Journal 21 (1975)109.

17. L. R. Glicksman, J. Valenzuela, and W. Lord, "Fluid Dynamics Component Model," in "Modeling of Fluidized Combustion of Coal," J. F. Louis and S. E. Tung, Quarterly Tech. Progr. Report No. 12, Contract No. E(49-18)-2295, MIT, Aug. 1979.

18. J. F. Davidson and D. Harrison, Fluidised Particles, Cambridge University Press, 1963.

19. J. M. Beér, A. F. Sarofim, S. S. Sandhu, M. Andrei, D. Bachovchin, L. K. Chan, T. Z. Chaung, and A. M. Sprouse, "NO_x Emission from Fluidized Coal Combustion," Final Report prepared for USEPA under Grant No. R804978020, 1981.

20. J. E. Mayo, "Determination of Solids Loading in the Freeboard Section of a Fluidized Bed Coal Combustor," B.S. Thesis, Dept. of Chemical Engineering, MIT, Cambridge, MA, 1980.

21. J. M. Beér, A. F. Sarofim, P. K. Sharma, T. Z. Chaung, and S. S. Sandhu, in Fluidization, Grace and Matsen, eds., Plenum, N.Y., 1980, p185.

22. Y. H. Song, Fate of Fuel Nitrogen During Pulverized Coal Combustion, Dissertation, MIT, Cambridge, MA, 1978.

23. H. Guerin, T. Siemieniewska, Y. Grillet, and M. François, Carbon 8 (1970)727.

24. I. W. Smith and R. J. Tyler, Combustion Science and Technology 9 (1974)87.

25. J. T. Ashu, N. Y. Nsakala, O. P. Mahajan, P. L. Walker, Fuel 57 (1978)250.

26. I. W. Smith, Fuel 57 (1978)409.

27. P. M. Walsh, A. K. Gupta, J. M. Beér, and K. S. Chiu, "Proceedings of the DOE/WVU Conference on Fluidized Bed Combustion System Design and Operation," Morgantown, WV, October 27-29, 1980, p455.

28. F. J. Pereira, J. M. Beér, and B. M. Gibbs, "Nitric Oxide Emissions from Fluidized Coal Combustion," presented at the Central States Section, The Combustion Institute, Spring Meeting, April 5-6, 1976.

29. Y. Mori and K. Ohtake, Combustion Science and Technology 16 (1977)11.

30. J. Duxbury and N. H. Pratt, Fifteenth Symposium (Int'l) on Combustion, The Combustion Institute, Pittsburgh, PA, 1975, p843.

31. G. G. De Soete, Fifteenth Symposium (Int'l) on Combustion, The Combustion Institute, Pittsburgh, PA, 1975, p1093.

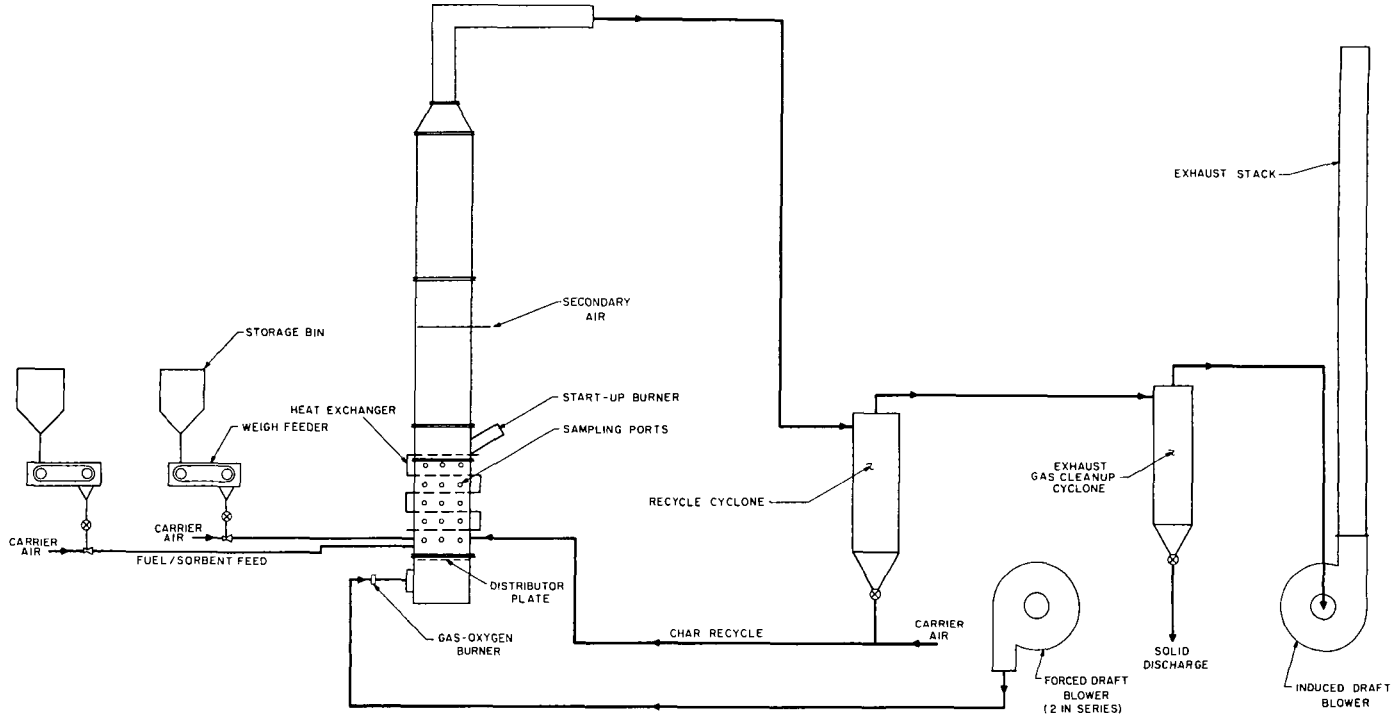

FIGURE 1. M.I.T. 0.6 m x 0.6 m, 500 kW (THERMAL) FLUIDIZED COMBUSTION RESEARCH FACILITY

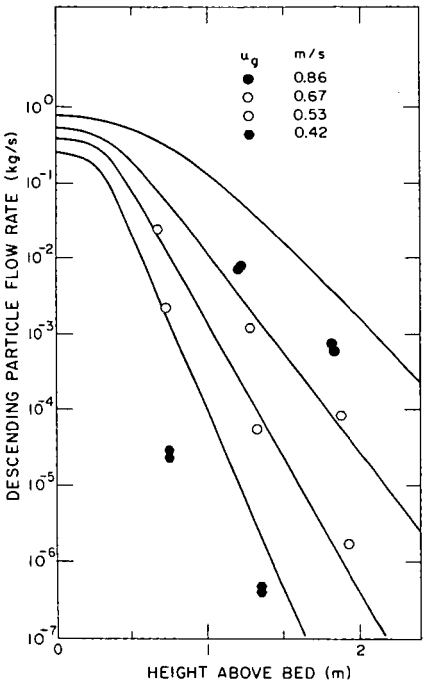

FIGURE 2. DESCENDING PARTICLE FLOW RATE VS. HEIGHT ABOVE THE BED. COMPARISON OF MODEL PREDICTIONS WITH EXPERIMENT.

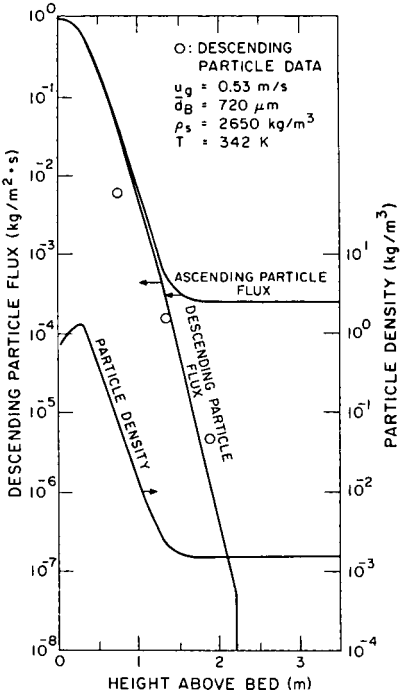

FIGURE 3. PARTICLE DENSITY, ASCENDING FLUX, AND DESCENDING FLUX VS. HEIGHT ABOVE THE BED.

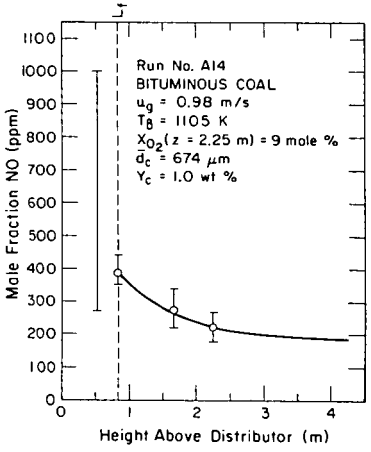

FIGURE 4. MOLE FRACTION NITRIC OXIDE VS. AXIAL POSITION
I MEASURED
— CALCULATED

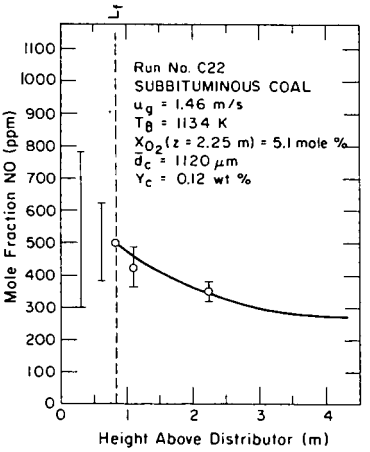

FIGURE 5. MOLE FRACTION NITRIC OXIDE VS. AXIAL POSITION
I MEASURED
— CALCULATED

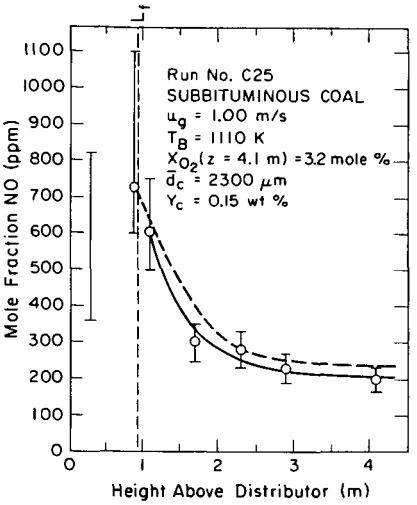

FIGURE 6. MOLE FRACTION NITRIC OXIDE VS. AXIAL POSITION
I MEASURED
CALCULATED

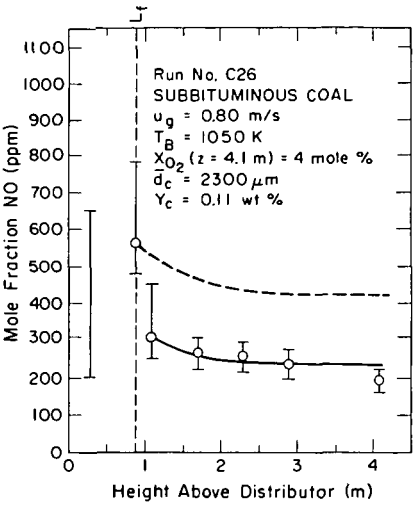

FIGURE 7. MOLE FRACTION NITRIC OXIDE VS. AXIAL POSITION
I MEASURED
CALCULATED

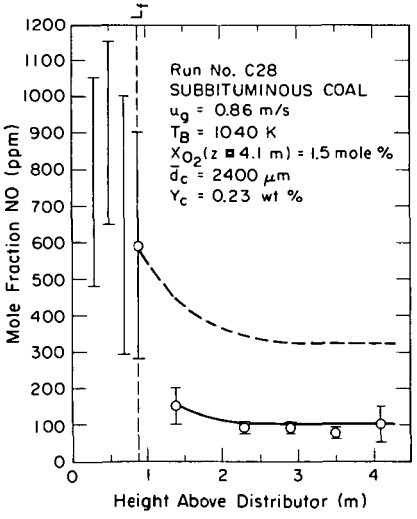

FIGURE 8. MDLE FRACTION NITRIC OXIDE VS. AXIAL POSITION
I MEASURED
CALCULATED

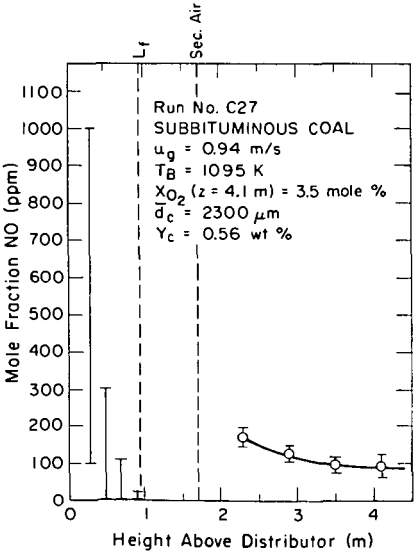

FIGURE 9. MOLE FRACTION NITRIC OXIDE VS. AXIAL POSITION
I MEASURED
CALCULATED

"NO_x" Formation and Kinetics of "NO_x" Reduction in Fluidized Bed Combustion of Carbonaceous Materials

Takehiko Furusawa, Mikio Tsunoda,
Seiichi Sudo, Shunichi Ishikawa and Daizo Kunii

Department of Chemical Engineering
University of Tokyo
Bunkyo-Ku Tokyo 113 JAPAN

In contrast with the extensive investigations concerning sulfer retention in the United States, the initial stage of development in Japan has focused on the nitric oxide emission control.

The staged air firing is considered to be the most promising method for control. In this operation the fluidized bed is maintained under a deficiency of air and the design factors influencing sulfur retention, formation and destruction of nitric oxide, ammonia and other nitrogeneous compounds, and combustion efficiency are complex interactions. The optimum design of a fluidized bed combustor requires sound qualitative information concerning the behavior of nitric oxide formation and quantitative descriptions of the kinetics of "NO" destruction. The objective of this report is to describe the recent findings concerning "NOx" formation and the kinetics of "NOx" reduction reactions in fluidized bed combustion of carbonaceous materials.

I. NITRIC OXIDE EMISSION FROM FLUIDIZED BED COMBUSTION

Equipment, Procedure and Materials

The combustors are stainless steel vessels, 50mm diam. 580mm long and 76mm diam. 850 mm long. The lower part of the vessel was packed with refactory materials and used for preheating. Fluidizing air or simulated air consisting of oxygen and argon enters the combustor through a multi-orifice plate distributor into a bed of microspherical particles whose chemidal and physical properties are given in Table 1. The multi-orifice plate was designed so that a pressure drop sufficient to achieve homogeneous fluidization could be obtained. In a series of experiments carried out to investigate the influence of air staging, the primary stage of the bed was maintained at substoichiometric conditions, while the balance of the air was introduced through the nozzles into the freeboard.

The static bed height was specified to be 10cm. The fluidized bed combustor was externally heated by an electric furnace. The temperature of the bed was controlled by a conventional PID electronic controller.

Feeding of the carbonaceous materials employed was done by means of a solid feeder developed in our laboratory. Thus continuous feed of a small flow rate of solids (such as 0.2 g/min) could be realized. The solids were sent into the fluidized bed combustor at a point 30~35mm above the distributor.

Ash was removed by elutriation and the elutriated solids were removed from the off-gas by a small cyclone separator. In a certain series of experiments, collected solids were used for chemical analysis to obtain the combustion efficiency.

Upstream from the cyclone separator, (5cm below the top cover of the combustor) the off-gas was continuously diverted to a gas-analysis system. A chemiluminescent NOx analyzer provided continuous measurement for NOx while gas chromatography provided intermittent analysis for H_2 N_2, CO, CO_2, CH_4 and C_2H_4. Known gas mixtures were used to calibrate the gas chromatograph. Kitagawa NH_3 low-range ditector tubes were used to analyze NH_3. the experimantal conditions employed are shown in Table 1, while the carbonaceous materials employed for the present series of experiments are shown in Table 2.

Table 1 Scope of experiment

Inert particles:	Microspherical particles
	SiO_2:8.93%, Al_2O_3:90.61%, Fe_2O_3: 0.46%
Surface mean particle diameter of the inert particles:	
	580 microns for coal and char, 613 microns and 322 microns for coke
Bulk density:	0.57 g/cm^3
Temperature of fluidized bed:	700-1000°C
Static height of bed:	10cm
Diameter of coal and char particels:	500-710 microns
Mean diameter of coke particles,	
	Coke I : 109 microns
	Coke II : 191 microns
	Coke III: 460 microns
(A) ID 50mm combustor (height 490mm)	
	Flow rate of fluidizing air and simulated air: 4.2-8.1 Nℓ/min
	Feed rate of fuel particles: 0.5-1.7 g/min
(B) ID 76mm combustor (height 850mm)	
	Flow rate of fluidizing air and simulated air: 3.9-10.4 Nℓ/min
	Feed rate of fuel particles: 0.37-1.27 g/min

The effects of volatile components on nitric oxide emission[4,6)]

Fundamental investigations concerning the effects of stoichiometric ratio and combustion temperature on "NO" emission were carried out by use of various types of carbonaceous materials indicated in Table 2. Typical results are shown in Fig.1 (a) and (b). Figure 1 (a) indicates that a considerably high level of "NO" emission in the presence of reducing gas (H_2, CO and CH_4) was observed under a substoichiometric combustion of coal while quite a low level of "NO" emission was detected under a starving combustion of char.

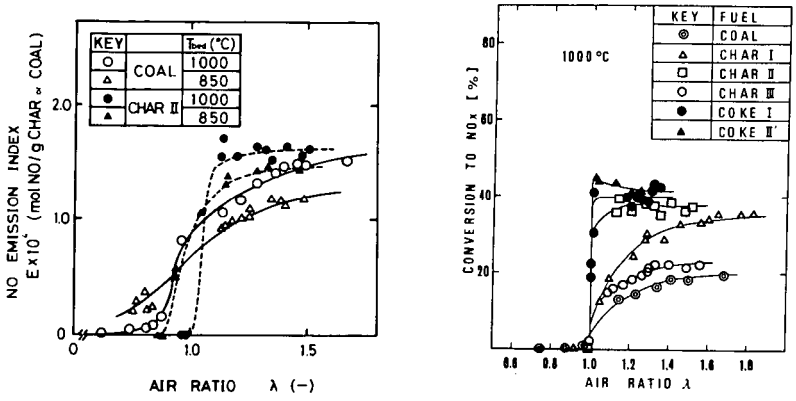

(a) (b)

Fig. 1 Effects of stoichiometric ratio and combustion temperature on "NO" emission

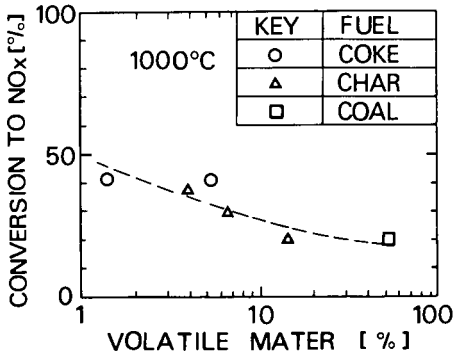

Fig. 2 Conversion of fuel nitrogen to NO with respect to volatile components

Table 2 Proximate and ultimate analyses of carbonaceous materials used

Proximate analysis [wt%]

		Volatile matter	Fixed-carbon	Ash	Moisture
Char I	*1	3.83	54.09	19.8	22.28
Char II	*2	2.74	66.00	24.47	6.69
Char III	*3	10.89	65.04	19.84	4.32
Coal	*4	43.3	39.1	12.7	4.9
Coke I	*5	1.4	96.0	1.4	1.2
Coke II	*5	3.7	92.5	0.2	3.6
Coke II'	*5	5.3	90.9	0.4	3.4
Coke III	*5	10.9	85.7	1.7	1.7
Carbon	*6	5.2	94.7	0.1	(3.2)

Ultimate analysis [dry%]

		C	H	N	S	O	Ash
Char I	*1	96.21	0.59	0.54	0.27	3.91	25.48
Char II	*2	71.66	1.03	0.61	0.01	0.34	26.35
Char III	*3	70.99	2.77	1.27	0.02	4.21	20.74
Coal	*4	66.9	5.4	1.4	0.1	13.2	13.0
Coke I	*5	94.0	1.3	0.7	2.7	-	1.3
Coke II	*5	89.2	2.1	1.5	2.9	4.1	0.2
Coke II'	*5	91.7	2.6	2.4	2.1	0.7	0.5
Coke III	*5	87.1	4.0	2.5	1.4	3.2	1.8
Carbon	*6	97.2	1.4	0.1	0.1	1.1	0.1

*1 Char I: produced from Liddell coal/Australia
*2 Char II: produced from Taiheiyo coal, pyrolysis temperature: 800°C
*3 Char III: produced from Taiheiyo coal, pyrolysis temparature: 600°C
*4 Coal: Taiheiyo coal
*5 Coke: originated from petroleum residue
*6 Carbon: activated carbon from petroleum residue

"NO" emission from char or coke, both of which contained less volatiles than coal is radically reduced as the stoichiometric ratio is reduced. This fact together with the reduced ammonia emission suggests that staged air firing may provide advantageous combustion modification for the control of "NOx" emission. This is discussed in the forth coming sections.

Figure 1(b) demonstrates the conversion ratio of fuel nitrogen to fuel NO of various carbonaceous materials. In this experiment the effect of thermal-NO was elimated by using AR/O_2 mixture instead of air. The level of NO emission under an excess air condition seemed to be considerably dependent on the volatile contents of fuel.

The fraction of fuel bond nitrogen which formed fuel-NO at $\lambda = 1.3$ is illustrated in Fig.2 where volatile contents were calculated on

ash and moisture free basis. This indicates that the conversion rate of fuel bond nitrogen to nitric oxide was reduced with the increased volatile contents.

Jonke et al.[3] reported that "NO" emission under a substoichiometric combustion of coal was increased at decreased temperature. This behavior was observed in Fig.1(a). Thus "NO" emission level from high volatile coal at elevated temperatures, approaches the level of "NO" emission from less volatile fuels at lower temperatures. This fact together with the decreased ammonia formation at elevated temperatures suggests also the efficient combustion modification for the reduction of "NO" emission.

Formation of nitrogenous compounds and staged combustion[4,5,6]

A series of experiments were carried out to investigate the influence of air staging. In this operation, the primary stage, which was a fluidized bed, was maintained at substoichiometric conditions while the balance of air, (the secondary air) was introduced through a nozzle into the freeboard. A significant reduction of "NO" emission by staged air firing can only be realized provided the emission of "NO" as well as other nitrogeneous compounds from the primary stage are significantly reduced. Thus the ammonia emission from coal and char are measured by the detector tube method. Typical results are shown in Fig. 3. Ammonia emission was not detected under an excess air condition. Under a substoichiometric condition, this could be reduced by elevating the combustion temperature, or reducing moisture, or volatile contents. In the case of char combustion, the ammonia emission under starving combustion at 850°C was approximately 1/7 of the "NO" emission under an excess air condition.

These results suggest that a significant reduction of "NO" emission can be achieved by a staged combustion of char. A preliminary experiment was carried out to evaluate the possibilities of staged air firing. Experimental results indicate that an approximately 90% reduction of "NO" emission was attained in the case of staged combustion of char where this was evaluated on the basis of an "NO" emission index obtained for conventional operations. However, the maximum level of "NO" reduction in this operation for coal remained at 33.5%.

Effect of in situ formed carbon on "NO" reduction[1,2,9]

Carbonaceous materials within the bed were reported to be effective in "NO" destruction. The steady state carbon concentration within the bed was measured. After terminating the feed of fuel solids, the amount of carbon dioxide and monoxide originating from the remaining carbon particles was measured by means of the gas bag method. The results obtained are compared with the level of "NO" emission in Fig. 4. These results indicate that "NO" emission was inversely related to the steady state carbon concentration. Furthermore, the steady state carbon concentration within the bed was found to be considerably small.

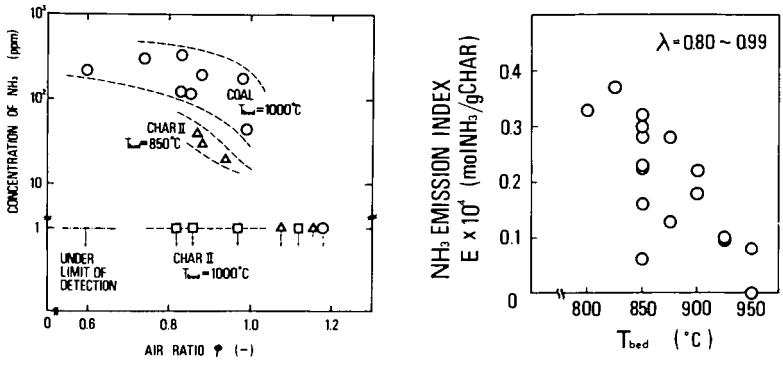

(a) (b)

Fig. 3 Emission of ammonia from combustion of coal and char

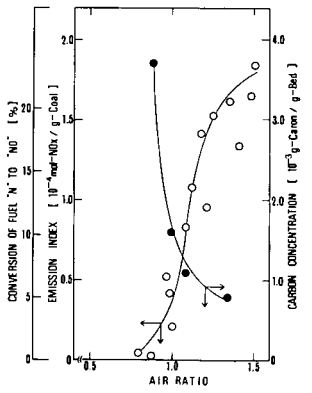

Fig. 4 NO emission decreased with the increase of steady state carbon concentration within the bed

Intrinsic Ratio of Fuel Nitrogen Conversion to Nitric Oxide

The significant magnitude of nitric oxide destruction by char or other reducing gas suggests that the concentration of nitric oxide measured at the top of the bed or freeboard did not reflect the intrinsic evolution level of nitric oxide from the combustion. Thus the measured value depended on the relative importance of the rate of "NO" formation reaction and the rate of "NO" reduction. The experimentally obtained concentration profiles along the height of the bed and freeboard may verify this mechanism. Information concerning the intrinsic evolution level of "NO" from char particles is required to describe the above process quantitatively. The response curve of "NO" formed within the combustor by the puls input char was measured so that the effect of the subsequent "NO" reduction by char or other reducing gas could be minimized. This is shown schematically in Fig. 5(a). The response peak of "NO" formed by the combustion with the reduced intensity of the input puls tends to a certain value from which the intrinsic ration of fuel nitrogen conversion to nitric oxide could be evaluated. Typical results are illustrated in Fig. 5(b). This value seems to be a little smaller than the value obtained by continuous combustion in a small experimental facility. This fact suggests that the emission level of nitric oxide is affected by the intensity of combustion, consequently the steady state carbon concentration within the bed. However, these results do not reduce the validity of the experimental results obtained by a small scale combustion facility concerning the behavior of nitric oxide emission.

II. KINETICS OF "NO" DESTRUCTION

Rate of "NO" reduction by char[7)]

An isothermal fixed bed tubular reactor of diluted char particles and activated carbon (char II, carbon in table 2) was used to measure the reaction rate over a temperature range which is of practical importance in fluidized bed combustion. Since the "NO" concentrations employed in the experiment were of the order of several hundred ppm, the amount of carbon could be assumed to be constant. The details were reported elsewhere.

The reduction of "NO" by char and activated carbon was first order with respect to "NO" concentration. Figure 6 represents the Arrhenius plot for char where alpha (α) denotes the ratio of the concentration of oxygen to the concentration of "NO" at the inlet. Thus the line coresponding to $\alpha=0$ indicates this rate.

At lower temperature ranges the activation energy for char was 16.3 kcal/mol and coincided with the data reported previously. Above 680°C the activation energy was 58.6 kcal/mol. The reason for the increase in the activation energy has not been explained. In the lower temperatures the desorption of carbon-oxygen surface complex was considered to control the overall rate. The gaseous reaction product was N_2, CO and CO_2. As the temperature was elevated, the fraction of CO in the reaction product increased.

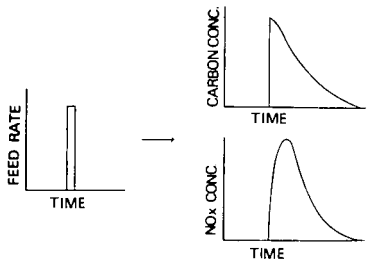

(a)

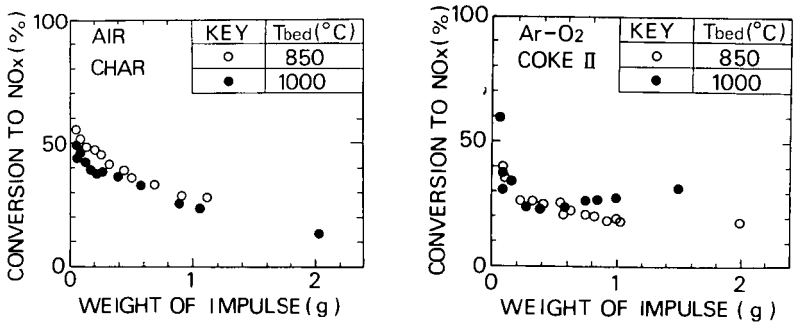

(b)

Fig. 5 Intrinsic conversion ratio of fuel nitrogen to nitric oxide

Rate of "NO" reduction by char under an excess air condition [10,11]

Kinetic information concerning whether or not "NO" can be reduced by char in the presence of oxygen is required in order to analyze the mechanism of "NO" destruction within the bed and freeboard. The use of a fixed bed of diluted char particles was restricted to a range of lower temperatures and lower oxygen concentrations since the char was consumed by combustion reaction. The rate of char combustion is approximately a hundred times faster than the "NO" reducton.

The "NO" destruction accompanied by oxidation of char was also assumed to be first order with respect to "NO" concentrations. This assumption was verified under low oxygen and "NO" concentrations. The results are shown in Fig. 6. The reaction was significantly accelerated by adding oxygen. An increased rate was also observed for "NO" destruction by activated carbon.

Over a range of higher temperatures the effects of the added oxygen on the rate could not be investigated since the carbon concentration

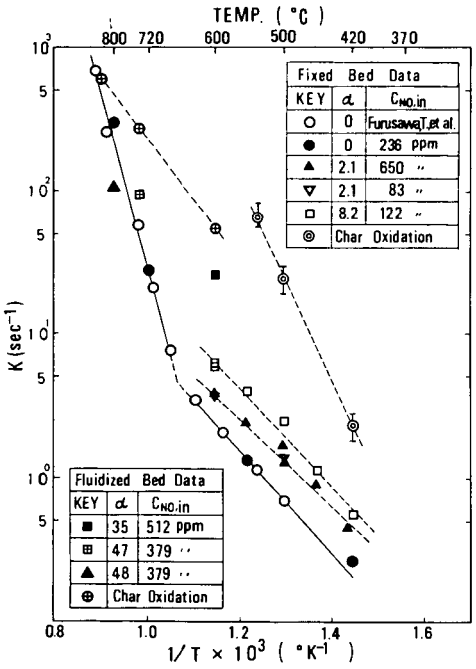

Fig. 6 Rate of NO reduction by char and the effect of oxygen on "NO" reduction

could not be assumed constant. Thus a fluidized bed reactor with a continuous feed and discharge of carbon (150mm height) was used to analyze the rate for higher oxygen concentration; namely, a large value of α and a higher temperature. Furthermore, the reduction of "NO" in a simulated combustion product containing CO_2 was studied. A remarkable result from these experiments is that a significant reduction of "NO" was realized even under an excess air condition in which oxygen remained in the outlet flow.

The simplified bubbling bed model by Kunii and Levenspiel was used to evaluate the reaction rate in the presence of oxygen. First, the effective bubble diameter was calculated as an adjustable parameter by curvefitting the experimental data obtained in the absence of oxygen to the curve calculated theoretically by the above model and the kinetic data shown previously. Then the increased rate in the presence of oxygen was evaluated by changing the rate, but by keeping the other parameter, including the effective bubble diameter, constant.

In this evaluation of the rate, the effect of fuel "NO" formed by the simultaneously occuring combustion of char was compensated for. The details are shown elsewhere. The estimated rate is shown in Fig. 5. An increased rate of "NO" reduction was observed in the presence of oxygen at both 600°C and 750°C. The rate was not significantly reduced by the presence of oxygen at 800°C. At 853°C the rate of "NO" destruction was reduced by coexisting oxygen. The extent of "NO" reduction by both char and activated carbon in both the absence and presence of oxygen was measured over a temperature range of 700 ∿ 900°C where the height of the bed was 150mm. The results together with the extent of oxygen consumption is shown in Fig. 7. The increased rate for char was verified up to approximately 750°C and that for the activated carbon up to 950°C.

Reduction of "NO" in the presence of carbon monoxide and hydrogen[8,12)]

The preliminary investigation concerning the reduction of nitric oxide by char in the presence of hydrogen or carbon monoxide was carried out over a temperature range of 700-800°C in a fixed bed reactor mentioned previously. The reaction was first order with respect to nitric oxide. Ammonia was formed in the nitric oxide hydrogen-char system. The presence of hydrogen and carbon monoxide decreased the consumption of carbon to nearly zero, as:

$$NO + CO \rightarrow CO_2 + \tfrac{1}{2} N_2 \quad (1)$$
$$NO + H_2 \rightarrow H_2O + \tfrac{1}{2} N_2 \quad (2)$$
$$NO + \tfrac{5}{2} H_2 \rightarrow NH_3 + H_2O \quad (3)$$

The rates and activation energies obtained for the above catalytic reactions for (1) or (2) + (3) agreed with the rate of noncatalytic reduction of nitric oxide by char within the experimental error. This strongly suggested that the activated adsorption of nitric oxide on the char surface controlled the overall rates. The ratio of ammonia formed by reaction (3) to the consumed nitric oxide which is found to be constant at each temperature is decreased with an increased temperature.

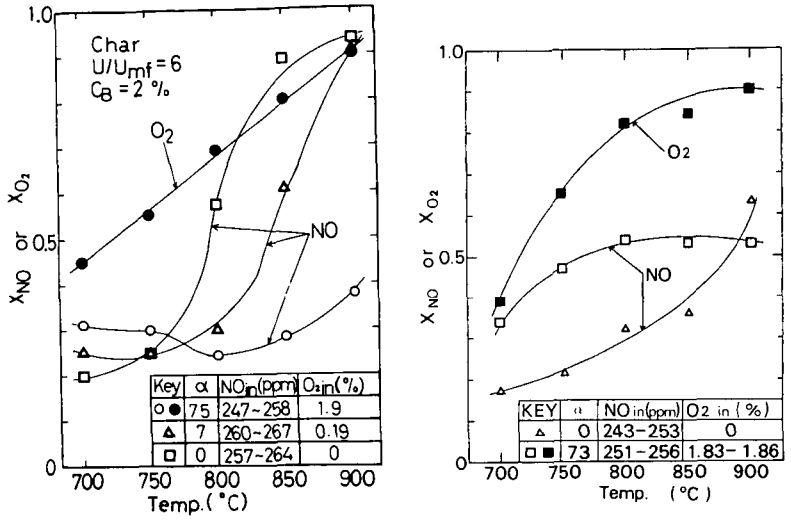

(a) Char (b) Carbon

Fig. 7 Increased extent of "NO" reduction caused by oxygen

Concluding Remarks

This paper descirbed the recent findings concerning the behavior of "NOx" formation in a fluidized bed combustor obtained by use of a variety of carbonaceous materials. The "NO" emission under an excess air condition was decreased with an increase in the volatile contents of fuels. The emission of "NO" and other nitrogeneous contents formed under a substoichiometric combustion was also strongly dependent on the volatile contents. The staged combustion of less volatile char and coke provided a radical reduction of "NO" emission. The steady state carbon concentration was measured and "NO" emission was found to be inversely related to the carbon concentration. The intrinsic conversion ratio of fuel nitrogen to "NO" was measured. The kinetics of "NO" destruction by char in both the absence and presence of oxygen was investigated. The rate for char was increased up to 750°C. "NO" was reduced catalytically by carbon monoxide and hydrogen over a char surface, but the rate was not increased.

Acknowledgement

D. K. whishes to express his thanks to Grant-in-Aid for Energy Research (NO 311604, NO 411003 & NO 505021) of the Ministry of Education. T.F. received Grant-in-Aid for Scientific Research (NO 455363 & NO 555374) from the same body. The experimental assistance by Mr. A. Kato was

greatly acknowledged.

Literature Cited

1) Beér, J.M., A.F. Sarofim, L. Chan & A. Sprouce: Proceedings of the 5th Int. Conference on Fluidized Bed Combustion, p577 - p592 (1977)
2) Beér, J.M., A.F. Sarofim & Y.Y. Lee, Proceedings of the 6th Int. Conference on Fluidized Bed Combustion, p942 - p955 (1980)
3) Jonke, A.A., G.J. Vogel, E.L. Carls et al.: Chem. Eng. Prog. Symp. Series 68, NO 126, 241 (1972)
4) Furusawa, T., T. Honda, J. Takano and D. Kunii: J. of Chem. Eng. Japan 11, 377 (1978)
5) Furusawa, T., N. Yamada, T. Sendo and D. Kunii: J. of Chem. Eng. Japan 12, 71 (1979)
6) Furusawa, T., T. Honda, J. Takano and D. Kunii: Fluidization, Proceedings of 2nd Eng. Found. Conf., Cambridge University Press (1978)
7) Furusawa, T., D. Kunii, N. Yamada and A. Oguma: Int. Chem. Eng. 20, 239 (1980) or Kagaku Kogaku Ronbunshu 4, 562 (1978)
8) Furusawa, T., D. Kunii and T. Tsunoda: under preparation
9) Gibbs, B.M., F.J. Pereira and J.M. Beér: 16th Symposium on Combustion, Cambridge, 461 (1976)
10) Kunii, D., K.T. Wu and T. Furusawa: Chem. Eng. Sci. 35, 170 (1980)
11) Kunii, D., T. Furusawa and K.T. Wu: ed. J.R. Grace and J.M. Matsen, Fluidization, Plenum Publishing Corp. New York, p175 - p183 (1980)
12) Cowley, L.T. and P.T. Roberts: Paper submitted for presentation at the Fluidized Combustion Conference, 28-30th Jan. (1981) held at the Energy Research Institute, University of Cape Town, South Africa

REDUCTION OF NITRIC OXIDE BY CARBONACEOUS SOLIDS IN AN ATMOSPHERIC PRESSURE FLUIDIZED-BED REACTOR

By

Z. Huang,[1] G. T. Chen,[1] and C. Y. Wen[2]
Department of Chemical Engineering
West Virginia University
Morgantown, WV 26506

J. Y. Shang,[3] J. S. Mei,[4] and J. E. Notestein[5]
Technology Development and Engineering Division
U.S. Department of Energy
Morgantown Energy Technology Center
Morgantown, WV 26505

Abstract

The fluidized-bed combustion process, due to its ability to control pollutant emissions and its inherent capability to accommodate a wide variety of fuels, has been the subject of accelerating development for industrial and utility applications. However, fluidized-bed combustion boilers based on the current design and operation may not be able to meet the future stringent standards on nitrogen oxides emissions without additional provisions. In this paper, a preliminary study on the reduction reactions of nitric oxide with three different carbonaceous solids using a 9.6-centimeter diameter, electrically heated, batch fluidized-bed reactor operated at various design and operating conditions is discussed. Results of this investigation indicates that the NO reduction reaction appears to be dependent upon not only the operating variables such as bed temperature, carbonaceous solid loading in the bed, but also on the physical properties of the carbonaceous solids as well. Prediction of NO reduction by one of the carbonaceous solids using a two-phase bubble model shows good agreement with experimental data within the range of experimental conditions.

Introduction

Among the various techniques for direct conversion of the chemical energy in coal to thermal energy, the fluidized-bed combustion (FBC) process appears to be one of the most attractive means due to its inherent features. The higher heat capacity of the solid bed material leads to good combustion stability which, consequently, permits use of essentially all fossil fuels including low-grade fuels high in ash and/or moisture content and low in heating value, such as coal refuses, peat, oil shales, etc. The use of a sulfur-accepting sorbent affords in situ capture of the sulfur dioxide evolving from the burning of sulfur-bearing fuels. Bed temperature is maintained sufficiently low and, thus, results in relatively low emissions of nitrogen oxides and less slagging and fouling problems than in conventional coal-fired boilers. Lastly, the presence of vigorous particle mixing in the fluidized bed provides higher bed-to-surface heat transfer rates which results in less heat exchange surface relative to conventional coal-fired boilers. As a consequence, fluidized-bed combustion boilers fueled by coals and low-grade fuels have been the subject of accelerating developments for industrial and utility applications both in the U.S. and abroad. In recent years a number of fluidized-bed boilers have been

[1]Visiting scholars from People's Republic of China.
[2]Benedum Professor.
[3]Division Deputy Director.
[4]Mechanical Engineer.
[5]Division Director.

constructed and operated to demonstrate a variety of industrial and utility applications and process reliability; for example[1,2,3] the commercial prototype fluidized-bed boiler at Georgetown University, the industrial application of a fluidized-bed boiler at Great Lakes Naval Training Station, and the prototype anthracite culm fluidized-bed combustion boiler at the industrial park in Shamokin, PA. In addition, a 20 MWe fluidized-bed boiler pilot plant is currently under construction by TVA for the utility application[3].

At present, the EPA nitrogen oxides emission standard is 0.6 lb NO_2/million Btu input; most of the fluidized-bed combustion boilers, which are based on the current design and operation principles, can meet the standard without additional efforts. However, it is anticipated that nitrogen oxides emission standard may become more stringent in the future. The fluidized-bed boilers using the current design and operation principles may not be able to meet the stringent standards for NO_x emissions without additional provisions. It is, therefore, the objective of this project to investigate and determine the pertinent design and operational variables which affect NO_x emissions from fluidized-bed combustion boilers. Results of this investigation may enable further insight to be gained into the mechanism of NO_x destruction in the bed and provide design and operational information for the future development of low-NO_x fluidized-bed combustion boilers to meet the anticipated stringent EPA nitrogen oxides emission standards.

Experimental Facility

Experiments on nitrogen oxides reduction were conducted using an electrically heated, laboratory-scale, fluidized-bed reactor, which is shown schematically in Figure 1. This laboratory-scale batch fluidized-bed reactor consists of a 9.6-cm diameter, 47 cm tall, stainless steel cylindrical vessel. The lower section of the vessel is surrounded by a 20-cm tall, 1.36 KW electric heater, such that the bed can be heated to about 1000°C. The stainless steel cylindrical vessel is also heavily insulated with Fiberfrax. The bed is supported on a 6.35 mm thick stainless steel perforated gas distributor with fifty-six (56), 0.8-mm diameter orifices.

Bed temperature was regulated and controlled by a transformer. Reaction temperature was measured by a chromel-alumel thermocouple with a Hastalloy sheath of 3.175 mm diameter. Readings were displayed in degrees on a digital thermometer. The thermocouple was suspended at a point which was 5 cm from the distributor; the axial temperature distribution in the bed and freeboard was measured by moving the thermocouple.

Temperature recordings in the bed above 2.5 cm from the distributor indicated that the bed temperatures were essentially uniform. However, a temperature gradient of approximately 18°C/cm was observed in the freeboard section of the reactor. The bed was fluidized by pure nitrogen gas; carbon monoxide, methane, and nitric oxide could also be introduced into the fluidizing gas stream in controlled amounts. All gas flow rates were measured by rotameters. Exit gas composition was continuously monitored by preset gas analyzers as shown below:

Compound	Principle of Operation	Instrument[1]
NO	Chemiluminescence	Thermo-Electron, Series 10
CO	IR	MSA-LIRA, Model 303
CO_2	IR	MSA-LIRA, Model 303
O_2	Paramagnetic	Leeds and Northrup
Total HC	Flame Ionization	Beckman, Model 400

[1]The use of brand names is for the identification purposes only and does not constitute endorsement by the Department of Energy.

The analyzed flue gas concentrations were registered on a six-channel strip chart recorder.

Materials Used for the Experiments, Chars and Coke

Nitric oxide reduction experiments were conducted using two different chars and a coke. Char 1 was produced from Wyoming sub-bituminous coal by Occidental Research Corporation's (OCR) Flash Pyrolysis process, with BET (Brunauer-Emmett-Teller) surface area of 290 m^2/g, a size range of 30 x 70 mesh, and a density of 2.010 g/cm^3. Its chemical composition is listed in Table 1. Char 2 was made in situ from Pittswick bituminous coal (8 x 12 mesh in size). The Pittswick coal was fed a little at a time into the bed where sand was fluidized and heated to a temperature of 850°C by the preheated nitrogen gas to prevent the coal from clinkering. The coal was then pyrolyzed in a nitrogen atmosphere for half an hour to produce Char 2. The chemical composition of Char 2 and its parent coal are also listed in Table 1. Char 2 had a BET surface area of 2.4683 m^2/g and a density of 2.288 g/cm^3. It is important to note that the analytical data for Char 2 on a weight basis, such as its chemical composition and surface area, are not as precise as desired because the char samples contained a certain amount of sand which could not be completely separated from the char before analysis.

Metallurgic coke, obtained from Mercury Coal and Coke, Inc., near Morgantown, was also used in these tests. It was ground and screened to obtain coke particles of 12 to 20 mesh size. The coke particles were then fluidized with nitrogen in the hot fluidized bed at 900°C for one hour. After the material was cooled, the test feedstock coke was obtained. The BET surface area of this coke was 0.8668 m^2/g and its density was 2.067 g/cm^3. Its chemical composition is listed in Table 1.

Bed Material

Glass sand with a mean particle diameter of 0.286 mm was used as the bed material. The size distribution of the sand is listed in Table 2. The BET surface area was 0.846 m^2/g and its density was 2.664 g/cm^3.

The minimum fluidization velocity of the sand was determined experimentally at elevated temperature. A pressure drop versus gas velocity is plotted in Figure 2. As can be seen, the minimum fluidization velocity is approximately 5.5 cm/sec at a bed temperature of 822°C.

Experimental Procedure

The experimental procedures for NO reduction by Char 1 and by metallurgic coke were precisely the same. First, the reactor containing 1164 g of sand was heated while the sand was simultaneously fluidized with preheated nitrogen. When the desired reaction temperature was reached, the fluidizing gas was turned off and a feed hopper with a long dipleg was inserted rapidly into the reactor through a stopcock in the feedline on top of the reactor. A weighed amount of char (or coke) was then poured into the hopper from which it dropped onto the hot sand. The hopper was then removed, the cock closed, and the nitrogen switch was turned on immediately such that the char was distributed evenly throughout the bed. When the bed temperature had restabilized at the desired level, a measured flow of nitric oxide was admitted. The concentrations of each component in the exit gas were continuously monitored and recorded on a six-channel strip chart recorder.

In order to reach the required steady-state conditions in a short duration of time, the experiments to determine NO reduction capability of Char 1 and coke were conducted in sequence from low temperature (600°C) to high temperature (850°C) at the same carbon loading.

The experimental procedure for the reduction of nitric oxide by Char 2 was similar to the procedure for Char 1 and metallurgic coke as described above, except that the tests were carried out in a temperature sequence from 850°C (highest) to lower temperatures, since Char 2 was produced "in situ" under a nitrogen atmosphere at 850°C which was the highest chosen reaction temperature for an experiment.

Experimental Results and Discussion

Experiments on the reduction of NO by carbonaceous solids were carried out at various operating conditions. Results of these experiments and their corresponding operating conditions are presented in Tables 3, 4, and 5 for Char 1, Char 2, and metallurgic coke respectively. A discussion of these data is presented below.

Effect of Char Surface Area and Porosity on Nitric Oxide Reduction

Experimental results of NO reduction by a batch of carbonaceous solids in the absence of oxygen were plotted in Figure 3 at identical operating conditions. Results shown in Figure 3 indicate that heterogeneous reduction of NO by Char 1 and Char 2 are significantly higher than that achieved with metallurgic coke. The reactivities of the three carbonaceous solids are compared in Table 6. Differences in the reduction of NO by these carbonaceous solids may be attributed to the differences in physical properties, such as specific surface area and porosity. Char 1, which gives the highest NO reduction, poses the highest specific surface area, although its carbon content is less than the metallurgic coke. Scanning Electron Microscope (SEM) porosity measurement also indicates that Char 1 exhibits the highest porosity. As can be seen in Figure 4, micropores with size ranging from 100 μm to 0.3 μm cover nearly 100 percent of its surface. Although the metallurgic coke has the highest carbon content among the three tested carbonaceous solids, its specific surface area is the smallest. The coke also has comparatively smaller pores which range in size from 10 μm to 1.5 μm and cover only about 1 percent of its surface as can be seen in Figure 5. Figure 6 shows the porosity measurement of Char 2, which has pore sizes ranging from 40 μm to 1 μm and covering 45 percent of its surface. A comparison of the data presented in Table 6 and the porosity measurements given by SEM indicates that the low NO conversion rate achieved by metallurgic coke may be attributed to its small BET surface area as well as its low porosity. Interpretation of these data suggests that internal diffusion may also play an important role in determining the overall reaction rate of a large porous solid particle, which has relatively low porosity and small BET surface area, with a reactant gas.

Effect of Bed Temperature in Nitric Oxide Reduction by Chars

The reduction reaction between NO and char was found to be strongly influenced by operating bed temperature. Figures 7 and 8 show the effect of bed temperature on NO reduction by Char 1 and Char 2. As can be seen, nitric oxide concentration in the exit gas decrease with increasing bed temperature of both Char 1 and Char 2. Within the range of operating conditions, NO reductions of 90 percent or better were attainable provided that the bed temperature was maintained at or above 800°C. As the bed temperature was raised further, NO outlet concentration decreased continuously, but at a decreasing rate. However, thermodynamic calculations indicated that at a temperature or 900°C, equilibrium concentrations of thermal NO may reach 500 ppm for a mixture of 2 percent oxygen and 75 percent nitrogen[4]. In view of the current practice in design and operation of fluidized-bed combustion boilers, the use of excess oxygen at higher bed temperatures may promote the formation of thermal NO. The higher bed temperature is also unfavorable to the sulfation reaction of natural sorbents in the atmospheric pressure fluidized bed. Therefore, an optimum temperature range for NO_x and SO_2 emission control appears to be 800° to 850°C.

Effect of Char Loading on Nitric Oxide Reduction

The effect of char loading in the fluidized bed on NO reduction by char is illustrated in Figure 9. As can be seen, the reduction of NO increases with increase in char loading. At bed temperature of 750°C, the effect of char loading is most important around 1 percent where it results in a NO reduction of 87 percent. At higher char loading, the reduction of NO is generally higher; however, the effect of the char loading becomes less significant. The same trend can also be observed at the temperature range below 750°C, even though the reduction of NO falls below 60 percent due to the strong temperature dependence of the reduction reaction. Higher char loading in the bed may increase the chances of clinker formation which is caused by local temperature excursion as a consequence of the poor solid mixing and the inability to dissipate the heat of combustion. In addition, the loss of unburnt carbon in the drained spent-bed material may become unacceptable if the char loading in the bed becomes too high. However, recent developments in fluidized-bed combustion technology have indicated that two-stage combustion systems with the increased char loading in the first stage enhances the overall reduction of nitric oxide emission significantly[5].

Prediction of NO Reduction by Char 1

Recent experimental studies[6] on the reduction reaction of nitric oxide with char have concluded that the reaction is first order with respect to the NO concentration. This practice is, hence, adopted in the present study. The reaction rate constants of the reaction of NO with Char 1 at the corresponding temperatures and char loadings were calculated based on the experimental data presented at Table 3. The activation energy and the frequency factor within the range of operating conditions are 31.7 kcal/mol and 9.66×10^8 sec^{-1} respectively. The rate constants of NO-char plotted as a function of inverse temperatures for several experimental studies[7] are compared with the present results in Figure 10. As can be seen, the reaction rate constants obtained from the present experiment show good agreement with previous investigations. The NO-char reaction kinetics can be represented by the following correlation and this was employed in the NO emission modeling. In view of the low

$$k = 9.66 \times 10^8 \exp\left(-\frac{31,700}{RT}\right) sec^{-1} ,$$

superficial velocity, the shallow bed, and relatively small bed diameter, a two-phase bubble model[8] with both the bubble and emulsion phases treated as plug flow was employed for the prediction of NO conversion. The NO reduction by Char 1 was calculated using this approach over the range of experimental conditions. The comparison of calculated versus test data values may be observed in Table 3, as well as Figure 7. As can be seen in Figure 7, the calculated values for NO reduction show excellent agreement with experimental data.

Conclusions

Tests to determine the NO reduction capability of two different chars and a metallurgic coke were conducted in an electrically heated, batch, fluidized-bed reactor in the absence of oxygen. Based on the experimental results, the following conclusions can be drawn.

- Reduction of nitric oxide depends strongly on the physical properties of the carbonaceous solids such as specific surface area and pore size distribution; and, to a lesser extent, on the carbon content.

- Reduction reaction between NO and carbonaceous solids was found to be strongly influenced by bed temperature. Within the range of operating conditions, the degree of NO reduction increases with bed temperature. However, the formation of thermal NO and the unfavorable sulfation reaction for natural sorbents in an

atmospheric pressure fluidized bed at higher temperature posts an upper limit on temperature range for NO_x and SO_x emission control. A preferred operating temperature range from this standpoint appears to be 800°-850°C.

- o NO reduction by char increases with char loading in the bed. With 1 percent of char loading in the bed, 90 percent or better NO reduction is attainable for both Char 1 and Char 2 provided that bed temperature is maintained at or above 800°C.

- o Reaction rate constants based on the present experimental data show good agreement with the previous investigations. The rate constant can be represented by the following correlation:

$$k = 9.66 \times 10^8 \exp\left(-\frac{31,700}{RT}\right) \text{ sec}^{-1}$$

- o Prediction of nitric oxide reduction by Char 1 using a two-phase bubble model gives good agreement with the experimental data within the range of experimental conditions.

References

1. Proceedings of the Fifth International Conference on Fluidized-Bed Combustion, Washington, DC, December 1977.

2. Proceedings of DOE/WVU Conference on Fluidized-Bed Combustion System Design and Operation, Morgantown, WV, October 1980.

3. The proceedings of the Sixth International Conference on Fluidized-Bed Combustion, Atlanta, Georgia, August 1980.

4. Pereira, F. J. M. A., "Nitric Oxide Emission from Fluidized Coal Combustion," Ph.D. Thesis, University of Sheffield, 1975.

5. Gibbs, B. M., F. J. Pereira, and J. M. Béer, "The Influence of Air Staging on the NO Emission from a Fluidized-Bed Coal Combustor," Paper Presented at 16th Symposium (International) on Combustion, The Combustion Institute, Pittsburgh, PA, 461, 1977.

6. Béer, J. M., A. F. Sarofim, S. S. Sandhu, M. Andrei, D. Bachovchin, L. K. Chan, T. Z. Chang, and A. M. Sprouse, "NO_x Emissions from Fluidized Coal Combustion," EPA Grand No. R804978020 Report, 1979.

7. Furusawa, T., D. Kunii, A. Oguma, and N. Yamada, "Kinetic Study of Nitric Oxide Reduction by Carbonaceous Materials," Kagaku Kogaku Rombunshu, 4 (6), 562 (1978).

8. Davidson, J. F. and D. Harrison, "Fluidized Particles," Cambridge University Press., 1963.

3:sw:515f

TABLE 1

Chemical Analysis of Carbonaceous Solids

	Char 1	Char 2	Pittswick Bituminous Coal	Metallurgic Coke
Ultimate Analysis, Wt %				
Moisture	2.09	0.63	1.35	0.09
Ash	16.79	60.05	14.15	10.07
Sulfur	0.83	1.64	3.85	0.83
Hydrogen	1.35	0.40	5.04	0.53
Nitrogen	0.96	0.66	0.98	0.84
Total Carbon	75.24	37.90	69.10	87.40
Oxygen (by difference)	2.74	1.28	5.53	0.23
Elemental Analysis, Wt %				
Silicon, SiO_2	35.06	84.51	49.16	44.19
Aluminum, Al_2O_3	16.91	7.62	23.66	19.34
Iron, Fe_2O_3	14.84	5.38	17.72	17.76
Calcium, CaO	11.32	0.49	1.55	5.75
Magnesium, MgO	4.48	0.01	0.85	0.98
Sodium, Na_2O	--	--	1.23	2.20
Potassium, K_2O	0.70	0.62	2.59	1.53
Phosphorus, P_2O_5	0.73	0.05	0.05	0.32
Titanium, TiO_2	0.85	0.34	1.21	1.21
Sulfur, SO_3	6.50	1.63	1.72	4.06

TABLE 2

Screen Analysis of Sand

Size Range, mm	Wt %
-0.589 + 0.419	2.2
-0.419 + 0.249	72.7
-0.249 + 0.179	18.9
-0.179 + 0.150	4.2
-0.150	1.0

Mean Diameter, d_p = 0.286 mm

TABLE 3

Experimental Results of NO Reduction by Char 1

Run No.	Char g	Char Wt %	Sand g	T °C	NO_{in} ppm	NO_{out} ppm	N_2 M^3/hr	U_{mf} cm/S	U cm/S	L_{mf} cm	L_f cm	ϵ_{mf}	$\left(\frac{NO_{out}}{NO_{in}}\right)$ exp.	$\left(\frac{NO_{out}}{NO_{in}}\right)$ cal.	k 1/sec
5-28-1	12	0.01031	1164	600	965	745	0.85	5.5	10.6	10	12.065	0.42	0.772	0.837	15.477
5-28-2	12	0.01031	1164	650	965	615	0.85	5.5	11.2	10	12.065	0.42	0.637	0.637	28.622
5-28-3	12	0.01031	1164	700	965	360	0.85	5.5	11.8	10	12.065	0.42	0.373	0.360	67.269
5-28-4	12	0.01031	1164	750	965	125	0.85	5.5	12.4	10	12.065	0.42	0.130	0.128	155.295
5-28-5	12	0.01031	1164	800	965	25	0.85	5.5	13.0	10	12.065	0.42	0.026	0.030	341.263
6-5-1	24	0.02062	1164	600	980	660	0.85	5.5	10.6	10	12.065	0.42	0.673	0.701	11.842
6-5-2	24	0.02062	1164	650	980	390	0.85	5.5	11.2	10	12.065	0.42	0.397	0.409	29.532
6-5-3	24	0.02062	1164	700	980	150	0.85	5.5	11.8	10	12.065	0.42	0.153	0.137	65.746
6-5-4	24	0.02062	1164	750	980	10	0.85	5.5	12.4	10	12.065	0.42	0.010	0.023	199.890
6-8-1	36	0.03093	1164	600	975	580	0.85	5.5	10.6	10	12.065	0.42	0.595	0.588	10.389
6-8-2	36	0.03093	1164	650	975	300	0.85	5.5	11.2	10	12.065	0.42	0.308	0.264	25.311
6-8-3	36	0.03093	1164	700	975	60	0.85	5.5	11.8	10	12.065	0.42	0.062	0.055	67.035
6-9-1	48	0.04124	1164	600	985	475	0.85	5.5	10.6	10	12.065	0.42	0.482	0.494	10.969
6-9-2	48	0.04124	1164	643	985	215	0.85	5.5	--	--	--	--	0.218	--	--

TABLE 4

Experimental Results of NO Reduction by Char 2

Run No.	Char* g	Sand g	T °C	NO_{in} ppm	NO_{out} ppm	N_2 M^3/hr	U cm/S	U_{mf} cm/S	$\frac{NO_{out}}{NO_{in}}$
6-1-7	12.85	1164	850	955	0	0.85	13.6	5.5	0
6-1-8	12.85	1164	800	955	75	0.85	13.0	5.5	0.079
6-1-9	12.85	1164	750	955	250	0.85	12.4	5.5	0.262
6-1-10	12.85	1164	700	955	525	0.85	11.8	5.5	0.550
6-1-11	12.85	1164	650	955	700	0.85	11.2	5.5	0.733
6-1-12	12.85	1164	600	955	790	0.85	10.6	5.5	0.827
6-3-1	25.7	1164	850	940	30	0.85	13.6	5.5	0.032
6-3-2	25.7	1164	800	940	62	0.85	13.0	5.5	0.066
6-3-3	25.7	1164	750	940	165	0.85	12.4	5.5	0.176
6-3-4	25.7	1164	700	940	490	0.85	11.8	5.5	0.521
6-3-5	25.7	1164	650	940	665	0.85	11.2	5.5	0.707
6-3-6	25.7	1164	600	940	760	0.85	10.6	5.5	0.809

*Calculated values based on the assumption that volatiles in the coal escaped during char formation.

TABLE 5

Experimental Results of NO Reduction by Metallurgic Coke

Run No.	Coke g	Sand g	T °C	NO_{in} ppm	NO_{out} ppm	N_2 M^3/hr	U cm/S	U_{mf} cm/S	$\frac{NO_{out}}{NO_{in}}$
6-3-7	24	1164	700	940	900	0.85	11.8	5.5	0.957
6-3-8	24	1164	750	940	855	0.85	12.4	5.5	0.910
6-3-9	24	1164	800	940	770	0.85	13.0	5.5	0.819
6-3-10	24	1164	850	940	620	0.85	13.6	5.5	0.660

TABLE 6

Comparison of Reactivity for Different Carbonaceous Solids

	Size Mesh	BET Surface Area m^2/g	Char g	Bed Material (Sand) g	N_2 M^3/hr	T °C	NO_{in} ppm	NO_{out} ppm	Reactivity $\frac{\text{Mole-of-NO-Reduced}}{\text{g-of-char} \cdot \text{hr}}$
Char 1	30 x 70	290	24	1164	0.85	700	980	150	1.31×10^{-3}
Char 2	8 x 12	2.4683	25.7	1164	0.85	700	940	490	6.64×10^{-4}
Coke	12 x 20	0.9	24	1164	0.85	700	940	900	6.32×10^{-5}

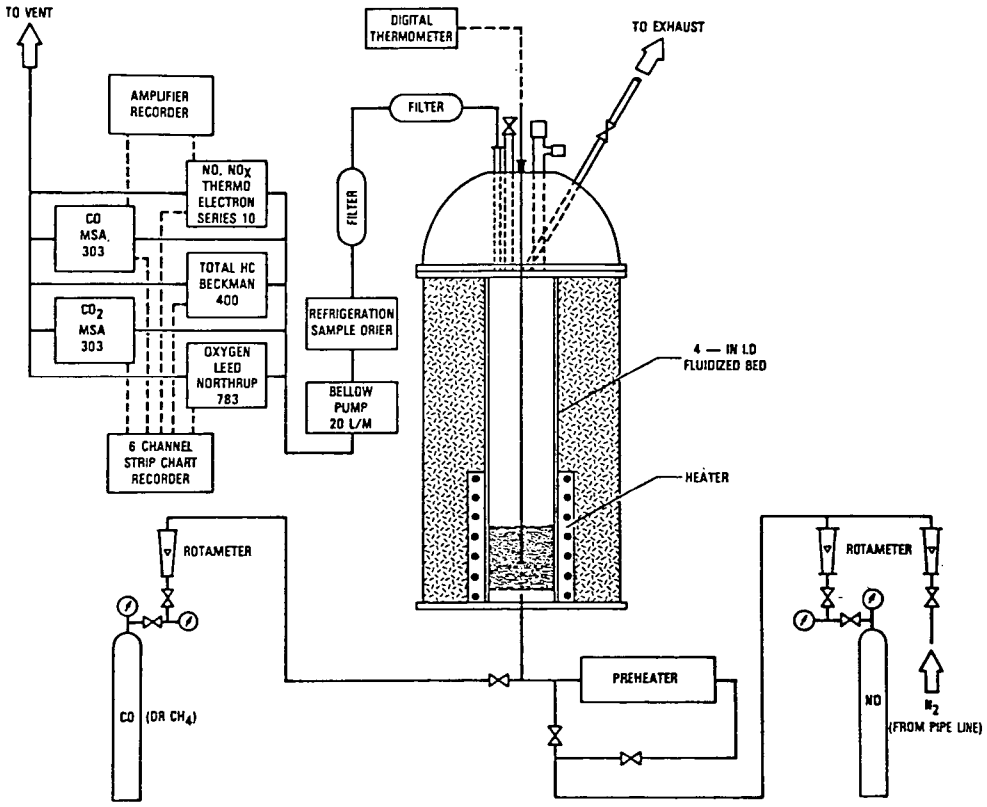

FIGURE 1 — SCHEMATIC DIAGRAM OF EXPERIMENTAL APPARATUS

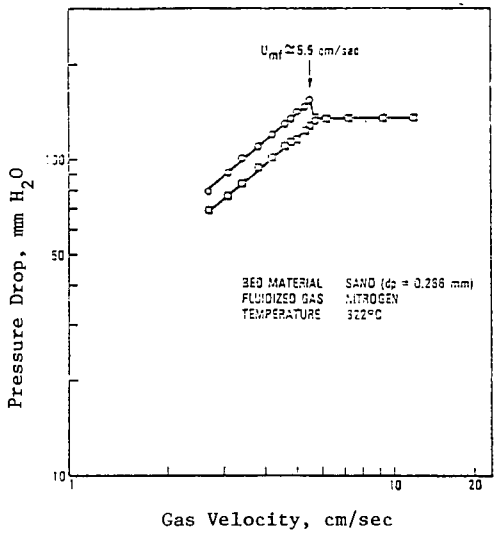

FIGURE 2. Pressure Drop Versus Gas Velocity

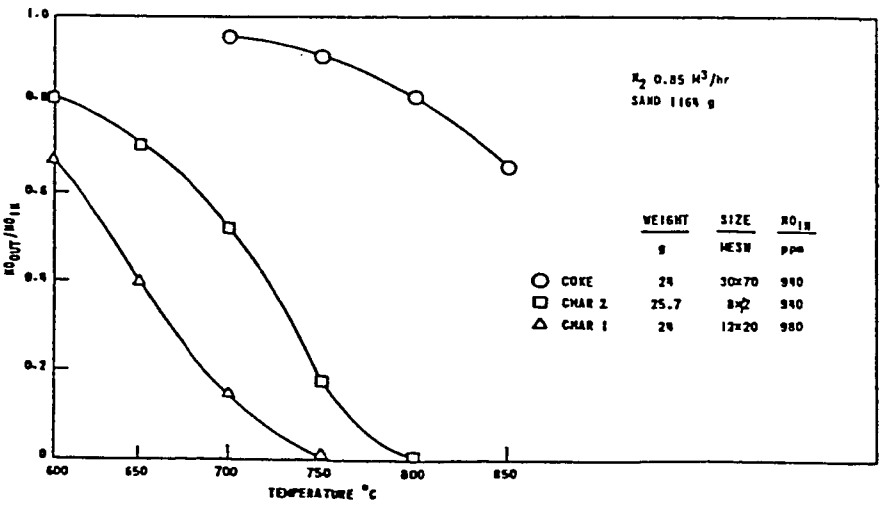

FIGURE 3. Comparison of NO Reduction by Different Carbonaceous Solids

FIGURE 4
IMAGE OF SEM POROSITY MEASUREMENT OF CHAR 1

FIGURE 5
IMAGE OF SEM POROSITY MEASUREMENT OF METALLURGIC COKE

FIGURE 6
IMAGE OF SEM POROSITY MEASUREMENT OF CHAR 2

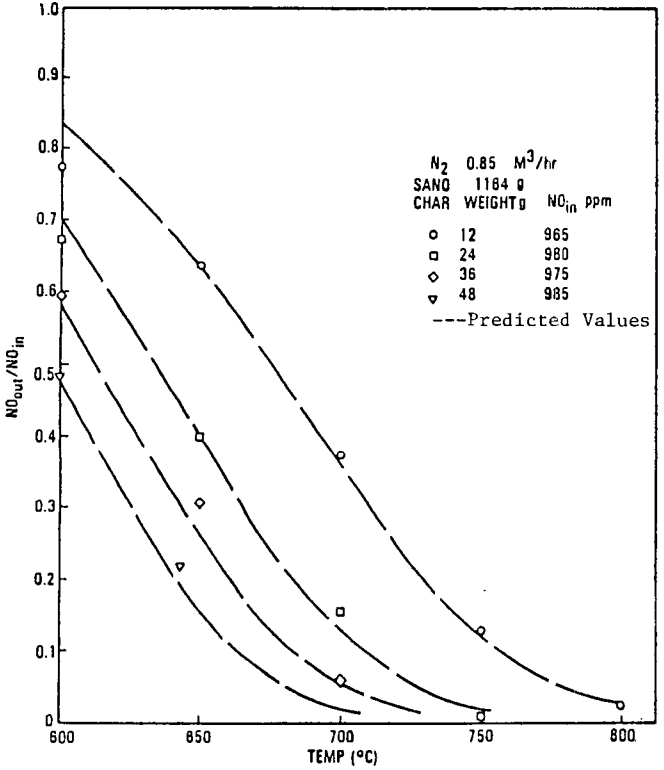

FIGURE 7. Temperature Effect on Reduction of NO by Char 1

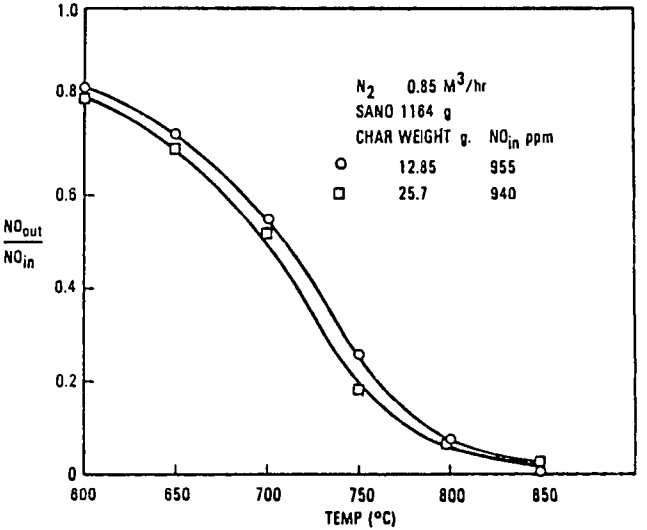

FIGURE 8. Temperature Effect on Reduction of NO by Char 2

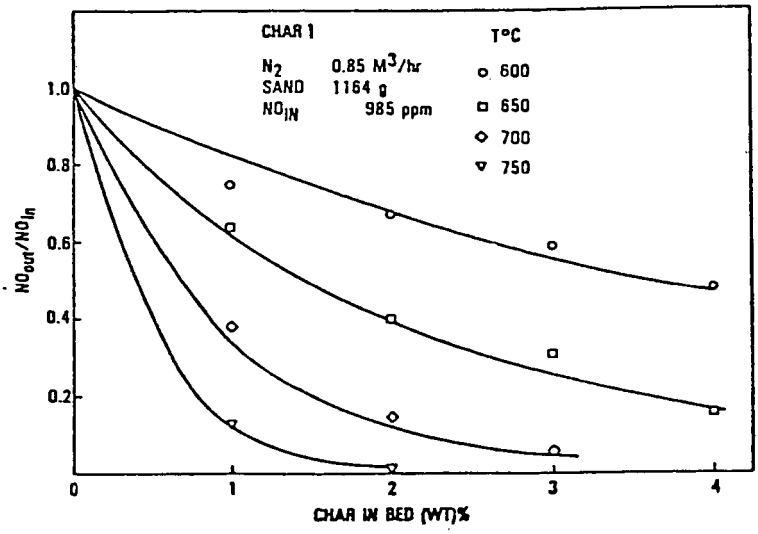

FIGURE 9. Effect of Char Loading on NO Reduction

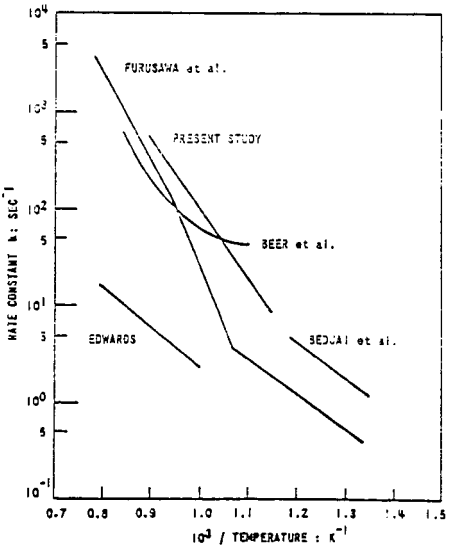

FIGURE 10. Comparison of Rate Constants for NO Reduction by Char

The effect of coal particle size on the performance of a fluidised bed coal combustor

by

M. Brikci-Nigassa, E.S. Garbett and A.B. Hedley

Sheffield Coal Research Unit, Department of Chemical Engineering and Fuel Technology, University of Sheffield Sheffield S1 3JD, United Kingdom.

Introduction

The technology of fluidised bed coal combustion (FBC) and its advantages over conventional coal burning systems is now well established and is extensively reported in the literature (1,2,3,4). A common way of introducing coal to the bed is via coal feed points in the distributor plate and for this method it is usual to use crushed coal of particles less then 6 mm. Problems associated with this method include the determination of the correct number and spacing of feed points, blockages and the obvious expense in coal preparation. Crushed coal is used because it was thought necessary to keep the coal particle sizes approximately equal to those making up the bulk of bed and so maintain good fluidisation characteristics. However, Highley et al. (5) showed that large coal particles (< 50 mm) could be burnt quite easily in an FBC whilst at the same time overcoming the coal feed problems outlined above by overbed feeding. Also, using uncrushed coal allows the bed and freeboard heights to be reduced (5) making obvious savings in capital and running costs. An increase in the size of coal particle fed to the combustor results in an increase in the bed carbon loading (6) which influence such important phenomena as NO emissions and elutriation (7). However, there is little information on the effect on the performance of an FBC due to a variation of particle size in the coal feed. This paper therefore, reports a study of the combustion of monosized coal fractions fed continuously to the bed via an overbed feeder. Data showing the effect of coal size, excess air and combustion efficiency are presented. Measurements using crushed coal (< 1.5 mm) fed pneumatically to the bed are included for comparison.

2. Experimental procedure

The fluidised bed combustor shown schematically in Fig. 1, was 0.3 m square section and 1.83 m high and constructed from stainless steel, the walls being insulated with kaowool. The bed which was 0.6 m deep, consisted of sand of mean particle size 600 μm. Fluidising air was introduced to the bed through a bubble cap distributor plate. Crushed coal (< 1.5 mm) was fed pneumatically into the bed from a sealed hopper via a calibrated rotary valve feeder (Fig. 1). Large coal (N.C.B. 501) previously sieved to give monosized fractions (6.3, 9.5 and 12.5 mm) was fed by a vibratory feeder from a pressurised hopper to the surface of the bed. A vibratory feeding system was adopted after degradation of the coal feed occurred when a screw feeder was initially used. The large coal passed over two grids which allowed any fines present to fall through. Start up of the bed was achieved using an overbed gas burner which preheated the bed to 725 K before coal was injected. Particulate carry over in the gaseous combustion products was removed by a two-stage cyclone. Solids separated by the cyclones dropped into catchpots (Fig. 1). In order to measure the rate of elutriation of material during steady-state combustion, the carry over from the combustor was diverted into a seperate catchpot. The temperature of the bed was controlled by a cooling coil immersed in the bed. Thermocouples were located in three positions in the bed: top, middle and bottom and also in the freeboard (Fig. 1). All bed and freeboard temperatures and the cooling water temperature were recorded continuously on chart recorders.

During all the experimental runs the fluidising velocity was kept constant ($\sim 0.8\ ms^{-1}$) and changes in stoichiometry were achieved by varying the coal feed rate to the combustor. Gas samples were obtained from the bed, freeboard and exit flue by means of sampling ports located along one wall of the combustor. Water cooled stainless steel probes lined with silica were used for gas sampling. An on-line chemiluminescent analysis (TECO Model 10A) was used to determine the nitric oxide content of the combustion gas.

3. Experimental results

3.1 NO emissions

NO concentrations throughout the bed and freeboard for the crushed coal (< 1.5 mm) are shown in Fig. 2 for bed temperatures ranging between 1043 and 1193 K. A sharp increase in NO concentration is observed from 400 to 1300 ppm for a bed temperature of 1043 K and concentrations rise to 1500 ppm at the top of the bed for T_b = 1193 K. For all the bed temperatures there is a sharp decrease in NO concentration through the freeboard giving exit values of 375 ppm for T_b = 1043 K and 700 ppm for T_b = 1193 K. Similar trends are seen in Fig. 3 for the large coals (6.3, 9.5 and 12.5 mm). The concentrations of NO at the top of the bed are of the order of 1400 ppm and at the exit they have fallen to 500 ppm for a bed temperature of 1143 K. These measurements were repeated for different values of excess air (XSA) and Fig. 4 shows the variation of NO concentration at the exit flue (corrected to 3% O_2) for XSA values of between 6 and 47% for all the large coals at T_b = 1043 and 1093 K. For the 6.3 mm coal at 10% XSA and T_b = 1043 the NO concentration is 360 ppm; the corresponding value at T_b = 1093 K is 475 ppm. After these initial values the NO concentrations at both temperatures show a sharp increase to about XSA = 25% followed by a levelling off for higher values of XSA. These trends are repeated for the 9.5 mm coal but with reduced concentrations throughout. It was expected that the 12.5 mm would show a further overall decrease in NO concentration but as can be seen in Fig. 4 the 12.5 mm curve falls between those of the 6.3 and 9.5 mm coals still, however, showing the same trends as the latter two sizes.

3.2 Elutriation rates

The measured elutriation rates under steady-state conditions are shown in Figs. 5, 6 and 7. Fig. 5 shows the total carry over (i.e. ash and carbon) leaving the combustor for the 9.5 mm coal at different levels of excess air and temperature. A sharp decrease in elutriated material is observed when the level of excess air is increased from 10% to about 20%; this rate of decrease reduces as the excess air is increased beyond 20%. The carbon content of the carry over material for the 9.5 mm coal is plotted against the excess air for the four bed temperatures (Fig. 6). The proportion of carbon in the carry over decreases with increasing temperature and excess air. The same trend is observed for all the coal sizes studied (17).

The effect of coal particle size on the carry over and carbon loss at 20% excess air is indicated in Fig. 7. A sharp decrease in carry over is observed when coal sizes of increasing diameters are used in the fluidised bed combustor. Beyond the 9.5 mm coal size, elutriation rates level off and as the bed temperature increases, show an upturn (Fig. 7). This unexpected behaviour of the carry over due to the 12.5 mm coal is in parallel with the NO results for the same coal as discussed above.

3.3 Combustion efficiency

The quantity of heat lost as carbon elutriated from the combustor is the major factor affecting the efficiency of fluidised bed coal combustors. Combustion effiency has been determined for each coal particle size at about 20% excess air. The results are shown in table 1 in terms of carbon percentage combustion efficiency. Loss of carbon occurred almost entirely by elutriation.

Table 1. Combustion Efficiency as a function of coal size and bed temperature.

Temp (K)	Combustion efficiency @ 20% XSA		
	6.3 mm	9.5 mm	12.5 mm
1043	84%	88%	90%
1093	88	90	91
1143	90	92	92
1193	-	95	93

An increased carbon combustion efficiency is achieved with the increase of air up to about 20-25%, a further increase in excess air beyond this value does not improve the carbon combustion efficiency significantly. The combustion efficiency is observed to increase with bed temperature for the 6.3 and 9.5 mm coals (table 1). The 12.5 mm results show only a slight sensitivity to bed temperature (1043 K - 1193 k, 20% excess air). The highest carbon combustion efficiency of 95% is achieved with the 9.5 mm at a bed temperature of 1193 K (table 1).

4. Discussion

The levels of NO at the exit of an FBC may be expressed as a sum of the rates of formation and reduction, without specifying any mechanisms, as follows

Rate of NO emitted at the flue	=	Rate of formation in the bed	-	Rate of reduction in the bed	+	Rate of formation in the freeboard	-	Rate of reduction in the freeboard	1)
		A		B		C		D	

It is clear from Figs. 2 and 3 that A > B and D > C for all the coals used in these experiments. There are many experimental data available which show that NO reduction in an FBC can take place via NO-char reactions (8,9,10) and so the level of NO reduction may be expected to be proportional to the carbon loading in the bed, which in turn is proportional to the diameter of the coal particles in the feed. When large coal is fed to the bed the rate of NO formation will be slower and lower than for crushed coal but the rate of reduction will also be lower even for larger carbon loading because of the low carbon surface area per unit mass.

This could explain why, as shown in Figures 2 and 3, approximately the same levels of NO concentration are observed at the top of the bed for both crushed and large coals. These similar levels of NO also contradict the suggestion (11) that overbed feeding of large coal may increase NO reduction at the top of the bed due to an increased carbon loading in that region. The NO concentrations in the 0.3 m square FBC, therefore, appear to be independent of coal feed position and size of coal fed. The major portion of NO reduction reported here, takes place in the freeboard (Figs. 2 and 3). In particular the highest reduction rate occurs in the region immediately above the bed where the char concentration is high due to splashing. It is in the freeboard then that the effect of carbon loading in the bed on NO reduction is most evident since the level observed for the 9.5 mm coal are lower than for the 6.3 mm and crushed coals. The NO levels in the freeboard are seen to decrease exponentially with height (Figs. 2 and 3) in the same manner as the solids population decreases (12).

Assuming that large coal particles do not break when introduced to the bed then it would be expected that the elutriation rate would be significantly reduced compared to when crushed coal is fed to the bed. Figure 5 shows a reduction in the elutriation rate of carbon as the coal feed particle size increases but the difference is not as great as would be expected bearing in mind that the large coal is a monosized feed and does not include any fines. In particular the carbon elutriation rate for the 12.5 mm coal although initially (T_b = 1043 K) less than that measured for the 9.5 mm subsequently becomes greater for T_b > 1093 K. This may be explained by the fact that this coal (12.5 mm) in particular suffers from breakage due to thermal shock when introduced to the bed. This also explains why the NO concentrations for this coal fall between those measured for the 6.3 and 9.5 mm coals (Fig. 4). Particle attrition may also be significant within the bed (13,14,15) particularly for the larger coals. Merrick and Highley (16) derive an expression for particle size reduction due to attrition based on Rittingers Law of abrasion and showed that the shrinkage rate was proportional to the particle size viz:

$$\frac{d\, d_p}{dt} = \frac{-K}{3}\, f\,(d_p)(U - U_{mf})\, d_p \qquad 2)$$

Thus the elutriation rate for the larger coals could be significantly enhanced due to attrition phenomena. The lowest elutriation rates observed (Fig. 7) are for the 9.5 mm coal at 1193 K and 20% XSA. The effect of increasing the bed temperature and excess air will be to increase the combustion rate with a consequent reduction in the amount of carbon thrown into the freeboard. Thus the elutriation rates will decrease for an increase in both T_b and XSA. This trend can be seen in Figs. 5 and 6.

5. Conclusions

The measurements of nitric oxide concentrations in the bed and freeboard of the 0.3 m square fluidised bed have shown that nitric oxide is produced within the bed and are reduced in the freeboard. Elutriation rates and NO concentrations measured at the exit of the freeboard both decrease with increasing coal particle size up to a size of 9.5 mm for most conditions. The combustion of monosized coal particles in the fluidised bed has highlighted the interdependence of elutriation rate, bed carbon content, carbon concentration in the freeboard and nitric oxide emissions. The results also indicate that an optimum operating condition for this particular fluidised bed combustor may exist for the 9.5 mm coal size at 20% XSA. However, further experimental results are necessary, in particular with respect to the complex phenomena occurring in the freeboard region.

6. Acknowledgements

This work forms part of the activities of the Sheffield Coal Research Unit sponsored by Shell Coal International and the National Coal Board, to whom the authors are grateful for financial assistance. The views expressed here are those of the authors and not necessarily those of the sponsors.

7. Nomenclature

d_p	coal particle dia.
$f(d_p)$	fraction of coal particles in bed smaller than d_p.
H	total bed height.
K	abrasion constant.
U	superficial fluidising velocity.
U_{mf}	minimum fluidising velocity.
y	vertical co-ordinance.
ε	dimensionless height (= y/H).

8. References

1. Skinner, D.G., Fluidised combustion of coal, Mills & Boon, Monograph No. CE/3, 1974.

2. Inst. of Fuel Symp. Ser. No. 1, Fluidised Combustion, 1975, Sessions B, C and D.

3. Gibson, J. and Highley, J., J. Inst. Energy, 1979, 52, 51.

4. Sixth Int. Conf. on Fluidised Bed Combustion, Atlanta, Proceedings, 1980.

5. Highley, J. et al., Inst. of Fuel Symp. Ser., No. 1, Fluidised Combustion, 1975, Paper B3.

6. Donsi, G. et al., 17th Symp. on Combustion (Int.), Leeds, 1978.

7. Sarofim, A.F. and Beer, J.M., 17th Symp. on Combustion (Int.), Leeds, 1978, 189.

8. Beer, J.M. et al., 5th Int. Conf. on Fluidised Bed Combustion, Washington D.C., 1977.

9. Furusawa, T. and Kunii, K., Soc. of Chem. Eng., Japan, 1977.

10. Gulyurtlu, I., Ph.D. Thesis, University of Sheffield, 1980.

11. Bachovchin, D.M., Beer, J.M. and Sarofin, A.F., A.I.Ch.E. Symp. Ser., 1981, 77, No. 205, 76.

12. Lewis, W.K. et al., Chem. Eng. Prog. Symp. Ser., 1962, 58, 38.

13. D'Amore et al., 6th Int. Conf. on Fluidised Bed Combustion, Atlanta, 1980, 2, 675.

14. Beer, J.M. et al., Inst. Energy Symp. Ser., No. 4, London, 1980, Paper IV-5.

15. Cowley, L.T. and Roberts, P.T., Fluidised Comb. Conf., Cape Town, 1981, 2, 443.

16. Merrick, D. and Highley, J., A.I.Ch.E. Symp. Ser., 1974, 70, No. 137, 366.

17. Brikci-Nigassa, M., Ph.D. Thesis, University of Sheffield, 1982.

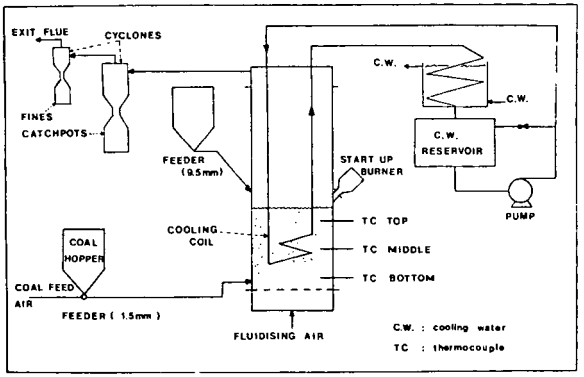

Fig. 1. (top). Fluidised bed combustor.

Fig. 2. (bottom). NO concentration as a function of excess air.

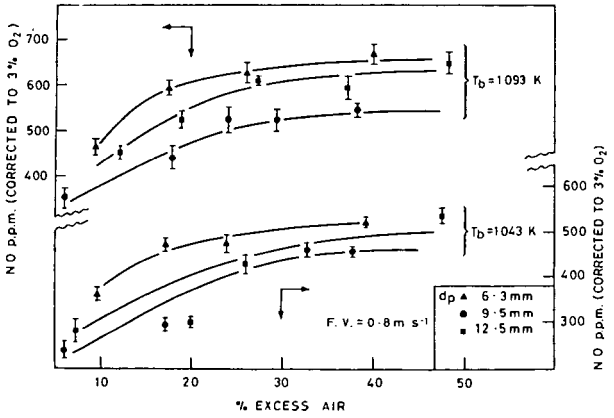

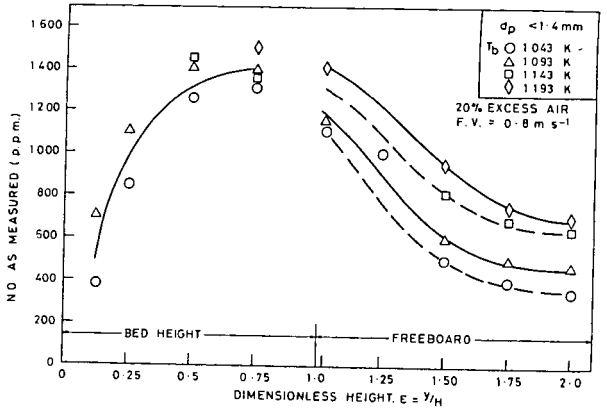

Fig. 3. (top). NO profiles for the crushed (< 1.5 mm) coal.

Fig. 4. (bottom). NO profiles for the large coals.

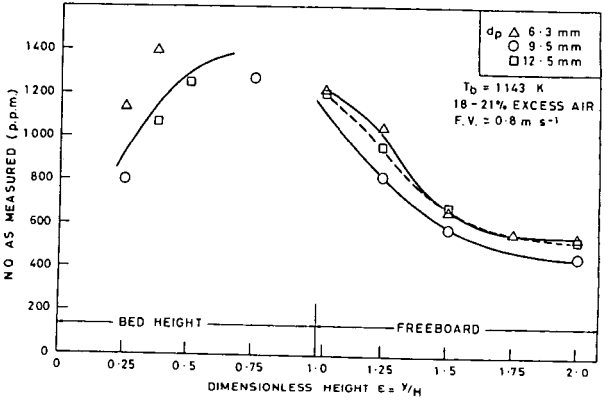

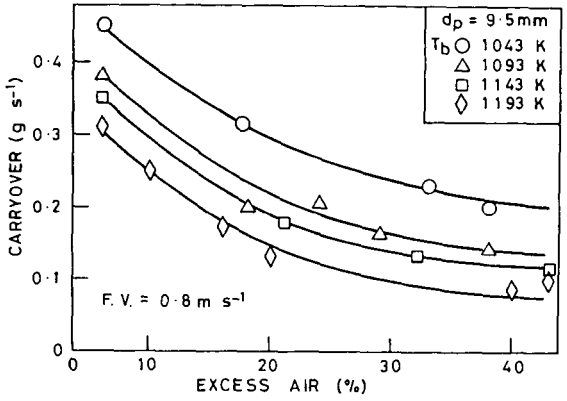

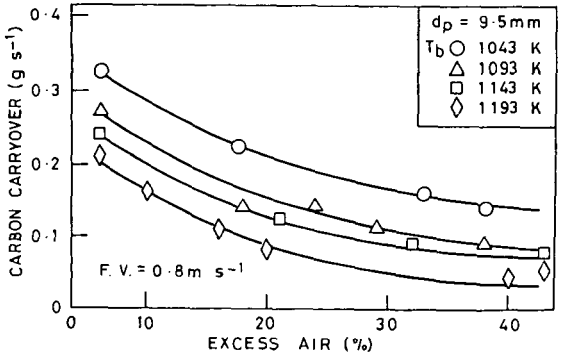

Fig. 5. (top). Carryover (carbon + ash) as a function of excess air (9.5 mm coal).

Fig. 6. (bottom). Carryover (carbon only) as a function of excess air (9.5 mm coal).

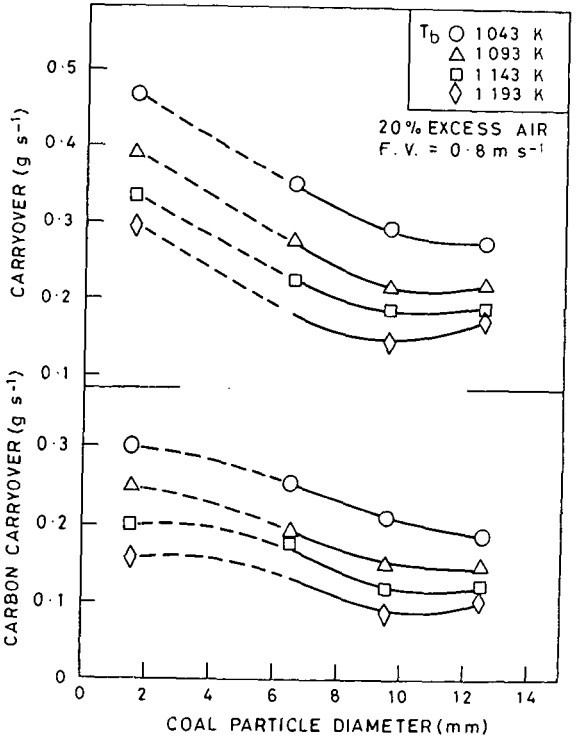

Fig. 7. Carbon and ash carryover (top) and carbon carryover only (bottom) as a function of coal particle diameter.

The influence of particle size distribution on the combustion rates in a batch fed fluidised bed

E.S. Garbett and A.B. Hedley

Sheffield Coal Research Unit, Department of Chemical Engineering and Fuel Technology, University of Sheffield, Sheffield, S1 3JD United Kingdom.

Introduction

The advantages of burning coal in fluidised bed combustors (FBC) have been repeatedly demonstrated over the past few years and commercial units are now being built and supplied to industry (1). The design of such FBC's is based on the practical experience gained from pilot plant studies and also on the predictions of mathematical models. Central to any model of coal combustion in FBC's is the rate at which particles burn in the bed which determines the carbon loading and hence pollutant emissions, heat release rates, coal feed rates and elutriation rates (2). Particle size and temperature usually indicate the controlling mechanism of combustion; large particles and high temperature suggest that diffusion is dominant whereas chemical kinetics became important for small particles and low temperatures (3). In a typical FBC the particle sizes range from that of the maximum of the input feed down to that of particles which are about to be elutriated and particle temperatures can have a value anywhere between the bed temperature T_b and T_b + 200K (4,5,6). It is not unreasonable to assume therefore, that the combustion of particles can be controlled by a combination of diffusional and chemical processes acting simultaneously. Indeed, the data of Avedesian and Davidson (7), where the combustion of char particles in a batch fed fluidised bed was assumed to be diffusion controlled, has recently (6) been shown to be consistent with the alternative situation described above where both processes are acting together. The effect on the carbon loading in an FBC where the combustion is either controlled by diffusion or by a combination process has been investigated by Garbett and Hedley (8) who also showed the importance of particle surface temperatures. The particle size distribution of the coal feed is a parameter which is important in the design of FBC's but whose influence on the combustion rates in the bed has not been studied. It is the purpose of this paper therefore, to develop a theory to predict the burnaway, burnout time and particulate phase oxygen concentration in a batch fed FBC and show their dependence on the input particle size distribution which is accurately known.

The Model

The model of the batch fed FBC employed here is essentially the two-phase bubbling bed model of Avedesian and Davidson (7) where a bed of inert particles at a temperature T_b is fluidised by air at a superficial velocity U_o and a minimum fluidised velocity U_{mf}. The oxygen required for combustion which is controlled by a combination of diffusion and chemical kinetics, is transferred to the char particles in the particulate phase from the bubbles and the reaction is given by $C + O_2 \rightarrow CO_2$. The batch is assumed to comprise solely of char particles so that devolatilisation is neglected. It is also assumed that the particles do not swell or break up when introduced to the bed and so retain their original size distribution.

The Theory

The reaction rate of a single particle of char of mass m_p in a fluidised bed where both diffusional and chemical kinetics are considered simultaneously, can be expressed in terms of diffusional and chemical resistances as follows (3).

$$R = \frac{K_c K_D C_p}{K_c + K_D} \qquad 1)$$

where $K_D = -k_1 x$ 2)

$K_c = -k_2 x^2$ 3)

(See equations 28) and 31) for values of k_1 and k_2)) C_p is the oxygen concentration (moles/m^3) in the particulate phase of the bed and is a function of time.

The rate of consumption of carbon at the particle surface is therefore given by

$$\frac{dm_p}{dt} = \frac{-k_1 k_2 x_p^3 M_o C_p}{k_1 x_p + k_2 x_p^2} \qquad 4)$$

leading to

$$\frac{dx_p}{dt} = \frac{-2M_o C_p}{\pi\rho} \left[\frac{1}{\frac{x_p}{k_1} + \frac{1}{k_2}}\right] \qquad 5)$$

where x_p is the diameter of a particle of mass m_p and M_o is the molecular weight of oxygen.

For convenience let $F(C) = \frac{2M_o C_p}{\pi\rho}$, $e = \frac{1}{k_2}$ and $f = \frac{1}{k_1}$

If after a time t a particle whose original diameter was x burns to give a diameter x_t, then

$$x_t = \frac{1}{f}\left[(e^2 + 2efx + f^2x^2 - 2f\int_o^t F(C)dt)^{\frac{1}{2}} - e\right] \qquad 6)$$

Let the original size distribution of a batch of carbon delivered to the fluidised bed be given by an equation of the form.

$$W_i = \theta(x) \qquad 7)$$

where W_i is the initial weight of the batch which consists of particles whose diameter is greater than or equal to x. It will be assumed that x must lie in the range $x_1 \leqslant x \leqslant x_2$ such that whatever the form of the function θ the conditions $\theta(x_1) = 1$ and $\theta(x_2) = 0$ are satisfied.

The initial mass of the batch which has particles whose diameters lie between x and x +dx is therefore, $m_i\, dW_i$, where m_i is the mass of the original batch. After a time t the mass will reduce to $m_i\, dW_i\, x_t^3/x^3$.

Therefore the mass of carbon in the bed after a time t is

$$m = \int_{x_1}^{x_2} m_i \frac{x_t^3}{x^3} \psi(x)\, dx \qquad 8)$$

where $\psi(x)\, dx = -dW_i$ and the lower limits of the integral are chosen to indicate

all the initial values of x for which $x_t > o$. Suppose an initial diameter y_o is defined so that all particles with an initial diameter $x < y_o$ would have burned away completely after a time t, then the mass fraction of carbon in the bed at this time t is

$$\frac{m}{m_i} = \int_{x=z}^{x=x_2} \frac{x^3 - t}{x^3} \psi(x)dx \qquad 9)$$

where $z = x_1$ if $y_o \leq x_1$

and $z = y_o$ if $y_o > x_1$

By substituting y_o in equation 6) we have

$$\int_o^t F(C)dt = ey_o + \frac{f}{2} y_o^2 \qquad 10)$$

Combining equations 6), 8) and 10) gives

$$\frac{m}{m_i} = \int_{x=z}^{x=x_2} \frac{\left\{\left[\left(\frac{k_1}{k_2}\right)^2 + 2\left(\frac{k_1}{k_2}\right)(x-y_o)+(x^2-y_o^2)\right]^{\frac{1}{2}} - \frac{k_1}{k_2}\right\}^3 \psi(x)}{x^3} dx \qquad 11)$$

Burnout time

To derive an expression for the burn-out time we need to investigate dm/dt or $d(m/m_i)/dt$. From an oxygen balance on the bed (7) we have

$$12(C_o - C_p)A[U_o - U_{mf})(\exp(-B))] = -\frac{dm}{dt} \qquad 12)$$

where C_o is the inlet oxygen concentration ($mole/m^3$).

Therefore $C_p = C_o + \frac{dm/dt}{F(U_o)}$ 13)

where $F(U_o) = 12A[U_o - (U_o - U_{mf})(\exp(-B))]$

It can therefore be shown that

$$\frac{dm}{dt} = \left[\frac{2C_o}{\frac{\pi\rho}{M_o}\cdot\frac{(e+fy_o)}{dm/dy_o} - \frac{2}{F(U_o)}}\right] \qquad 14)$$

Also, from equation 13)

$$C_p = C_o\left[1 + \frac{1}{\left(\frac{F(U_o)\pi\rho(e+fy_o)}{2M_o dm/dy_o}\right) - 1}\right] \qquad 15)$$

dm/dy_o can be found using the mathematical identity,

$$\frac{d}{dy_o}\left[\int_a^b g(x,y_o)\,dx\right] = \int_a^b \frac{\partial}{\partial y_o}\left(g(x,y_o)dx\right) + g(b,y_o)\frac{db}{dy_o} - g(a,y_o)\frac{da}{dy_o} \qquad 16)$$

Applying this to equation 11) gives

$$\frac{dm}{dy_o} = -3k_1(e+fy_o)m_i \int_{x=z}^{x=x_2} F_1(x,y_o)\ \psi(x)\,dx \qquad 17)$$

where

$$F_1(x,y_o) = \frac{\left\{\left[\left(\frac{k_1}{k_2}\right)^2 + 2\left(\frac{k_1}{k_2}\right)(x-y_o)+(x^2-y_o^2)\right]^{\frac{1}{2}} - \frac{k_1}{k_2}\right\}^2}{x^3\left[\left(\frac{k_1}{k_2}\right)^2 + 2\left(\frac{k_1}{k_2}\right)\cdot(x-y_o)+(x^2-y_o^2)\right]} \qquad 18)$$

Substituting dm/dy_o from equation 17) into equation 14)

re-arranging and integrating the result gives

$$\int_o^t dt = -\frac{1}{F(U_o)C_o}\int_{m_i}^{m} dm - \frac{\pi\rho}{6M_oC_ok_1m_i}\cdot\int_{m_i}^{m}\frac{dm}{\int_z^{x_2} F_1(x,y_o)\psi(x)dx} \qquad 19)$$

It can be shown that equation 19) reduces to

$$t = \frac{m_i\,(1-m/m_i)}{F(U_o)C_o} + \frac{\pi\rho\ y_o^2}{128C_ok_1} + \frac{\pi\rho\ y_o}{64C_ok_2} \qquad 20)$$

The form of the initial size distribution

Assume that the original carbon sample before any sieving into limited size range fractions, can be described by a Rosin-Rammler distribution

$$W = \exp(-bx^n) \qquad 21)$$

where b and n are constants. If the original material is then sieved into limited size fractions and only particles with diameters in the range $x_1<x<x_2$ are retained then the weight fraction W_i of the sieved material is (9)

$$W_i = \frac{\exp(-bx^n) - \exp(-bx_2^n)}{\exp(-bx_1^n)-\exp(-bx_2^n)}$$

Therefore

$$\psi(x) = \frac{bnx^{n-1}\exp(-bx^n)}{\exp(-bx_1^n)-\exp(-bx_2^n)} \qquad 22)$$

and the initial weighted mean particle size $\bar{x}_i$ is (9)

$$\bar{x}_i = \frac{\left[\left(\frac{1}{n}+1\right)\right]}{b^{1/n}} \qquad 23)$$

Defining dimensionless parameters $X = \frac{x}{\bar{x}_i}$ and $Y = \frac{y_o}{\bar{x}_i}$ then from equation 22) we get

$$\psi(\bar{x}_i, x) = \frac{naX^{n-1}\exp(-aX^n)}{\exp(-aX_1^n)-\exp(-aX_2^n)} \qquad 24)$$

where $a = \left[\left(\frac{1}{n}+1\right)\right]^n$

Substitution of $\psi(\bar{x}_i, x)$ from equation 24) into equation 11) and making other appropriate terms dimensionless gives

$$\frac{m}{m_i} = \frac{1}{N}\int_Z^{X_2}\left\{F_2(\bar{x}_i, X, Y) - \left(\frac{k_1}{k_2\bar{x}_i}\right)\right\}^3 an\, X^{n-4}\, e^{-ax^n}\, dx \qquad 25)$$

where

$$F_2(\bar{x}_i, X, Y) = \left[\left(\frac{k_1}{k_2\bar{x}_i}\right)^2 + \left(\frac{2k_1}{k_2\bar{x}_i}\right)(X-Y) + (X^2-Y^2)\right]^{\frac{1}{2}}$$

$N = \exp(-aX_1^n) - \exp(-aX_2^n)$ and $Z = \frac{z}{\bar{x}_i}$

The lower limit of integration in equation 25) is given by

$Z = X_1$ if $Y \leq X_1$

and

$Z = Y$ if $Y > X_1$

Similarly equation 20) for the burn-out time, becomes

$$t = \frac{m_i\,(1-m/m_i)}{F(U_o)C_o} + \frac{\pi\rho(\bar{x}_i^2 Y^2)}{128C_o k_1} + \frac{\pi\rho(\bar{x}_i Y)}{64C_o k_2} \qquad 26)$$

and equation 15), the particulate phase oxygen concentration, becomes

$$C_p = C_o\left[1 - \frac{1}{\left(\frac{F(U_o)\,\pi\rho}{192k_1 m_i}\int_Z^{X_2} F_3(\bar{x}_i, X, Y)\,d\right) + 1}\right] \qquad 27)$$

where

$$\int_Z^{X_2} F_3(\bar{x}, X, Y)\,dX = \frac{na}{N\bar{x}_i^{3/2}}\int_Z^{X_2}\left[F_2(\bar{x}_i, X, Y)\left(\frac{k_1}{k_2\bar{x}_i}\right)\right]^2 X^{n-4}\, e^{-aX^n}\, dX$$

Numerical Calculations

The diffusion constant k_1 from equation 2) can be expressed as follows (7)

$$k_1 = 2\pi k D_E \qquad 28)$$

where k is a constant relating the mass of carbon consumed to the mass of O_2 transported to the particle surface. It is assumed here that the carbon-oxygen reaction can be represented by $C + O_2 \rightarrow CO_2$ so that k = 12/32

D_E is the effective diffusion coefficient and can be represented by (7)

$$D_E = \frac{D_G \, Sh}{2} \qquad 29)$$

where Sh is the local particle Sherwood Number and D_G is the diffusion coefficient calculated from (3)

$$D_G = D_i \frac{(P_i)}{P} \left(\frac{T}{T_i}\right)^{1.75} \qquad 30)$$

The chemical constant k_2 can be represented by (10,11)

$$k_2 = k' \, T_b^{\frac{1}{2}} \exp(-E/R_g T_p) \qquad 31)$$

The above data is summarised in Table 1. The bed data used in the calculations are that of Avedesian and Davidson (7).

Table 1

Data used in calculations

Symbol	Value	Reference
k	0.375	
T_i	1000 K	(3)
D_i	1.61	(3)
T_b	1173 K	(7)
T_p	1173 K	(7)
k´	1034	(11,12)
Sh	1.8	(8)
E	15 K cal/mole K	
P/P_i	1	

The three distributions used in the calculations are summarised in Table 2. In all the results presented here the top and bottom size of each distribution were constant at 3 and 0.3mm respectively.

Table 2

Particle size data

	b=11.12	b=625	b=10000
n	1.5	4	4
$\bar{x}_i$	0.1813	0.1813mm	0.0906mm
Γ	0.9033	0.9064	0.9064
x_1	0.3mm	0.3mm	0.3mm
x_2	3mm	3mm	3mm
m_i	5gm	5gm	5gm

Results and Discussion

Evaluation of m/m_i

To demonstrate the type of results to be expected from the theory equation 25) was numerically integrated to give values of m/m_i for increasing values of Y using the values of k_1 and k_2 indicated in Table 1 and the distributions in Table 2. For comparison the values of m/m_i for the pure diffusional and chemical cases were calculated using a method similar to that described by Leesley and Siddall (9) for pulverised fuel. Figures 1, 2 and 3 show the variation of m/m_i, the unburnt fraction of carbon remaining, with the dimensionless particle diameter Y for the three original distributions. In every case the combined curve m_{C+D}/m_i falls inside the envelope of the two extreme conditions of pure diffusional (m_D/m_i) and of pure chemical (m_C/m_i). The curves represented in these figures (1,2, and 3) are not burnaway rates but indicate the changing particle size distribution as the batch disappears. For example, in figure 1, when 50% of the batch has burnt away (i.e. $m/m_i = 0.5$) the combined case requires that all particles of a size below 18% of the maximum particle size in the original batch must have disappeared. Corresponding values for the pure diffusion case and pure chemical case are 34% and 12% respectively. Thus for a given carbon loading the carbon particle size distribution in the bed will be different for different combustion mechanisms and this will obviously influence important phenomena such as elutriation, and NO reduction by char. To combine Figures 1 to 3 for comparison purposes the data have been represented in Figure 4 as a ratio of unburnt fraction for the combined case (m_{C+D}) to that for the diffusion case (m_D) as a function of the particle diameter Y. It is clearly seen that as the original size distribution moves from a wide one (n=1.5, b=11.12) to a fine one (n=4.0, b=10,000) the difference between m_{C+D} and m_D increases

Evaluation of t

The burnaway rates of the batch for each original size distribution and for a combustion mechanism where both diffsuion and chemical kinetics are acting simoultaneously were calculated from equation 26) and are shown in Figure 5. The burnaway rate is higher for the distribution represented by n=4.0, b=10,000 than for the other two distributions as would be expected. What is not evident

from Figure 5, due to the scale, is that the time for total burnaway is the same for each distribution since they all have the same maximum particle size of 3mm.

Evaluation of C_p

Equation 27) was numericatly integrated to give the particulate oxygen concentration C_p for the three distributions. The results are shown in Figure 6. An interesting feature of these results is the value of C_p at t=o. According to Avedesian and Davidson (7) the value of C_p should be almost zero for the batch fed system but it is clear from Figure 6 that this is not the case.

Equations 25), 26) and 27) are valid only for constant temperature and pressure. These conditions are usually met in FBC's except that the particle temperature T_p can vary during burnaway and can be appreciably higher than the bed temperature (4,5,6). The effect of increasing T_p would be to increase the value of k_2 relative to k_1 and the controlling mechanism would tend towards that of diffusion. Increasing the pressure of the system would only have a significant effect if the combustion rate was initially dominated by chemical kinetics.

Conclusions

A theoretical model has been developed which predicts the change in size distribution during burnaway, burn-out times and particulate phase oxygen concentrations as a function of original particle size distribution in a batch fed fluidised bed. If the original size distribution is accurately known a batch fed experiment could be devised to determine the role of chemical kinetics for a given type of coal and would thus be an aid to modelling of fluidised bed combustion.

Acknowledgements

The work described here form part of the activities of the Sheffield Coal Research Unit sponsored by Shell Coal International and the N.C.B.. The authors are grateful for the financial assistance of the Sponsors and wish to point out that the views expressed here are those of the authors and not necessarily those of the Sponsors. We are also grateful to Dr. R.G. Siddall and Dr. P.J. Foster for many illuminating discussions.

Nomenclature

a	Constant defined by equation 24)
A	Area of fluidised bed (m^2)
b	Rosin-Rammler constant - equation 21)
B	Oxygen exchange parameter - equation 12)
C_o	Oxygen concentration of fluidising air ($mole/m^3$)
C_p	Particulate phase oxygen concentration ($mole/m^3$)
D_G	Gas diffusion coefficient (m^2/s)
e	constant ($= 1/k_2$)
f	constant ($= 1/k_1$)
$F(U_o)$	Defined by equation 12)
F(C)	Function of Oxygen concentration ($= 2M_oC_p/\pi\rho$)

k_1	Constant defined by equation 2)	
k_2	Constant defined by equation 3)	
k'	Constant defined by equation 31)	
K_c	Chemical rate constant	
K_D	Diffusional rate constant	
m	Mass of char in bed at time t	(kg)
m_i	Initial mass of batch	(kg)
m_p	Mass of single char particle	(kg)
N	Function of particle size - equation 25)	
P	Pressure	(atm)
R	Reaction rate of single particle	(kg/s)
R_g	Gas constant	
t	Burnaway time	(s)
T	Temperature	(K)
T_b	Bed temperature	(K)
T_i	Reference temperature - equation 30)	(K)
T_p	Particle surface temperature	(K)
U_{mf}	Minimum fluidising velocity	(m/s)
U_o	Superficial fluidising velocity	(m/s)
W	Weight fraction of coal	(kg)
x	Particle diameter	(mm)
$\bar{x}_i$	Initial weighted mean particle size	(mm)
x_p	Particle diameter	(mm)
x_t	Particle diameter	(mm)
X	Dimensionless particle diameter	(= $x/\bar{x}_i$)
y_o	Particle diameter	(mm)
Y	Dimensionless particle diameter	(= $y_o/\bar{x}_i$)
z	Particle diameter (lower limit of integration)	mm
Z	Dimensionless particle diameter	(= $z/\bar{x}_i$)

Greek Symbols

ρ	Char density
θ	Size distribution function equation 7)
ψ	Size distribution function equation 8)
Γ	Gamma function

References

1. Gibson, J. and Highley, J., J. Inst. E., 1979, 52, 51.
2. Sarofim, A.F. and Beer, J.H. Combustion Inst. Conf. No. 17, 1978, 189.
3. Field, M.A. Gill, D.W., Morgan, B.B. and Hawksley, P.G.W., Combustion of Pulverised Coal, 1967, BCURA.
4. Basu, P., Fuel, 1977, 56, 390.
5. Yates, J.R. Witkowski, A.R. and Harrison, D., Trans. I. Chem. E. 1980, 58, 69.
6. Garbett, E.S. and Hedley, A.B. Power Ind. Research, 1981, 1, 91.
7. Avedesian, M.M. and Davidson, J.F., Trans. I. Chem. E.
8. Garbett, E.S. and Hedley, A.B., Inst. Energy Symp. Series No. 4, 1980, paper IV-6.
9. Leesley, M.E. and Siddall, R.G., J. Inst. F., 1972, 45, 169.
10. Marsden, C., Ph.D. Thesis, University of Sheffield, 1964.
11. Beer, J.M., Ph.D. Thesis, University of Sheffield, 1959.

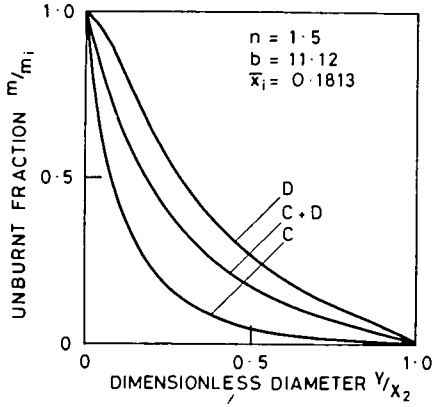

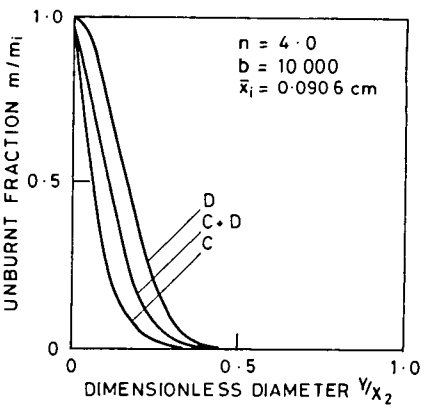

Fig. 3. (top). Unburnt mass fraction (m/m_i) of the batch during burnaway.

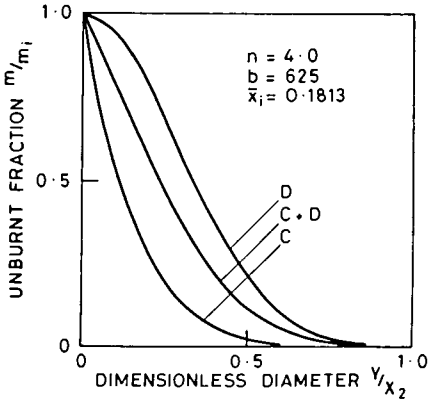

Fig. 1. (top) and Fig. 2. (bottom). Unburnt mass fraction (m/m_i) of the batch during burnaway.

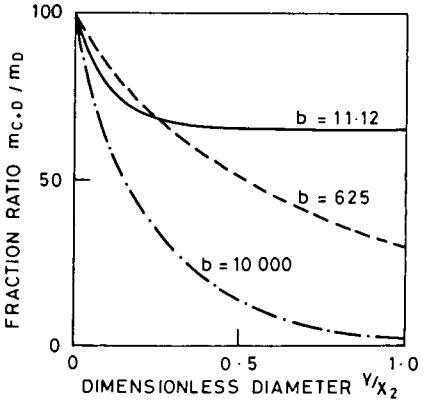

Fig. 4. (bottom). Unburnt mass fraction ratio (m_{C+D}/m_D) during burnaway for the three distributions.

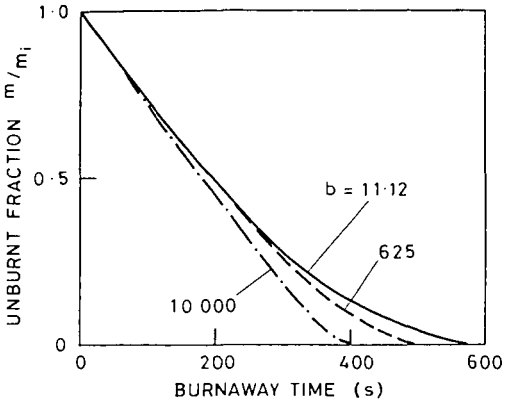

Fig. 5. (top). Burnaway rate of the batch for the three distributions.

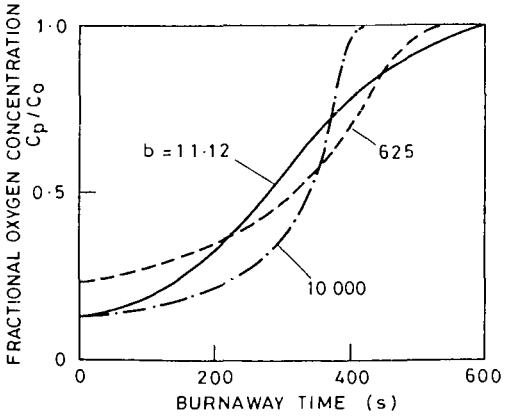

Fig. 6. (bottom). Particulate phase oxygen concentration (C_p) during burnaway for the three distributions.